國立臺灣大學工學院材料科學與工程學系暨研究所

碩士論文

Department of Materials Science and Engineering

College of Engineering

National Taiwan University

Master Thesis

$L1_2$析出強化型中熵合金$(CrCoNi)_{94}Al_3Nb_3$之顯微結構與機械性質分析

Microstructure and Mechanical Properties Characterization of $L1_2$-precipitate Hardening $(CrCoNi)_{94}Al_3Nb_3$ Medium-entropy-alloy

駱炯源

Chiung-Yuan Lo

指導教授：楊哲人 博士

Advisor: Jer-Ren Yang, Ph.D.

中華民國 112年 07月

July 2023

doi:10.6342/NTU202302391

國立臺灣大學碩士學位論文
口試委員會審定書

論文中文題目： $L1_2$ 析出強化型中熵合金 $(CrCoNi)_{94}Al_3Nb_3$ 之顯微結構與機械性質分析

論文英文題目： Microstructure and Mechanical Properties Characterization of $L1_2$-precipitate Hardening $(CrCoNi)_{94}Al_3Nb_3$ Medium-entropy-alloy

本論文係**駱炯源**君**(R10527007)**在國立臺灣大學材料科學與工程學系、所完成之碩士學位論文，於民國 112 年 7 月 28 日承下列考試委員審查通過及口試及格，特此證明

口試委員： 楊哲人 楊哲人
（指導教授）

黃慶淵 黃慶淵

李驊登 李驊登

蔡劭璞 蔡劭璞

系主任、所長 蔡豐羽 蔡豐羽 （簽名）

doi:10.6342/NTU202302391

Acknowledgements

我很慶幸能夠加入台大材料所楊哲人的實驗室，我想藉此機會表達我對您在我碩士班的指導之感謝。在這段時間中，您以豐富的知識和豁達的心胸，引導我們學術上的成長與進步。此外，我也想感謝您在我的研究過程中提供的支持和協助。您總是願意花時間與我們討論問題，提供有價值的建議和指導。您的耐心和專業，讓我們克服了許多研究上的困難，讓我們能夠達成研究目標。

此外，我也想感謝指導我的陳家俊、邱柏翰、曹梓敬、呂仕淵與戴正淩學長們，不僅指導我如何操作電子顯微鏡，也分享許多將照片優化的方法，甚至是後續的繞射圖案分析，讓我更快速的上手顯微結構分析的領域。學長們也在我實驗挫折時，給予我許多鼓勵與調整的建議，讓我得以完善我的研究，非常感謝學長們的用心。

我也感謝同屆的實驗室同學們，林宜嫺、曾千育、朱芊瑜、鄒祥琳與林冠名，大家互相討論數據的疑點，分享自己的看法，都是互相進步與學習的機會，我很幸運能夠有一群一起互相努力的同伴們，能夠在晚上一起磨 TEM 試片，實則是難忘的回憶。

我也想感謝曾詩雅、林泓任、梁書誠與游雨蓁學弟妹們，感謝學弟妹們時常陪我去滾壓室處理試片，也在我失敗的時候給予我許多改進的建議，也感謝學弟妹們分享許多新穎的文獻，讓我得以在繁忙的時候，還能後汲取到文獻上的新知識。

最後，感謝在 seminar 上給予我許多建議的陳致遠老師與蘇德徵老師，老師們的建議都非常寶貴且精確，讓我在 seminar 後，能夠思考更多來修正我的實驗。

感謝 Yang group 的每一位貴人，謝謝你們的用心與付出。

摘要

高熵合金擁有優異的機械性能，其中以 CrCoNi 三元中熵合金表現最為突出。然而，單相面心立方高熵合金與中熵合金的降伏強度僅有 200 MPa 至 500 MPa，並不適合應用於需要高降伏強度的環境中。因此，本研究設計 L1$_2$ 析出強化中熵合金(CrCoNi)$_{94}$Al$_3$Nb$_3$，透過在 700°C 和 800°C 進行時效處理，在 FCC 基底中引入均勻分布的 L1$_2$-Ni$_3$(Al,Nb)奈米析出物，以提高 FCC 型的中熵合金的降伏強度和機械性能。在微結構分析顯示顯示，L1$_2$-Ni$_3$(Al,Nb)的尺寸約為 5 至 10 奈米且在 FCC 基底當中分布的非常均勻，此外，也發現尚未被報導過的 δ 相轉變與 HCP 相生成。在拉伸試驗中，經過 700ºC 尖峰時效處理後降伏強度和極限拉伸強度分別達到 1412 ± 22 MPa 與 1553 ± 45 MPa，且伸長率達到 7.8 ± 0.94 %。在霍普金森快速撞擊試驗中，相較於未進行析出的中熵合金 FeCrCoNi，(CrCoNi)$_{94}$Al$_3$Nb$_3$ 在相同真實應變量下，達到約 2600MPa 的真實應力，約為 FeCrCoNi 的兩倍強度，展現其優異的衝擊性能。在變形組織分析中，本研究，探討 L1$_2$ 析出物與缺陷、疊差和變形雙晶之間的相互作用，也探討造成材料延展性下降與高降伏強度的因素。

Abstract

High-entropy alloys (HEAs) exhibit excellent mechanical properties, with the CrCoNi ternary medium-entropy alloy being particularly outstanding. However, the yield strength of single-phase face-centered cubic (FCC) high-entropy alloys (HEAs) and medium-entropy alloys (MEAs) ranges approximately from 200 MPa to 500 MPa, which is not suitable for applications requiring high yield strength. Therefore, in this study, a $L1_2$ precipitate-hardening MEA, $(CrCoNi)_{94}Al_3Nb_3$, was designed. Through aging treatments at 700°C and 800°C, uniformly distributed $L1_2$-$Ni_3(Al,Nb)$ nanoscale precipitates were introduced into the FCC matrix to enhance the yield strength of the FCC-type MEA. Microstructure analysis revealed that the $L1_2$-$Ni_3(Al,Nb)$ precipitates had sizes of approximately 5 to 10 nanometers and were distributed very uniformly within the FCC matrix. Additionally, the transformation of δ phase and the generation of hexagonal close-packed (HCP) phase were also observed. In tensile tests, after peak aging treatment at 700°C, the yield strength and ultimate tensile strength reached 1412 ± 22 MPa and 1553 ± 45 MPa, respectively, with an elongation of 7.8 ± 0.94%. In Hopkinson bar impact tests, $(CrCoNi)_{94}Al_3Nb_3$ demonstrated a true stress of approximately 2600 MPa with 20% true strain, showing twice the strength of FeCrCoNi and exhibiting excellent impact performance compared to the non-precipitated medium-entropy alloy FeCrCoNi. In the deformation microstructure analysis, this study explored the interactions between $L1_2$ precipitates and defects, stacking faults, and deformation twins. It also investigated the factors contributing to the reduction in material ductility and the high yield strength.

doi:10.6342/NTU202302391

Table of contents

doi:10.6342/NTU202302391

List of Figures

doi:10.6342/NTU202302391

doi:10.6342/NTU202302391

doi:10.6342/NTU202302391

doi:10.6342/NTU202302391

List of Tables

doi:10.6342/NTU202302391

Chapter One Introduction

High-entropy alloys (HEAs) are novel alloys composed of multiple elements mixed with equimolar or near equimolar ratios[1-3]. HEAs can tend to form a single-phase solid solution subjected to extremely high configuration entropy, such as CrCoFeMnNi (FCC), VNbMoTaW (BCC), $\mathrm{Al_{20}Li_{20}Mg_{10}Sc_{20}Ti_{30}}$(HCP)[4-6]. HEAs successfully resolved the problems of intermetallic compounds or second phases in traditional alloys. HEAs has been reported with several superior properties, such as high strength [7-9], exceptional cryogenic strength [10, 11], refractory applications [5, 12, 13], and corrosion resistance [14-16]. As a result, novel designs of HEAs demonstrate the promising possibility of substituting conventional alloys such as stainless steels and nickel-based superalloys.

In recent years, FCC medium-entropy alloys (MEAs), such as FeCoCrNi/CoCrNi, have exhibited outstanding mechanical properties through reducing the stacking-fault energy (γ). Dislocations in low stacking-fault energy would dissociate into partial dislocations since it is more energy favorable. Low stacking-fault energy alloys maintain work hardening rate through introducing deformation twins. In other words, strong twinning induced plasticity (TWIP) effect dominates the deformation processes to increase both strength and ductility [17-20]. The stacking-fault energies of CrCoNi,

doi:10.6342/NTU202302391

FeCrCoNi and CrCoFeMnNi have been reported to be 18 ± 4 ($mJ \cdot m^{-2}$) 27 ± 4 ($mJ \cdot m^{-2}$) and $30 \pm 5\,(mJ \cdot m^{-2})$ [21-23]. Low stacking-fault energy alloys demonstrate better mechanical properties since strong TWIP effect dominate the deformation processes rather than conventional dislocation interactions. Furthermore, high-density nanotwins and nano-HCP phases are generated, high-density bundles of nanotwins being favorable while reducing the stacking-fault energy. Because of its low stacking-fault energy, CrCoNi alloy has been found to possess a higher ultimate tensile strength with a better elongation as compared to FeCrCoNi and CrCoFeMnNi alloys [10, 22, 24, 25].

Although FCC MEAs present exceptional mechanical properties, they encounter the problem of low yield strength. For example, the yield strength of CrCoNi is in the range between 350 to 500 MPa, depending mainly on the grain sizes [7, 10, 22, 23, 26, 27]. To enhance the yield strength in FCC-based MEAs, the similar concepts of precipitate hardening in nickel-based superalloys were applied in MEAs [28-31]. In nickel-based superalloys, γ' ($L1_2$ structure) or γ'' ($D0_{22}$ structure) was the strengthening phases in the FCC matrix through adding Al, Ti, and Nb as precipitate forming elements [32]. In MEAs, CrCoNi or FeCrCoNi, single phase FCC, have been substituted the nickel matrix in nickel-based superalloys. Subsequently, Al and Ti, the precipitate forming elements, were added to generate γ' as the strengthening phase.

For example, He et al. [9] proposed a $L1_2$-precipitate hardening MEA, $(FeCrCoNi)_{94}Al_4Ti_2$. Nanoscale $L1_2$-$Ni_3(Al,Ti)$ particles were successfully produced in the FCC matrix. The corresponding yield strength and ultimate tensile strength were 1094 MPa and 1273 MPa, respectively with 17 % elongation. For another similar work [33], Zhao et al. suggested a MEA strengthened by $L1_2$-$Ni_3(Al,Ti)$ in $(CrCoNi)_{94}Al_3Ti_3$ alloy. The yield strength and ultimate tensile strength were 780 MPa and 1.3 GPa, respectively with 45 % elongation. These two works had demonstrated that $L1_2$ particles can significantly improve the strength of FCC-based MEAs. However, some problems have not been resolved in the Al/Ti addition MEAs. First, the $L1_2$ particles were not uniformly distributed in the FCC matrix. $L1_2$ particles might have become abnormal coarse near the grain boundary, which were not quite effective to strength the alloys (see Figure 1-1) [9]. Therefore, uniformly-distributed $L1_2$ precipitate particles may potentially promote the yield strength to a higher level. Second, Ti addition would cause η-$NiTi_3$ formation with the lamellar-like morphology [34-37]. Though η-Ni_3Ti indeed contributed to yield strength, it would compete the Ti element with $L1_2$-$Ni_3(Al,Ti)$, causing the non-uniformity problems (see Figure 1-2). Therefore, with Ti addition, a mixed precipitation microstructure of η and $L1_2$ would present in the FCC matrix. However, uniform nano-$L1_2$ precipitates in the FCC matrix without η phase might have had better potential to promote the strength in MEAs.

doi:10.6342/NTU202302391

We attempted to design a $L1_2$-precipitate hardening MEA, $(CrCoNi)_{94}Al_3Nb_3$ (at%). For the strong precipitate-forming elements, Al, Ti and Nb, are presumed all favorably to form $L1_2$-$Ni_3(Al,Ti,Nb)$. However, in the present work, the addition of Al and Nb without Ti to promote the formation of $L1_2$ is based on the following three considerations. First, without Ti addition to avoid η-$NiTi_3$ formation, the uniformly-distributed nano-precipitate $L1_2$ can possibly produce. Second, in the previous work of $(FeCrCoNi)_{94}Al_4Ti_2$ [9], the abnormal coarsening of $L1_2$-$Ni_3(Al,Ti)$ precipitates at grain boundaries might be caused by grain boundary diffusion. $L1_2$-$Ni_3(Al,Ti)$ particles could reduce the lattice strain through coarsening, which was energy favorable, and grain boundaries could fast replenish Ni, Al and Ti while these elements were consumed by $L1_2$-$Ni_3(Al,Ti)$. Therefore, in this work, to hinder grain boundary diffusion, lattice misfit was created by adding Nb because Nb possessed larger atomic radii than other elements in this MEA, which could become obstacles of diffusion. ($a_{Cr} = 166pm, a_{Co} = 152pm, a_{Ni} = 149pm, a_{Al} = 118pm, a_{Ti} = 176pm, a_{Nb} = 198pm$) [38]. Third, the optimal $L1_2$ forming elements in MEAs is approximately 6 at % [9, 39-42]. In this work, instead of adding 6 at % Al, 3 at % Al and 3 at % Nb were added to generate $L1_2$ precipitates because the previous simulation results suggested that Al-Al bond could have caused detwinning in MEAs [43]. Excess Al addition may diminish the ability of twinning, which is the advantage of low-stacking fault energy alloys, MEAs.

This work attempted to improve the strength in FCC-based MEAs through introducing L1_2-$Ni_3(Al,Nb)$ nano-precipitates in the FCC matrix. For mechanical properties, tensile tests were performed at room temperature for pre-aging samples and peak aging samples. For TEM microstructure analysis, the precipitate evolutions of L1_2-$Ni_3(Al,Nb)$ and δ-Ni_3Nb will be illustrated. Additionally, a disorder HCP phase and ordered HCP phase have been observed in the FCC matrix, which did not been reported before. Furthermore, newly early-stage evidence of δ-Ni_3Nb transformation from L1_2 have been found. Finally, the deformed interaction of precipitates and matrix has been investigated in this work.

doi:10.6342/NTU202302391

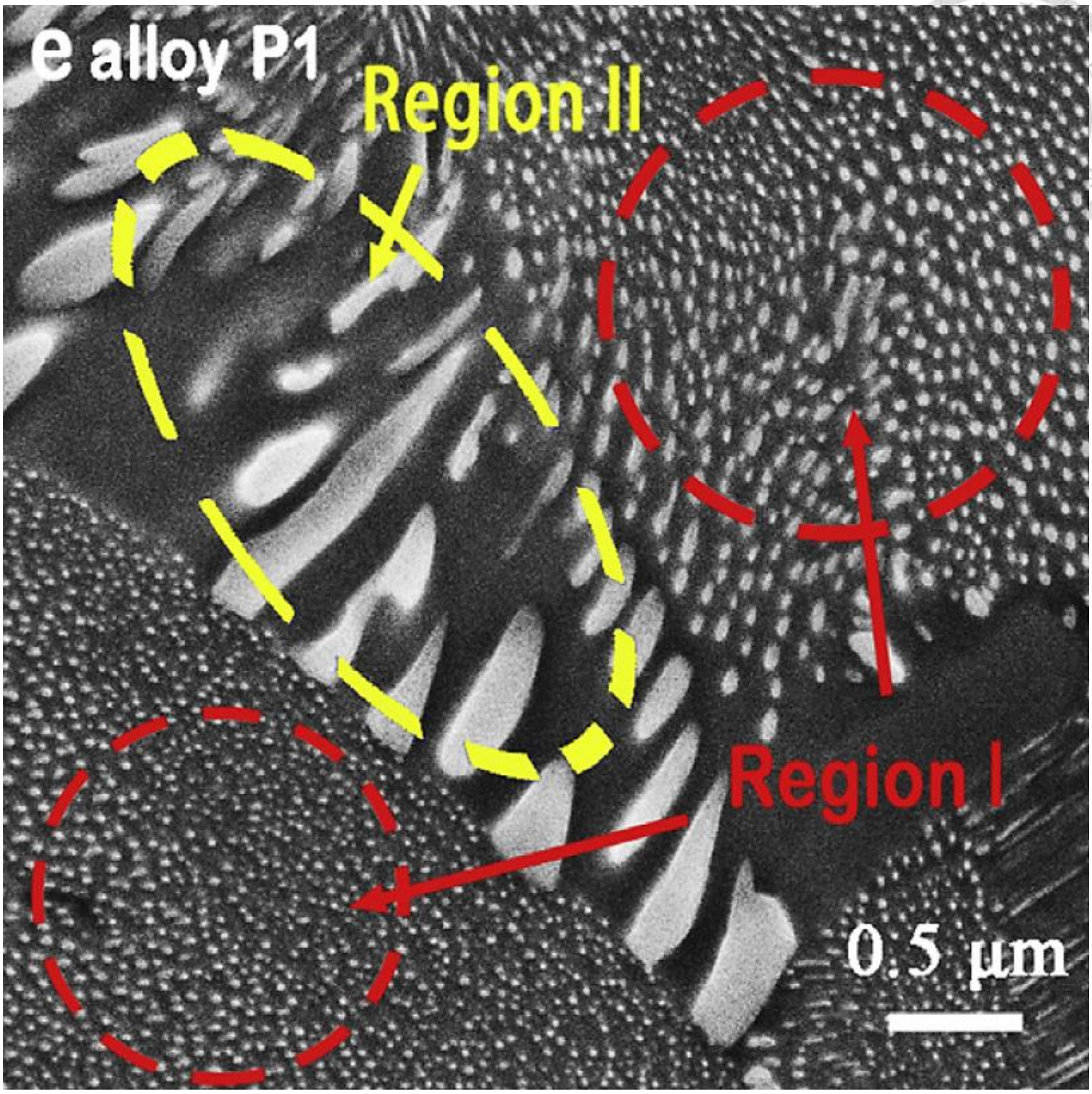

Figure 1-1 $(FeCrCoNi)_{94}Al_4Ti_2$ TEM bright field image [9].

doi:10.6342/NTU202302391

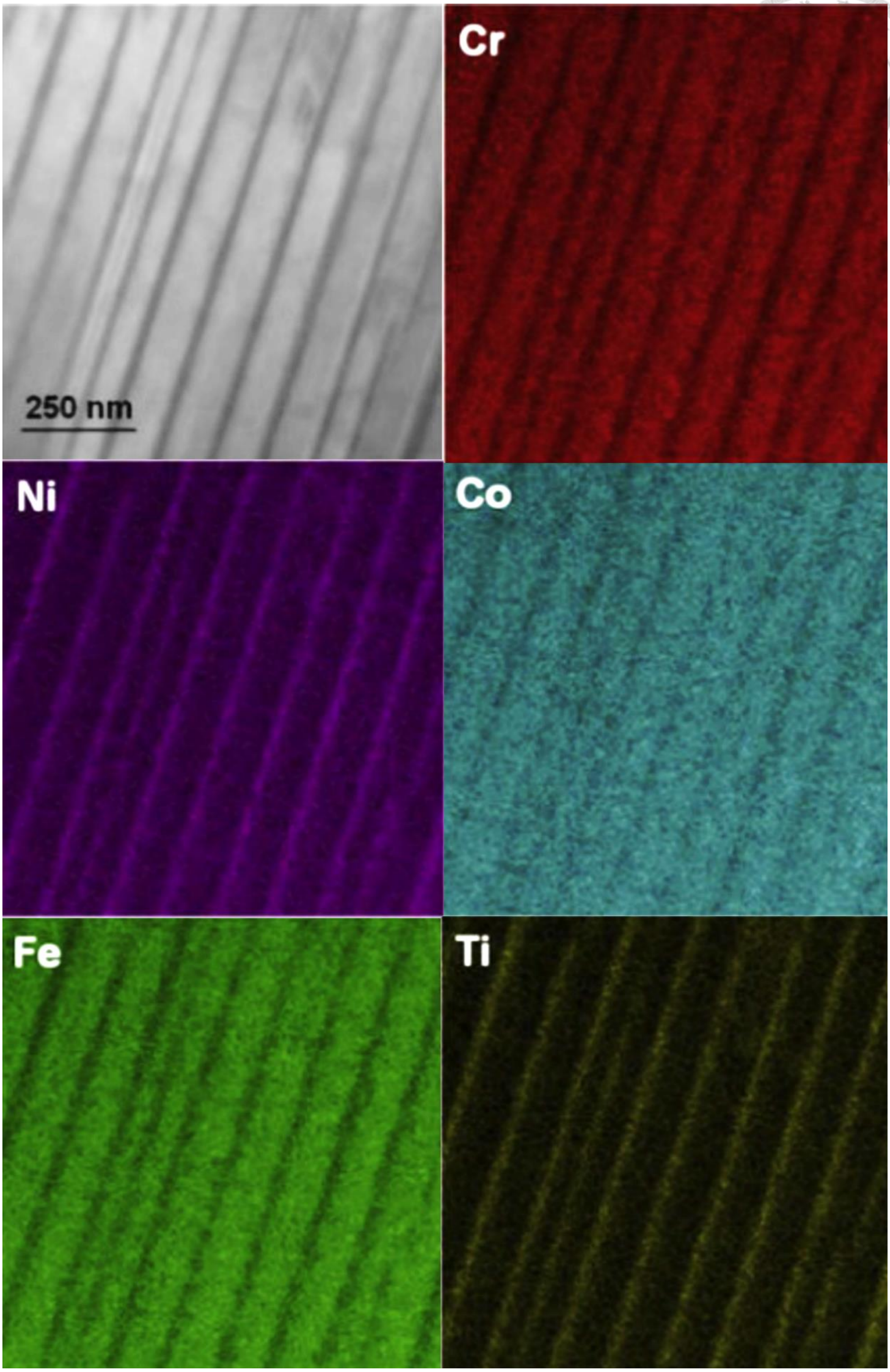

Figure 1-2 FeCrCoNiTi$_{0.2}$ STEM image and EDS Mapping [35].

doi:10.6342/NTU202302391

Chapter Two Literature Review

2.1 High-entropy alloy

2.1.1 Core effects in high-entropy alloys

1. High Entropy Effect [3]

According to the thermodynamic formula of Gibbs free energy (Eq. 2-1), a lower change in free energy (ΔG_{mix}) corresponds to a more stable phase. Due to the high mixing entropy (ΔS_{mix}, Eq. 2-2) of high entropy alloys, their phases differ from those of conventional alloys.

$$\Delta G_{mix} = \Delta H_{mix} - T\Delta S_{mix} \qquad \text{Eq. 2-1}$$

$$\Delta S_{mix} = -nR(x_1 ln x_1 + x_2 ln x_2) \qquad \text{Eq. 2-2}$$

In general, the difference in mixing entropy (ΔS_{mix}) between solid and liquid phases of metals is R (gas constant), but in five-component high entropy alloys, it is 1.61R. Therefore, high entropy alloys have more stable solid solutions, which is particularly evident at high temperatures, where the magnitude of $-T\Delta S_{mix}$ is larger, resulting in lower and more stable free energy (ΔG_{mix}).

Although mixing entropy (ΔS_{mix}) dominates the entire alloy system, the influence of mixing enthalpy (ΔH_{mix}) cannot be ignored. For example, the mixing enthalpy (ΔH_{mix}) of intermetallic compounds is very large, but they still form in high entropy alloys. Therefore, whether or not compounds form in high entropy alloys can be described as a result of the mutual influence between mixing entropy (ΔS_{mix}) and mixing enthalpy (ΔH_{mix}). For instance, (Cr, Fe)-rich borides were observed in AlBxCoCrCuFeNi[44].

2. Sluggish Diffusion Effect

Compared to pure metals or alloys with fewer types of elements, diffusion in high-entropy alloys is very slow. This is because many different types of atoms occupy lattice sites, causing the potential energy of adjacent lattice positions to vary. Atoms with lower potential energy are more difficult to move to positions with higher potential energy, while atoms with higher potential energy are more likely to return to positions with lower potential energy. Thus, from an atomic perspective, the atoms inside high-entropy alloys do not move easily.

In multi-component high-entropy alloys, diffusion of certain elements can be very slow, resulting in diffusion being dominated by that element, which can be considered the rate-limiting factor in the kinetics. From a kinetic perspective, nano-precipitates with supersaturation are easily formed in high-entropy alloys because the growth of precipitates requires nucleation and growth, and the atoms in the alloy system need to be rearranged. However, the slow diffusion rate in high-entropy alloys makes the

doi:10.6342/NTU202302391

growth of precipitates difficult, resulting in smaller precipitate sizes compared to traditional alloys.

Table 2-1 shows the diffusion coefficients of Ni on different FCC substrates obtained from the experiments by Tsai et al. [45]. It can be seen that the more complex the alloy system, the lower the diffusion coefficient of Ni. For applications that require the suppression of diffusion, such as in the IC packaging industry where a diffusion barrier is needed to prevent interlayer reaction, increasing the number of base elements can effectively lower the diffusion coefficient and greatly improve the effect of suppressing diffusion.

Table 2-1 Diffusion coefficients of Ni in different FCC-based metal [45].

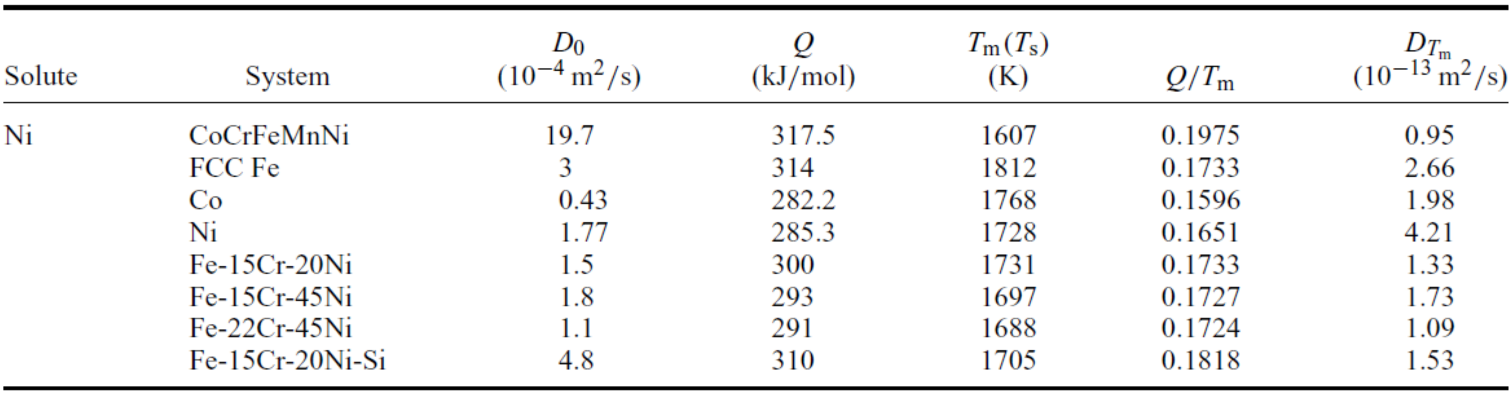

Solute	System	D_0 (10^{-4} m^2/s)	Q (kJ/mol)	$T_m(T_s)$ (K)	Q/T_m	D_{T_m} (10^{-13} m^2/s)
Ni	CoCrFeMnNi	19.7	317.5	1607	0.1975	0.95
	FCC Fe	3	314	1812	0.1733	2.66
	Co	0.43	282.2	1768	0.1596	1.98
	Ni	1.77	285.3	1728	0.1651	4.21
	Fe-15Cr-20Ni	1.5	300	1731	0.1733	1.33
	Fe-15Cr-45Ni	1.8	293	1697	0.1727	1.73
	Fe-22Cr-45Ni	1.1	291	1688	0.1724	1.09
	Fe-15Cr-20Ni-Si	4.8	310	1705	0.1818	1.53

3. Severe Lattice Distortion Effect

High entropy alloys consist of various elements with different atomic diameters, crystal structures, valence electrons, and electronegativities. Table 2-2 shows the basic properties of the elements in AlxCoCrCuFeNi [46, 47]. It can be observed that the atomic diameters of Co, Cr, Cu, Fe, and Ni range from 1.24-1.28 Å, while that of Al is 1.43 Å, which is approximately 20% larger than the other atomic diameters. Therefore, introducing Al atoms into CoCrCuFeNi results in lattice distortion and introduces larger lattice strain, which enhances the material's strength and hardness.

Table 2-2 Common fundamental properties in $Al_xCoCrCuFeNi$ [46, 47].

Element	**Al**	**Co**	**Cr**	**Cu**	**Fe**	**Ni**
Atomic size	1.43	1.25	1.25	1.28	1.24	1.25
Crystal structure at 25°C	FCC	HCP	BCC	FCC	BCC	FCC
Chemical valance	+3	+2,+3	+3,+6	+1,+2	+2,+3	+2
Electronegativity	1.5	1.8	1.6	1.9	1.8	1.8

4. Cocktail Effect

High-entropy alloys contain many different elements, and the interactions between these elements can give rise to properties that are different from those of the constituent elements themselves. For example, pure aluminum has relatively low strength, but

doi:10.6342/NTU202302391

incorporating Al into an AlxCoCrCuFeNi alloy in a BCC phase significantly increases its strength. I believe that the cocktail effect in high-entropy alloys requires more rigorous discussion and explanation.

2.1.2 Crystal structures in high-entropy alloys

Some notations are used to describe the phases of high-entropy alloys. Their explanations are described as follows, simple/complex and ordered/disordered.

1. Simple/Complex: Whether the common crystal structures FCC, BCC, and HCP can be used to express them. For example, $L1_2$ can be expressed by FCC and is defined as simple, while the Laves phase cannot be expressed by FCC, BCC, and HCP and is defined as complex.
2. Ordered/Disordered: Whether the atoms occupy specific lattice sites. For example, B2 has a specific arrangement structure and is defined as ordered, while FCC has no specific types of atoms occupying lattice sites and is defined as disordered.

Zhang et al. and Guo et al. conducted research and found that the formation of simple or complex phases depends on the mixing enthalpy (ΔH_{mix}), mixing entropy (ΔS_{mix}), and atomic size difference (δ) [48, 49]. They summarized the thermodynamic criteria and superposition effect in a diagram (Figure 2-1), where the phases inside the

doi:10.6342/NTU202302391

dashed line represent the simple phases:

1. simple phase including order and disorder phase : $-22 \leq \Delta H_{mix} \leq 7\ (\frac{kJ}{mol})$, $11 \leq \Delta S_{mix} \leq 19.5\ (\frac{J}{K \cdot mol})$ and $\delta \leq 8.5$
2. simple disorder phase : $-15 \leq \Delta H_{mix} \leq 5\ (\frac{kJ}{mol})$, $12 \leq \Delta S_{mix} \leq 17.5\ (\frac{J}{K \cdot mol})$ and $\delta \leq 4.3$

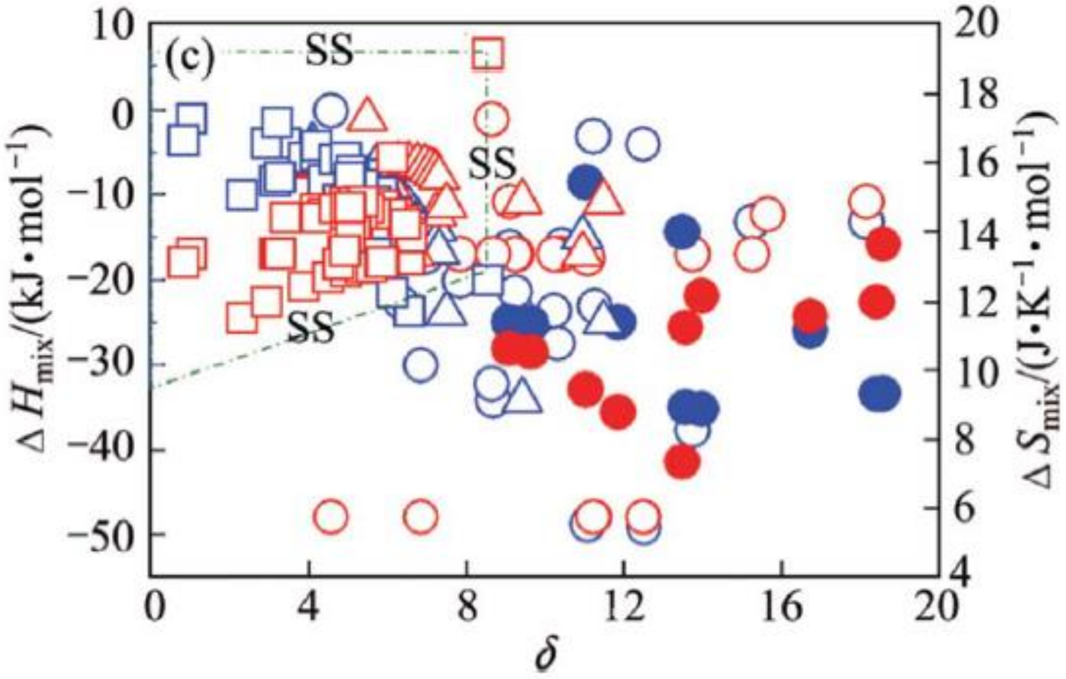

Figure 2-1 Overview of stacking effects of ΔH_{mix} ,ΔS_{mix} and δ (○ represents amorphous alloys，● represents atomic ratio amorphous alloys，□ represents single phase，△ represents intermetallic compounds) [49].

The results of this study are consistent with the traditional concepts of thermodynamics. If ΔH_{mix} is a large positive value, the material tends to be unstable and prone to separation. Conversely, if ΔH_{mix} is a large negative value, the material tends to form intermetallic compounds (IMCs). A larger ΔS_{mix} favors the formation

doi:10.6342/NTU202302391

of simple phases in stable high-entropy alloys, while hindering the formation of complex phases such as Laves phases. A larger atomic size difference (δ) leads to larger strains within the crystal lattice, making the material more unstable.

2.1.3 High-entropy alloy categorization

The current mainstream high-entropy alloys can be roughly divided into three types. There are as-cast HEAs, low stacking-fault energy HEAs, and precipitate-hardening HEAs.

1. As-cast high-entropy alloy

Without undergoing subsequent heat treatment, the strengthening effect is mainly achieved through a plate-like structure, as exemplified by AlCoCrCuFeNi [50], AlxCoCrCuFeNi [51], and AlCoCrFeNi [52].

The typical cast microstructure is shown below.

Figure 2-2 shows the spinodal decomposition TEM bright field image of AlxCoCrCuFeNi alloy with x=1.0[51], where the α-phase has a disordered A2 structure and the β-phase has a disordered B2 structure.

Figure 2-3 shows the Widmanstätten precipitate TEM bright field image of AlxCoCrCuFeNi alloy with x=1.5 [23].

doi:10.6342/NTU202302391

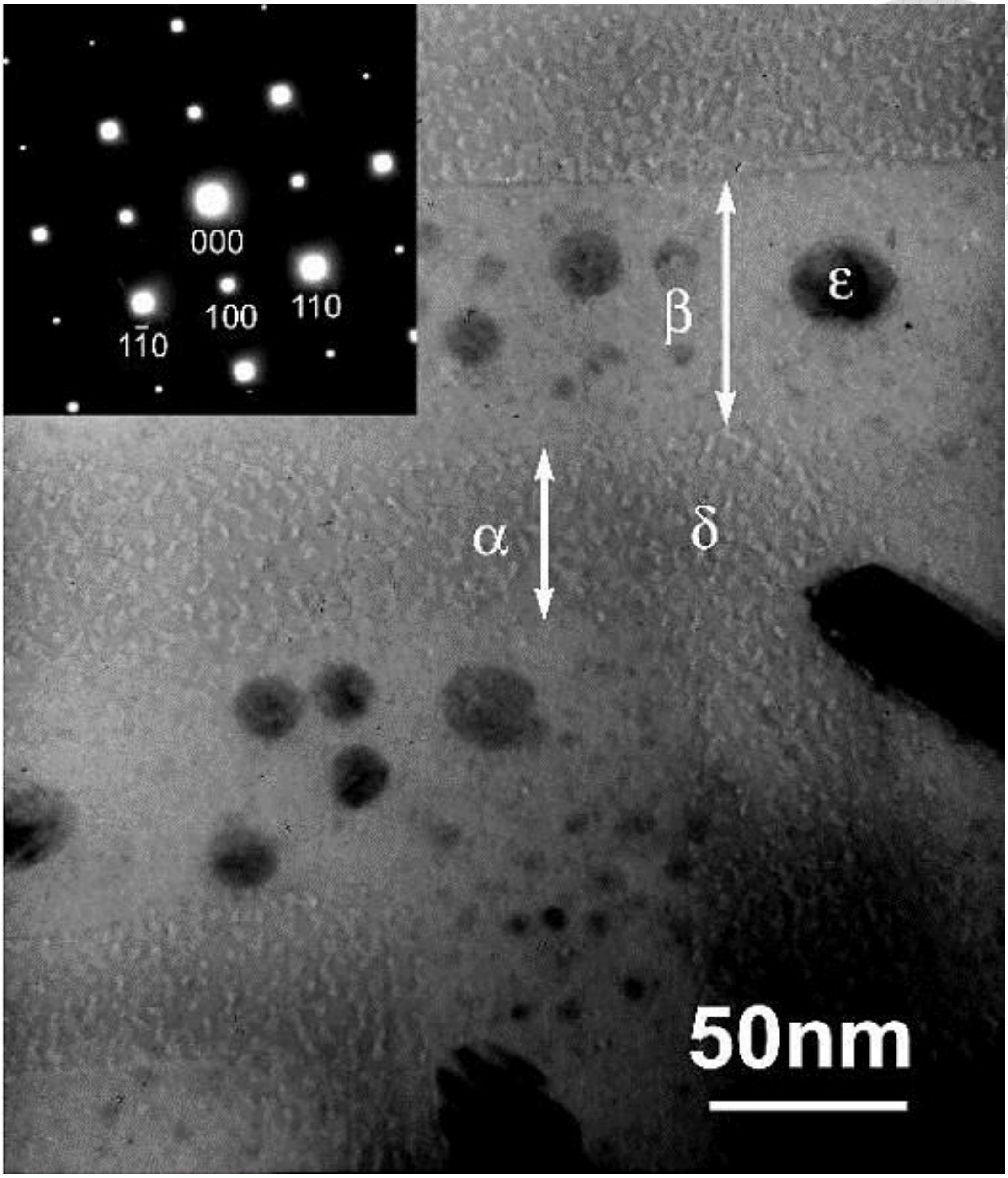

Figure 2-2 TEM bright field image of spinodal decomposition in $Al_xCoCrCuFeNi$, $x = 1.0$ [51].

doi:10.6342/NTU202302391

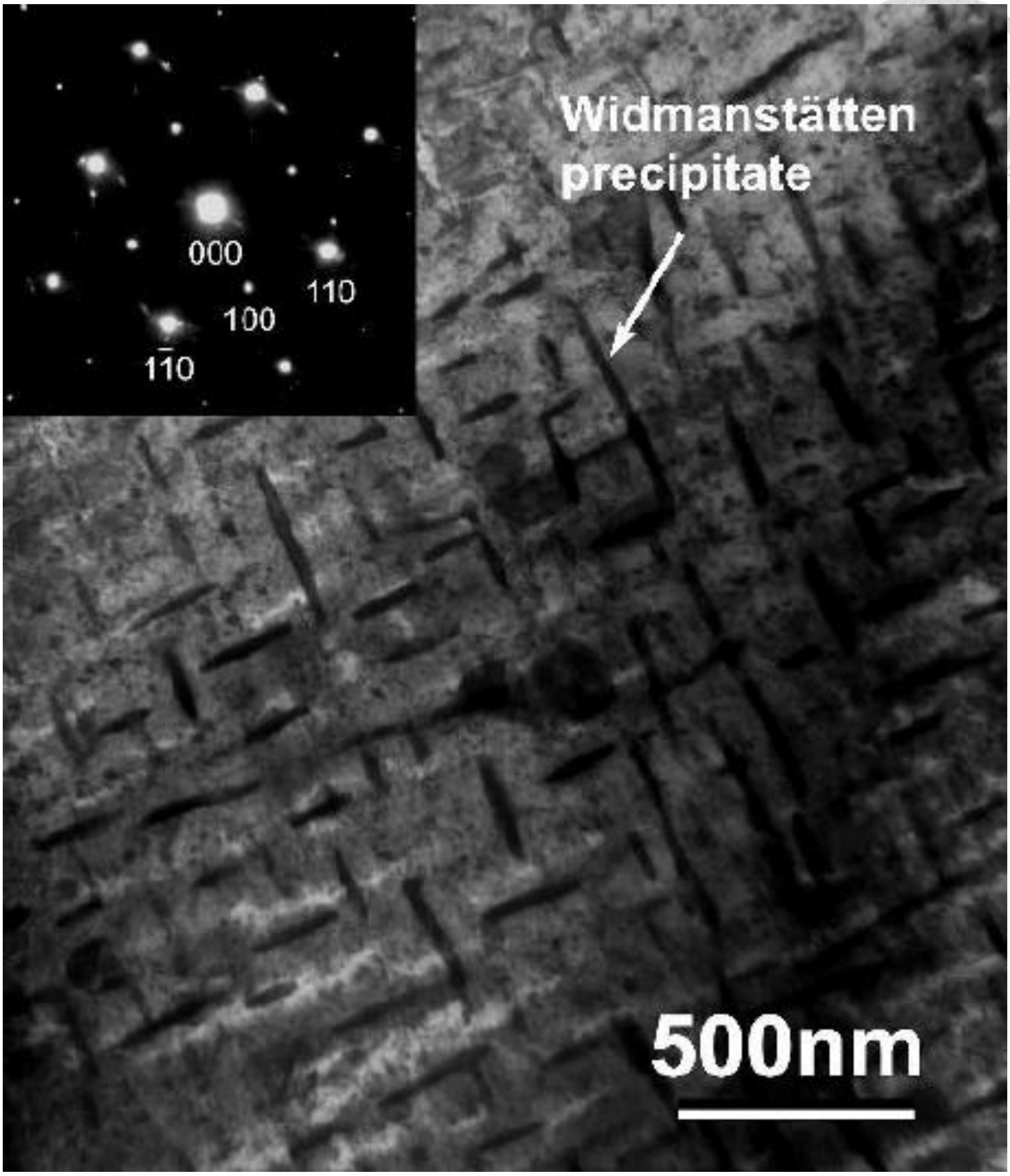

Figure 2-3 TEM bright field image of spinodal decomposition in $Al_xCoCrCuFeNi$, x = 1.5 [51].

2. Low stacking-fault energy high-entropy alloys

By reducing the stacking fault energy to generate more deformation twins, strength can be enhanced, particularly in single-phase face-centered cubic systems, such as CrMnFeCoNi [53]、CrCoNi [54]、CrCoNiSix [55]. Figure 2-4 shows the TEM bright

doi:10.6342/NTU202302391

field images and dark field images of nanoscale deformation twins in CrCoNi.

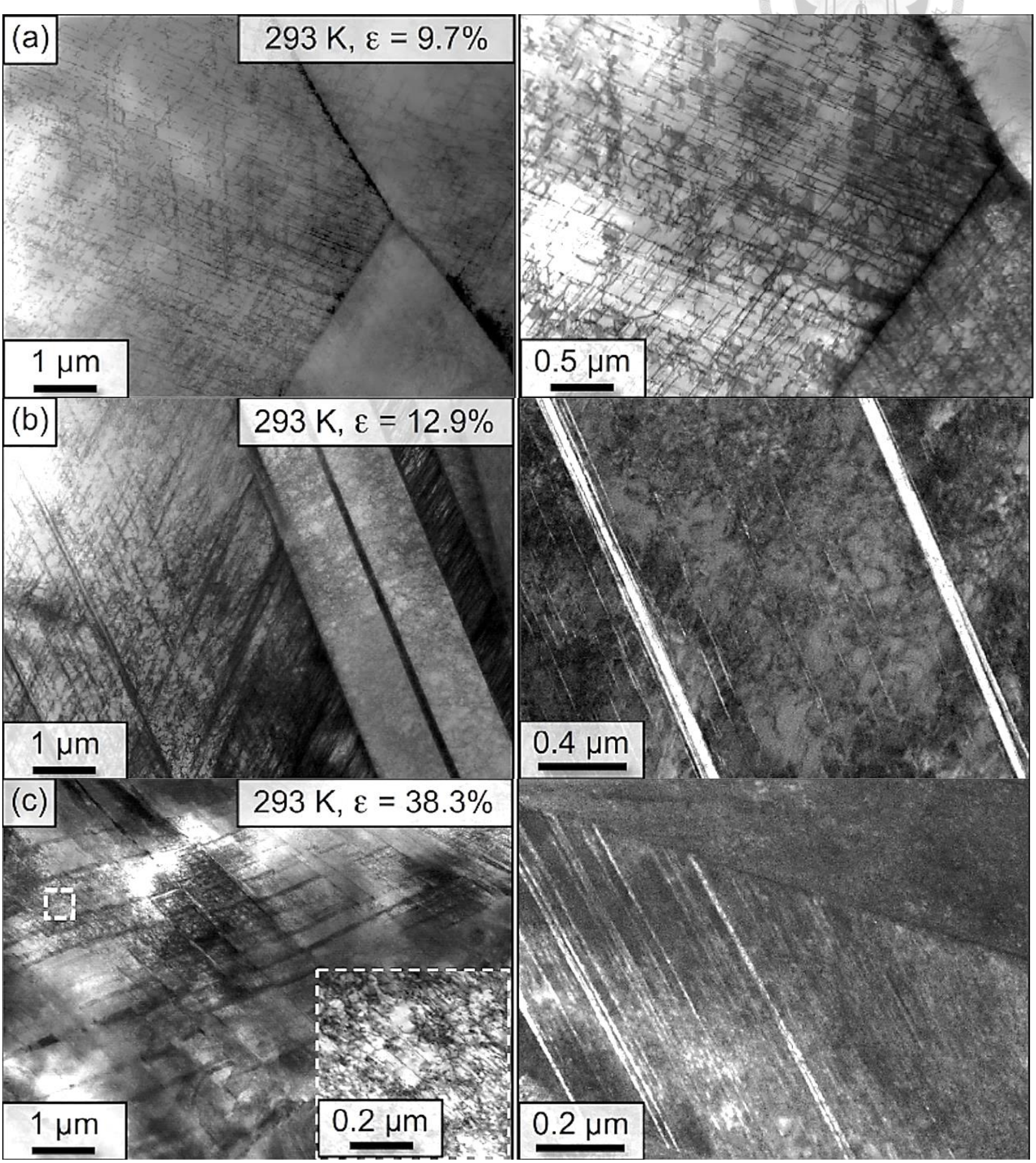

Figure 2-4 TEM images of CrCoNi deformation evolution under different strain after tensile test with 0.001s^{-1} strain rate (a)$\varepsilon = 9.7\%$ (b)$\varepsilon = 12.9\%$ (c)$\varepsilon = 38.3\%$ [54].

3. $L1_2$-precipitate hardening high-entropy alloys

Based on a single-phase face-centered cubic system, the precipitation of $L1_2$ phase is utilized to enhance mechanical properties, as demonstrated in $(FeCoCrNi)_{96}Ti_2Al_4$ [9], $(CoCrNi)Al_3Ti_3$ [33], $(CrCoNi)_{93}Al_4Ti_2Nb$ [56]. Figure 2-6 and Figure 2-6 and shows the bright field and dark field TEM images of $(FeCoCrNi)_{96}Ti_2Al_4$, where the small dots correspond to $L1_2$-$Ni_3(Al,Ti)$ precipitates.

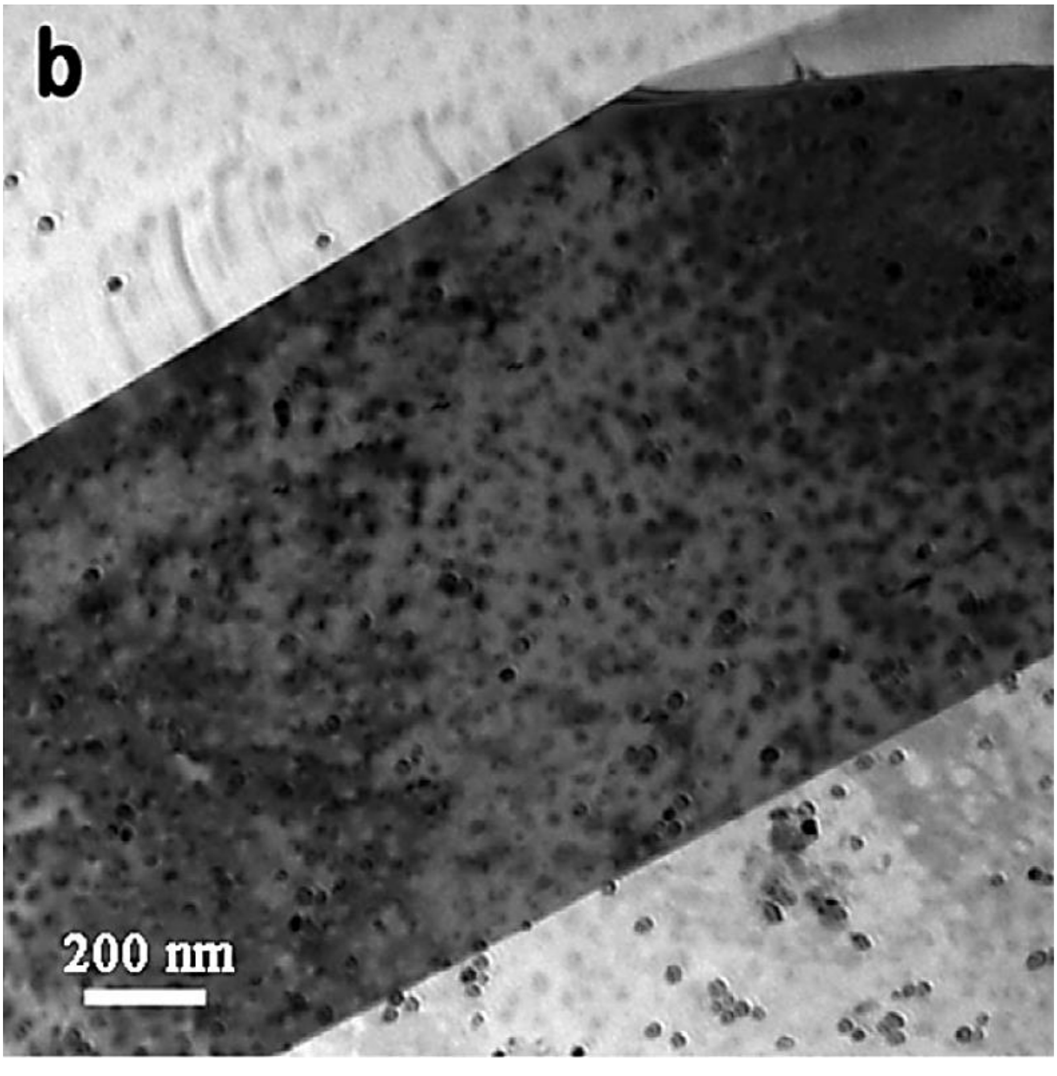

Figure 2-5 Bright field image of $(FeCoCrNi)_{96}Ti_2Al_4$ [9].

doi:10.6342/NTU202302391

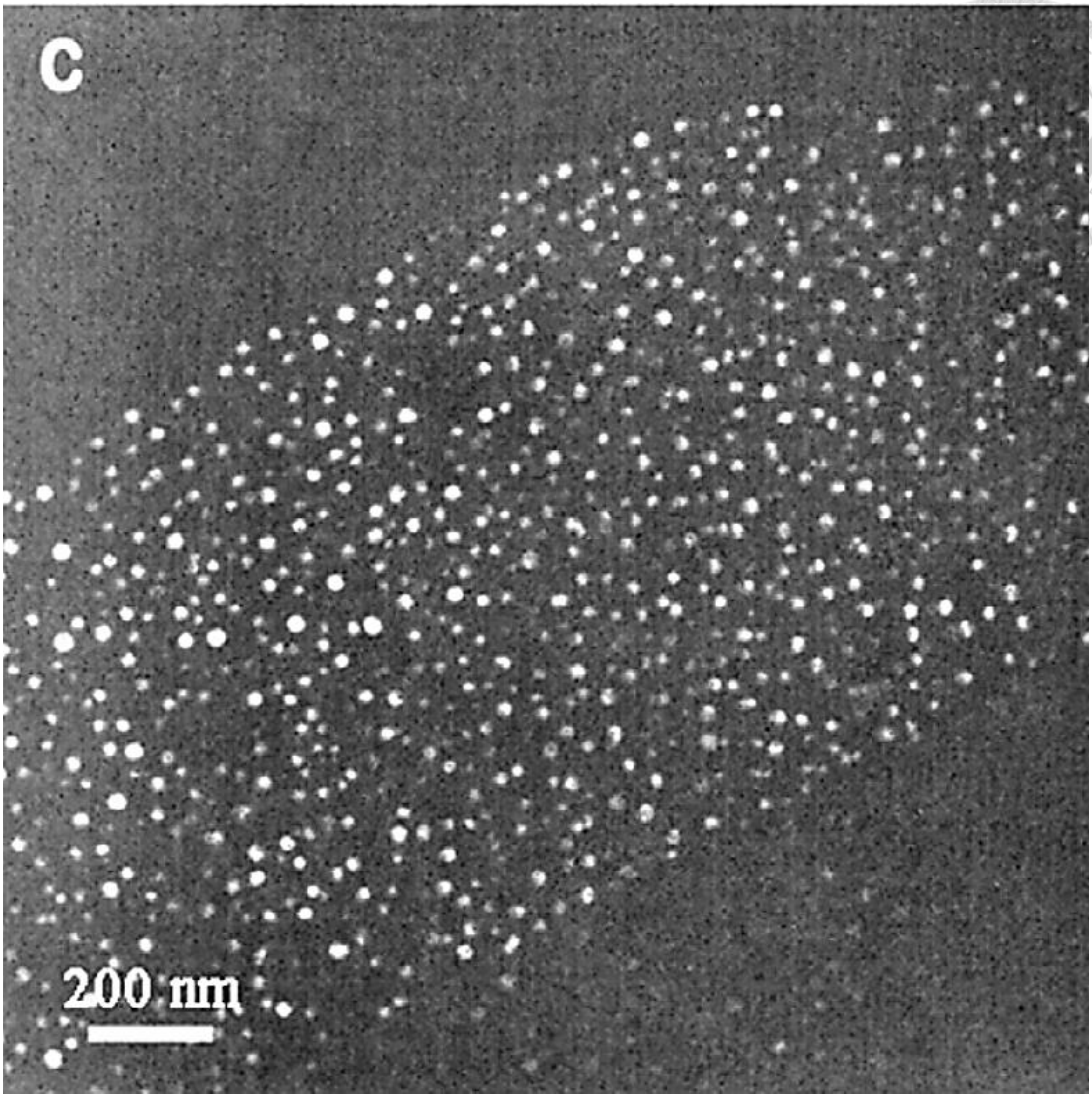

Figure 2-6 dark field image (right) of $(FeCoCrNi)_{96}Ti_2Al_4$ [9].

doi:10.6342/NTU202302391

2.2 Concepts of precipitation in nickel-based superalloys related to high-entropy Alloys

Nickel-based superalloys can be applied in many harsh environments, such as aircraft engine blades, marine propellers, submarines, nuclear reactors, and more. In high-temperature environments, nickel-based superalloys can maintain excellent strength, toughness, resistance to creep and corrosion, have a long life under continuous stress at high temperatures, and can maintain a certain level of mechanical properties [30, 57]. The performance of nickel-based superalloys in high-temperature environments is superior to other types of superalloys, and will be discussed in more detail in the following chapters. Table 2-3 shows the composition of various commercial nickel-based superalloys [30], and Table 2-4 illustrates the basic properties of nickel-based superalloys.

doi:10.6342/NTU202302391

Table 2-3 chemical composition of Ni-based superalloys (wt%, bal Ni) [30].

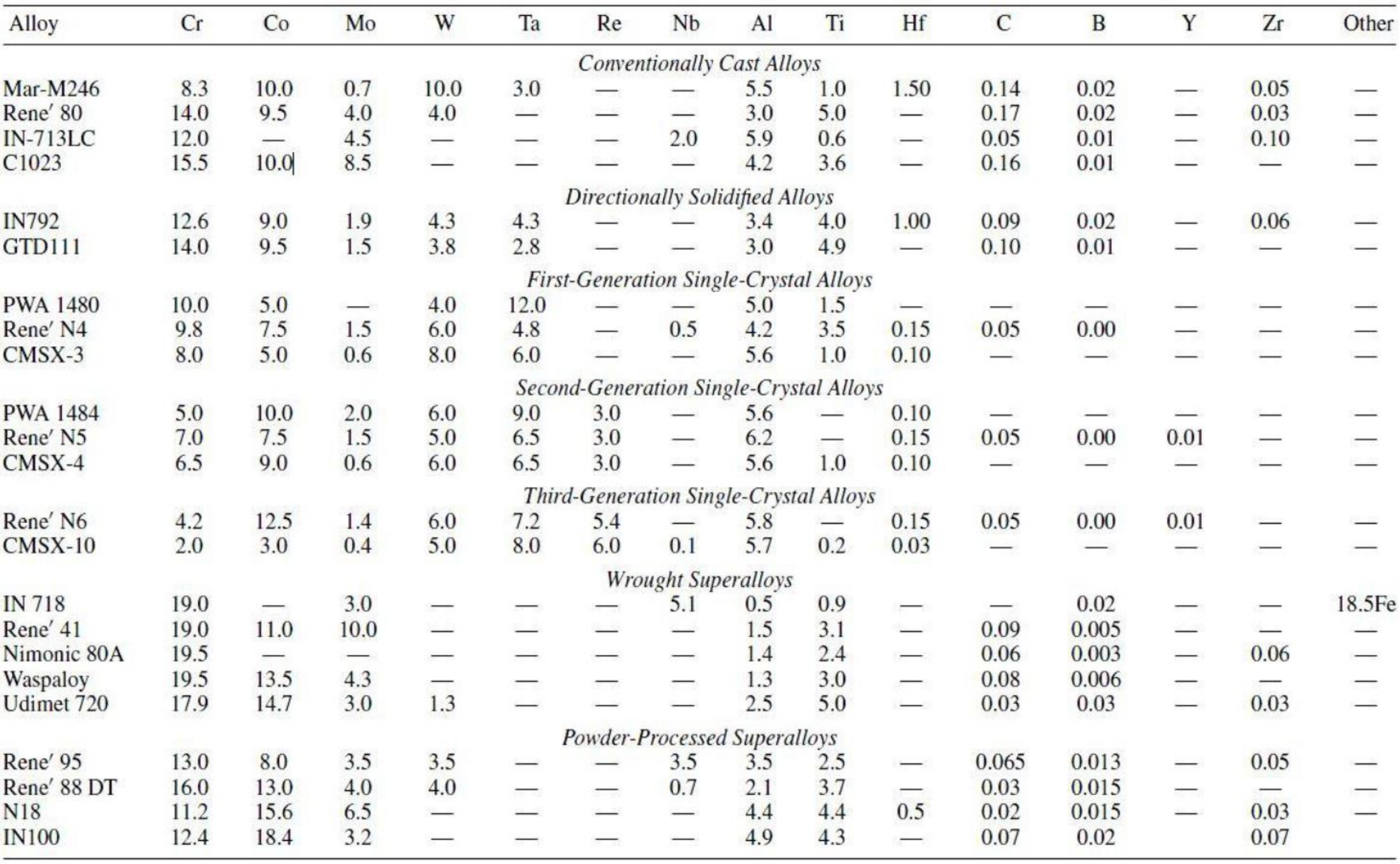

Alloy	Cr	Co	Mo	W	Ta	Re	Nb	Al	Ti	Hf	C	B	Y	Zr	Other
Conventionally Cast Alloys															
Mar-M246	8.3	10.0	0.7	10.0	3.0	—	—	5.5	1.0	1.50	0.14	0.02	—	0.05	—
Rene′ 80	14.0	9.5	4.0	4.0	—	—	—	3.0	5.0	—	0.17	0.02	—	0.03	—
IN-713LC	12.0	—	4.5	—	—	—	2.0	5.9	0.6	—	0.05	0.01	—	0.10	—
C1023	15.5	10.0	8.5	—	—	—	—	4.2	3.6	—	0.16	0.01	—	—	—
Directionally Solidified Alloys															
IN792	12.6	9.0	1.9	4.3	4.3	—	—	3.4	4.0	1.00	0.09	0.02	—	0.06	—
GTD111	14.0	9.5	1.5	3.8	2.8	—	—	3.0	4.9	—	0.10	0.01	—	—	—
First-Generation Single-Crystal Alloys															
PWA 1480	10.0	5.0	—	4.0	12.0	—	—	5.0	1.5	—	—	—	—	—	—
Rene′ N4	9.8	7.5	1.5	6.0	4.8	—	0.5	4.2	3.5	0.15	0.05	0.00	—	—	—
CMSX-3	8.0	5.0	0.6	8.0	6.0	—	—	5.6	1.0	0.10	—	—	—	—	—
Second-Generation Single-Crystal Alloys															
PWA 1484	5.0	10.0	2.0	6.0	9.0	3.0	—	5.6	—	0.10	—	—	—	—	—
Rene′ N5	7.0	7.5	1.5	5.0	6.5	3.0	—	6.2	—	0.15	0.05	0.00	0.01	—	—
CMSX-4	6.5	9.0	0.6	6.0	6.5	3.0	—	5.6	1.0	0.10	—	—	—	—	—
Third-Generation Single-Crystal Alloys															
Rene′ N6	4.2	12.5	1.4	6.0	7.2	5.4	—	5.8	—	0.15	0.05	0.00	0.01	—	—
CMSX-10	2.0	3.0	0.4	5.0	8.0	6.0	0.1	5.7	0.2	0.03	—	—	—	—	—
Wrought Superalloys															
IN 718	19.0	—	3.0	—	—	—	5.1	0.5	0.9	—	—	0.02	—	—	18.5Fe
Rene′ 41	19.0	11.0	10.0	—	—	—	—	1.5	3.1	—	0.09	0.005	—	—	—
Nimonic 80A	19.5	—	—	—	—	—	—	1.4	2.4	—	0.06	0.003	—	0.06	—
Waspaloy	19.5	13.5	4.3	—	—	—	—	1.3	3.0	—	0.08	0.006	—	—	—
Udimet 720	17.9	14.7	3.0	1.3	—	—	—	2.5	5.0	—	0.03	0.03	—	0.03	—
Powder-Processed Superalloys															
Rene′ 95	13.0	8.0	3.5	3.5	—	—	3.5	3.5	2.5	—	0.065	0.013	—	0.05	—
Rene′ 88 DT	16.0	13.0	4.0	4.0	—	—	0.7	2.1	3.7	—	0.03	0.015	—	—	—
N18	11.2	15.6	6.5	—	—	—	—	4.4	4.4	0.5	0.02	0.015	—	0.03	—
IN100	12.4	18.4	3.2	—	—	—	—	4.9	4.3	—	0.07	0.02		0.07	

Table 2-4 the basic properties of nickel-based superalloys [58].

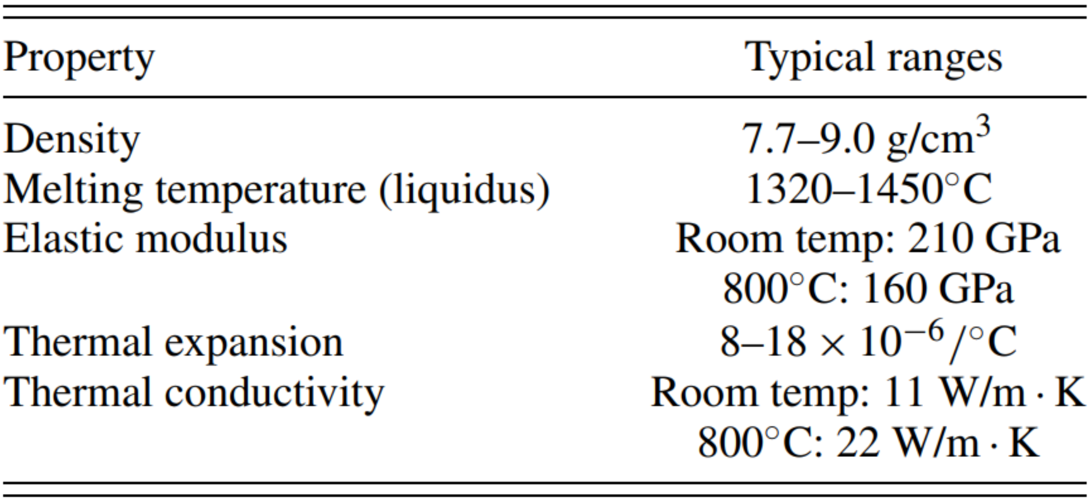

Property	Typical ranges
Density	7.7–9.0 g/cm^3
Melting temperature (liquidus)	1320–1450°C
Elastic modulus	Room temp: 210 GPa 800°C: 160 GPa
Thermal expansion	8–18 × 10^{-6}/°C
Thermal conductivity	Room temp: 11 W/m · K 800°C: 22 W/m · K

doi:10.6342/NTU202302391

2.2.1 Strengthening mechanisms and microstructures in Ni-based superalloys

The strengthening mechanism of superalloys is based on nickel, which is typically used as the substrate in a face-centered cubic (FCC) crystal structure, with the addition of 5-10 different elements. The added elements do not exceed 40 wt%, as shown in Figure 2-7 of commonly added alloy elements in nickel-based superalloys [59]. The Ni-Al binary system is the basis of nickel-based superalloys, where Ni_3Al, also known as γ', with an $L1_2$ crystal structure, is formed in this system. Many nickel-based superalloys are derived from modifications of the Ni-Al system [30]. γ' is formed as a supersaturated solid solution of γ-Ni below the liquidus line. The growth kinetics of γ' is highly dependent on the cooling rate below the liquidus line, for example, when the cooling rate is 40K/min, the γ' size presents a unimodal distribution of approximately 300-500nm, but when the cooling rate continues to decrease, the γ' size shows a bimodal distribution, with sizes greater than 500nm and smaller than 50nm.

In nickel-based superalloys, the volume ratio of γ' is one of the key factors in material strengthening. Even with the addition of several alloy elements, the material still maintains a $\gamma + \gamma'$ structure. Figure 2-8 shows the structure of a typical nickel-based superalloy[58], where after 1310°C /2 h + 1313°C /2 h + 1130°C /4 h + 900°C /16 h, γ' presents a rectangular distribution in γ. In addition, refractory elements (Mo, W, Nb, Re) have significantly different electronic energy levels and atomic radii from Ni, and

doi:10.6342/NTU202302391

appropriate addition can effectively increase the material's melting point. The addition of Ti, Ta, and Nb promotes the formation and strengthening of γ′ [60, 61], while the addition of B and C forms borides and carbides, respectively, controlling the grain size.

Figure 2-9 shows the microstructure image of a nickel-based superalloy airplane engine blade after use [30]. The block-shaped γ′ and the substrate γ can be observed in the figure. The block-shaped γ′ can effectively hinder the initial dislocation slip, making the dislocation need to pass through the channel of γ to move, and the dislocation aggregates in the channel of γ, which can effectively hinder the dislocation movement. After more severe deformation, the shear force on the dislocation is sufficient to penetrate γ′, causing the formation of dislocations in both γ and γ′, which mutually restrain each other. Due to the difference in lattice constants between γ and γ′, the sliding of dislocations in both phases is relatively difficult, achieving the strengthening effect.

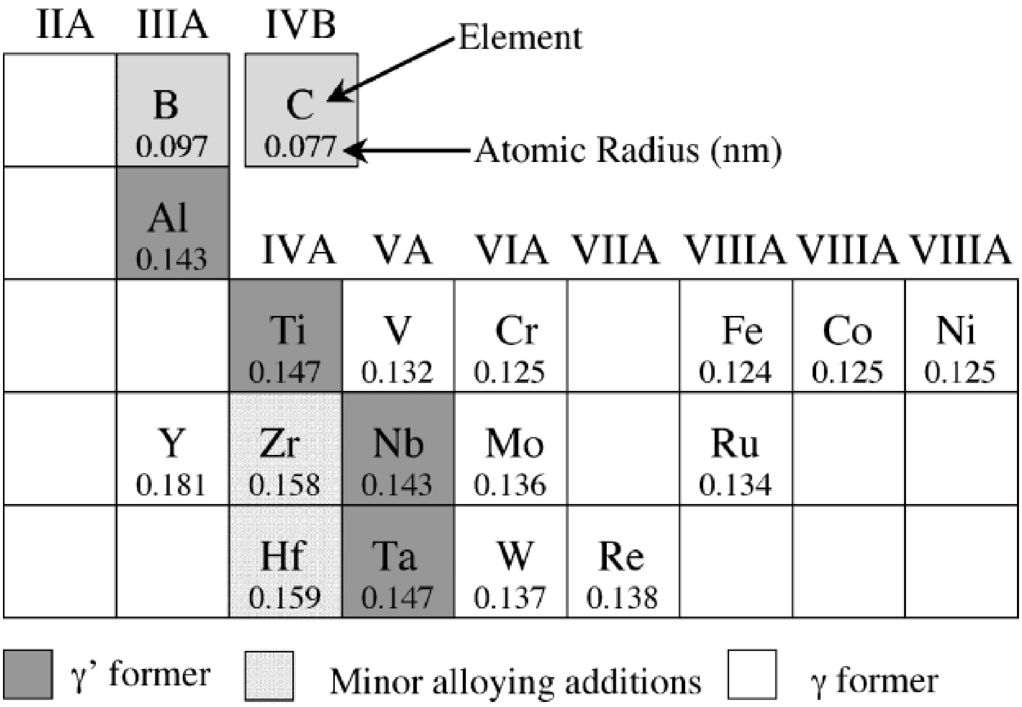

Figure 2-7 common additives in Ni-based superalloys [59].

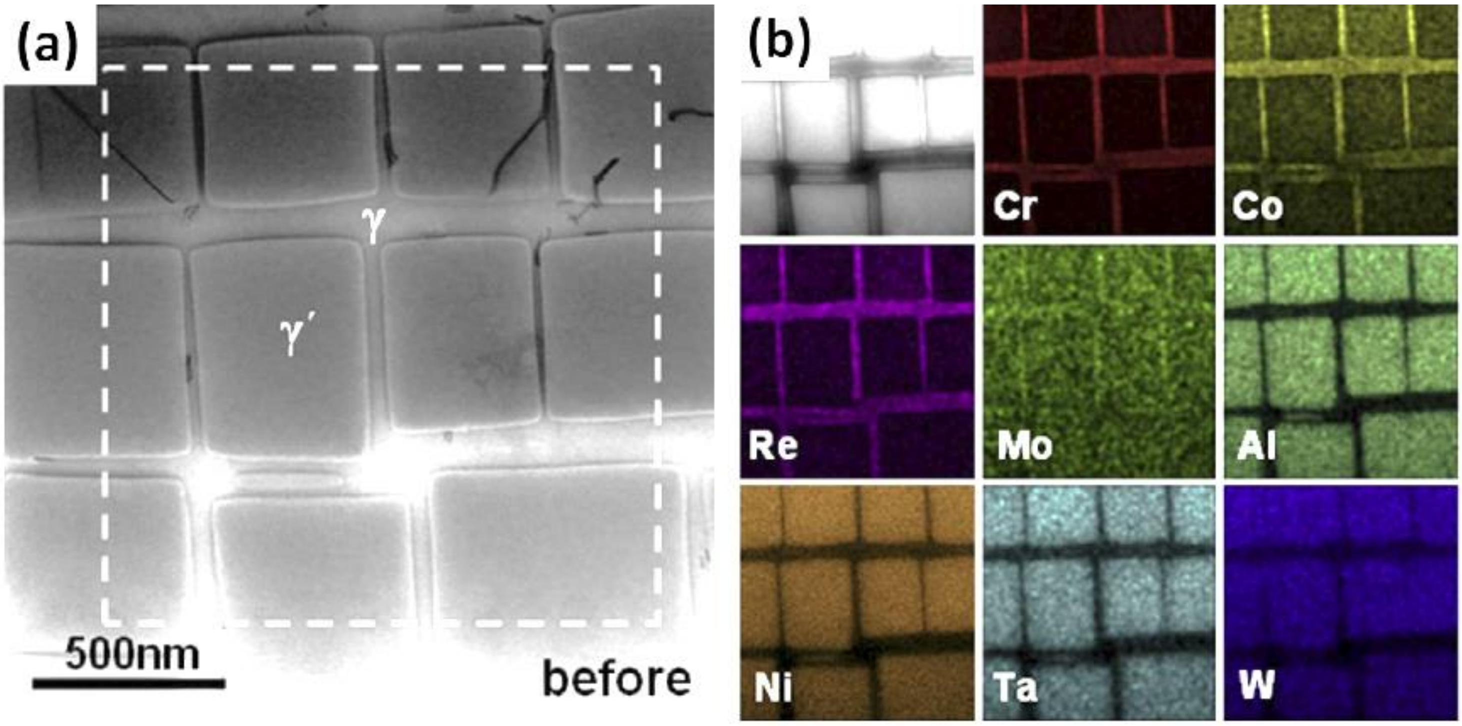

Figure 2-8 Microstructure of refractory element addition in Ni-based superalloys (a) SEM inage (b) EDS mapping [58].

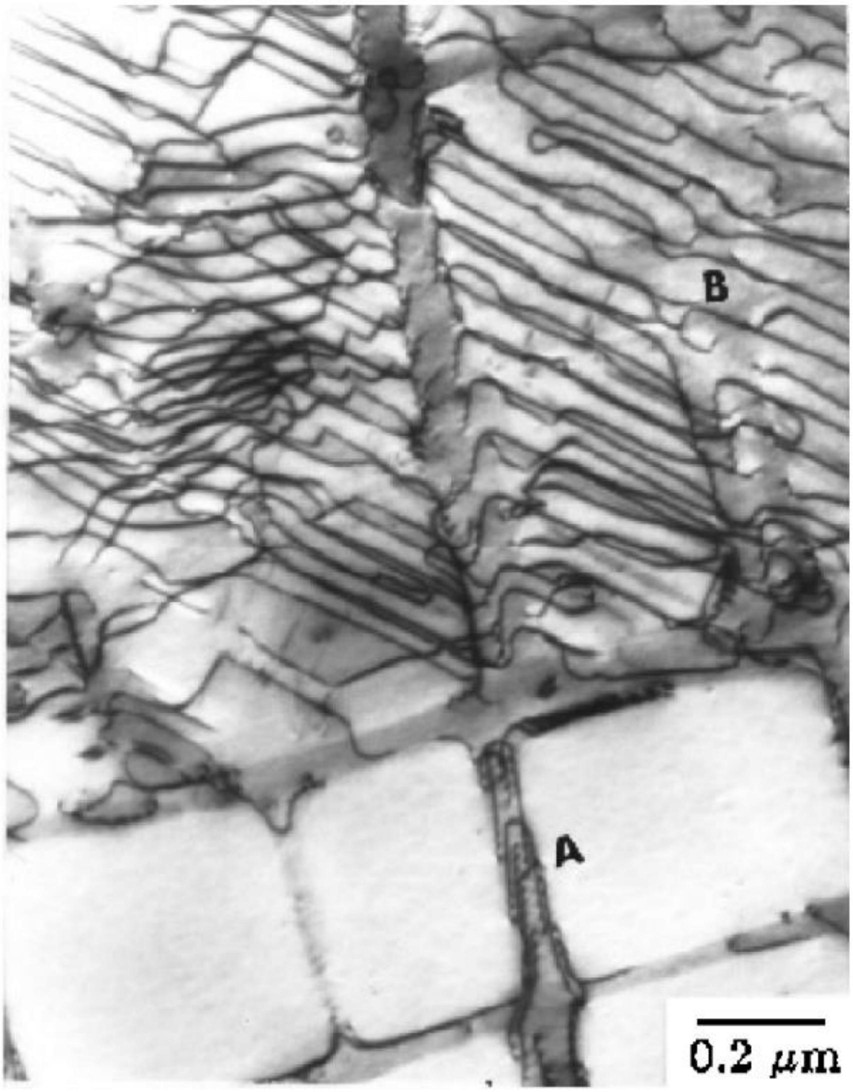

Figure 2-9 Microstructure image of a nickel-based superalloy aircraft engine blade after services. [30].

2.2.2 Influence of lattice misfit in Ni-based superalloys

The degree of coherency in a certain alloy system is often discussed in terms of lattice misfit (δ). Eq. 2-3 defines the lattice misfit (δ), which can be either positive or negative. For example, in nickel-based superalloys, when Al (0.143Å) is added to replace Ni (0.125Å), δ is a positive value, indicating that the insertion of Al atoms will cause an expansion micro stress in the lattice.

doi:10.6342/NTU202302391

In nickel-based superalloys, the lattice constant of γ′ is generally larger than that of γ at room temperature, but the lattice constant of γ′ is generally smaller than that of γ at high temperatures due to the different thermal expansion coefficients of the two phases [62, 63]. The lattice misfit (δ) of the γ phase itself is also influenced by the solid solution of solute atoms [64].

$$\delta = 2 \times [(a_{r'} - a_{r})/(a_{r'} + a_{r})] \qquad \text{Eq. 2-3}$$

The degree of lattice misfit (δ) directly affects the growth of precipitates. The coarsening of precipitates is due to the interfacial energy between γ and γ′. At high temperatures, the coarsening of precipitates can reduce the interfacial energy between them. Therefore, the smaller the degree of lattice misfit (δ), the smaller the interfacial energy between γ and γ′, making the phase relatively stable. In addition, JS Van et al. have shown that if the lattice misfit (δ) is too small[65], the precipitates will form a spherical structure instead of a blocky structure, which is not conducive to strengthening the material and resisting creep. Figure 2-10 shows the effect of lattice misfit on the microstructure of nickel-based superalloys. The study suggests that the optimal degree of lattice misfit is 0.4 and the optimal volume ratio of γ′ is 0.6.

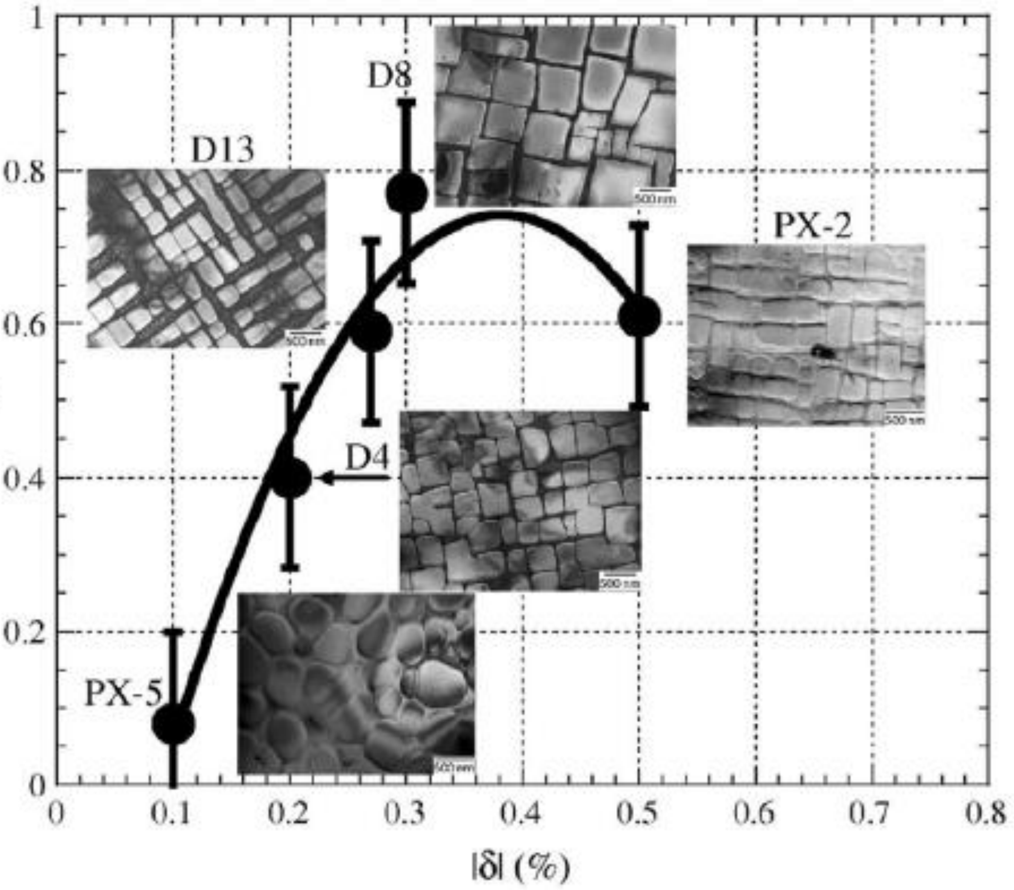

Figure 2-10 Influence of lattice misfit to microstructure in Ni-based superalloys [65].

2.2.3 TCP phases in Ni-based superalloys

The full name of the TCP phase is topologically close-packed phase, and the commonly known Laves phase is a type of TCP phase that is generally considered harmful to materials. Related studies have shown that adding refractory elements (Re, Mo, W, etc.) to nickel-based superalloys is beneficial to the formation of TCP phases [66, 67]. The formation of TCP phases is mainly dominated by element diffusion. Xianzi et al. [68]found that Re, as an element with a very slow diffusion rate, can reduce the overall diffusion rate of materials when added to nickel-based superalloys, and can also enhance the segregation of other elements in the γ and γ′ phases. For example, in the γ′ phase, Ni, Al, Ti, and other elements are mainly present. After adding Re, the proportion of Ni, Al, Ti, and other elements in the γ′ phase will increase.

The generation of TCP phases is related to temperature, pressure, and time. Figure 2-11 shows the effect of changing time and temperature on the microstructure of TCP phases. Observation of the results of the high-temperature test of nickel-based superalloys at 950°C shows that the needle-shaped TCP phases grow along the γ/γ′ interface, and the proportion of TCP phases increases with time. When the temperature is increased to 1100°C, the γ/γ′ interface gradually becomes fuzzy, and the TCP phases do not grow according to a certain rule. In principle, they avoid growing in the γ′ phase, and the shape of the TCP phases becomes thicker and shorter. In summary, TCP phases inhibit nucleation rate but grow faster in high-temperature environments. As the test time is prolonged, TCP phases tend to form a lath-like structure.

doi:10.6342/NTU202302391

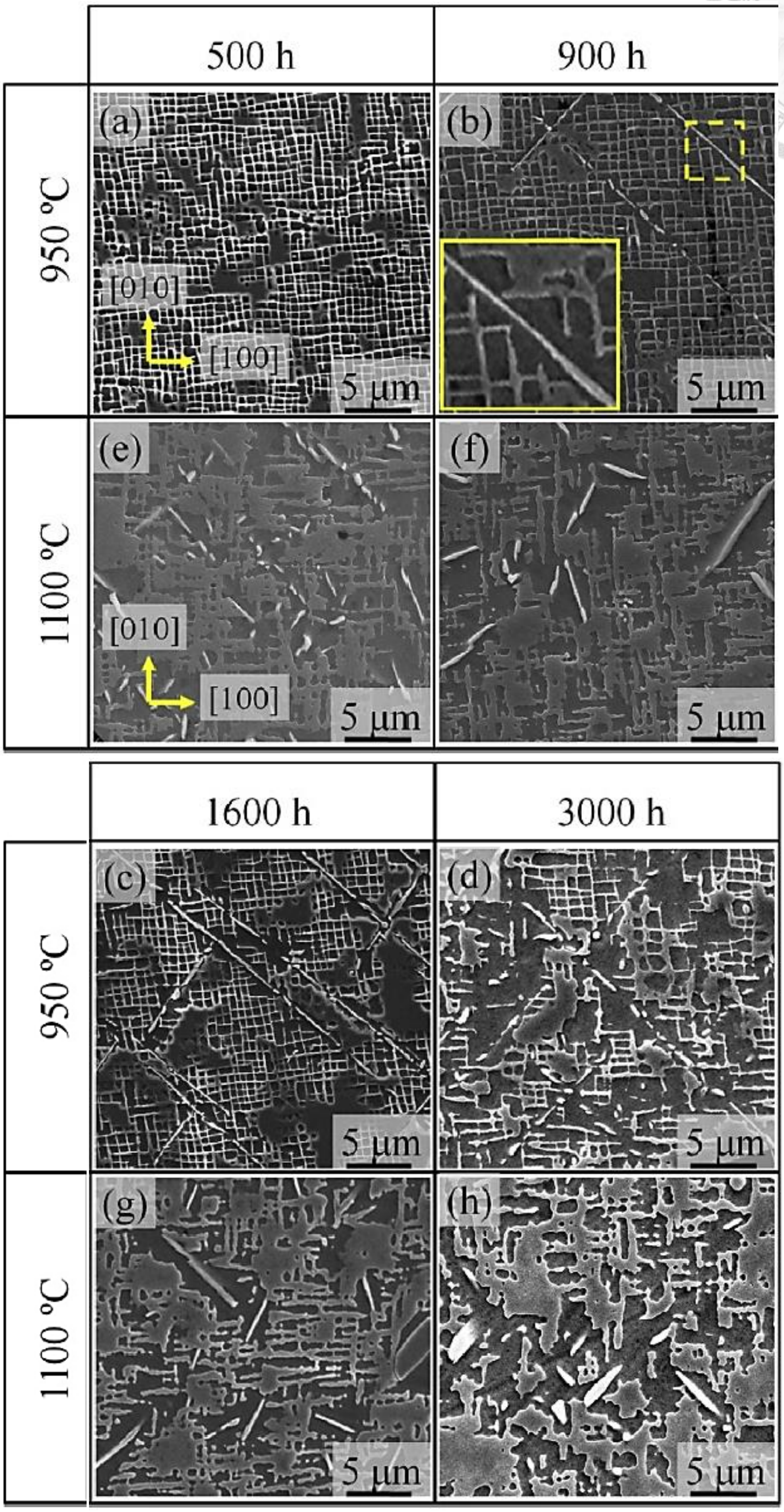

Figure 2-11 TCP phases evolution in Ni-based superalloy under different temperature and time [69].

2.3 Alloy design

For $L1_2$-strengthened high-entropy alloys, the FCC + $L1_2$ system is the most ideal, also written as γ + γ′. Three-element, four-element, or five-element high-entropy alloys in the CrCoFeMnNi system are commonly used as substrates, among which Al, Ti, and Nb are used as stabilizers to promote the formation of $L1_2$ [42].

2.3.1 The impact of adding Al on high-entropy alloys

Al is considered a stabilizer for $L1_2$ phase, but literature indicates that adding Al alone to medium/high entropy alloys is not enough to stabilize $L1_2$. If too much Al is added, B2 phase may precipitate in the alloy, making the material brittle.

In the as-cast state, $L1_2$ phase can be found in $Al_{0.3}CoCrFeNi$ [70] and $Al_{0.3}CuCrFeNi_2$[71] , but the $L1_2$ phase in $Al_{0.3}CoCrFeNi$ can only be stable at 550°C. When the temperature is increased to 700°C, the $L1_2$ phase will transform into B2-NiAl. The stability of $L1_2$ phase in $Al_{0.3}CuCrFeNi_2$ is better than that in $Al_{0.3}CoCrFeNi$ because Cu can stabilize the nucleation of $L1_2$ phase.

By changing the Al content in $AlxCuCrFeNi_2$ [72], it can be observed that increasing the aluminum content does not effectively stabilize the $L1_2$ phase. Instead, it forms other phases and structures (as shown in Table 2-5), which are in the order of

doi:10.6342/NTU202302391

FCC solid solution, FCC+$L1_2$, FCC+$L1_2$/BCC+B2, and BCC+B2. Therefore, adding an appropriate amount of Al is more appropriate.

Table 2-5 Composition and phase ratio of $Al_xCuCrFeNi_2$(as-cast) [72].

Comp(x)	fcc1		fcc2		bcc+B2		Rwp(fit%)
	a(Å)	wt(%)	a(Å)	wt(%)	a(Å)	wt(%)	
0	3.584	74(fcc)	3.599	24(Cu-rich fcc)	2.874	2	23.37
0.8	3.604	16(Cu-rich fcc)	3.599	74($L1_2$)	2.873	10	20.44
1.0	3.618	12(Cu-rich fcc)	3.600	51($L1_2$)	2.874	37	24.51
1.3	3.623	20(Cu-rich fcc)	3.595	4(fcc)	2.877	76	17.10
1.5	3.636	20(Cu-rich fcc)	-	-	2.880	80	16.51

2.3.2 The impact of adding Ti on high-entropy alloys

Using single-phase FCC medium/high-entropy alloys as a base, adding a suitable amount of Al and Ti can precipitate nano-scale $L1_2$ phase $Ni_3(Al,Ti)$ and achieve excellent mechanical properties, such as $(CoCrNi)_{94}Al_3Ti_3$[33] and $(FeCoNiCr)_{94}Ti_2Al_4$ [9]. However, excessive Ti elements will form incoherent precipitates such as $L2_1$ Heusler phases or η phases, both of which will cause embrittlement of the material. It is worth mentioning that in the two successful cases mentioned above, $L2_1$ Heusler phases and η phases were still found, but the amount precipitated was very small and not enough to cause serious material embrittlement.

Research by He et al. [9] suggests that $(FeCoNiCr)_{94}Ti_2Al_4$ may contain secondary phases such as σ, μ, Laves, B2-NiAl, BCC, carbides, $L1_2$ phases, and $L2_1$ Heusler phases. Among them, $L1_2$ phase is relatively stable at 650-850°C, but when the temperature is higher than 850°C, a large amount of Heusler phases precipitate, causing serious material embrittlement. Therefore, when conducting aging treatment, a temperature below 850°C should be used to avoid the formation of $L2_1$ phases.

2.3.3 The impact of adding Nb on high-entropy alloys

Regarding Nb, Slone et al. added Al and Nb to precipitate the $L1_2$ phase [73], using elements such as Al, Co, Cr, Fe, Nb, and Ni. The study found that Nb tends to bond with Co and Fe, and that adding too much Nb will result in the formation of brittle Laves or B2 phases (as shown in Figure 2-12). So far, an optimal alloy composition has not been found. In the study, as the alloy composition approaches equiatomic proportions, the entropy of the alloy system increases, causing both the melting point of the substrate and the $L1_2$ phase to decrease, resulting in poorer high-temperature performance of the material.

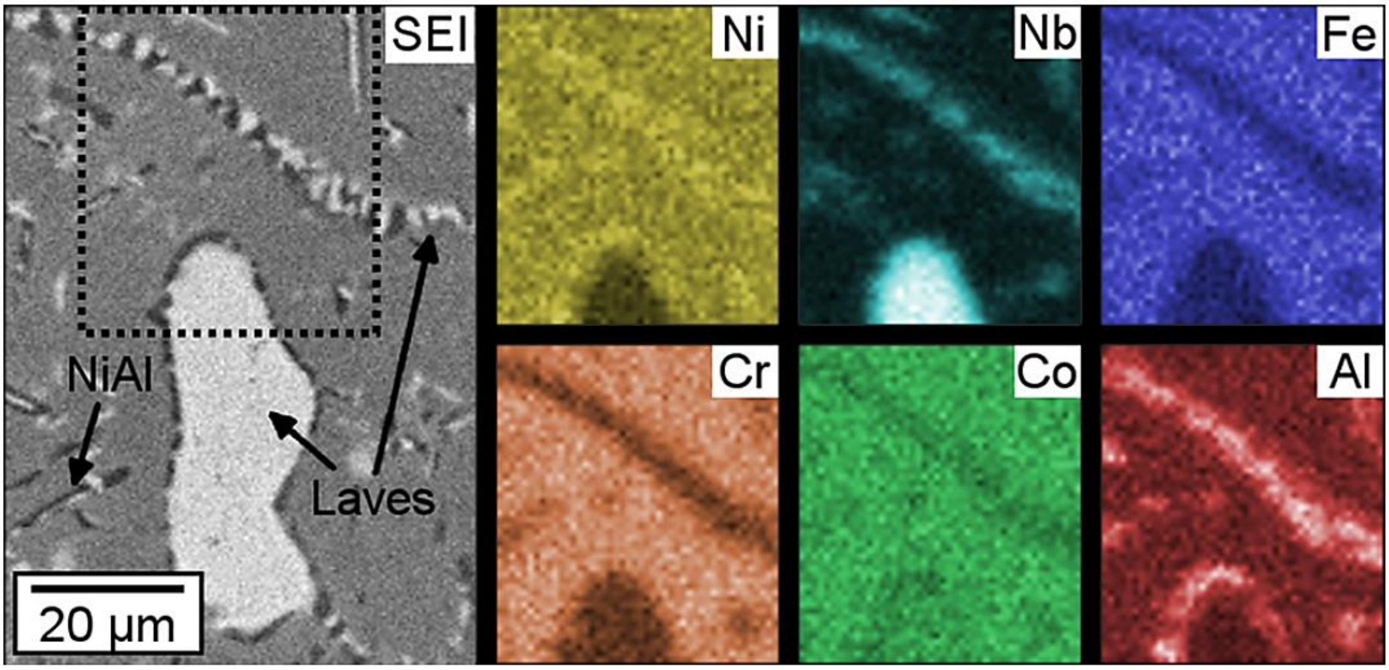

Figure 2-12 SEM image of B2-NiAl and C14-Laves(Nb,Co) in $Al_{8.8}Co_{29}Cr_{19}Fe_{18}Ni_{20.4}Nb_{4.8}$ after 1000° C aging treatment [73].

Ma et al.'s research indicated that by varying the Nb content (x=0, 0.1, 0.25, 0.5, 0.75) in AlCoCrFeNbxNi without homogenization and annealing [74], typical as-cast microstructures were observed using SEM (see Figure 2-13). Figure 2-14 shows the $AlCoCrFeNb_xNi$ phase diagram based on the experimental results drawn by Ma et al. It can be seen that even if the Nb content is reduced to avoid the brittle Laves phase, the substrate is not an ideal FCC but rather a BCC. Therefore, to generate a stable FCC+$L1_2$ structure, the Al content should be appropriately reduced to enable the formation of an FCC structure.

doi:10.6342/NTU202302391

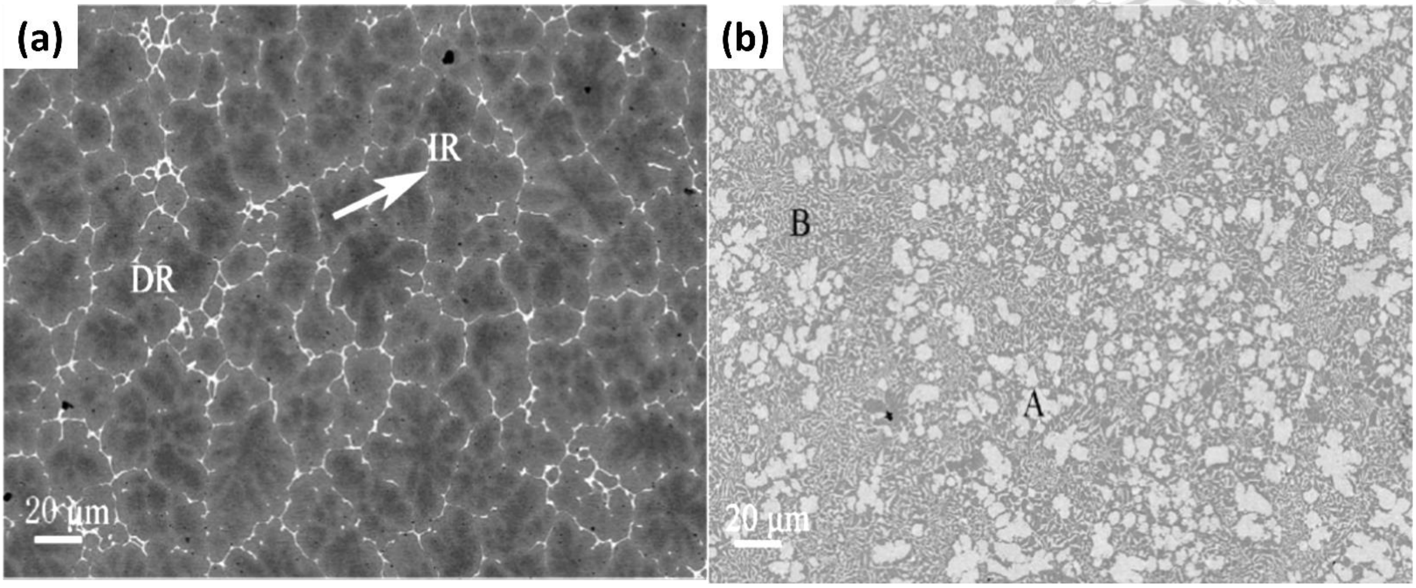

Figure 2-13 SEM image of (a)$AlCoCrFeNb_{0.1}Ni$ (b) $AlCoCrFeNb_{0.75}Ni$ [74].

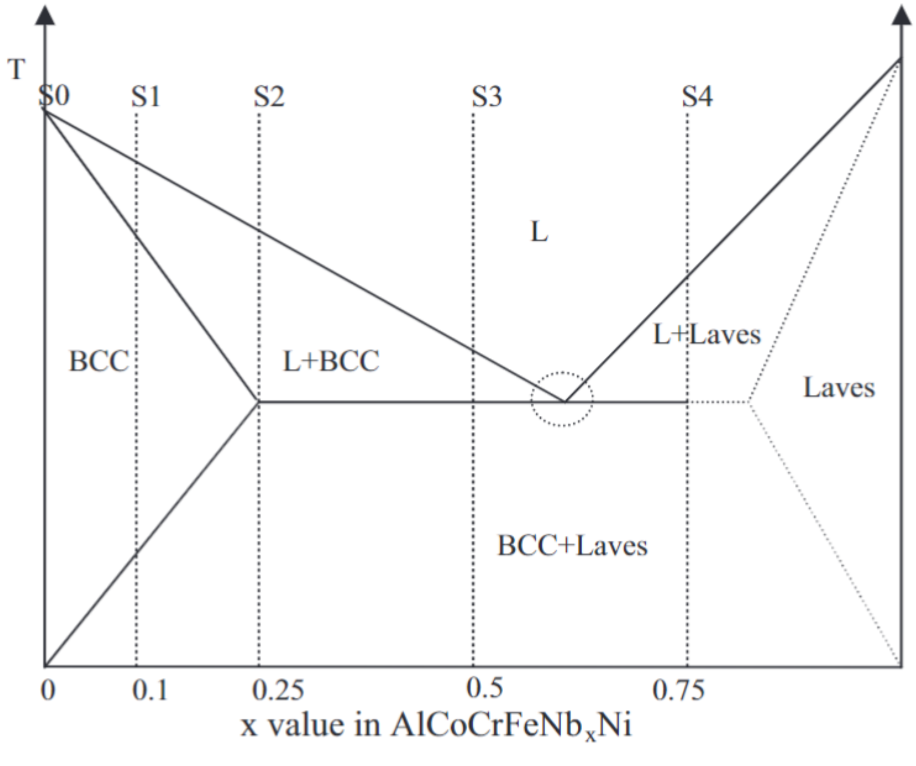

Figure 2-14 Empirical phase diagram of $AlCoCrFeNb_xNi$ [74].

Regarding the effect of individual elements, Fe suppresses the nucleation of $L1_2$ phase because Fe and Nb will form Nb-rich Laves phase. The effect of Co is not yet clearly explained, as some studies have shown that Co reduces $L1_2$ phase, while others have shown that Co stabilizes $L1_2$ phase. This part still needs to be clarified.

doi:10.6342/NTU202302391

2.4 Thermal stability of $L1_2$ phase

2.4.1 Fundamentals of high-entropy alloys and Ni-based superalloys

Tsao et al. [75] showed that the thermal stability of a material is related to its atomic bonding strength. Stronger atomic bonding can enhance the thermal stability of a material. The stability of a material can be determined by thermodynamic calculations. Table 2-7 show a series of simulation calculations on the binary mixing enthalpy (ΔH_{mix}) of each atom by Takeuchi et al. [76].

Assuming that the mixing entropy (ΔS_{mix}) of each system is the same, the thermal stability of $L1_2$-$Ni_3(Al, Ti)$ in nickel-based superalloys and medium-entropy alloys in NiCoFe can be compared using the mixing enthalpy (ΔH_{mix}). The main bonds in nickel-based superalloys and $L1_2$-$Ni_3(Al, Ti)$ are Ni-Al (-22 kJ/mol) and Ni-Ti (-35 kJ/mol). In NiCoFe medium-entropy alloys, in addition to Ni-Al and Ni-Ti bonds, more Ni is replaced by Co, resulting in Co-Al (-19 kJ/mol) and Co-Ti (-28 kJ/mol) bonds. The overall mixing enthalpy (ΔH_{mix}) of NiCoFe medium-entropy alloys increases. According to Eq. 2-4,the free energy (ΔG_{mix}) also increases, making the system less stable. Therefore, from the perspective of mixing enthalpy (ΔH_{mix}), the liquid phase line temperature in the phase diagram will decrease, consistent with the simulation trend.

$$\Delta G_{mix} = \Delta H_{mix} - T\Delta S_{mix} \qquad \text{Eq. 2-4}$$

doi:10.6342/NTU202302391

The conventional working temperature of nickel-based superalloys is about 900°C. In high-temperature environments, TCP (Topologically Close Pack) phases are easily formed inside the material, and suppressing the generation of TCP phases is one of the challenges for the application of materials at high temperatures. For example, the RR2071 and Rene N6 series nickel-based superalloys start to generate TCP phases after 900°C/100h aging treatment [77, 78], but the medium-entropy alloy HA-3 does not generate TCP phases after 900°C/300h aging treatment [75], indicating that medium/high-entropy alloys have certain potential for high-temperature applications. Three alloys, Hastelloy X [79], RR2071 [77]與 HA-3 [75], are compared and discussed below:

1. Hastelloy X (Ni-22Cr-18.5Fe-9Mo-1.5Co-0.6W-0.15C wt%)
2. RR2071(Ni-6.6Cr-4.5Mo-9.5Co-5.6Al-1.3Ti-0.3Nb-2.8Re-7.3Ta wt%)
3. HA-3(Ni-11.7Cr-11.8Fe-22.3Co-3.9Al-6.3Ti wt%)

Hastelloy X contains a higher amount of Cr and Fe, which easily forms Fe-Cr-rich σ phase. RR2071 does not contain Fe and has a significantly reduced Cr content. Instead, it contains more refractory elements to improve high-temperature properties, but a large amount of μ phase forms at 900°C. HA-3 contains Fe and a higher amount of Cr, but no formation of TCP phase was observed.

From the perspective of mixing entropy (ΔS_{mix}), the mixing entropy (ΔS_{mix}) of nickel-based superalloys is much lower than that of entropy alloys in NiCoFe. Eq. 2-5 and Eq. 2-6 are formulas for mixing entropy (ΔS_{mix}) in binary and multicomponent alloy systems. The chemical compositions can be obtained from Table 2-8. Taking CM247LC nickel-based superalloy [80] and HA-1 entropy alloy as examples, their mixing entropies (ΔS_{mix}) are 1.17R and 1.55R, respectively. Experimental results indicate that higher mixing entropy (ΔS_{mix}) can stabilize the γ phase, improve the solid solubility of alloy elements, reduce the formation of $L1_2$ phase and suppress the formation of TCP phase, thereby improving its performance in high-temperature environments.

$$\Delta S_{mix} = -nR(x_1 ln x_1 + x_2 ln x_2) \qquad \text{Eq. 2-5}$$

$$\Delta S_{mix} = -nR\sum_{i}^{k}(x_i ln x_i) \qquad \text{Eq. 2-6}$$

Table 2-6 binary mixing enthalpy(ΔH_{mix}) by Miedema [76].

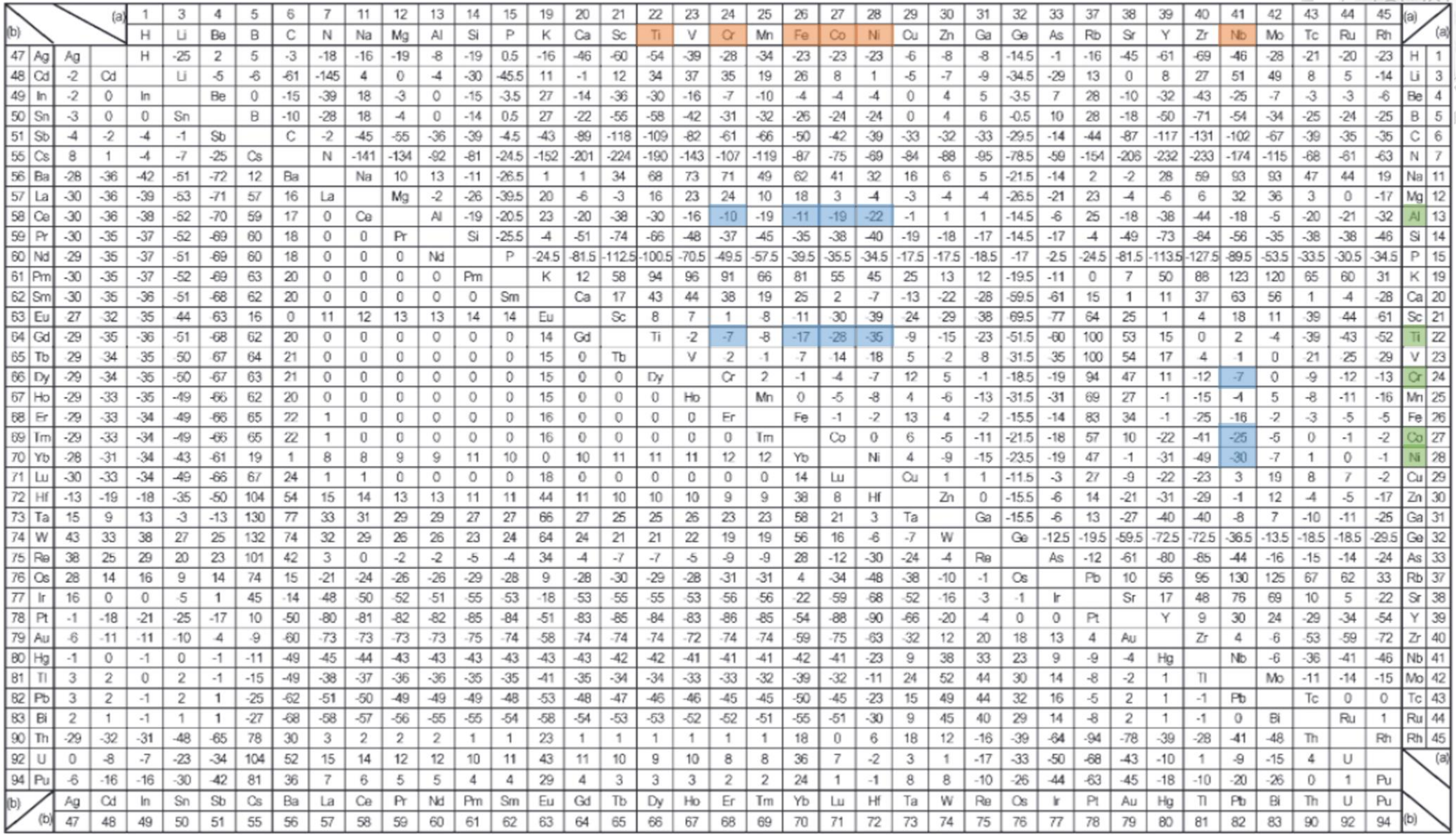

			(a)	1	3	4	5	6	7	11	12	13	14	15	19	20	21	22	23	24	25	26	27	28	29	30	31	32	33	37	38	39	40	41	42	43	44	45	(a)	
(b)				H	Li	Be	B	C	N	Na	Mg	Al	Si	P	K	Ca	Sc	Ti	V	Cr	Mn	Fe	Co	Ni	Cu	Zn	Ga	Ge	As	Rb	Sr	Y	Zr	Nb	Mo	Tc	Ru	Rh		(a)
47	Ag	Ag		H	-25	2	5	-3	-18	-16	-19	-8	-19	0.5	-16	-46	-60	-54	-39	-28	-34	-23	-23	-23	-6	-8	-8	-14.5	-1	-16	-45	-61	-69	-46	-28	-21	-20	-23	H	1
48	Cd	-2	Cd		Li	-5	-6	-61	-145	4	0	-4	-30	-45.5	11	-1	12	34	37	35	19	26	8	1	-5	-7	-9	-34.5	-29	13	0	8	27	51	49	8	5	-14	Li	3
49	In	-2	0	In		Be	0	-15	-39	18	-3	0	-15	-3.5	27	-14	-36	-30	-16	-7	-10	-4	-4	-4	0	4	5	-3.5	7	28	-10	-32	-43	-25	-7	-3	-3	-6	Be	4
50	Sn	-3	0	0	Sn		B	-10	-28	18	-4	0	-14	0.5	27	-22	-56	-58	-42	-31	-32	-26	-24	-24	0	4	6	-0.5	10	28	-18	-50	-71	-54	-34	-25	-24	-25	B	5
51	Sb	-4	-2	-4	-1	Sb		C	-2	-45	-55	-36	-39	-4.5	-43	-89	-118	-109	-82	-61	-66	-50	-42	-39	-33	-32	-33	-29.5	-14	-44	-87	-117	-131	-102	-67	-39	-35	-35	C	6
55	Cs	8	1	-4	-7	-25	Cs		N	-141	-134	-92	-81	-24.5	-152	-201	-224	-190	-143	-107	-119	-87	-75	-69	-84	-88	-95	-78.5	-59	-154	-206	-232	-233	-174	-115	-68	-61	-63	N	7
56	Ba	-28	-36	-42	-51	-72	12	Ba		Na	10	13	-11	-26.5	1	1	34	68	73	71	49	62	41	32	16	6	5	-21.5	-14	2	-2	28	59	93	93	47	44	19	Na	11
57	La	-30	-36	-39	-53	-71	57	16	La		Mg	-2	-26	-39.5	20	-6	-3	16	23	24	10	18	3	-4	-3	-4	-4	-26.5	-21	23	-4	-6	6	32	36	3	0	-17	Mg	12
58	Ce	-30	-36	-38	-52	-70	59	17	0	Ce		Al	-19	-20.5	23	-20	-38	-30	-16	-10	-19	-11	-19	-22	-1	1	1	-14.5	-6	25	-18	-38	-44	-18	-5	-20	-21	-32	Al	13
59	Pr	-30	-35	-37	-52	-69	60	18	0	0	Pr		Si	-25.5	-4	-51	-74	-66	-48	-37	-45	-35	-38	-40	-19	-18	-17	-14.5	-17	-4	-49	-73	-84	-56	-35	-38	-38	-46	Si	14
60	Nd	-29	-35	-37	-51	-69	60	18	0	0	0	Nd		P	-24.5	-81.5	-112.5	-100.5	-70.5	-49.5	-57.5	-39.5	-35.5	-34.5	-17.5	-17.5	-18.5	-17	-2.5	-24.5	-81.5	-113.5	-127.5	-89.5	-53.5	-33.5	-30.5	-34.5	P	15
61	Pm	-30	-35	-37	-52	-69	63	20	0	0	0	0	Pm		K	12	58	94	96	91	66	81	55	45	25	13	12	-19.5	-11	0	7	50	88	123	120	65	60	31	K	19
62	Sm	-30	-35	-36	-51	-68	62	20	0	0	0	0	0	Sm		Ca	17	43	44	38	19	25	2	-7	-13	-22	-28	-59.5	-61	15	1	11	37	63	56	1	-4	-28	Ca	20
63	Eu	-27	-32	-35	-44	-63	16	0	11	12	13	13	14	14	Eu		Sc	8	7	1	-8	-11	-30	-39	-24	-29	-38	-69.5	-77	64	25	1	4	18	11	-39	-44	-61	Sc	21
64	Gd	-29	-35	-36	-51	-68	62	20	0	0	0	0	0	0	14	Gd		Ti	-2	-7	-8	-17	-28	-35	-9	-15	-23	-51.5	-60	100	53	15	0	2	-4	-39	-43	-52	Ti	22
65	Tb	-29	-34	-35	-50	-67	64	21	0	0	0	0	0	0	15	0	Tb		V	-2	-1	-7	-14	-18	5	-2	-8	-31.5	-35	100	54	17	-4	-1	0	-21	-25	-29	V	23
66	Dy	-29	-34	-35	-50	-67	63	21	0	0	0	0	0	0	15	0	0	Dy		Cr	2	-1	-4	-7	12	5	-1	-18.5	-19	94	47	11	-12	-7	0	-9	-12	-13	Cr	24
67	Ho	-29	-33	-35	-49	-66	62	20	0	0	0	0	0	0	15	0	0	0	Ho		Mn	0	-5	-8	4	-6	-13	-31.5	-31	69	27	-1	-15	-4	5	-8	-11	-16	Mn	25
68	Er	-29	-33	-34	-49	-66	65	22	1	0	0	0	0	0	16	0	0	0	0	Er		Fe	-1	-2	13	4	-2	-15.5	-14	83	34	-1	-25	-16	-2	-3	-5	-5	Fe	26
69	Tm	-29	-33	-34	-49	-66	65	22	1	0	0	0	0	0	16	0	0	0	0	0	Tm		Co	0	6	-5	-11	-21.5	-18	57	10	-22	-41	-25	-5	0	-1	-2	Co	27
70	Yb	-28	-31	-34	-43	-61	19	1	8	8	9	9	11	10	0	10	11	11	11	12	12	Yb		Ni	4	-9	-15	-23.5	-19	47	-1	-31	-49	-30	-7	1	0	-1	Ni	28
71	Lu	-30	-33	-34	-49	-66	67	24	1	1	0	0	0	0	18	0	0	0	0	0	0	14	Lu		Cu	1	1	-11.5	-3	27	-9	-22	-23	3	19	8	7	-2	Cu	29
72	Hf	-13	-19	-18	-35	-50	104	54	15	14	13	13	11	11	44	11	10	10	10	9	9	38	8	Hf		Zn	0	-15.5	-6	14	-21	-31	-29	-1	12	-4	-5	-17	Zn	30
73	Ta	15	9	13	-3	-13	130	77	33	31	29	29	27	27	66	27	25	25	26	23	23	58	21	3	Ta		Ga	-15.5	-6	13	-27	-40	-40	-8	7	-10	-11	-25	Ga	31
74	W	43	33	38	27	25	132	74	32	29	26	26	23	24	64	24	21	21	22	19	19	56	16	-6	-7	W		Ge	-12.5	-19.5	-59.5	-72.5	-72.5	-36.5	-13.5	-18.5	-18.5	-29.5	Ge	32
75	Re	38	25	29	20	23	101	42	3	0	-2	-2	-5	-4	34	-4	-7	-7	-5	-9	-9	28	-12	-30	-24	-4	Re		As	-12	-61	-80	-85	-44	-16	-15	-14	-24	As	33
76	Os	28	14	16	9	14	74	15	-21	-24	-26	-26	-29	-28	9	-28	-30	-29	-28	-31	-31	4	-34	-48	-38	-10	-1	Os		Pb	10	56	95	130	125	67	62	33	Rb	37
77	Ir	16	0	0	-5	1	45	-14	-48	-50	-52	-51	-55	-53	-18	-53	-55	-55	-53	-56	-56	-22	-59	-68	-52	-16	-3	-1	Ir		Sr	17	48	76	69	10	5	-22	Sr	38
78	Pt	-1	-18	-21	-25	-17	10	-50	-80	-81	-82	-82	-85	-84	-51	-83	-85	-84	-83	-86	-85	-54	-88	-90	-66	-20	-4	0	0	Pt		Y	9	30	24	-29	-34	-54	Y	39
79	Au	-6	-11	-11	-10	-4	-9	-60	-73	-73	-73	-73	-75	-74	-58	-74	-74	-74	-72	-74	-74	-59	-75	-63	-32	12	20	18	13	4	Au		Zr	4	-6	-53	-59	-72	Zr	40
80	Hg	-1	0	-1	0	-1	-11	-49	-45	-44	-43	-43	-43	-43	-43	-43	-42	-42	-41	-41	-41	-42	-41	-23	9	38	33	23	9	-9	-4	Hg		Nb	-6	-36	-41	-46	Nb	41
81	Tl	3	2	0	2	-1	-15	-49	-38	-37	-36	-36	-35	-35	-41	-35	-34	-34	-33	-33	-32	-39	-32	-11	24	52	44	30	14	-8	-2	1	Tl		Mo	-11	-14	-15	Mo	42
82	Pb	3	2	-1	2	1	-25	-62	-51	-50	-49	-49	-49	-48	-53	-48	-47	-46	-46	-45	-45	-50	-45	-23	15	49	44	32	16	-5	2	1	-1	Pb		Tc	0	0	Tc	43
83	Bi	2	1	-1	1	1	-27	-68	-58	-57	-56	-55	-55	-54	-58	-54	-53	-53	-52	-52	-51	-55	-51	-30	9	45	40	29	14	-8	2	1	-1	0	Bi		Ru	1	Ru	44
90	Th	-29	-32	-31	-48	-65	78	30	3	2	2	2	1	1	23	1	1	1	1	1	1	18	0	6	18	12	-16	-39	-64	-94	-78	-39	-28	-41	-48	Th		Rh	Rh	45
92	U	0	-8	-7	-23	-34	104	52	15	14	12	12	10	11	43	11	10	9	10	8	8	36	7	-2	3	1	-17	-33	-50	-68	-43	-10	1	-9	-15	4	U			(a)
94	Pu	-6	-16	-16	-30	-42	81	36	7	6	5	5	4	4	29	4	3	3	3	2	2	24	1	-1	8	8	-10	-26	-44	-63	-45	-18	-10	-20	-26	0	1	Pu		
(b)		Ag	Cd	In	Sn	Sb	Cs	Ba	La	Ce	Pr	Nd	Pm	Sm	Eu	Gd	Tb	Dy	Ho	Er	Tm	Yb	Lu	Hf	Ta	W	Re	Os	Ir	Pt	Au	Hg	Tl	Pb	Bi	Th	U	Pu		
	(b)	47	48	49	50	51	55	56	57	58	59	60	61	62	63	64	65	66	67	68	69	70	71	72	73	74	75	76	77	78	79	80	81	82	83	90	92	94	(b)	

doi:10.6342/NTU202302391

Table 2-7 binary mixing enthalpy(ΔH_{mix}) by Miedema [76].

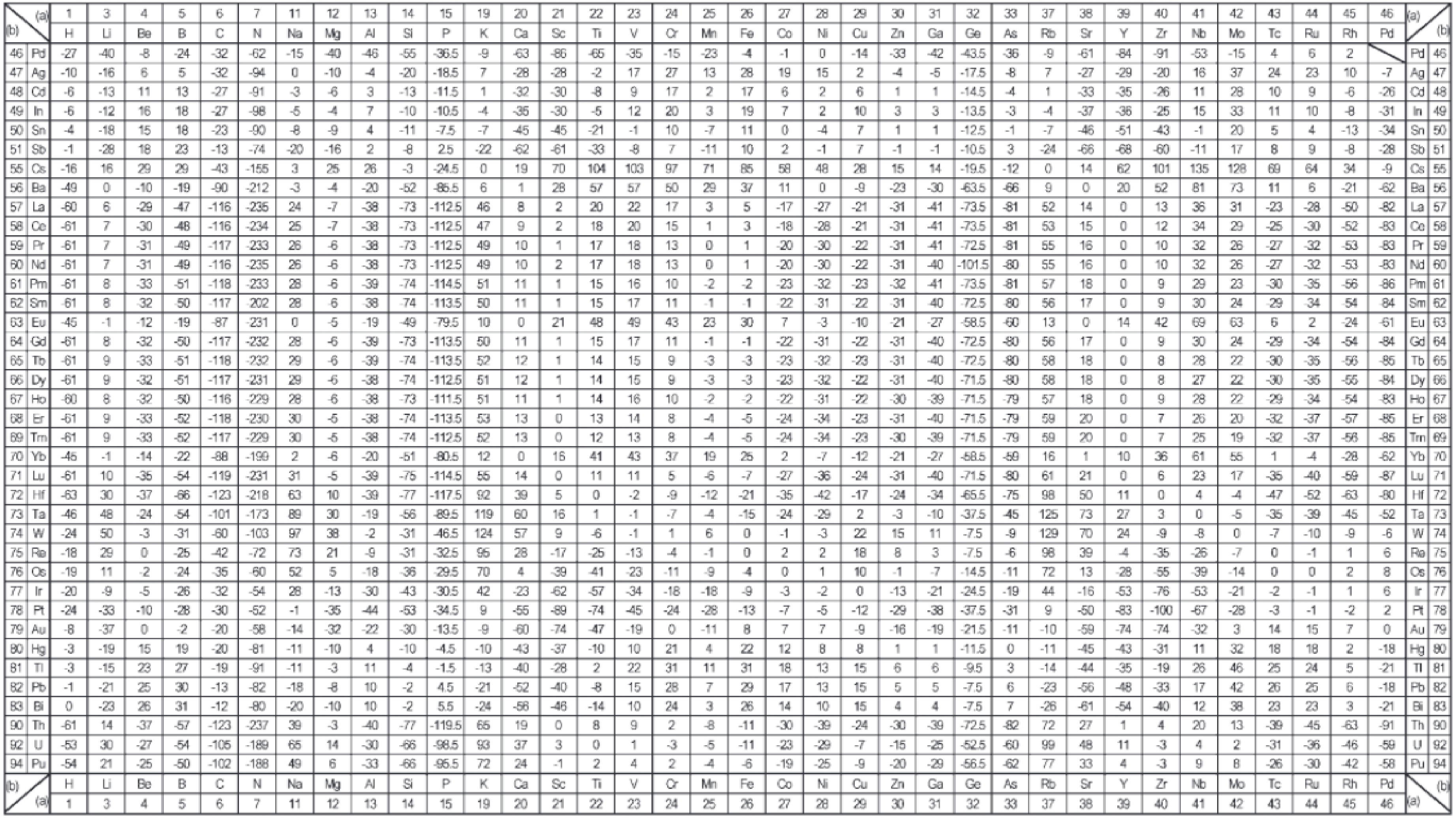

(a)		1	3	4	5	6	7	11	12	13	14	15	19	20	21	22	23	24	25	26	27	28	29	30	31	32	33	37	38	39	40	41	42	43	44	45	46	(a)	
(b)		H	Li	Be	B	C	N	Na	Mg	Al	Si	P	K	Ca	Sc	Ti	V	Cr	Mn	Fe	Co	Ni	Cu	Zn	Ga	Ge	As	Rb	Sr	Y	Zr	Nb	Mo	Tc	Ru	Rh	Pd		(b)
46	Pd	-27	-40	-8	-24	-32	-62	-15	-40	-46	-55	-36.5	-9	-63	-86	-65	-35	-15	-23	-4	-1	0	-14	-33	-42	-43.5	-36	-9	-61	-84	-91	-53	-15	4	6	2		Pd	46
47	Ag	-10	-16	6	5	-32	-94	0	-10	-4	-20	-18.5	7	-28	-28	-2	17	27	13	28	19	15	2	-4	-5	-17.5	-8	7	-27	-29	-20	16	37	24	23	10	-7	Ag	47
48	Cd	-6	-13	11	13	-27	-91	-3	-6	3	-13	-11.5	1	-32	-30	-8	9	17	2	17	6	2	6	1	1	-14.5	-4	1	-33	-35	-26	11	28	10	9	-6	-26	Cd	48
49	In	-6	-12	16	18	-27	-98	-5	-4	7	-10	-10.5	-4	-35	-30	-5	12	20	3	19	7	2	10	3	3	-13.5	-3	-4	-37	-36	-25	15	33	11	10	-8	-31	In	49
50	Sn	-4	-18	15	18	-23	-90	-8	-9	4	-11	-7.5	-7	-45	-45	-21	-1	10	-7	11	0	-4	7	1	1	-12.5	-1	-7	-46	-51	-43	-1	20	5	4	-13	-34	Sn	50
51	Sb	-1	-28	18	23	-13	-74	-20	-16	2	-8	2.5	-22	-62	-61	-33	-8	7	-11	10	2	-1	7	-1	-1	-10.5	3	-24	-66	-68	-60	-11	17	8	9	-8	-28	Sb	51
55	Cs	-16	16	29	29	-43	-155	3	25	26	-3	-24.5	0	19	70	104	103	97	71	85	58	48	28	15	14	-19.5	-12	0	14	62	101	135	128	69	64	34	-9	Cs	55
56	Ba	-49	0	-10	-19	-90	-212	-3	-4	-20	-52	-86.5	6	1	28	57	57	50	29	37	11	0	-9	-23	-30	-63.5	-66	9	0	20	52	81	73	11	6	-21	-62	Ba	56
57	La	-60	6	-29	-47	-116	-235	24	-7	-38	-73	-112.5	46	8	2	20	22	17	3	5	-17	-27	-21	-31	-41	-73.5	-81	52	14	0	13	36	31	-23	-28	-50	-82	La	57
58	Ce	-61	7	-30	-48	-116	-234	25	-7	-38	-73	-112.5	47	9	2	18	20	15	1	3	-18	-28	-21	-31	-41	-73.5	-81	53	15	0	12	34	29	-25	-30	-52	-83	Ce	58
59	Pr	-61	7	-31	-49	-117	-233	26	-6	-38	-73	-112.5	49	10	1	17	18	13	0	1	-20	-30	-22	-31	-41	-72.5	-81	55	16	0	10	32	26	-27	-32	-53	-83	Pr	59
60	Nd	-61	7	-31	-49	-116	-235	26	-6	-38	-73	-112.5	49	10	2	17	18	13	0	1	-20	-30	-22	-31	-40	-101.5	-80	55	16	0	10	32	26	-27	-32	-53	-83	Nd	60
61	Pm	-61	8	-33	-51	-118	-233	28	-6	-39	-74	-114.5	51	11	1	15	16	10	-2	-2	-23	-32	-23	-32	-41	-73.5	-81	57	18	0	9	29	23	-30	-35	-56	-86	Pm	61
62	Sm	-61	8	-32	-50	-117	-202	28	-6	-38	-74	-113.5	50	11	1	15	17	11	-1	-1	-22	-31	-22	-31	-40	-72.5	-80	56	17	0	9	30	24	-29	-34	-54	-84	Sm	62
63	Eu	-45	-1	-12	-19	-87	-231	0	-5	-19	-49	-79.5	10	0	21	48	49	43	23	30	7	-3	-10	-21	-27	-58.5	-60	13	0	14	42	69	63	6	2	-24	-61	Eu	63
64	Gd	-61	8	-32	-50	-117	-232	28	-6	-39	-73	-113.5	50	11	1	15	17	11	-1	-1	-22	-31	-22	-31	-40	-72.5	-80	56	17	0	9	30	24	-29	-34	-54	-84	Gd	64
65	Tb	-61	9	-33	-51	-118	-232	29	-6	-39	-74	-113.5	52	12	1	14	15	9	-3	-3	-23	-32	-23	-31	-40	-72.5	-80	58	18	0	8	28	22	-30	-35	-56	-85	Tb	65
66	Dy	-61	9	-32	-51	-117	-231	29	-6	-38	-74	-112.5	51	12	1	14	15	9	-3	-3	-23	-32	-22	-31	-40	-71.5	-80	58	18	0	8	27	22	-30	-35	-55	-84	Dy	66
67	Ho	-60	8	-32	-50	-116	-229	28	-6	-38	-73	-111.5	51	11	1	14	16	10	-2	-2	-22	-31	-22	-30	-39	-71.5	-79	57	18	0	9	28	22	-29	-34	-54	-83	Ho	67
68	Er	-61	9	-33	-52	-118	-230	30	-5	-38	-74	-113.5	53	13	0	13	14	8	-4	-5	-24	-34	-23	-31	-40	-71.5	-79	59	20	0	7	26	20	-32	-37	-57	-85	Er	68
69	Tm	-61	9	-33	-52	-117	-229	30	-5	-38	-74	-112.5	52	13	0	12	13	8	-4	-5	-24	-34	-23	-30	-39	-71.5	-79	59	20	0	7	25	19	-32	-37	-56	-85	Tm	69
70	Yb	-45	-1	-14	-22	-88	-199	2	-6	-20	-51	-80.5	12	0	16	41	43	37	19	25	2	-7	-12	-21	-27	-58.5	-59	16	1	10	36	61	55	1	-4	-28	-62	Yb	70
71	Lu	-61	10	-35	-54	-119	-231	31	-5	-39	-75	-114.5	55	14	0	11	11	5	-6	-7	-27	-36	-24	-31	-40	-71.5	-80	61	21	0	6	23	17	-35	-40	-59	-87	Lu	71
72	Hf	-63	30	-37	-66	-123	-218	63	10	-39	-77	-117.5	92	39	5	0	-2	-9	-12	-21	-35	-42	-17	-24	-34	-65.5	-75	98	50	11	0	4	-4	-47	-52	-63	-80	Hf	72
73	Ta	-46	48	-24	-54	-101	-173	89	30	-19	-56	-89.5	119	60	16	1	-1	-7	-4	-15	-24	-29	2	-3	-10	-37.5	-45	125	73	27	3	0	-5	-35	-39	-45	-52	Ta	73
74	W	-24	50	-3	-31	-60	-103	97	38	-2	-31	-46.5	124	57	9	-6	-1	1	6	0	-1	-3	22	15	11	-7.5	-9	129	70	24	-9	-8	0	-7	-10	-9	-6	W	74
75	Re	-18	29	0	-25	-42	-72	73	21	-9	-31	-32.5	96	28	-17	-25	-13	-4	-1	0	2	2	18	8	3	-7.5	-6	98	39	-4	-35	-26	-7	0	-1	1	6	Re	75
76	Os	-19	11	-2	-24	-35	-60	52	5	-18	-36	-29.5	70	4	-39	-41	-23	-11	-9	-4	0	1	10	-1	-7	-14.5	-11	72	13	-28	-55	-39	-14	0	0	2	8	Os	76
77	Ir	-20	-9	-5	-26	-32	-54	28	-13	-30	-43	-30.5	42	-23	-62	-57	-34	-18	-18	-9	-3	-2	0	-13	-21	-24.5	-19	44	-16	-53	-76	-53	-21	-2	-1	1	6	Ir	77
78	Pt	-24	-33	-10	-28	-30	-52	-1	-35	-44	-53	-34.5	9	-55	-89	-74	-45	-24	-28	-13	-7	-5	-12	-29	-38	-37.5	-31	9	-50	-83	-100	-67	-28	-3	-1	-2	2	Pt	78
79	Au	-8	-37	0	-2	-20	-58	-14	-32	-22	-30	-13.5	-9	-60	-74	-47	-19	0	-11	8	7	7	-9	-16	-19	-21.5	-11	-10	-59	-74	-74	-32	3	14	15	7	0	Au	79
80	Hg	-3	-19	15	19	-20	-81	-11	-10	4	-10	-4.5	-10	-43	-37	-10	10	21	4	22	12	8	8	1	1	-11.5	0	-11	-45	-43	-31	11	32	18	18	2	-18	Hg	80
81	Tl	-3	-15	23	27	-19	-91	-11	-3	11	-4	-1.5	-13	-40	-28	2	22	31	11	31	18	13	15	6	6	-9.5	3	-14	-44	-35	-19	26	46	25	24	5	-21	Tl	81
82	Pb	-1	-21	25	30	-13	-82	-18	-8	10	-2	4.5	-21	-52	-40	-8	15	28	7	29	17	13	15	5	5	-7.5	6	-23	-56	-48	-33	17	42	26	25	6	-18	Pb	82
83	Bi	0	-23	26	31	-12	-80	-20	-10	10	-2	5.5	-24	-56	-46	-14	10	24	3	26	14	10	15	4	4	-7.5	7	-26	-61	-54	-40	12	38	23	23	3	-21	Bi	83
90	Th	-61	14	-37	-57	-123	-237	39	-3	-40	-77	-119.5	65	19	0	8	9	2	-8	-11	-30	-39	-24	-30	-39	-72.5	-82	72	27	1	4	20	13	-39	-45	-63	-91	Th	90
92	U	-53	30	-27	-54	-105	-189	65	14	-30	-66	-98.5	93	37	3	0	1	-3	-5	-11	-23	-29	-7	-15	-25	-52.5	-60	99	48	11	-3	4	2	-31	-36	-46	-59	U	92
94	Pu	-54	21	-25	-50	-102	-188	49	6	-33	-66	-95.5	72	24	-1	2	4	2	-4	-6	-19	-25	-9	-20	-29	-56.5	-62	77	33	4	-3	9	8	-26	-30	-42	-58	Pu	94
(b)		H	Li	Be	B	C	N	Na	Mg	Al	Si	P	K	Ca	Sc	Ti	V	Cr	Mn	Fe	Co	Ni	Cu	Zn	Ga	Ge	As	Rb	Sr	Y	Zr	Nb	Mo	Tc	Ru	Rh	Pd		(b)
	(a)	1	3	4	5	6	7	11	12	13	14	15	19	20	21	22	23	24	25	26	27	28	29	30	31	32	33	37	38	39	40	41	42	43	44	45	46	(a)	

Table 2-8 The chemical composition of γ/γ' and the liquidus temperature of γ' in NiCoFe high-entropy alloys and conventional nickel-based superalloys [75].

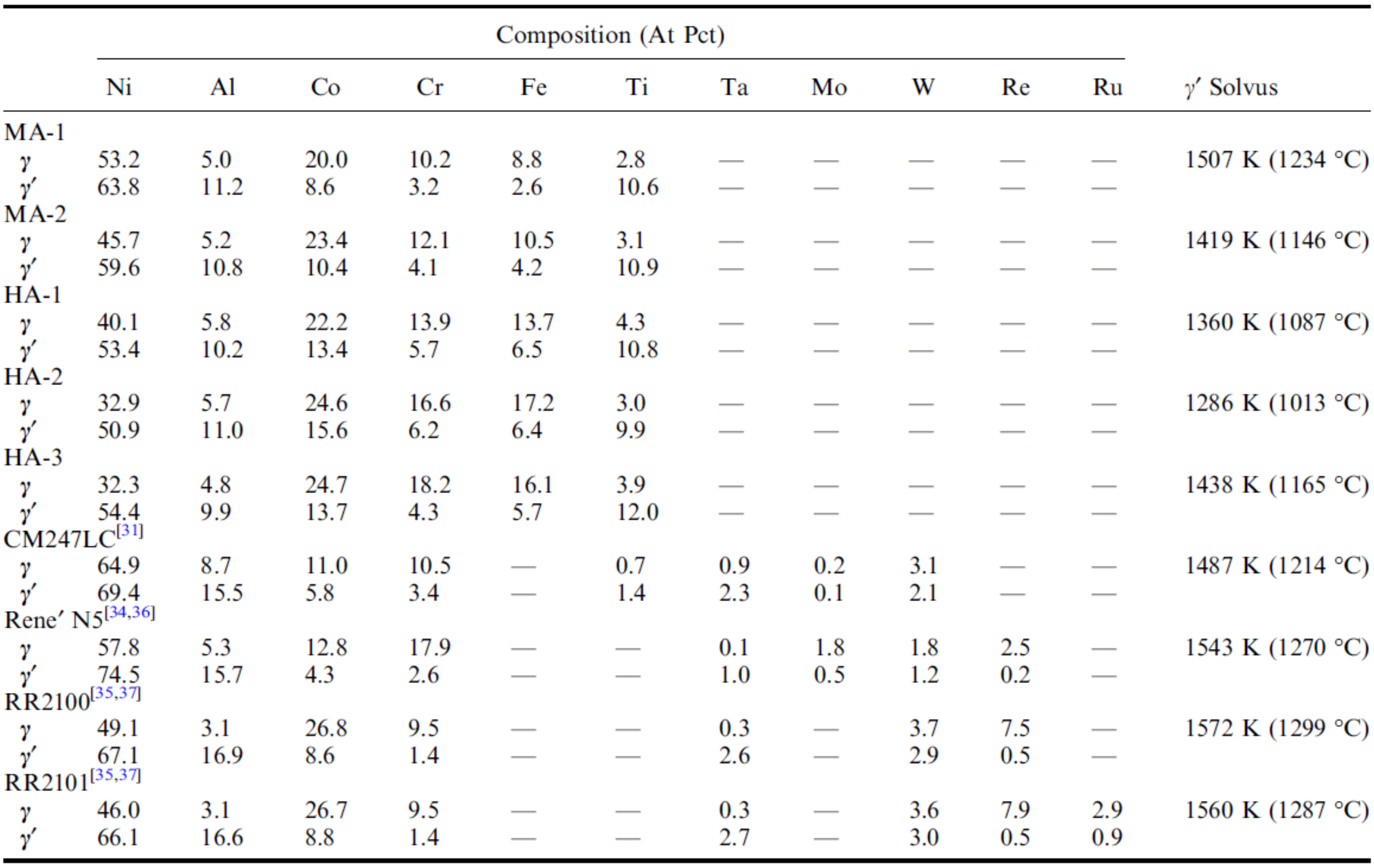

	Composition (At Pct)											
	Ni	Al	Co	Cr	Fe	Ti	Ta	Mo	W	Re	Ru	γ' Solvus
MA-1												
γ	53.2	5.0	20.0	10.2	8.8	2.8	—	—	—	—	—	1507 K (1234 °C)
γ'	63.8	11.2	8.6	3.2	2.6	10.6	—	—	—	—	—	
MA-2												
γ	45.7	5.2	23.4	12.1	10.5	3.1	—	—	—	—	—	1419 K (1146 °C)
γ'	59.6	10.8	10.4	4.1	4.2	10.9	—	—	—	—	—	
HA-1												
γ	40.1	5.8	22.2	13.9	13.7	4.3	—	—	—	—	—	1360 K (1087 °C)
γ'	53.4	10.2	13.4	5.7	6.5	10.8	—	—	—	—	—	
HA-2												
γ	32.9	5.7	24.6	16.6	17.2	3.0	—	—	—	—	—	1286 K (1013 °C)
γ'	50.9	11.0	15.6	6.2	6.4	9.9	—	—	—	—	—	
HA-3												
γ	32.3	4.8	24.7	18.2	16.1	3.9	—	—	—	—	—	1438 K (1165 °C)
γ'	54.4	9.9	13.7	4.3	5.7	12.0	—	—	—	—	—	
CM247LC[31]												
γ	64.9	8.7	11.0	10.5	—	0.7	0.9	0.2	3.1	—	—	1487 K (1214 °C)
γ'	69.4	15.5	5.8	3.4	—	1.4	2.3	0.1	2.1	—	—	
Rene′ N5[34,36]												
γ	57.8	5.3	12.8	17.9	—	—	0.1	1.8	1.8	2.5	—	1543 K (1270 °C)
γ'	74.5	15.7	4.3	2.6	—	—	1.0	0.5	1.2	0.2	—	
RR2100[35,37]												
γ	49.1	3.1	26.8	9.5	—	—	0.3	—	3.7	7.5	—	1572 K (1299 °C)
γ'	67.1	16.9	8.6	1.4	—	—	2.6	—	2.9	0.5	—	
RR2101[35,37]												
γ	46.0	3.1	26.7	9.5	—	—	0.3	—	3.6	7.9	2.9	1560 K (1287 °C)
γ'	66.1	16.6	8.8	1.4	—	—	2.7	—	3.0	0.5	0.9	

Otto et al. conducted a series of simulations on single-phase high-entropy alloys [81], and Troparevsky et al. visualized the results in a graphical representation (as shown in Figure 2-15) [82]. The pink central area in the figure represents the mixing enthalpy (ΔH_{mix}) of common high-entropy alloy elements, and it can be seen that the values of ΔH_{mix} are relatively small, indicating that they are not prone to the formation of intermetallic compounds (IMC) and can form stable single-phase solid solutions. In the figure, Fe-Mo and Ni-Ti have particularly high values of ΔH_{mix}. Taking these two element pairs as examples, Fe-Mo is often used in refractory steel due to the addition of Mo, which prevents the growth and dissolution of precipitates at high temperatures. Ni-Ti, on the other hand, is often used in nickel-based superalloys to precipitate Ni_3Ti. In recent years, it has also been applied to high-entropy alloys to precipitate Ni_3Ti, which has shown excellent performance in high-temperature environments [83].

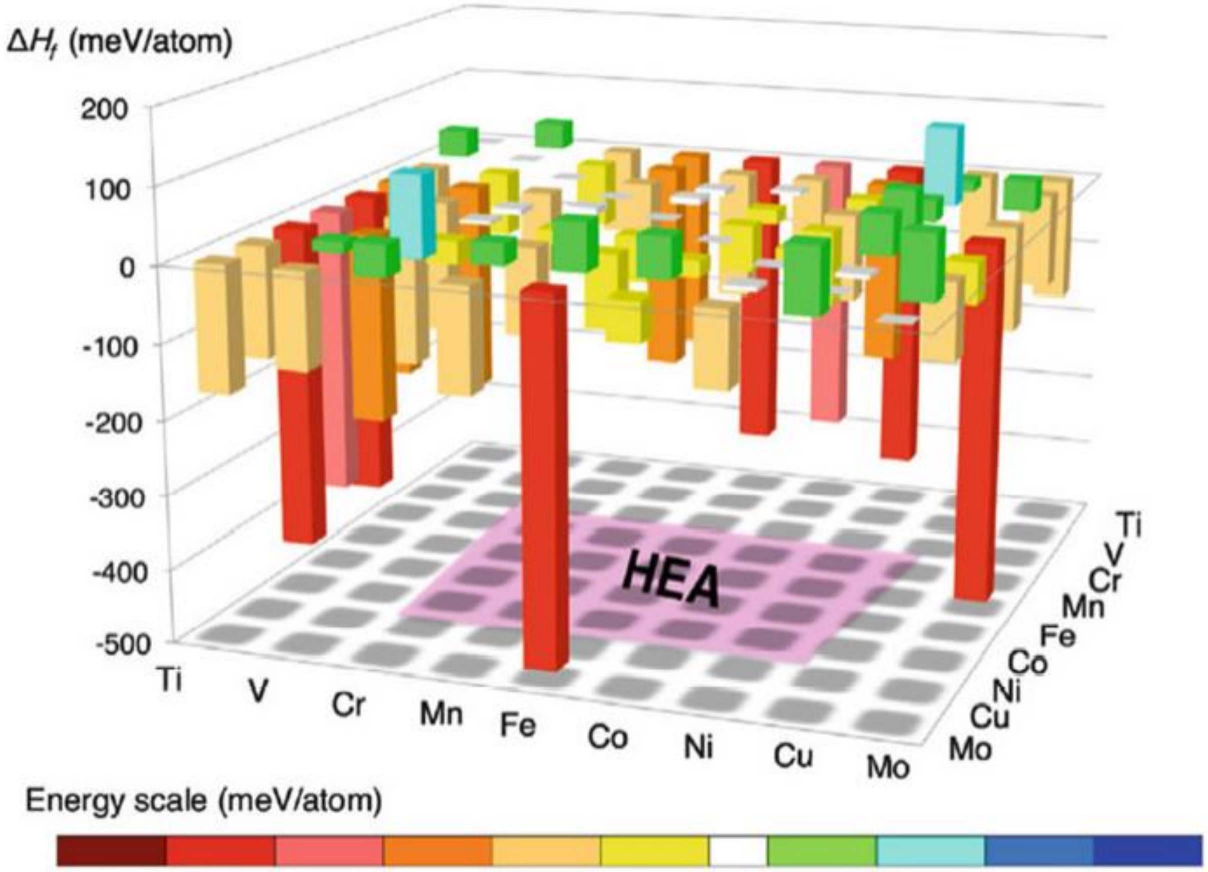

Figure 2-15 Simulated binary mixing enthalpy of single phase high-entropy alloys [82].

Figure 2-16 shows the results of Troparevsky et al.'s first-principles (DFT) simulations of binary mixing enthalpy (ΔH_{mix}) of high-entropy alloy elements [82].

Taking $(FeCoNiCr)_{94}Ti_2Al_4$, which only forms $L1_2$-$Ni_3(Al,Ti)$, as an example [9], the binary mixing enthalpies (ΔH_{mix}) of Fe-Ti, Co-Ti, Ni-Ti, and Cr-Ti are -418, -386, -435, and -372 meV/atom, respectively. According to thermodynamic criteria, if only one type of precipitation occurs in the alloy system, Ni-Ti phase is expected to appear due to its lowest binary mixing enthalpy (ΔH_{mix}). In $(FeCoNiCr)_{94}Ti_2Al_4$, only $L1_2$-$Ni_3(Al,Ti)$ was found, and no other Ti-containing phases were observed, which is consistent with the results.

In addition, Gerold et al. found that the binary mixing enthalpy(ΔH_{mix}) of Nb-Fe is -2505 meV/atom, while those of Nb-Co, Nb-Cr, and Nb-Ni are -178, -47, and -316 meV/atom, respectively. The binary mixing enthalpy (ΔH_{mix}) of Nb-Fe is much larger than that of the other three groups, so according to thermodynamic criteria, a large amount of Nb-Fe intermetallic compounds is expected to appear. This result is consistent with Slone et al.'s study[73], which found a significant amount of (Fe-Nb)-rich Laves phase in $AlCoCrFeNb_xNi$.

doi:10.6342/NTU202302391

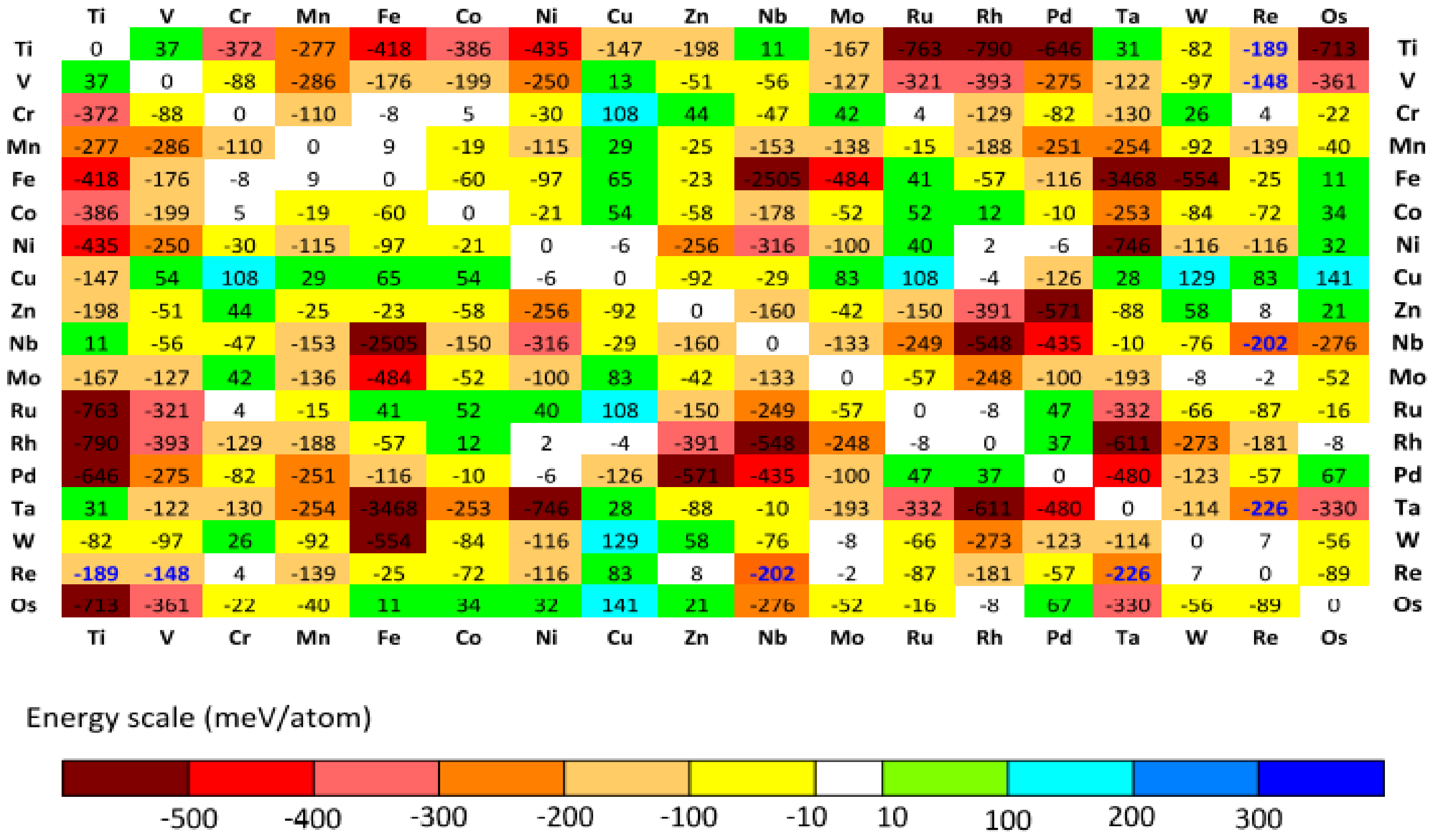

	Ti	V	Cr	Mn	Fe	Co	Ni	Cu	Zn	Nb	Mo	Ru	Rh	Pd	Ta	W	Re	Os	
Ti	0	37	-372	-277	-418	-386	-435	-147	-198	11	-167	-763	-790	-646	31	-82	-189	-713	Ti
V	37	0	-88	-286	-176	-199	-250	13	-51	-56	-127	-321	-393	-275	-122	-97	-148	-361	V
Cr	-372	-88	0	-110	-8	5	-30	108	44	-47	42	4	-129	-82	-130	26	4	-22	Cr
Mn	-277	-286	-110	0	9	-19	-115	29	-25	-153	-138	-15	-188	-251	-254	-92	-139	-40	Mn
Fe	-418	-176	-8	9	0	-60	-97	65	-23	-2505	-484	41	-57	-116	-3468	-554	-25	11	Fe
Co	-386	-199	5	-19	-60	0	-21	54	-58	-178	-52	52	12	-10	-253	-84	-72	34	Co
Ni	-435	-250	-30	-115	-97	-21	0	-6	-256	-316	-100	40	2	-6	-746	-116	-116	32	Ni
Cu	-147	54	108	29	65	54	-6	0	-92	-29	83	108	-4	-126	28	129	83	141	Cu
Zn	-198	-51	44	-25	-23	-58	-256	-92	0	-160	-42	-150	-391	-571	-88	58	8	21	Zn
Nb	11	-56	-47	-153	-2505	-150	-316	-29	-160	0	-133	-249	-548	-435	-10	-76	-202	-276	Nb
Mo	-167	-127	42	-136	-484	-52	-100	83	-42	-133	0	-57	-248	-100	-193	-8	-2	-52	Mo
Ru	-763	-321	4	-15	41	52	40	108	-150	-249	-57	0	-8	47	-332	-66	-87	-16	Ru
Rh	-790	-393	-129	-188	-57	12	2	-4	-391	-548	-248	-8	0	37	-611	-273	-181	-8	Rh
Pd	-646	-275	-82	-251	-116	-10	-6	-126	-571	-435	-100	47	37	0	-480	-123	-57	67	Pd
Ta	31	-122	-130	-254	-3468	-253	-746	28	-88	-10	-193	-332	-611	-480	0	-114	-226	-330	Ta
W	-82	-97	26	-92	-554	-84	-116	129	58	-76	-8	-66	-273	-123	-114	0	7	-56	W
Re	-189	-148	4	-139	-25	-72	-116	83	8	-202	-2	-87	-181	-57	-226	7	0	-89	Re
Os	-713	-361	-22	-40	11	34	32	141	21	-276	-52	-16	-8	67	-330	-56	-89	0	Os
	Ti	V	Cr	Mn	Fe	Co	Ni	Cu	Zn	Nb	Mo	Ru	Rh	Pd	Ta	W	Re	Os	

Figure 2-16

First principle simulated binary mixing enthalpy of single phase high-entropy alloys [82].

doi:10.6342/NTU202302391

2.4.2 Thermal stability of $L1_2$ precipitates

In order to apply superalloys in even higher temperature environments, previous researchers have developed nickel-based refractory superalloys by adding refractory elements such as Mo, Ta, W, and Re. The precipitates inside the superalloys do not easily grow, so they can maintain certain mechanical properties at high temperatures. Zhao et al. pointed out in their research that $L1_2$-$Ni_3(Al,Ti)$ in $(NiCoFeCr)_{94}Ti_2Al_4$ has good thermal stability due to the slow diffusion effect in high-entropy alloys [83], and the growth rate of $L1_2$-$Ni_3(Al,Ti)$ is much slower than that of nickel-based refractory superalloys (as shown in Figure 2-17), for example, the coarsening rate of $(NiCoFeCr)_{94}Ti_2Al_4$ at 800°C is one-tenth of that of Inconel 939. In addition, its peak aging treatment is at 750°C / 48 h (as shown in Figure 2-18, while the peak aging treatment for traditional nickel-based superalloys is less than 750°C / 10 h, such as Ni-Al, Ni-Ti, and Inconel 718, proving that $L1_2$-$Ni_3(Al,Ti)$ in $(NiCoFeCr)_{94}Ti_2Al_4$ is less likely to grow, which is consistent with the study on coarsening rate, and shows that this precipitate has considerable superior thermal stability in this alloy system.

doi:10.6342/NTU202302391

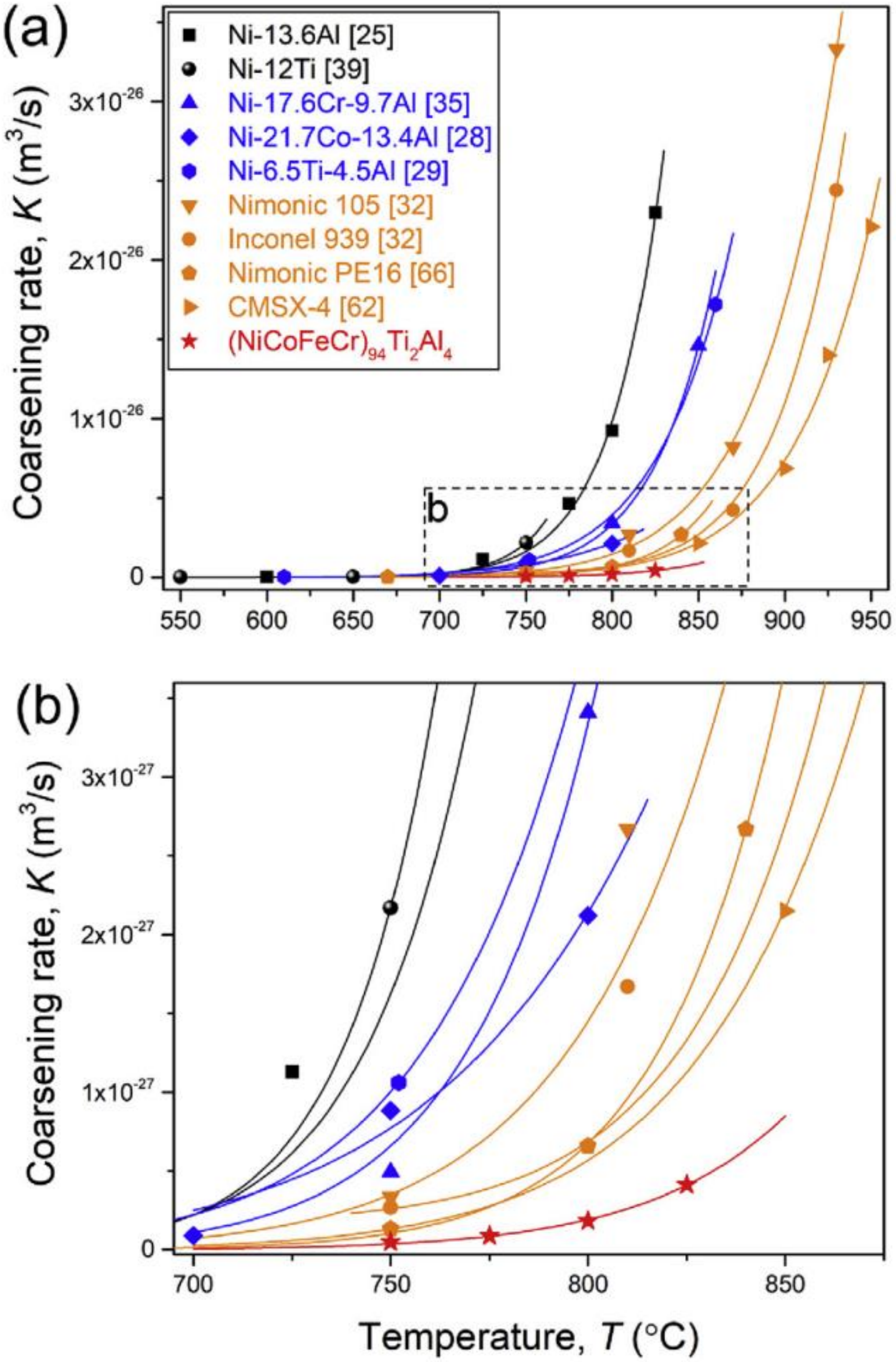

Figure 2-17 Corasing rate of Ni-based superalloys and (NiCoFeCr)$_{94}$Ti$_2$Al$_4$ under different temperature interval(a)550°C-950°C (b)700°C-900°C [83].

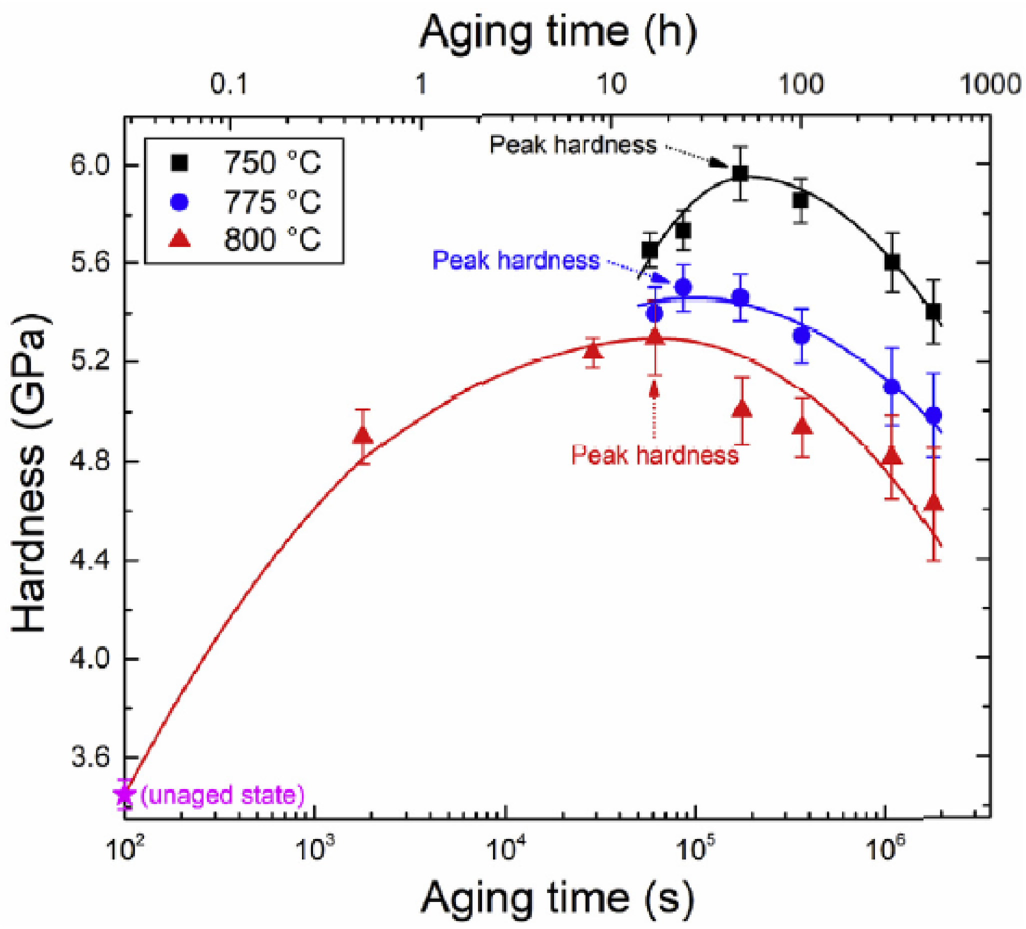

Figure 2-18 Hardness and aging time relationship in $(NiCoFeCr)_{94}Ti_2Al_4$ [83].

doi:10.6342/NTU202302391

2.5 Mechanical properties and microstructures of $L1_2$ precipitate hardening high-entropy alloys

2.5.1 Introduction to high-entropy alloy precipitate hardening

"Precipitation hardening" refers to the process of improving the strength of materials by obstructing dislocation movement through the generation of precipitates. Precipitates in high-entropy alloys can generally be divided into two categories:

1. Incoherent precipitates

Examples include B2-NiAl, η-phase, σ-phase, and μ-phase. Research has shown that incoherent precipitates can cause material embrittlement, which is not conducive to simultaneously improving strength and ductility. He et al. found that the degree of embrittlement caused by incoherent precipitates is related to the number of precipitates. Although $L2_1$-Heusler phase has been found in $(NiCoFeCr)_{94}Ti_2Al_4$, the number of precipitates is not significant enough to cause serious embrittlement effects.

2. $L1_2$ coherent precipitates:

$L1_2$ precipitates are most commonly used in nickel-based superalloys, but in recent years there has been much research on $L1_2$ precipitation in high-entropy alloys, such as $L1_2$-$Ni_3(Al,Ti)$ in $(FeCoCrNi)_{94}Ti_2Al_4$ [9] and $L1_2$-Ni_3Ti in $FeCoNiCrTi_{0.2}$. Table 2-9 shows the tensile test results of $L1_2$-precipitation strengthened high-entropy alloys. The high-entropy alloys listed in the table are all based on a single-phase FCC structure.

doi:10.6342/NTU202302391

Several studies with outstanding strength and ductility performance are enumerated as follows: $(FeCoCrNi)_{94}Ti_2Al_4$ has a tensile strength and elongation of 1.27 GPa and 17%, respectively [9], while $(CoCrNi)Al_3Ti_3$ has a tensile strength and elongation of 1.3 GPa and 45%, respectively [33].

Figure 2-19 compares the tensile strength and elongation of solid solution strengthened superalloys (SSH), precipitation hardened superalloys (PH), and $(CoCrNi)_{94}Al_3Ti_3$, which achieves strengthening through $L1_2$ precipitates. From the figure, we can see that this material does not sacrifice ductility to improve strength, but instead exhibits outstanding performance in both strength and elongation.

doi:10.6342/NTU202302391

Table 2-9 Tensile test results of $L1_2$-PH high-entropy alloys [42].

Composition (at.%)	Aging condition	Strengthening phase	YS, MPa	UTS, MPa	EL, %	Ref.
$Fe_{25}Co_{25}Ni_{25}Cr_{25}$	800 °C/1 h	Nil	~276	~705	~39	18
$Fe_{20}Co_{20}Ni_{20}Cr_{20}Mn_{20}$	800 °C/1 h	Nil	~265	~460	~47	18
$Al_7Co_{23.26}Cr_{23.26}Fe_{23.26}Ni_{23.26}$	550 ℃/150 h	$L1_2$	~285	~540	~50	67
	620 ℃/50 h	B2 + $L1_2$	~490	~825	~48	67
$(Fe_{25}Co_{25}Ni_{25}Cr_{25})_{94}Ti_2Al_4$	700 ℃/18 h	$L1_2$ + $L2_1$	~551	~981	~42	30
	800 ℃/18 h	$L1_2$ + $L2_1$	~645	~1094	~39	30
	900 ℃/18 h	$L2_1$	~301	~715	~46	30
	Cold roll +700 ℃/4 h	$L1_2$ + $L2_1$	~1005	~1273	~17	26
$Al_{3.7}Cr_{18.5}Fe_{18.5}Co_{18.5}Ni_{37}Cu_{3.7}$	700 °C/20 h	$L1_2$	~719	~1048	~30.4	39
	800 °C/1 h	$L1_2$	~460	~732	~31.7	39
$Al_{3.64}Co_{40.9}Cr_{27.27}Fe_{27.27}Ni_{40.9}Ti_{5.45}$	750 °C/50 h	$L1_2$	~640	~830	~10	62
$Al_{3.31}Co_{27}Cr_{18}Fe_{18}Ni_{27.27}Ti_{5.78}$	Hot forging	$L1_2$	~952	~1306	~20.5	33
$Al_8Co_{17}Cr_{17}Cu_8Fe_{17}Ni_{33}$	700 °C/5 h	$L1_2$	~365	~365	~0.1	68
	1150 °C/5 h	$L1_2$	~215	~489	~39	68
$Al_{10}Co_{25}Cr_8Fe_{15}Ni_{36}Ti_6$	900 °C/5 h	$L1_2$	~568	~786	~12	34
	900 °C/50 h	$L1_2$	~596	~1039	~20	34
$Ni_{47.9}Al_{10.2}Co_{16.9}Cr_{7.4}Fe_{8.9}Ti_{5.8}Mo_{0.9}Nb_{1.2}W_{0.4}C_{0.4}$	800 °C/20 h	$L1_2$	~847	Nil	Nil	38

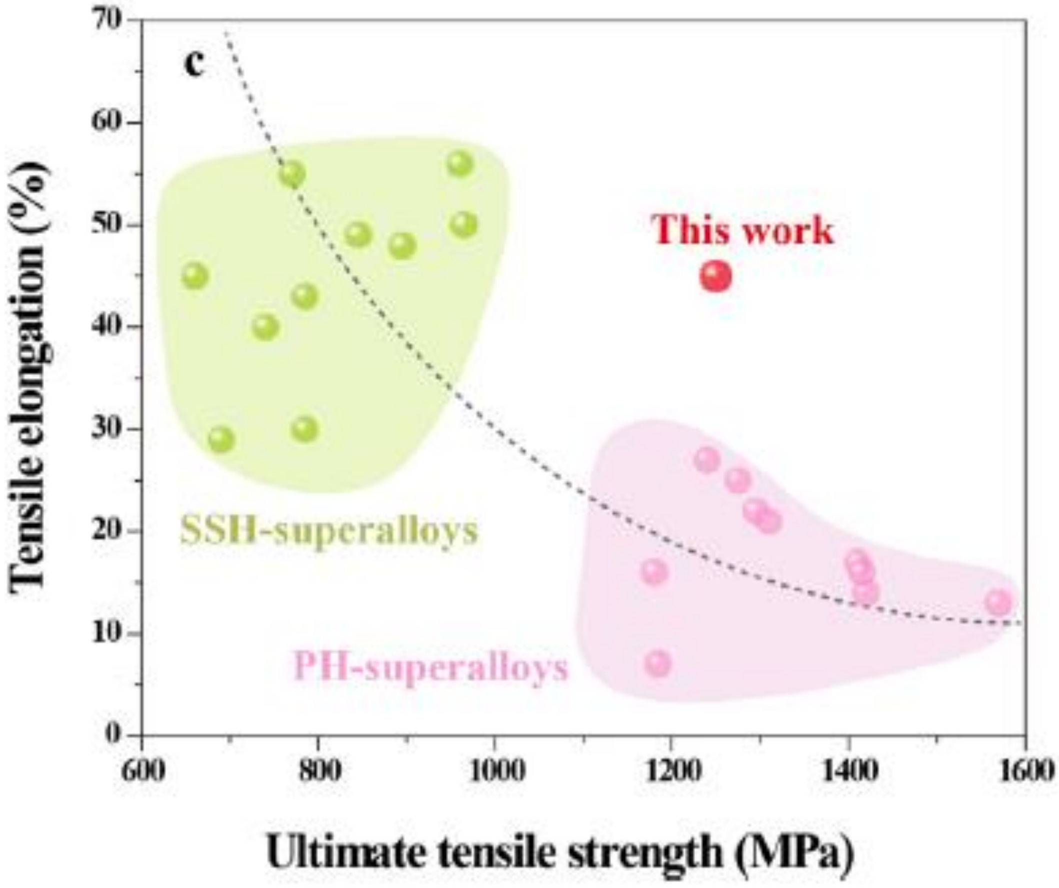

Figure 2-19 Comparison chart of tensile strength and elongation of solid solution strengthened superalloys (SSH-superalloys), precipitation hardened superalloys (PH-superalloys), and $(CoCrNi)_{94}Al_3Ti_3$ [33].

2.5.2 Dislocation pair and anti-phase boundary

If a material is strengthened through coherent precipitates, a large part of its deformation behavior depends on the "size of the precipitates". For example, in Co-rich superalloys [84, 85], the initial deformation behavior is mainly due to dislocation pairs on the anti-phase boundary (APB) with 1/2⟨110⟩, and as the precipitates grow, the deformation behavior transitions to being dominated by stacking-faults (SF) with partial dislocations expressed by 1/6⟨112⟩, and finally to Orowan bypassing. Additionally, Chaturvedi and Miao [86, 87] also found shear behavior of dislocation pairs and APBs in nickel-based superalloys.

Miao et al. had a more in-depth discussion regarding dislocation pairs [56]. Their study analyzed the microstructure of $(CrCoNi)_{93}Al_4Ti_2Nb$ cast state after cold rolling and 1050°C solid solution treatment followed by water quenching. The study did not specify the duration of the solid solution treatment. After the above process, the original γ phase and LRO (long-range order) $L1_2$ area can be found in the material. Figure 2-20 shows TEM analysis of LRO $L1_2$ in $(CrCoNi)_{93}Al_4Ti_2Nb$. By selecting the diffraction point of 011 using the SAD circle in (b), it can be observed from the dark field image in (a) that the distribution of precipitates is very chaotic, and the size of the precipitates is generally small, all below 5nm.

In $(CrCoNi)_{93}Al_4Ti_2Nb$, many dislocation pairs can be observed slipping on the

doi:10.6342/NTU202302391

slip plane {111}. Through observation of the [100] zone, a very clear dislocation pair can be seen in Figure 2-21 and Figure 2-22 has a clearer image, and the schematic diagram of its formation mechanism can be referred to in Figure 2-23 and Figure 2-24. Assuming that the $L1_2$ area is dominated by Ni_3Ti, when a single dislocation pair needs to penetrate the $L1_2$ area under shear force, the bonds in $L1_2$ will change from Ni-Ti bonds to Ni-Ni and Ti-Ti bonds, forming an anti-phase boundary (APB), with a displacement of a Bragg vector $(\vec{b})$. For the material, this is a relatively unstable state, so a large amount of energy is needed for a single dislocation pair to penetrate the $L1_2$ area, which achieves the effect of strengthening the material. In addition, the APB of the $L1_2$ area under shear of a single dislocation pair is an unstable state, so usually another dislocation pair is involved in the process of penetration, which is called a dislocation pair, and after two shear processes, the $L1_2$ area still maintains Ni-Ti bonds, which is a more stable state for the material.

Mutipole is another special microstructure in $(CrCoNi)_{93}Al_4Ti_2Nb$. Figure 2-25 shows the schematic diagram of the formation mechanism of mutipole. Here, the array of dislocations on the slip plane is called an array. Assuming that two arrays collide with each other and the distance between them (Y) is short enough to interact, the Burgers vector $(\vec{b})$ of the front dislocations in the two arrays cancels out to 0. From the perspective of strain energy, the mutual cancellation of the two dislocations can reduce the strain energy in the lattice. Therefore, this phenomenon will occur and the front ends of the two arrays will constrain each other to form a dipole [88, 89]. The dislocations behind the two arrays can break the first dipole and form two dipole pairs, which not only reduce more strain energy but also enable the material to continue to accept deformation from shear bands. As the interaction between the two arrays becomes stronger, mutipole can be formed, and the two arrays can not only constrain each other but also hinder the slip of dislocations in another direction.

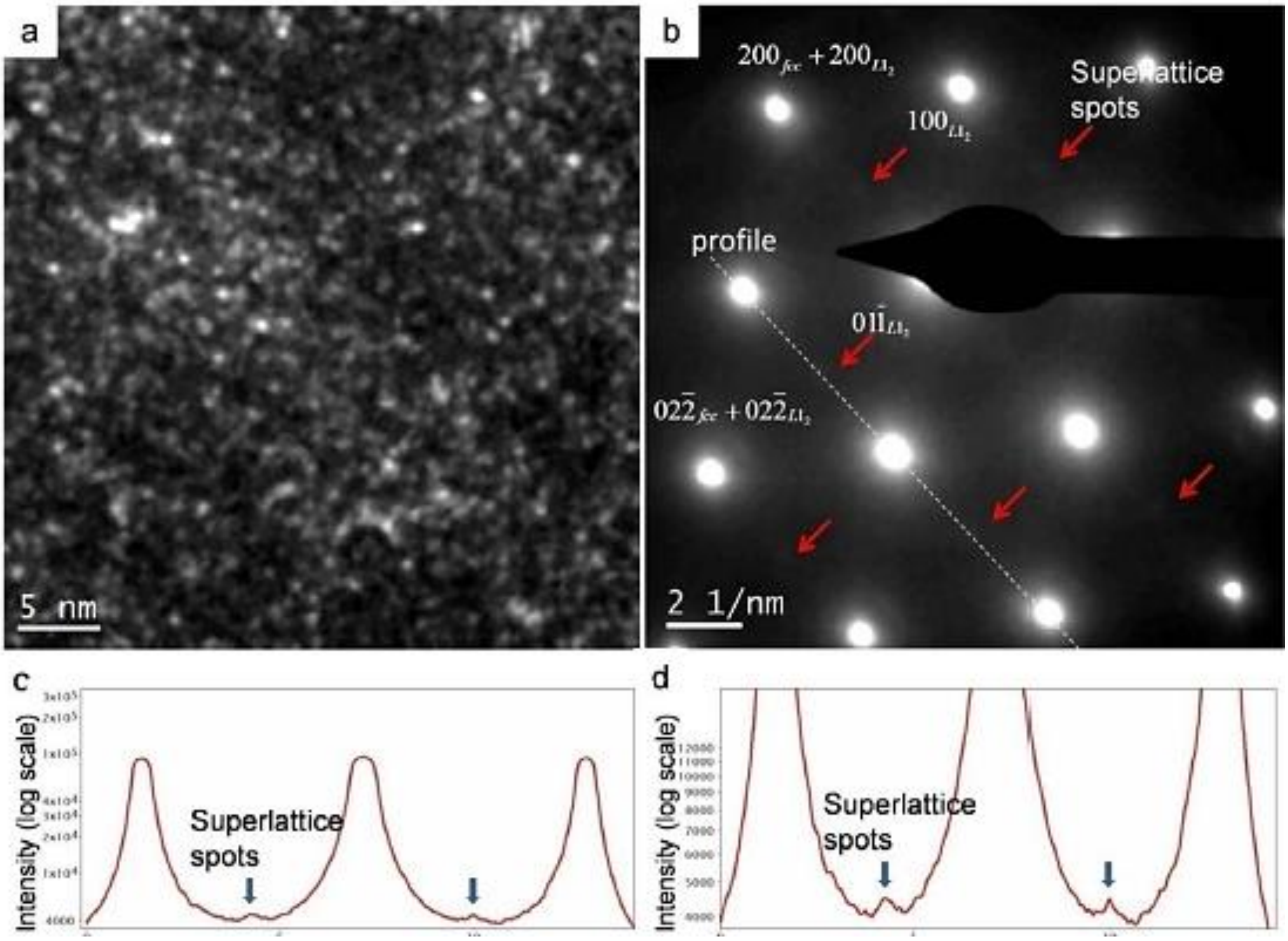

Figure 2-20 TEM analysis of LRO L1$_2$ in (CrCoNi)$_{93}$Al$_4$Ti$_2$Nb (a)dark field inage (b) [011]zone diffraction pattern (c) intensity distribution of figure b (d) intensity distribution of figure b in a larger scale [56].

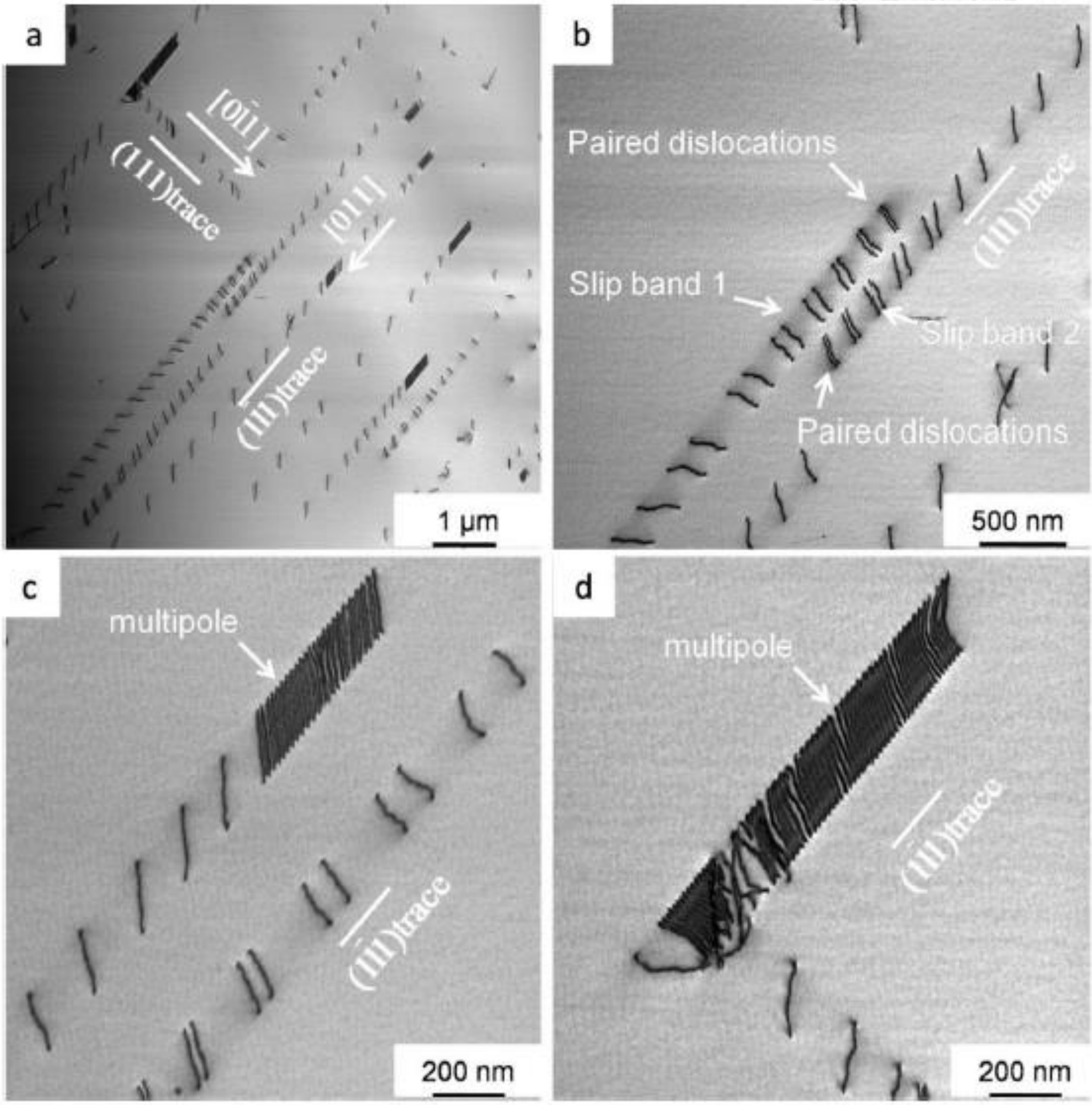

Figure 2-21 STEM images of $(CrCoNi)_{93}Al_4Ti_2Nb$ under [100] zone: (a) low magnification, (b) dislocation pairs on the slip plane, (c) multipole on the slip plane, and (d) interaction between multipole on $(1\bar{1}1)$ and dislocations on (111) slip plane [56].

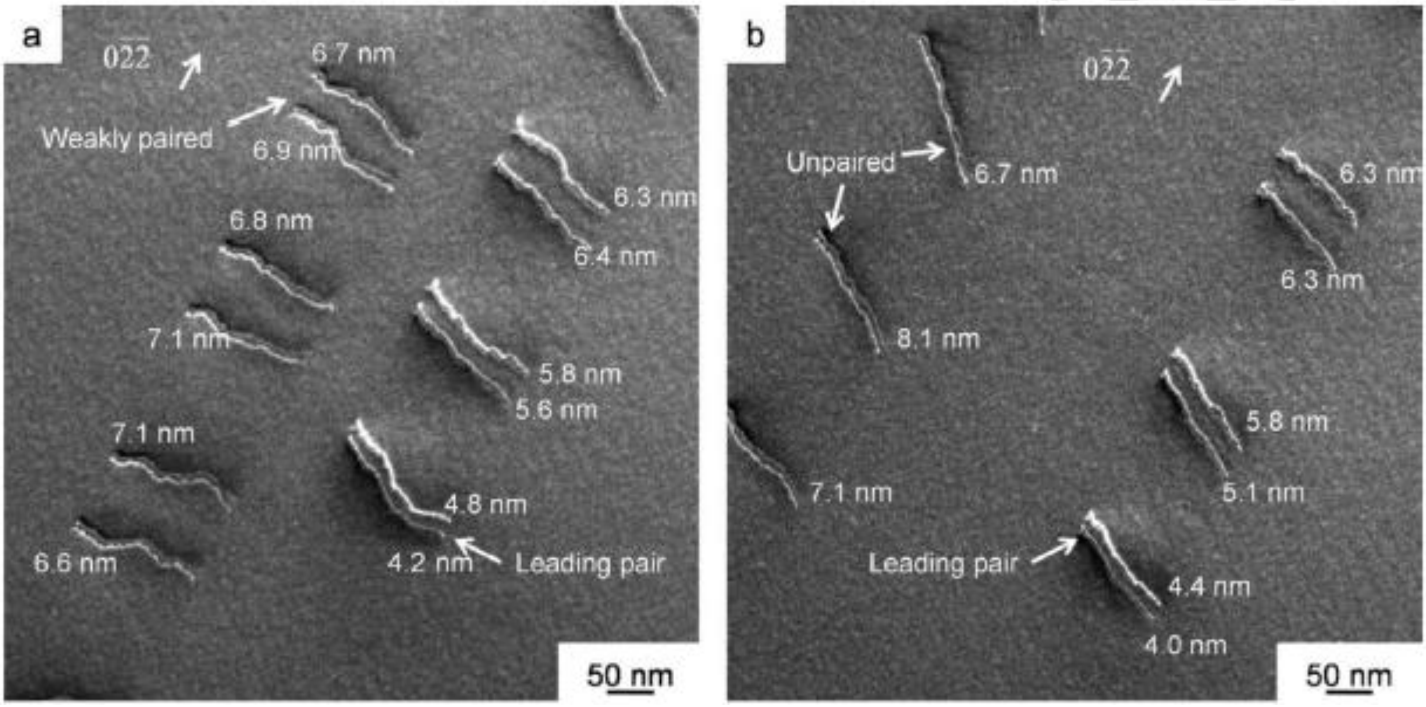

Figure 2-22 TEM analysis of LRO $L1_2$ in $(CrCoNi)_{93}Al_4Ti_2Nb$: (a) dark-field TEM image, (b) diffraction pattern under [011] zone, (c) intensity distribution of the virtual line in image (b) marked with dashed line, and (d) enlarged image of (c) showing the intensity distribution [56].

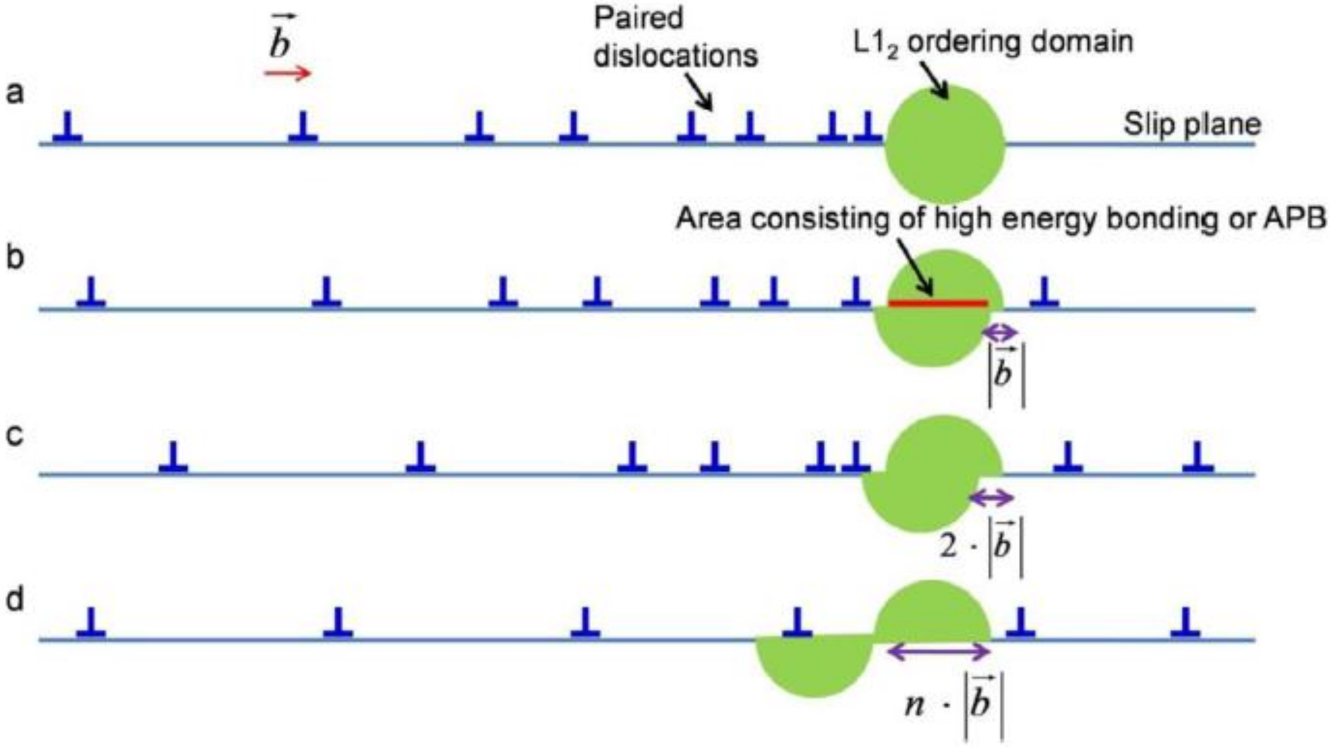

Figure 2-23 Schematic diagram of dislocation pairs penetrating the γ' phase via shear force [56].

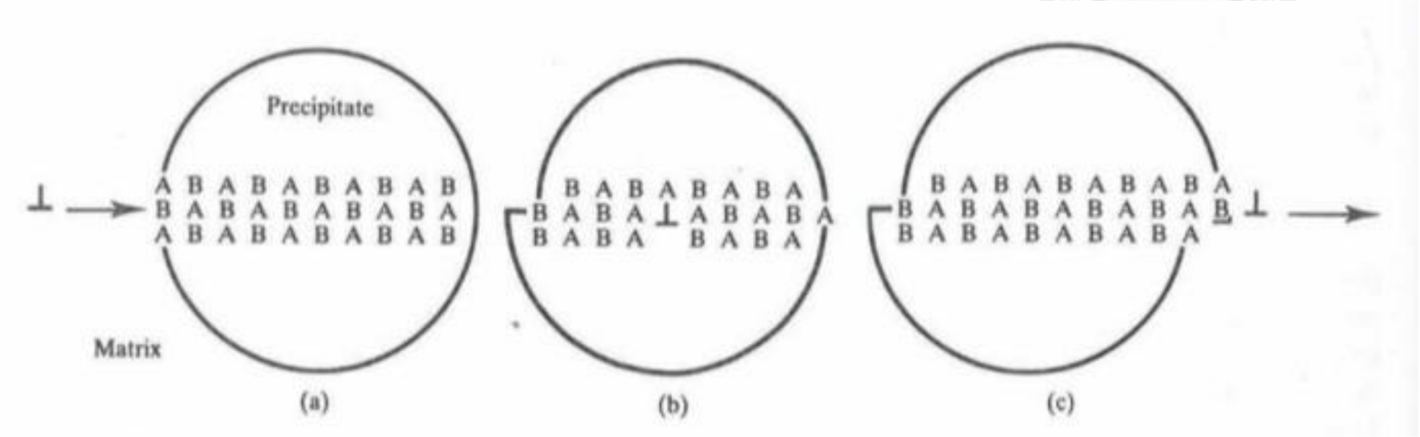

Figure 2-24 Schematic diagram of dislocation shearing the γ' phase to generate a reverse boundary.

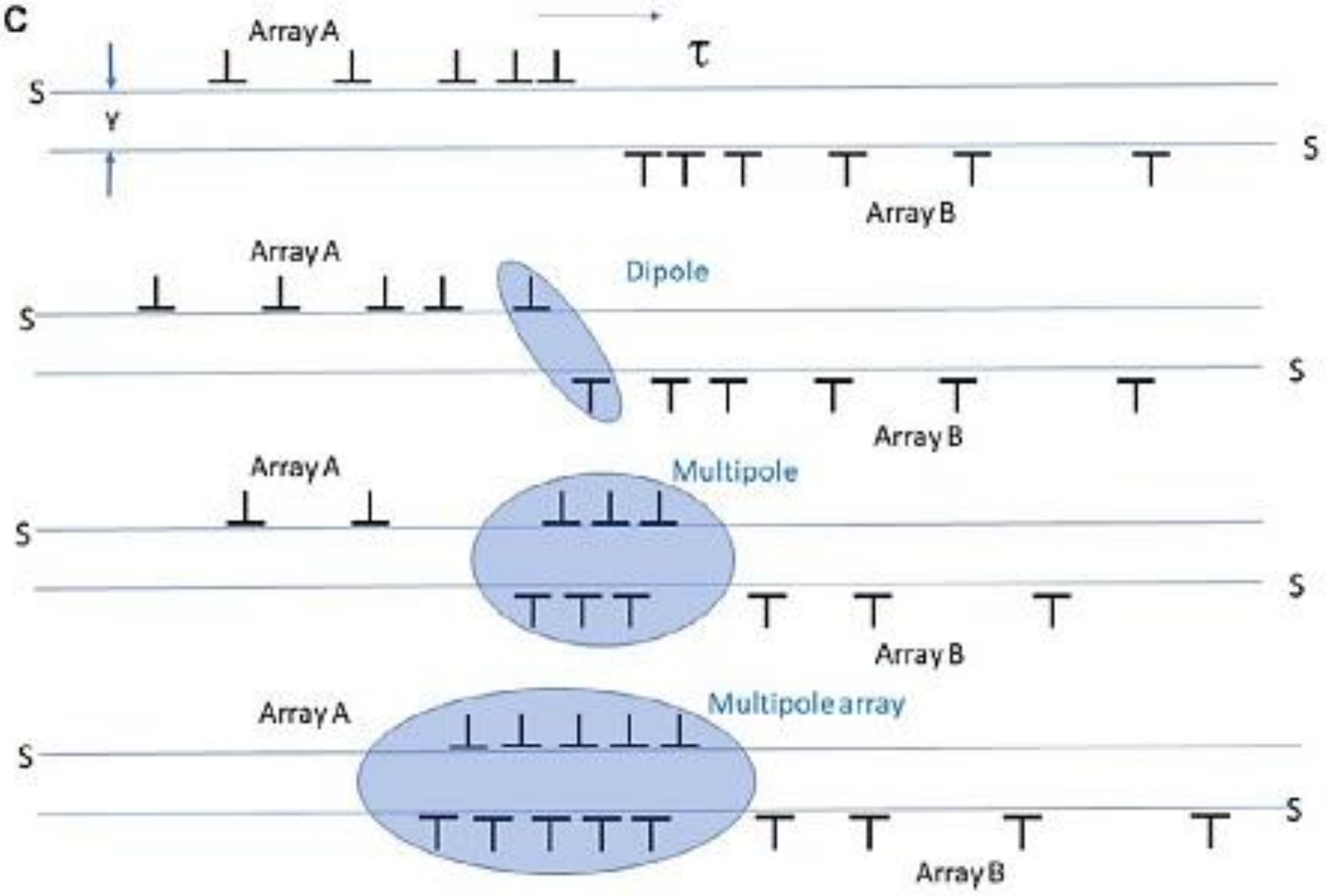

Figure 2-25 schematic diagram of mutipole formation mechanism [56].

2.5.3 Impacts of $L1_2$ phase on the deformation mechanism

Although the phenomenon of dislocation movement along the slip planes can be observed in both CrCoNi and $(CrCoNi)_{93}Al_4Ti_2Nb$, there are many differences in the deformation mechanism between the two. In CrCoNi, a large number of deformation twin boundaries or local FCC to HCP transformation microstructures can be found [90], but neither of these two phenomena were observed in $(CrCoNi)_{93}Al_4Ti_2Nb$. This phenomenon can be discussed by calculating the critical twin stress (τ_{crit}) [91].

$\mathrm{b_p}$ is the Burgers vector of partial dislocations, and γ is the stacking-fault energy (SFE). For CrCoNi, $\gamma = 16\frac{\mathrm{mJ}}{\mathrm{m^2}}$, $\tau_{\mathrm{crit,theo}} = 256$ Mpa, which is in agreement with the experimental measurement result of $\tau_{\mathrm{crit,expi}} = 260 \pm 30$ Mpa. Because the LRO $L1_2$ region exists in $(CrCoNi)_{93}Al_4Ti_2Nb$, the calculation method of τ_{crit} is modified [56], where γ_{m} is the SFE of the FCC matrix, $\mathrm{f_m}$ is the area ratio occupied by the FCC matrix in the system, γ_{ord} is the complex stacking fault energy from the $L1_2$ phase, $\mathrm{f_{ord}}$ is the area ratio occupied by the $L1_2$ phase in the system. Using $(CrCoNi)_{93}Al_4Ti_2Nb$ for the modified calculation, $\gamma = 25\frac{\mathrm{mJ}}{\mathrm{m^2}}$, $\tau_{\mathrm{crit,theo}} = 400$ Mpa, which is significantly higher than that of CrCoNi, indicating that the critical shear stress for generating deformation twins is higher in $(CrCoNi)_{93}Al_4Ti_2Nb$. Using the Taylor factor measured by EBSD, a value of 3.1 is obtained, and estimating the critical stress for the formation of deformation twins using the Taylor factor gives a value of 1240

MPa, which is lower than the tensile strength of $(CrCoNi)_{93}Al_4Ti_2Nb$, which is 1346 MPa. This estimation suggests that deformation twins are not easily formed in $(CrCoNi)_{93}Al_4Ti_2Nb$.

2.5.4 Microstructure of precipitation strengthened high entropy alloy of typical $L1_2$ phase

Figure 2-26 shows the microstructure of $(CoCrNi)_{94}Al_3Ti_3$ after 2% deformation, where typical planar slip can be observed. The material undergoes slip along two directions with a slip plane of {111}. The included angle between the two slip planes in the image is 71°, and the average spacing of criss-crossing planes is 200nm. In addition, both short-range order (SRO) and long-range order (LRO) in the substrate and precipitates increase the chance of planar slip in the material [92]. (b) The TEM image in the CP (continuous precipitate) region shows smaller and more evenly distributed precipitates, with stacking fault fringes and pair-wise dislocations indicating that the $L1_2$ precipitates undergo stacking fault shearing or anti-phase boundary (APB) shearing. (c) The TEM image in the DP (discontinuous precipitate) region shows more varied sizes and distribution of precipitates, but all precipitates are found to undergo stacking fault shearing regardless of their size. Furthermore, no Orowan loops were found in $(CoCrNi)_{94}Al_3Ti_3$..

Figure 2-27 shows the microstructure of $(CoCrNi)_{94}Al_3Ti_3$ after 30% deformation,

doi:10.6342/NTU202302391

where a large amount of stacking faults can be observed in both CP and DP regions. Stacking faults serve as a source of plastic deformation strengthening. It is noteworthy that in the CP region, stacking faults can be observed in two directions belonging to two {111} planes, while in the DP region, stacking faults are only observed in one direction, which the authors attribute to the shape of the precipitates in the DP region. Furthermore, no deformation twins were found in this image, as no twin diffraction spots were observed in the diffraction pattern. When imaging the positions belonging to twin diffraction spots using the aperture, no twin structure was observed.

Figure 2-28 shows the microstructure and EDS elemental analysis of $(CoCrNi)_{94}Al_3Ti_3$ after 30% deformation. In (a), a significant banded structure precipitate can be observed, which was identified by EDS and diffraction patterns as $L1_2$-$Ni_3(Al,Ti)$. A large number of stacking faults and very few nanotwins can be found in the banded structure. It is very difficult to observe nanotwins in $(CoCrNi)_{94}Al_3Ti_3$, which only accounts for about 2.5% of defects in the material, while stacking faults dominate. These deformed nanotwins are believed to nucleate from stacking faults [93].

doi:10.6342/NTU202302391

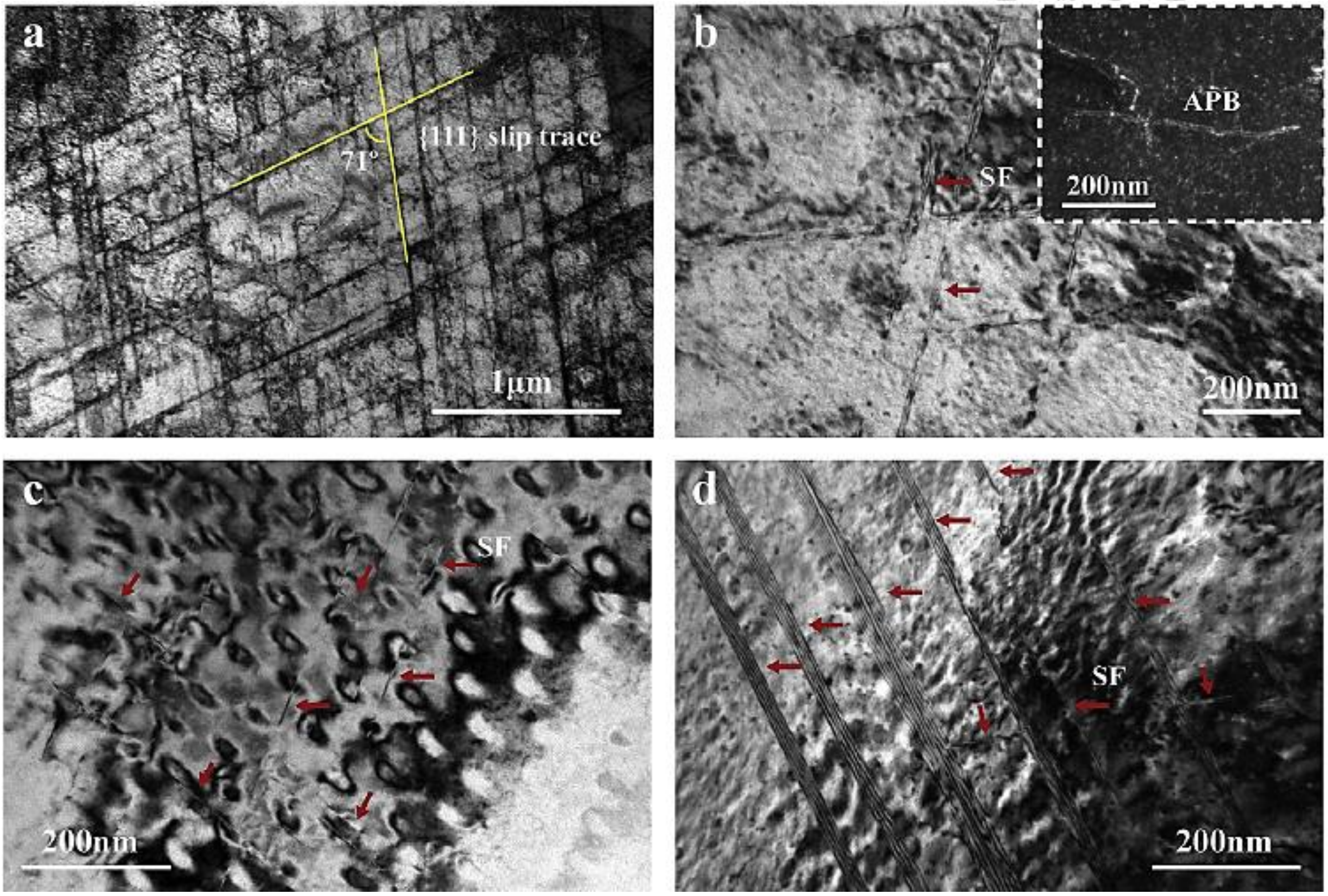

Figure 2-26 TEM images of $(CoCrNi)_{94}Al_3Ti_3$ after approximately 2% deformation. (a) Planar slip with dislocations in CP region. (b) Precipitates subjected to stacking faults and anti-phase boundary shearing. (c,d) Severe deformation of precipitates due to stacking faults in CP region [33].

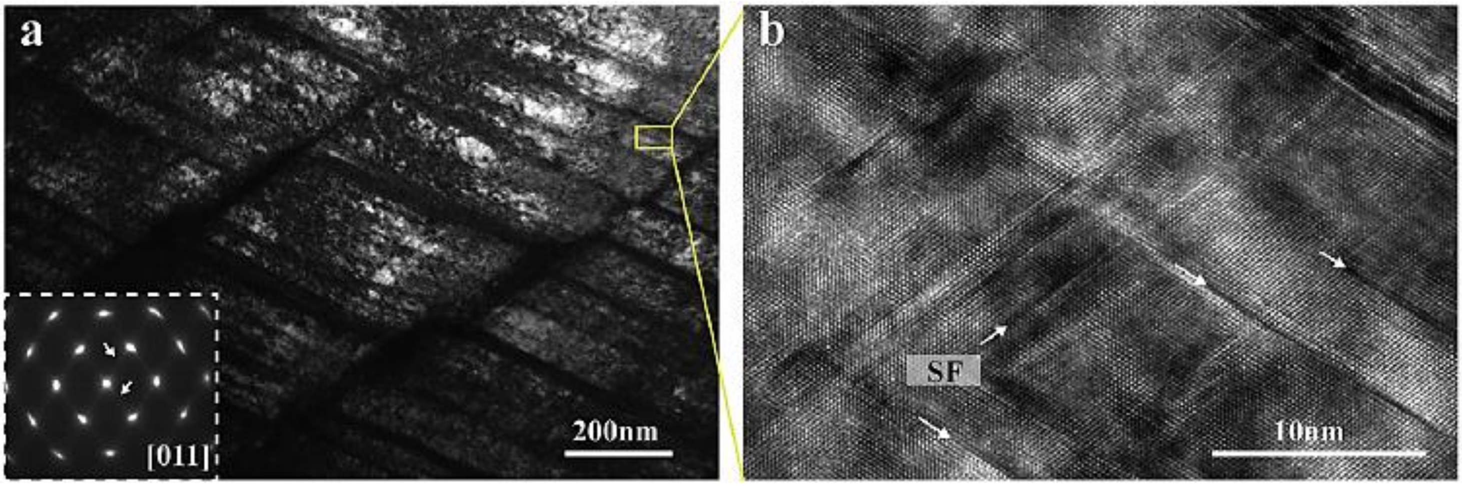

Figure 2-27 TEM and HRTEM images of $(CoCrNi)_{94}Al_3Ti_3$ after approximately 30% true strain in CP region (a,b) showing high density of dislocations [33].

doi:10.6342/NTU202302391

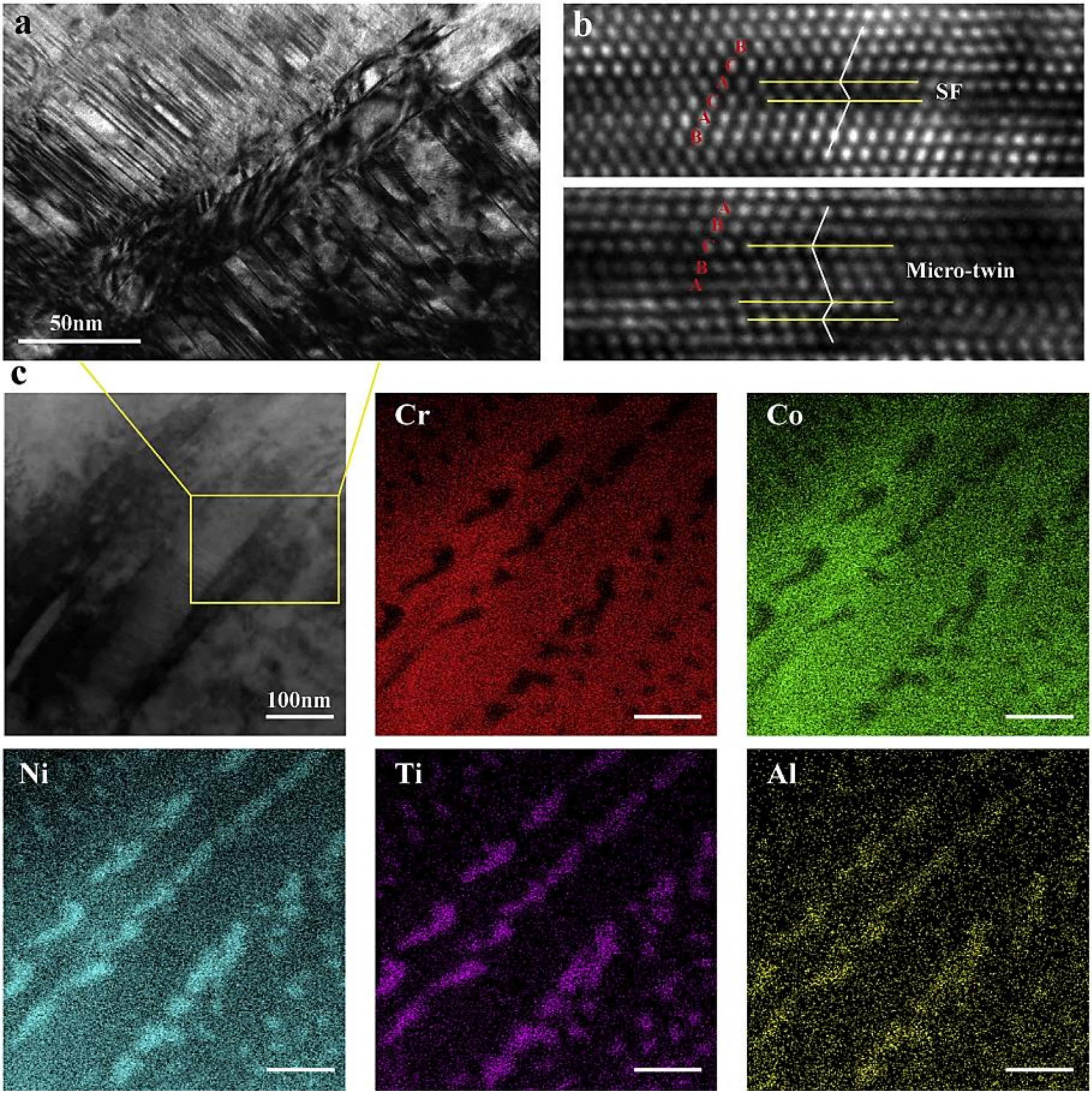

Figure 2-28 Images of $(CoCrNi)_{94}Al_3Ti_3$ after approximately 30% true strain. (a) Striped structure with high density of dislocations. (b) HRTEM image of dislocations and nanotwins. (c) EDS compositional analysis using STEM [33].

2.5.5 Quantification of various strengthening mechanisms in high-entropy alloys

He et al. conducted a study on the quantification of various strengthening mechanisms in $(FeCoNiCr)_{94}Ti_2Al_4$ [9]. Two processing routes were performed, referred to as P1 and P2. P1 involved homogenization at 1200°C for 4 hours, followed by 30% cold rolling, recrystallization at 1000°C for 2 hours, aging at 800°C for 18 hours, and water quenching. P2 involved homogenization at 1200°C for 4 hours, followed by 70% cold rolling, aging at 750°C for 4 hours, and water quenching. In addition, the FeCoNiCr alloy homogenized at 1200°C for 4 hours was referred to as Alloy A, while $(FeCoNiCr)_{94}Ti_2Al_4$ homogenized at 1200°C for 4 hours was referred to as Alloy B. Figure 2-29 shows the tensile test results of $(FeCoNiCr)_{94}Ti_2Al_4$ subjected to different heat treatment processes.

The strengthening mechanisms of polycrystalline materials can be roughly divided into four types: solid-solution hardening, grain-boundary hardening, dislocation hardening, and precipitation hardening. These four types of strengthening mechanisms operate independently and do not interfere with each other. Therefore, the yield strength is the sum of the contributions of the four strengthening mechanisms. Kamikawa et al. expressed this relationship in Eq. 2-7 [94].

doi:10.6342/NTU202302391

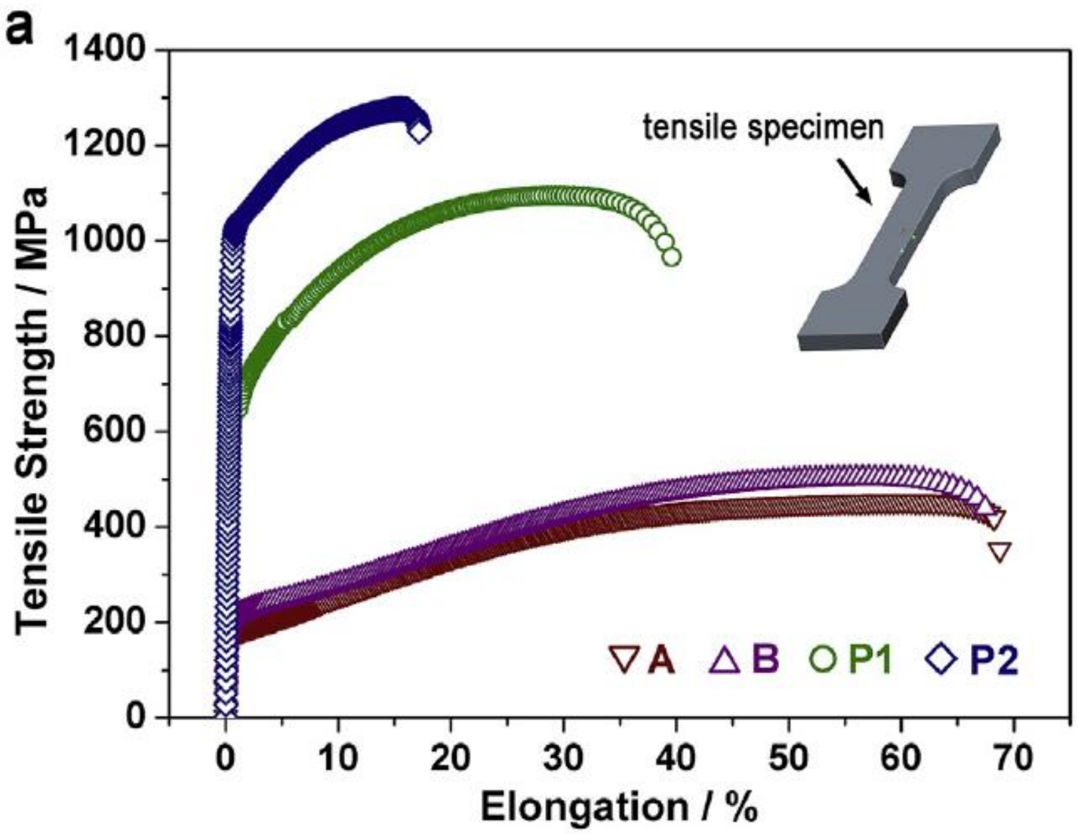

Figure 2-29 $(FeCoNiCr)_{94}Ti_2Al_4$ tensile test results [9].

$$\sigma_{0.2} = \sigma_A + \Delta\sigma_S + \Delta\sigma_G + \Delta\sigma_D + \Delta\sigma_P \qquad \text{Eq. 2-7}$$

σ_A is the yield strength of Alloy A (FeCoNiCr), corresponding to lattice friction, which is an inherent property of the material. For Alloy A (FeCoNiCr), $\sigma_A = 165Mpa$

$\Delta\sigma_S, \Delta\sigma_G, \Delta\sigma_D\ and\ \Delta\sigma_P$ correspond to the contributions of solid-solution, grain-boundary, dislocation, and precipitation hardening, respectively.

1. Solid solution hardening

To discuss solid-solution hardening, it is necessary to first define solvent and solute. Early studies mainly investigated the addition of dilute solute atoms to solvents

doi:10.6342/NTU202302391

and discussed them in simple binary alloy systems [95, 96]. However, in high-entropy alloys, the alloy system is more complex, making it difficult to use a single element as a solvent. Toda-Carabolla et al. made a series of modifications and discussions on the binary model and high-entropy alloy model [97]. To apply the formula for solid-solution hardening to high-entropy alloys, the elements within the material should be evenly distributed, and there should be no specific arrangement of organization such as short-range order. Currently, most studies use a single-phase FCC base as the solvent. For example, in $(FeCoNiCr)_{94}Ti_2Al_4$, FeCoNiCr is used as the base. Al and Ti are added as elements to discuss solid-solution hardening. Once the solvent and solute are defined, the elastic dislocation-solute interaction model (Eq. 2-8) can be applied [96, 98] to calculate the contribution of solid- hardening to the overall mechanical properties.

$$\Delta\sigma_S = M\frac{G \cdot \varepsilon_S^{3/2} \cdot c^{1/2}}{700} \qquad \text{Eq. 2-8}$$

G : shear modulus for material

c : total molar ratio of solute in alloy

M : Taylor factor

ε_S : interaction parameter

In $(FeCoNiCr)_{94}Ti_2Al_4$，G=78.5GPa, M=3.06, and the parameter c can be estimated semi-quantitatively by EDS. The interaction parameter (ε_S) can be further divided into the effects of elastic (ε_G) and atomic size mismatch(ε_a). See Eq. 2-9, Eq. 2-10 and Eq. 2-11.

doi:10.6342/NTU202302391

$$\varepsilon_S = \frac{\varepsilon_G}{1 + 0.5\varepsilon_G} - 3 \cdot \varepsilon_a \tag{Eq. 2-9}$$

$$\varepsilon_G = \frac{1}{G}\frac{\partial G}{\partial c} \tag{Eq. 2-10}$$

$$\varepsilon_a = \frac{1}{a}\frac{\partial a}{\partial c} \tag{Eq. 2-11}$$

ε_G : elastic effect

ε_a : atomic size mismatches effect

a : lattice constant

ε_a can be measured by XRD (the lattice constants of alloy A, P1, and P2 are 0.3578nm, 0.3594nm, and 0.3590nm, respectively). The contribution of ε_G is usually very small, so ε_G can be approximated by the value of ε_a. Thus, all the parameters needed to calculate solid solution strengthening are known. Comparing the values contributed by solid solution strengthening in FeCrCoNi (Alloy A) and $(FeCoNiCr)_{94}Ti_2Al_4$ (P1, P2), $\Delta\sigma_{S1} = 25.4MPa$ and $\Delta\sigma_{S2} = 14.4MPa$ can be obtained. Compared with the yield strength and tensile strength of the material, the strength contributed by solid solution strengthening is only a small part. Therefore, in this study, solid solution strengthening is not the main strengthening mechanism.

2. Grain boundary hardening

Small grains can produce more grain boundaries. Grain boundaries can effectively hinder dislocation slip. The strengthening effect of grain boundaries can be represented by the Hall-Petch equation (Eq. 2-12) [99].

$$\sigma_y = \sigma_0 + \frac{k_y}{d^{1/2}} \qquad \text{Eq. 2-12}$$

σ_y : yield stress
σ_0 : lattice friction stress
k_y : strengthening coefficient
d : average grain diameter

According to the above equation, it can be deduced that the contribution of grain size changes to the yield strength after heat treatment of the material is represented by $\Delta\sigma_G$. (see Eq. 2-13)。

$$\Delta\sigma_G = k_y(d_p^{-1/2} - d_A^{-1/2}) \qquad \text{Eq. 2-13}$$

d_p : grain size of treated material
d_A : grain size of original material

In this study, the value of k_y for FeCoNiCrMn was estimated to be $k_y = 226MPa \cdot \mu m^{-1/2}$. In addition, the grain size was measured using SEM and TEM. Not many twin boundaries were found in $(FeCoNiCr)_{94}Ti_2Al_4$, so twin boundaries were also included in the estimation of grain boundaries during statistics. The results are as follows: $d_A = 289.7\,\mu m$, $d_{P1} = 15.7\,\mu m$, $d_{P2} = 2.8\,\mu m$. By substituting the grain size into the above equation, the influence of grain size on the yield strength can be

doi:10.6342/NTU202302391

obtained, $\Delta\sigma_{G1} = 43.7MPa$, $\Delta\sigma_{G2} = 122.6MPa$.

Compared with the yield strength of the material, the estimated value of grain boundary strengthening is relatively small. Therefore, grain boundary strengthening is not the main strengthening mechanism in $(FeCoNiCr)_{94}Ti_2Al_4$.

3. Dislocation strengthening

Plastic deformation mainly enhances strength by hindering dislocation slip. According to the well-known Bailey-Hirsch formula [96] (Eq. 2-14), the effect of dislocation strengthening is mainly contributed by the dislocation density (ρ). In FCC, $\alpha = 0.2$ 、 $b = \sqrt{2}/2 \times a_{Ti2Al4}$.

$$\Delta\sigma_D = M\,\alpha\,Gb\,\rho^{\frac{1}{2}} \qquad \text{Eq. 2-14}$$

α : lattice structure factor
G : shear modulus
b : burgers vector
ρ : dislocation density

Regarding the dislocation density, He et al. measured it using the Williamson-Hall method, which is commonly used to determine the micro strain and crystallite size [100, 101]. The XRD peak broadening, denoted as β, comes from the broadening of crystallite size (β_G) and strain (β_S) [102, 103]. A Cauchy-type function is used to express it in equations (Eq. 2-15, Eq. 2-16, Eq. 2-17 and Eq. 2-18).

$$\beta = \beta_G + \beta_S \qquad \text{Eq. 2-15}$$

$$\beta_G = K\,\lambda\,/(D \cdot \cos\theta) \qquad \text{Eq. 2-16}$$

doi:10.6342/NTU202302391

$$\beta_S = 4\,\varepsilon \cdot \tan\theta \tag{Eq. 2-17}$$

$$\beta\cos\theta = \frac{K\,\lambda}{\mathrm{D}} + (4\sin\theta)\cdot\,\varepsilon \tag{Eq. 2-18}$$

K : constant (~0.9)
λ : wavelength of Cu K_α radiation (0.15405 nm)
D : crystallite size
ε : micro strain
θ : Bragg angle of certain peak

By plotting the $\beta\cos\theta - 4\sin\theta$ relationship graph and using the slope of linear approximation, ε can be obtained. ε represents the micro-strain in the crystal. Figure 2-30 shows the $\beta\cos\theta - 4\sin\theta$ relationship graph, with the slope of P2 alloy being 0.102 and that of P1 alloy considered to be 0, since the slope is too low and can be viewed as an error.

From a physical perspective, the behavior of $\varepsilon = 0$ in P1 alloy can be discussed. P1 alloy is annealed to near complete annealing, and after annealing at 1273K/2h (greater than $0.75T_m$), the dislocation content in the material is negligible and can be calculated as if there are no dislocations.

The calculation of dislocation density can be expressed by the micro-strain Eq. 2-19 [101, 104]. By substituting the micro-strain ε of P1 and P2 alloys respectively, the dislocation density of P1 and P2 alloys can be obtained as $\rho_1 = 0, \rho_2 = 5.02 \times 10^{14}$. Substituting the dislocation density back into the dislocation strengthening formula, the effect of dislocation strengthening can be obtained as $\Delta\sigma_{D1} = 0$, $\Delta\sigma_{D2} = 274.5MPa$. The calculation results show that dislocation strengthening is one of the main strengthening mechanisms in P2 alloy. In addition, since P2 alloy is annealed at 923K, the results also show that annealing at 923K is not enough to completely anneal the 70% cold-rolled $(FeCoNiCr)_{94}Ti_2Al_4$, and a large number of dislocations still exist.

$$\rho = 2\sqrt{3} \cdot \varepsilon / (Db) \qquad \text{Eq. 2-19}$$

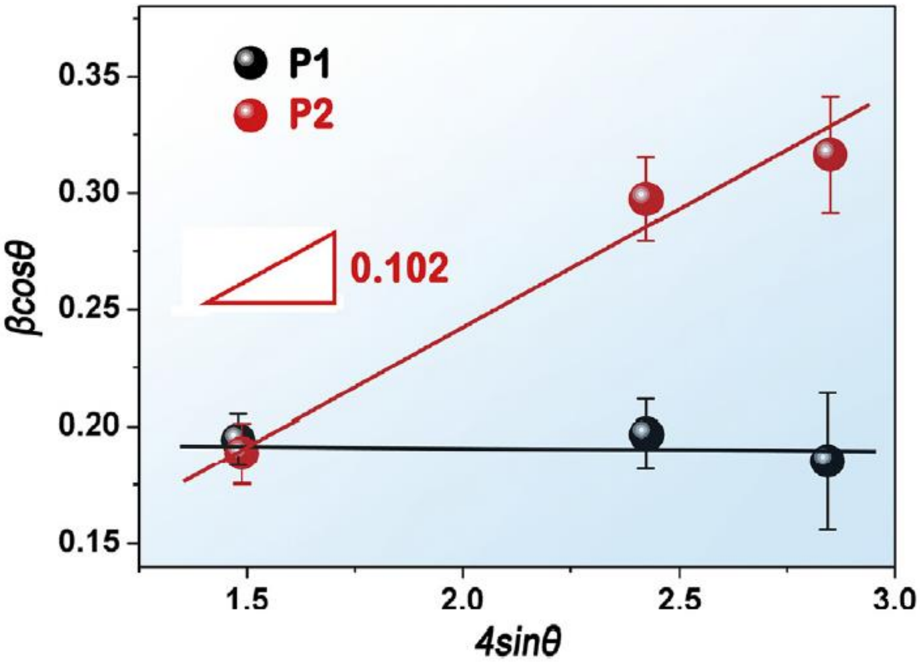

Figure 2-30 βcosθ − 4sinθ relationship in $(FeCoNiCr)_{94}Ti_2Al_4$ [9].

4. Precipitate hardening

Regarding precipitation strengthening, it can be mainly classified into two categories based on the characteristics of the precipitates. If the precipitate size is large and incoherent, the strengthening mechanism tends to be dominated by the Orowan-type dislocation bypass mechanism. If the precipitate size is small and coherent, the strengthening mechanism tends to be dominated by the particle shearing mechanism.

doi:10.6342/NTU202302391

Figure 2-31 shows the TEM bright-field images of $(FeCoNiCr)_{94}Ti_2Al_4$ P1 and P2 alloys. Two types of $Ni_3(Al,Ti)$ precipitates can be observed in the P1 alloy: Region I contains small, granular precipitates, while Region II contains plate-like precipitates (approximated as spheres by the authors). The two different types of precipitate morphologies contribute different strengths, so the precipitation strengthening expression for the material can be expressed as Eq. 2-20. The volume fraction and size statistics of the precipitates are shown in Table 2-10. In the P1 alloy, the spherical radius of Region II is approximated by the width of the plate-like precipitates, while Ni_2AlTi is ignored in the P2 alloy due to its low content.

$$\sigma_{P1} = \sigma_I \cdot C_I + \sigma_{P1} \cdot C_{II} \qquad \text{Eq. 2-20}$$

σ_{P1} : overall strength
σ_I : intrinsic strength of Region I
σ_{II} : intrinsic strength of Region II
C_I : volume fraction of Region I
C_{II} : volume fraction of Region II

Table 2-10 P1 and P2 precipitate volume fraction [9].

Alloys	Region or particles	Region fraction C (%)	Precipitates fraction f (%)	Precipitates radius r(nm)	Particle spacing Lp(nm)
P1	I	68.1	23.3	12.6	17.2
	II	31.9	16.2	46.3	90.9
P2	γ’	-	26.8	9.7	11.3
	Ni_2AlTi	-	2.77	25.9	182.9

doi:10.6342/NTU202302391

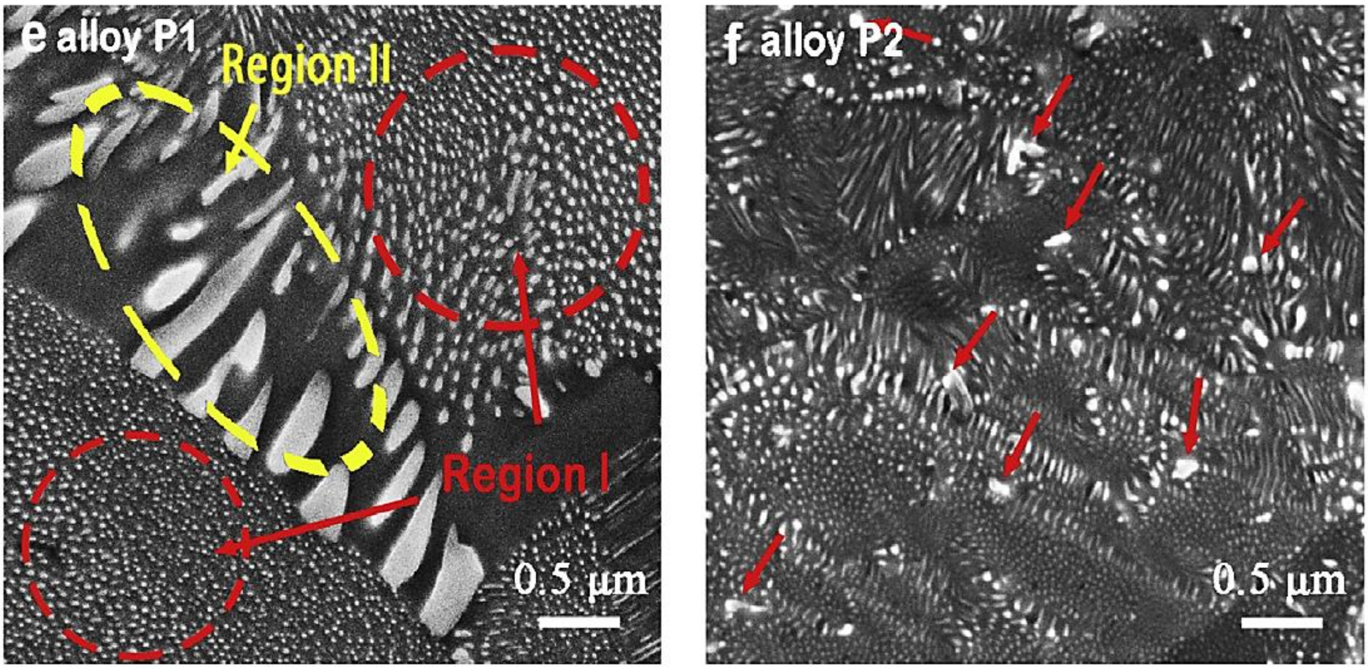

Figure 2-31 P1 and P2 TEM bright image $(FeCoNiCr)_{94}Ti_2Al_4$ [9].

When calculating the shearing of precipitates by dislocations, three factors mainly affect it: particle-matrix coherency ($\Delta\sigma_{CS}$), modulus mismatch ($\Delta\sigma_{MS}$) and atomic ordering ($\Delta\sigma_{OS}$) [105-107]. The first two mechanisms mainly contribute before the shear occurs, while the last mechanism mainly contributes during the shearing process. In principle, the larger value between $\Delta\sigma_{CS} + \Delta\sigma_{MS}$ and $\Delta\sigma_{OS}$ will dominate the result. The mathematical expressions for each mechanism's contribution are as follows[108]:

$$\Delta\sigma_{CS} = M \cdot \alpha_{\varepsilon}(G \cdot \varepsilon)^{3/2}(\frac{rf}{0.5Gb})^{1/2} \quad \text{Eq. 2-21}$$

$$\Delta\sigma_{MS} = M \cdot 0.0055(\Delta G)^{\frac{3}{2}}\left(\frac{2f}{G}\right)^{\frac{1}{2}}\left(\frac{r}{b}\right)^{\frac{3m}{2}-1} \quad \text{Eq. 2-22}$$

doi:10.6342/NTU202302391

$$\varDelta\sigma_{OS} = M \cdot 0.81\frac{\gamma_{APB}}{2b}(\frac{3\pi f}{8})^{1/2} \qquad \text{Eq. 2-23}$$

For FCC crystals, $\alpha_{\varepsilon} = 2.6\,, m = 0.85\,, \varepsilon \sim 2/3 \cdot (\varDelta a/a)$ ，in this study, where $(\varDelta a/a) \sim 0.0026$ and $\varDelta a$ is the difference between the Ni_3Ti precipitate lattice constant and the matrix lattice constant. f is the volume fraction of precipitates, $\varDelta G$ is the difference in shear modulus between the precipitate and the matrix, and γ_{APB} is the interfacial energy between the precipitate and the matrix. In this study, data for Ni_3Ti in a nickel-based superalloy was used, with $\varDelta G = 81 - 77 = 4GPa\,, \gamma_{APB} = 0.12J\,/m^2$ [109]. Table 2-11 summarizes the contributions of various shear mechanisms to strength.

The mechanical strength contributions from different shear mechanisms were discussed, with $\varDelta\sigma_{SH1-I} = 305.6MPa\,, \varDelta\sigma_{SH1-II} = 371.9MPa$ for P1 alloy, and $\varDelta\sigma_{SH2-Ni3(Ti,Al)} = 305.6MPa$ for P2 alloy. After correcting for the volume fraction of different precipitate morphologies, the strengthening contributions from precipitates were $\varDelta\sigma_{P1} = 326.7MPa, \varDelta\sigma_{P2} = 327.7MPa$ respectively. The results showed that the strengthening effect of precipitates on P1 and P2 alloys was very similar.

Table 2-11 Quantification of mechanical property strengthening in P1 and P2 alloys [9].

Alloys	Regions or particles	$\Delta\sigma_{CS}$(MPa)	$\Delta\sigma_{MS}$(MPa)	$\Delta\sigma_{OS}$(MPa)	$\Delta\sigma_{CS}+\Delta\sigma_{MS}$(MPa)	$\Delta\sigma_{SH}$(MPa)
P1	I	216.8	29.8	305.6	246.6	305.6
	II	346.5	35.6	254.8	382.1	382.1
P2	-	204.0	29.8	327.7	233.8	327.7

Based on the discussion of various strengthening mechanisms described above, we can obtain Figure 2-32 which shows the contribution of different strengthening mechanisms to the strength of $(FeCoNiCr)_{94}Ti_2Al_4$ alloy. The yield strengths of P1 and P2 alloys are $\sigma_1 = 560.8MPa$ and $\sigma_2 = 904.2MPa$, respectively, and the calculated results are consistent with the experimental results.

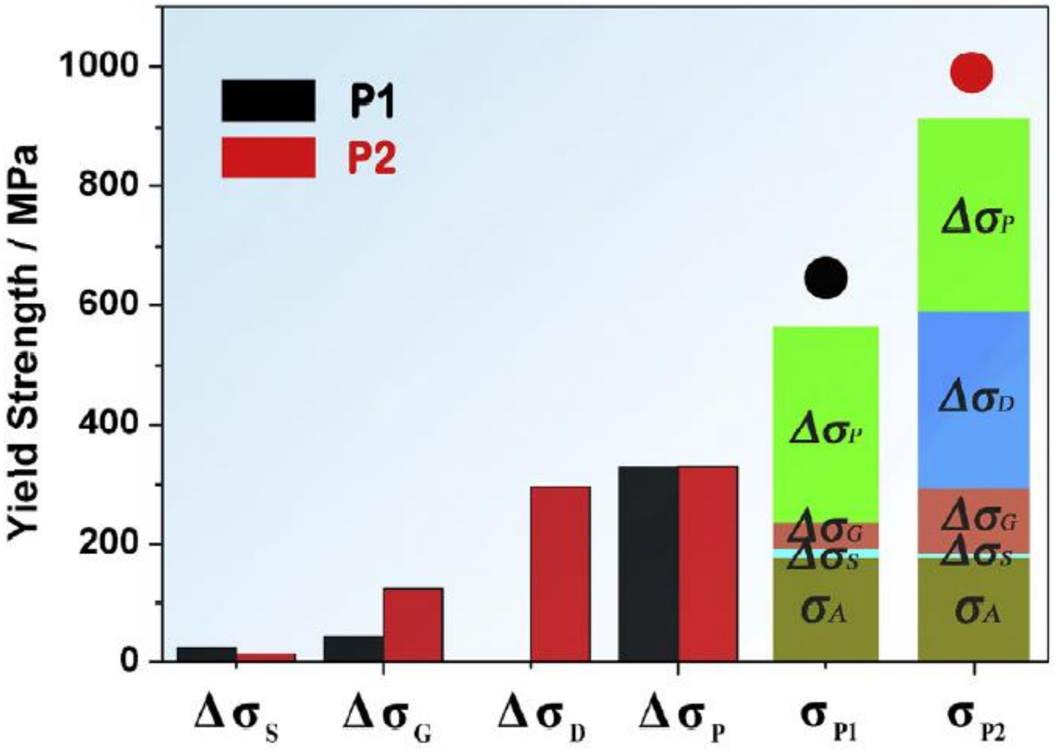

Figure 2-32 Different strength contributions from different strengthening mechanisms in $(FeCoNiCr)_{94}Ti_2Al_4$ [9].

2.6 Conclusion

In conclusion, this extensive exploration into high-entropy alloys (HEAs) reveals their immense potential as revolutionary materials in the field of engineering and material science. The investigation of core effects in HEAs uncovers the remarkable interplay of multiple elements, leading to unique mechanical properties and enhanced performance. Understanding the crystal structures in HEAs showcases their remarkable diversity, offering a versatile platform for tailored materials with desired functionalities.

The categorization of HEAs provides a valuable framework for organizing and understanding this diverse class of alloys, paving the way for targeted alloy design and application. Moreover, the study on alloy design, specifically the impact of adding Al, Ti, and Nb to HEAs, highlights the significance of alloying elements in fine-tuning material properties for specific engineering needs.

The in-depth exploration of thermal stability of $L1_2$ precipitates elucidates the behavior of HEAs at elevated temperatures, enabling the design of microstructures that exhibit both stability and desired mechanical properties. Additionally, the study on mechanical properties and microstructures of $L1_2$ precipitate-hardening HEAs provides valuable insights into the various strengthening mechanisms at play, guiding the development of high-performance materials with exceptional mechanical

doi:10.6342/NTU202302391

characteristics. Overall, this review of high-entropy alloys advances our understanding of HEAs and their potential applications, opening doors to new horizons in materials engineering.

doi:10.6342/NTU202302391

Chapter Three Experiment designs and procedures

3.1 Introduction

Figure 3-1 is the experiment process flow chart. To achieve high yield strength in medium-entropy alloy, aluminum and niobium were added in the CrCoNi medium-entropy alloy to implement precipitate hardening. Before performing precipitate hardening, proper heat treatments should be done. The detailed heat treatment process would be discussed in 3.1.2. Afterward, peak aging condition could be identified through Vickers hardness tests. The peak-aged samples would be tested in tensile test and Hopkinson bar compression test. The strain rates are $0.001s^{-1}$ and $5000s^{-1}$ respectively, representing slow strain rate and extreme high strain rate. To investigate the deformed behaviors, EBSD and TEM analysis would be used to analyzed nanoscale mechanical behaviors.

doi:10.6342/NTU202302391

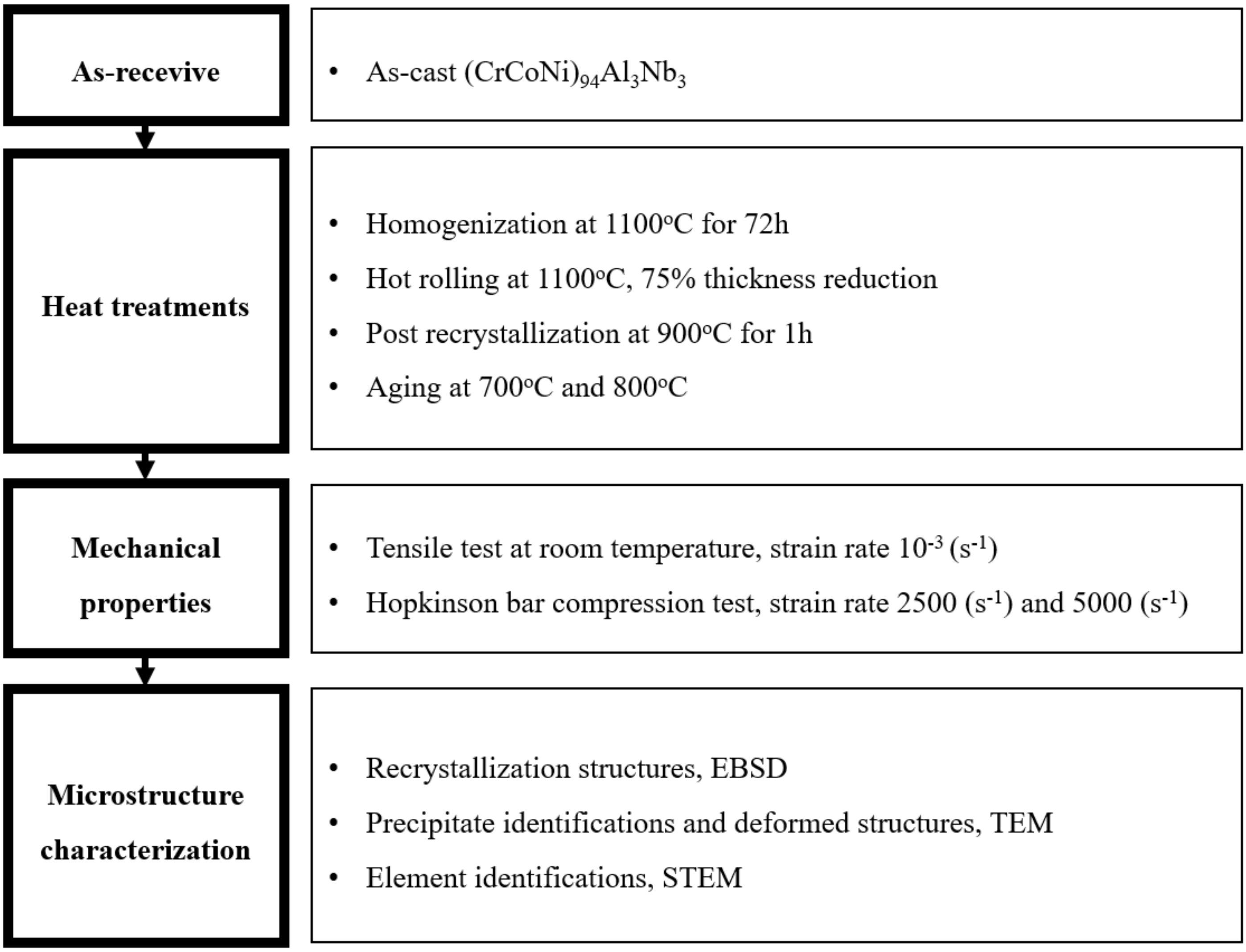

Figure 3-1 Experiment flow chart.

doi:10.6342/NTU202302391

3.1.1 Experiment material

The experiment materials are provided TRANSCRYSTAL ALLOY INDUSTRIAL CORPORATION. The company conducts vacuum induction melting with high purity raw materials (purity > 99.9wt%). To achieve high purity, it remelts the materials for more than three times. Then, it pours the liquid phase material into a plate-like ceramic mold. The cooling rate is slower than 0.1°C/min. Therefore, a cast material $(CrCoNi)_{94}Al_3Nb_3$ has created. The size of the ingots is $9cm \times 9cm \times 3cm$.

3.1.2 Heat treatments

The heat treatment flow chart is shown as Figure 3-2.The original as-cast microstructure is eliminated by the homogenization process at 1100°C for 72 hours. Water quenching is immediately conducted after homogenization. Also, a homogenization can provide saturated solid solution for the aging treatments. After, to achieve a fine-grain microstructure, hot rolling is performed at 1100°C with 75% thickness reduction. Each hot rolling process is followed by a 3-minute annealing to temper the material. Once the thickness reduction is reached, water quenching is executed. It is necessary to have a fully recrystallized microstructure before aging. Therefore, the material undergoes a post annealing process at 900°C for an hour with water quenching. Afterward, aging processes are conducted at 700°C and 800°C. Then,

$L1_2$ nanoprecipitates are distributed in the single-phase FCC matrix.

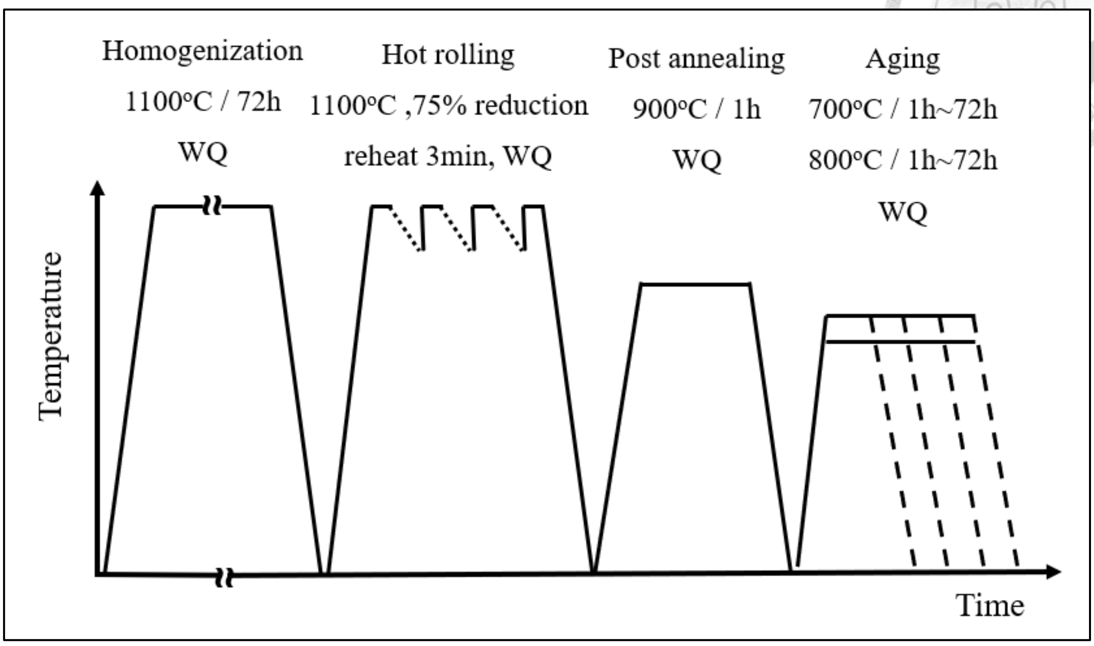

Figure 3-2 Heat treatment process flow chart.

3.1.3 Hot rolling methods

Hot rolling processes are not easily conducted in the experiment because brittle Laves phase would induce cracks during the hot rolling processes. Figure 3-3 demonstrates the failure of hot rolling processes. A lot of cracks can be observed through eyes. However, Figure 3-4 gives the results of successful hot rolling processes. The significant difference between two results depends on temperature controls. Figure 3-5 is the COMSOL thermal heat transfer simulation result. A rolling machine model is constructed with 304 stainless steels, and the experiment material is put on the rolling machine after taking out from a 1100°C furnace. Therefore, it is possible to find the time that the temperature would be lower than recrystallization temperature. On the

doi:10.6342/NTU202302391

other word, if the rolling processes are performed under the recrystallization temperature, cracks would be induced. In this experiment, the recrystallization temperature is set at 900°C. Overall, when conducting hot rolling processes with $(CrCoNi)_{94}Al_3Nb_3$, the materials should be reheated in the furnace no more than 30 seconds.

Figure 3-3 Failed hot rolling materials at 1100°C.

doi:10.6342/NTU202302391

Figure 3-4 Successful hot rolling materials at 1100°C.

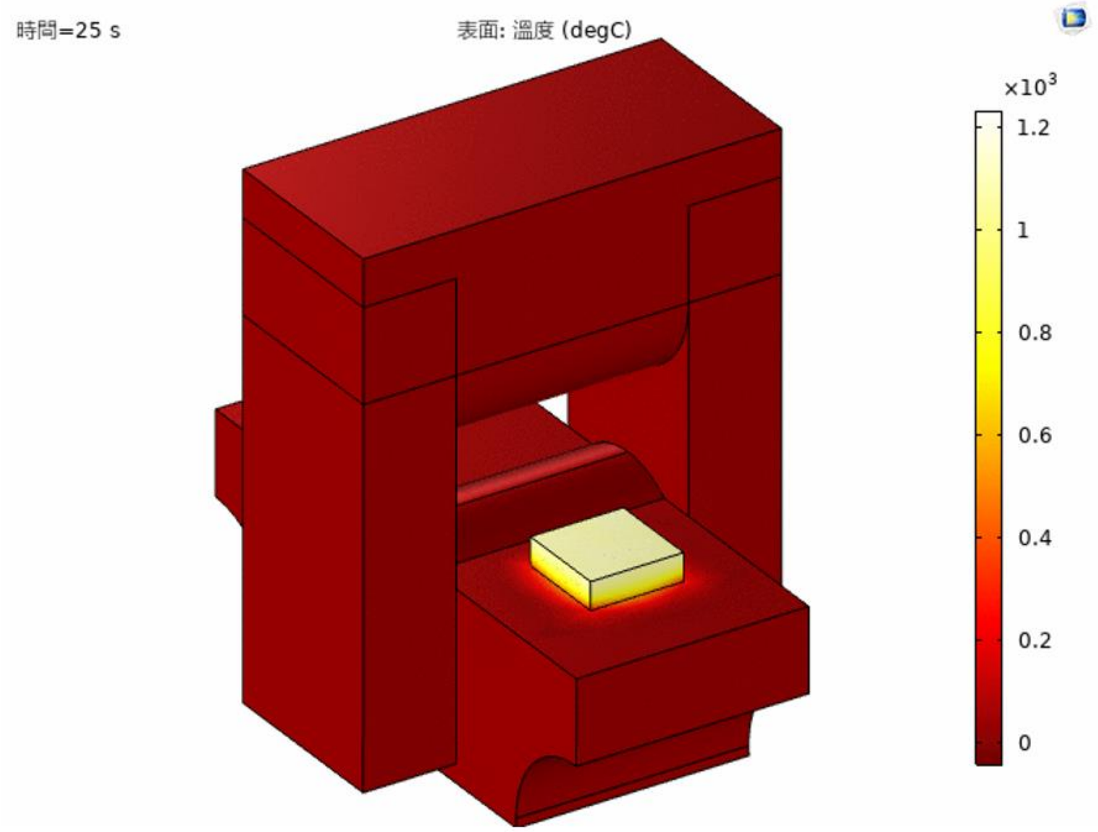

Figure 3-5 COMSOL time dependent thermal module simulation.

doi:10.6342/NTU202302391

3.1.4 Tensile test

The sample that has undergone annealing at 900°C for an hour and aging at 700°C for 16 hours are processed into a dog-bone-shaped tensile specimen with a gauge length of 10mm, a width of 3mm, and a thickness of 1.5mm (see Figure 3-6 (a)). Subsequently, a tensile test was conducted at room temperature, with a strain rate controlled at $0.001 s^{-1}$, to calculate the yield strength, ultimate tensile strength, and strain, and to observe the deformation structure using TEM and investigate the interaction between precipitates and dislocations.

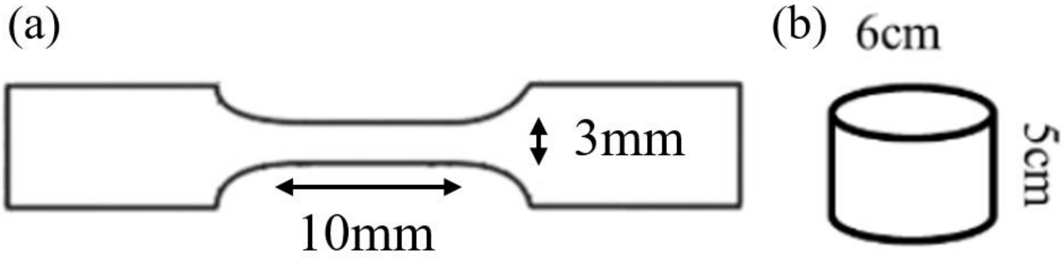

Figure 3-6 specimen geometry (a)Tensile test (b)Hopkinson bar specimen.

3.1.5 Hopkinson compression test

The sample that has undergone annealing at 900°C for an hour and aging at 700°C for 16 hours are processed into a cylinder shape specimen (see Figure 3-6 (b)). Nitrogen is used as acceleration gas to shoot the samples at room temperature. The strain rates are controlled at $2500 s^{-1}$ and $5000 s^{-1}$. Afterward, the deformed structures are inspected by TEM.

doi:10.6342/NTU202302391

3.2 Experimental instruments and equipment.

3.2.1 Rolling machine

The rolling machine locates at the previous math building. The oxidized surface of homogenized $(CrCoNi)_{94}Al_3Nb_3$ was grinded before rolling. Before starting the rolling process, the material was heated at 1100°C for 30 minutes. Each rolling process was controlled at 5% thickness reduction, and reheating for 3 minutes before another rolling process. The initial thickness is 2.25cm. After 70% thickness reduction, the materials could be prepared as Hopkinson bar specimen and tensile test sample.

3.2.2 MTS Landmark tensile test machine

MTS Landmark tabletop test systems are highly suitable for analyzing the dynamic characteristics of materials and components, with a maximum force capacity of 25 kN (see Figure 3-7). They have the ability to perform reliable and precise testing on a range of materials, including plastics, elastomers, aluminum, and other small components, through tension, compression, bend, creep, durability, and fatigue crack growth testing. The dog-bone shape specimens were fixed in the chunks. The strain rate is set at 10^{-3} s^{-1} until the samples are snapped. Therefore, yield strength, ultimate tensile strength and elongation can be obtained by engineering stress-strain curves. Afterward, the true stress-strain curve can be obtained by differentiating the engineering stress-strain curve.

Figure 3-7 MTS Landmark 370.02 (25 kN) Dynamic Test System.

3.2.3 Hopkinson bar compression test

The Split Hopkinson Pressure Bar (SHPB) is a commonly used instrument for high strain rate testing, typically in the range of $10^3(s^{-1})$ to $10^4(s^{-1})$. In collaboration with the Impact Mechanics Laboratory of the Department of Mechanical Engineering at National Cheng Kung University, the SHPB was used for rapid impact testing, as shown in Figure 3-8. By adjusting the length of the bars and the gas pressure, the desired strain rate can be achieved.

doi:10.6342/NTU202302391

The experimental method involves using one-dimensional elasticity theory to measure the three stress waves generated when the impact bar strikes the input and output bars: the incident wave, reflected wave, and transmitted wave. These waves are detected by strain gauges attached to the bars and processed by a signal processor. The resulting signals can be used to plot four graphs: stress-strain, stress-time, strain-time, and strain rate-time, providing insights into the dynamic plastic deformation behavior of materials.

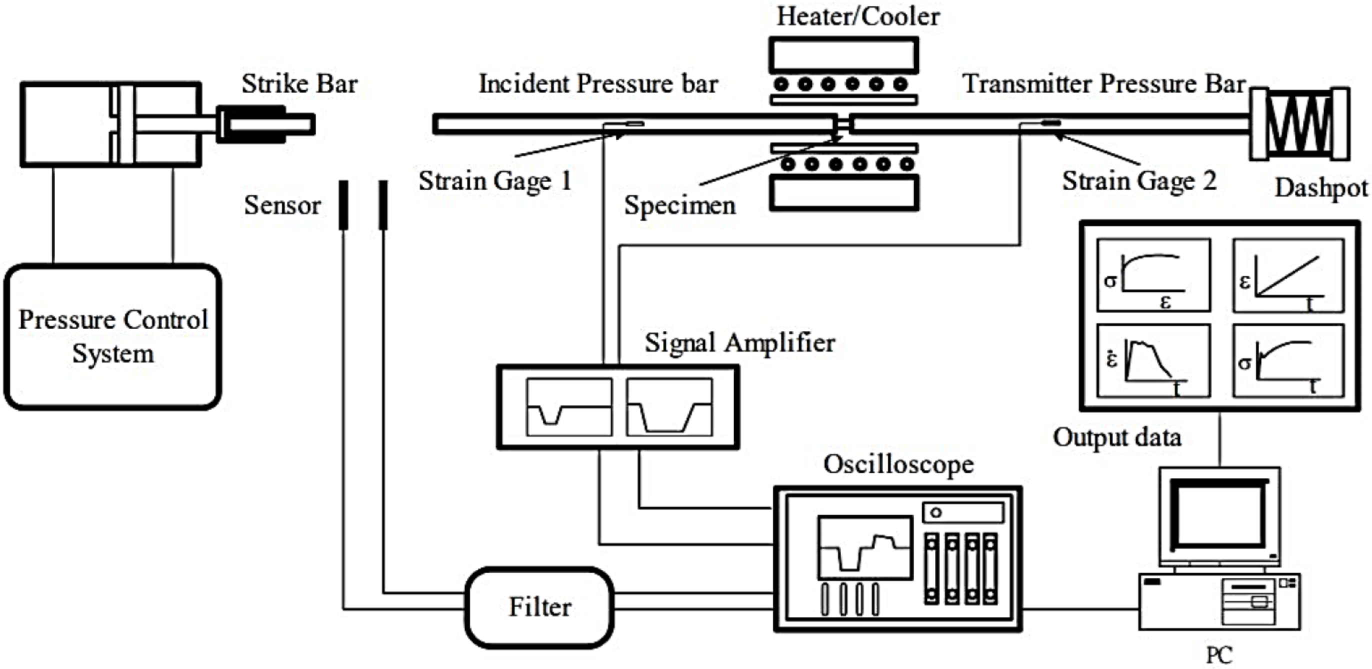

Figure 3-8 Schematic diagram of Hopkinson bar compression system.

3.2.4 Electron Probe Microanalysis (EPMA)

Electron Probe Microanalysis (EPMA) is a technique used to analyze the elemental composition of solid materials. The sample is placed in the EPMA instrument and the electron beam is directed onto the surface of the sample. The beam interacts with the atoms in the material, causing them to emit characteristic X-rays. The X-rays are detected by Wavelength Dispersive Spectroscopy (WDS) and analyzed to determine the quantitative composition of the material. The data obtained from the EPMA analysis can be used to determine the quantitative composition of the material, as well as the spatial distribution of elements in the sample.

3.2.5 Differential Scanning Calorimetry (DSC)

Differential Scanning Calorimetry (DSC) is a technique commonly used in material science to study the thermal behavior of materials. The sample is placed in the DSC instrument and the instrument is programmed to heat the sample at a specified rate. In this experiment, heating rate and cooling rate are 10°C / min and -10°C / min, and the carrying gas is argon. As the sample is heated, it undergoes thermal changes, such as phase transitions or chemical reactions. These changes are reflected in the amount of heat absorbed or released by the sample, which is detected by the DSC instrument. Therefore, various thermal properties can be detected such as melting point, glass transition temperature, crystallization temperature, and specific heat capacity.

3.2.6 Scanning electron microscope (SEM)

Scanning electron microscopy (SEM) and backscattered electron diffraction (EBSD) are two widely used techniques in material science for imaging and characterization of materials.

1. Sample Preparation: The sample must be prepared for SEM analysis by first being mounted on a suitable substrate, such as a thin metal foil. The sample is then polished and cleaned to remove any surface contamination and to ensure a smooth, flat surface. The polishing condition is 30V / 5 seconds in 5% perchloric acid.
2. SEM Imaging: The prepared sample is then inserted into the SEM chamber, and the imaging parameters are set, such as the electron beam energy and the working distance. The electron beam is then directed at the sample surface, causing it to emit secondary electrons that are detected by the SEM to form an image of the sample surface.
3. EBSD Analysis: Once SEM imaging is complete, the EBSD analysis can be performed. This involves tilting the sample to a specific angle, typically between 70 and 90 degrees, and then directing the electron beam at the sample. As the beam interacts with the sample, it produces backscattered electrons that are detected by an EBSD detector to generate a diffraction pattern.
4. Data Interpretation: The diffraction pattern obtained from EBSD analysis can be

doi:10.6342/NTU202302391

used to determine various crystallographic information, such as crystal orientation, grain size, and texture. This information can be used to gain insights into the microstructure and mechanical properties of the material.

3.2.7 Transmission electron microscope (TEM)

Transmission electron microscopy (TEM) is a powerful technique used in material science to obtain high-resolution images and detailed information about the microstructure of materials.

1. Sample Preparation: The sample must be prepared for TEM analysis by first being cut into a thin specimen, typically less than 100 nanometers thick. This is done using a twin-jet polishing under 60V for approximately 3 minutes until the light pass through the hole.
2. TEM Imaging: The prepared sample is inserted into the TEM chamber, and the imaging parameters are set, such as the electron beam energy and the working distance. The electron beam is then directed at the sample, and the transmitted electrons are detected to form an image of the sample. The high-energy electrons can penetrate the thin specimen, providing information about its internal structure.
3. Electron Diffraction: In addition to imaging, TEM can also be used for electron diffraction. The electron beam is directed at the sample, and the electrons that are

doi:10.6342/NTU202302391

diffracted by the sample are detected to generate a diffraction pattern. The diffraction pattern can provide information about the crystal structure and orientation of the material.

4. Data Interpretation: The images and diffraction patterns obtained from TEM analysis can be used to determine various microstructural information, such as crystal structure, grain size, and defect density. This information can be used to gain insights into the physical and mechanical properties of the material.

3.3 Conclusion

In conclusion, a comprehensive overview of the experimental designs and procedures employed to achieve high yield strength in a medium-entropy alloy through precipitate hardening with the addition of aluminum and niobium was presented. The chapter covered the experiment material, heat treatment process, and various mechanical tests conducted, including tensile tests and Hopkinson bar compression tests at different strain rates. Advanced analysis techniques, such as EBSD and TEM, were utilized to study nanoscale mechanical behaviors and deformation structures.

The careful selection of experiment materials and precise heat treatments played a crucial role in obtaining the desired microstructure with $L1_2$ nanoprecipitates. The successful hot rolling processes also demonstrated the importance of temperature controls in avoiding cracks and ensuring the material's integrity. The tensile and compression tests provided valuable data on yield strength, ultimate tensile strength, and deformation behavior. Overall, this chapter laid a solid foundation for further investigations into the mechanical properties and potential applications of medium-entropy alloys with precipitate hardening.

doi:10.6342/NTU202302391

Chapter Four Microstructure and Mechanical Properties of $(CrCoNi)_{94}Al_3Nb_3$

4.1 Introduction

Detailed analysis would be presented in this chapter to support the temperature selections in homogenization, recrystallization, and aging. SEM, EDS, DSC, and Thermo-Calc were used to characterize the microstructures to find the optimal temperature designs. Furthermore, microstructure characterization details through EBSD and TEM to completely demonstrate every phase in this material. Afterward, mechanical properties would be tested through tensile tests and Hopkinson bar compression tests. To investigate the reasons of presenting high strength, the defect types, precipitate distribution, and interaction between precipitates and defects in deformed samples would be observed by TEM.

doi:10.6342/NTU202302391

4.2 Homogenization and recrystallization

4.2.1 As-cast microstructures

Figure 4-1 and Figure 4-2 demonstrates the metallography of as-cast $(CrCoNi)_{94}Al_3Nb_3$. A classic dendritic structure can be observed. The distance between dendrites is longer than 50μm, representing the cooling rate is very slow. Figure 4-3 is the as-cast SEM and EDS mapping results. The dendritic regions are Nb-rich. Figure 4-4 is the phase diagram of Inconel 718, which has a similar chemical composition to $(CrCoNi)_{94}Al_3Nb_3$. The Nb concentration in $(CrCoNi)_{94}Al_3Nb_3$ is around 10wt%. As a result, cooling from liquidus phase, the γ would form first, and the remaining liquid would be Nb-rich liquid. After, the remaining liquid would become solidification under the eutectic temperature. More details please refer to the thermo-calc section. In Figure 4-1 and Figure 4-2, a layered eutectic structure can be observed. Referring to the phase diagram, the layered structures are γ+Laves. Therefore, the matrix is γ, and the dendrite is γ+Laves.

doi:10.6342/NTU202302391

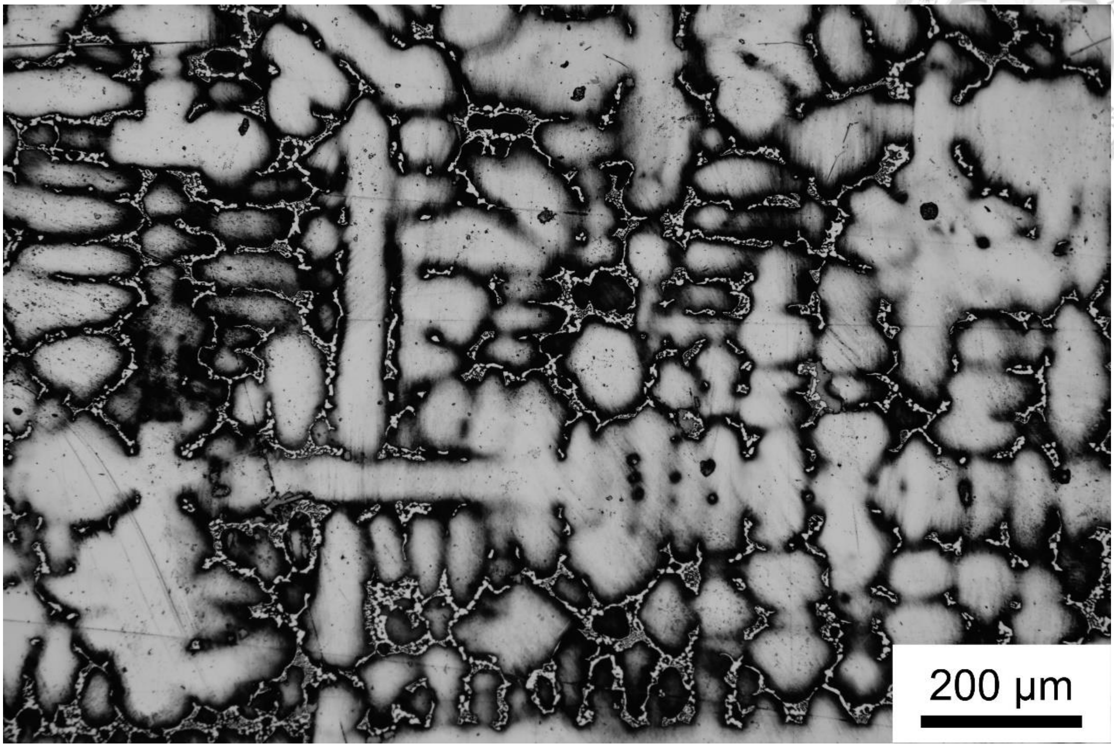

Figure 4-1 As-cast $(CrCoNi)_{94}Al_3Nb_3$ OM image.

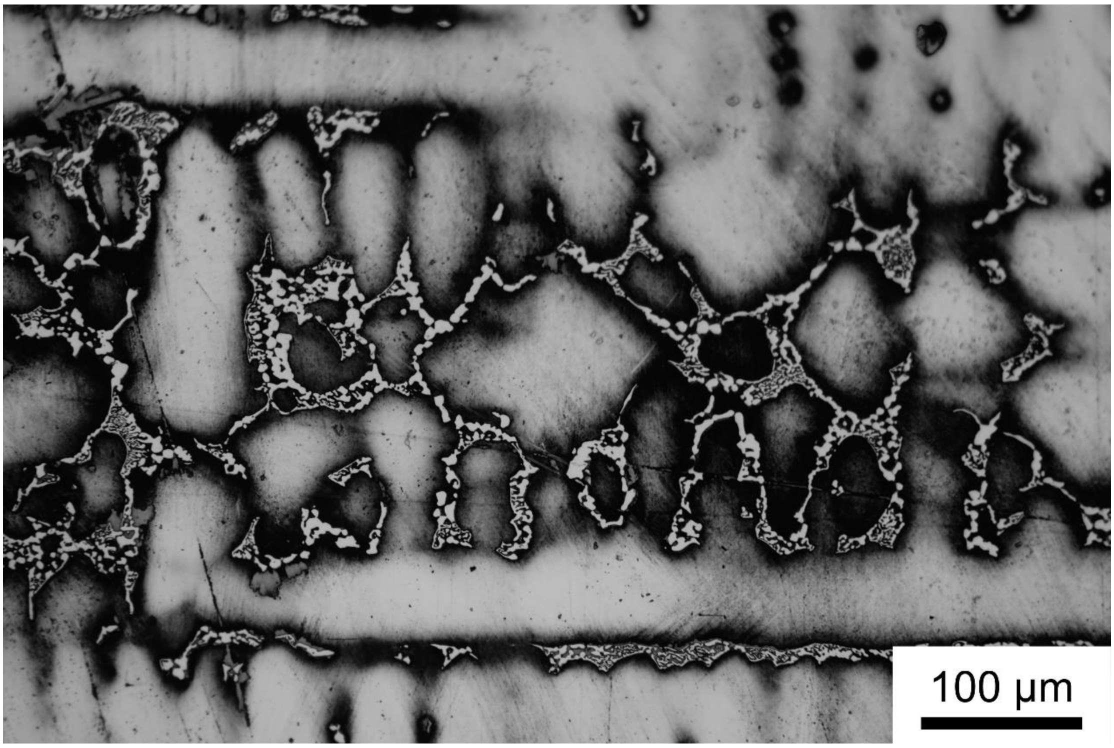

Figure 4-2 As-cast $(CrCoNi)_{94}Al_3Nb_3$ OM image.

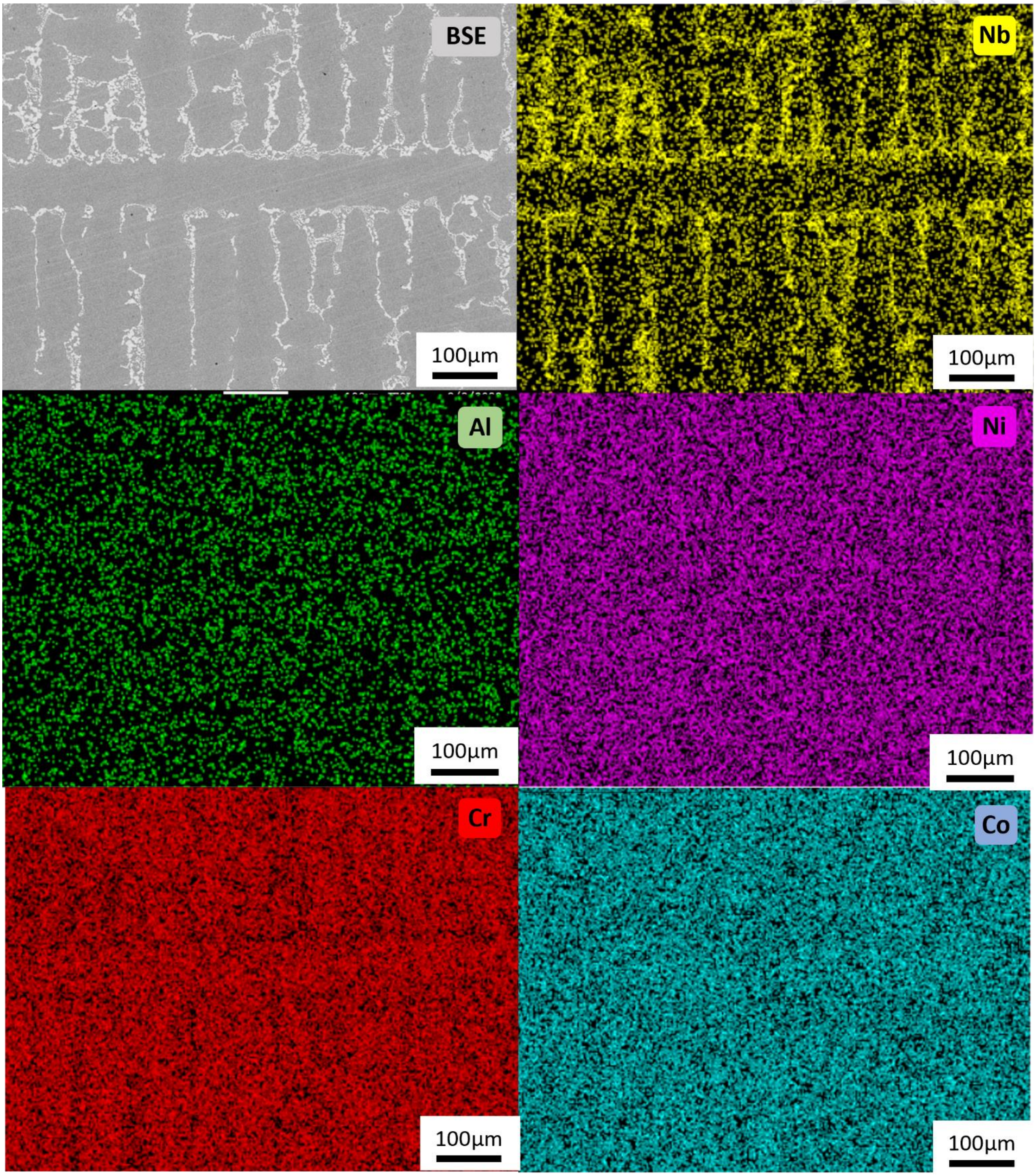

Figure 4-3 As-cast $(CrCoNi)_{94}Al_3Nb_3$ BSE image and EDS mapping.

doi:10.6342/NTU202302391

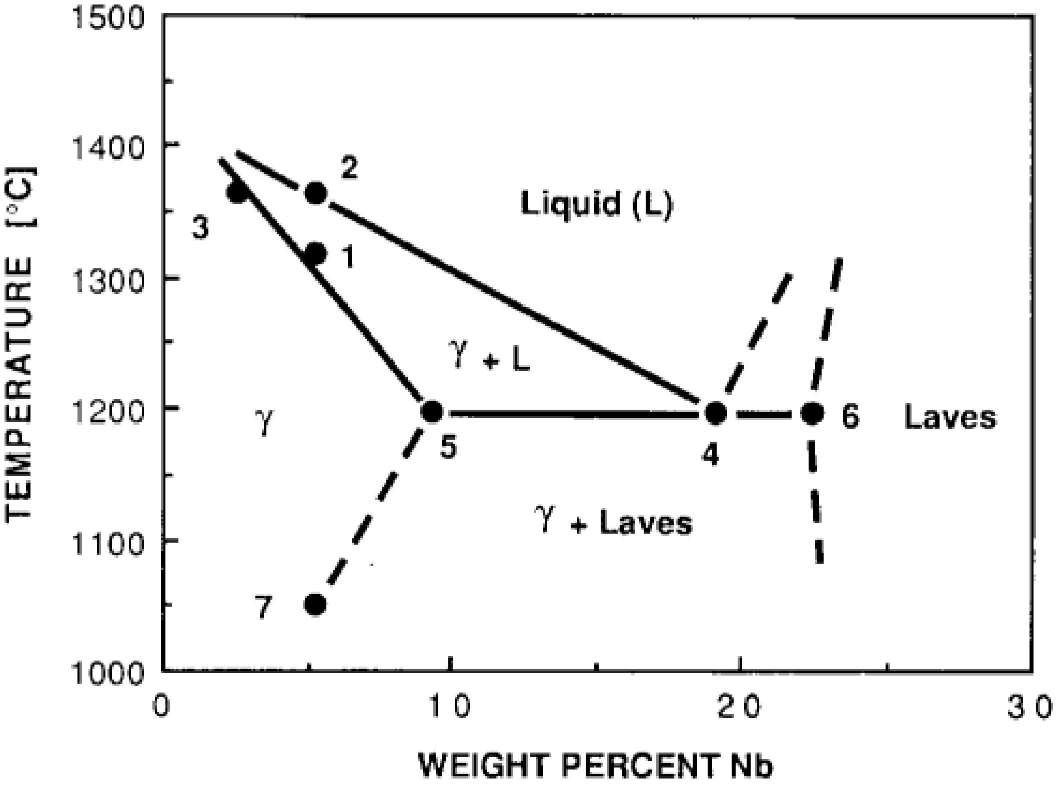

Figure 4-4 Phase diagram of Inconel 718 [110].

4.2.2 Incipient melting and homogenization microstructures

Incipient melting is common in superalloys and high-entropy alloys. This phenomenon results from excess element addition. The materials cannot become a single-phase solid solution after homogenization. To elaborate, the solidification structures could be detrimental to mechanical properties, fatigue life and creep resistance. Therefore, the differential scanning dilatometer method needs to be conducted to avoid the solidification structures.

Figure 4-5 is the differential scanning dilatometer result at RT-1500°C, and the testing material is as-cast $(CrCoNi)_{94}Al_3Nb_3$. The scanning rate is 10°C/min, and the

doi:10.6342/NTU202302391

carrier gas is argon. During the heating process (shown as red line), a significant melting point could be observed (shown as red peak). From the peak, this material starts melting at 1347.4°C, and it becomes total liquid at 1379.9°C. The peak melting temperature is 1372.9°C. Referring to the Inconel 718 melting region at 1370°C-1430°C [110], the DSC result of $(CrCoNi)_{94}Al_3Nb_3$ is reasonable.

In Figure 4-5, the cooling process (shown as green line) presents two major peaks. The first peak at 1336.9°C represents the solidification of γ. The second peak at 1198.2°C behaves as the solidification of Nb-rich phase because Figure 4-3 shows the dendritic regions are Nb-rich. By referring to the phase diagram in Figure 4-4, this peak has the meaning of γ + Laves eutectic solidification. As a result, during homogenization we should avoid using temperature higher than 1190.8°C, which is the solidification temperature of γ + Laves eutectic.

Figure 4-6 is BSE image of solidification structures after homogenization at 1200°C for 72 hours. Referring to the DSC result, it is a temperature would generate solidification structures. In Figure 4-7a, Laves phase segregates in grain boundaries. Additionally, in Figure 4-7b there are some Laves segregation far from grain boundaries. These structures cannot be annihilated by other processes. On the other word, solidification structures should be avoided during homogenization.

doi:10.6342/NTU202302391

Figure 4-6 is the BSE image after homogenization at 1100°C for 72 hours. Referring to the DSC result, it is a temperature would not generate solidification structures because it is below the melting temperature of eutectic γ + Laves. Furthermore, Laves phase would not segregate at grain boundaries like Figure 4-7a. The crystal structure of Laves phase in $(CrCoNi)_{94}Al_3Nb_3$ is C14-Laves (see Supplementary Figure 1). This microstructure is workable for post treatments like aging and tensile test.

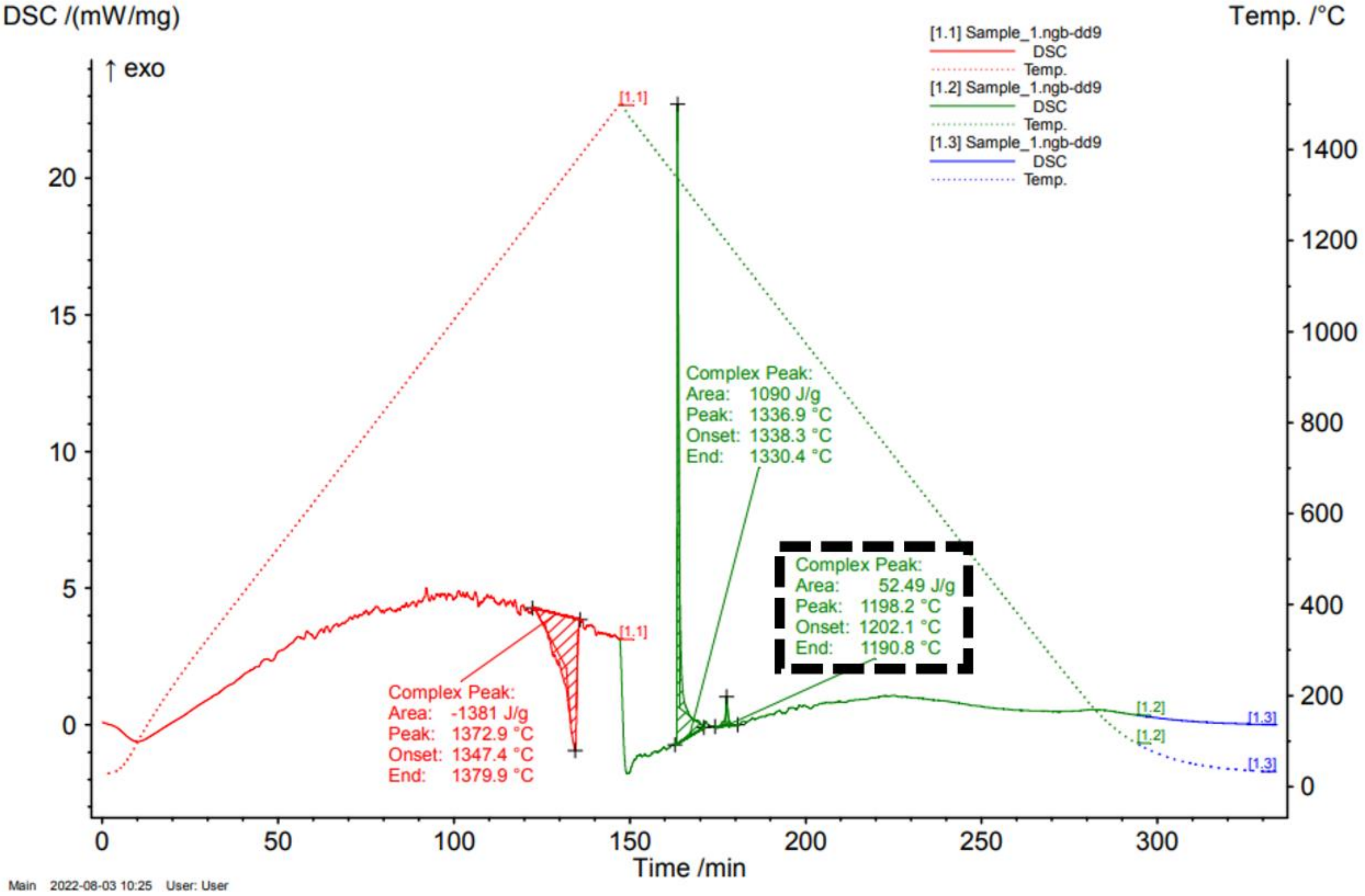

Figure 4-5 $(CrCoNi)_{94}Al_3Nb_3$ differential scanning dilatometer result at RT-1500°C.

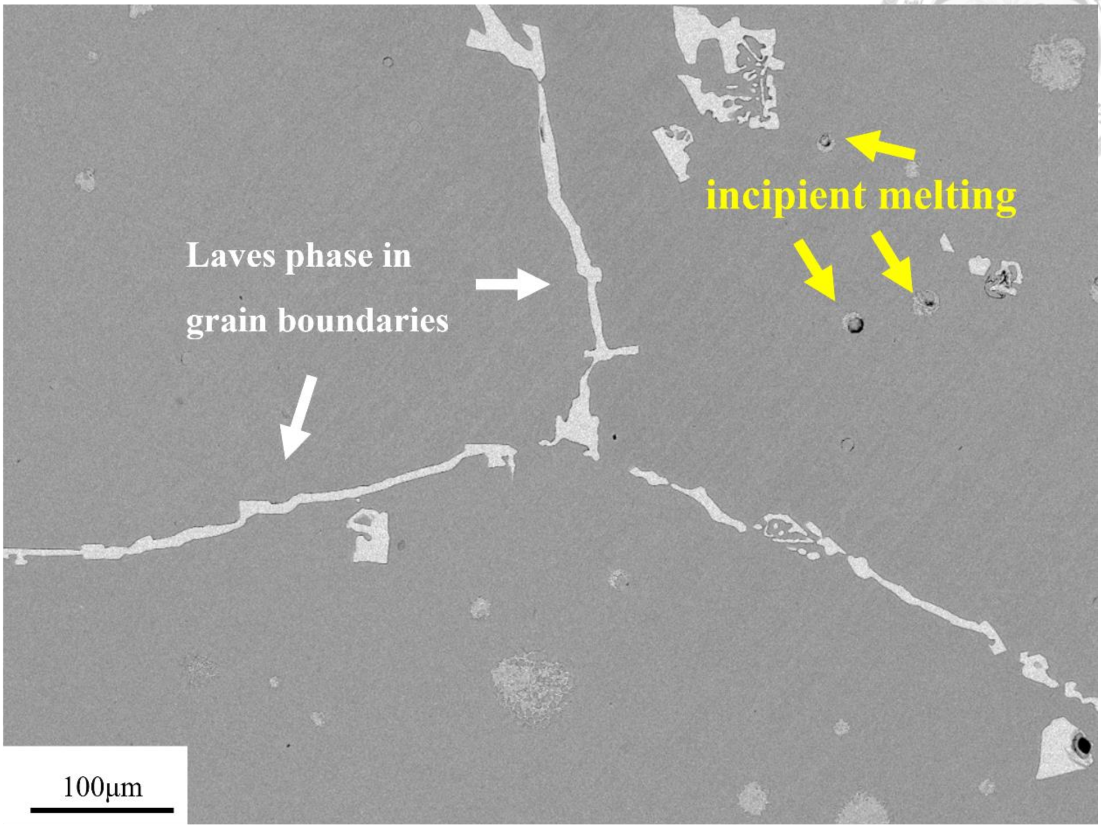

Figure 4-6 Solidification structures at grain boundaries after homogenization at 1200^{o}C for 72 hours.

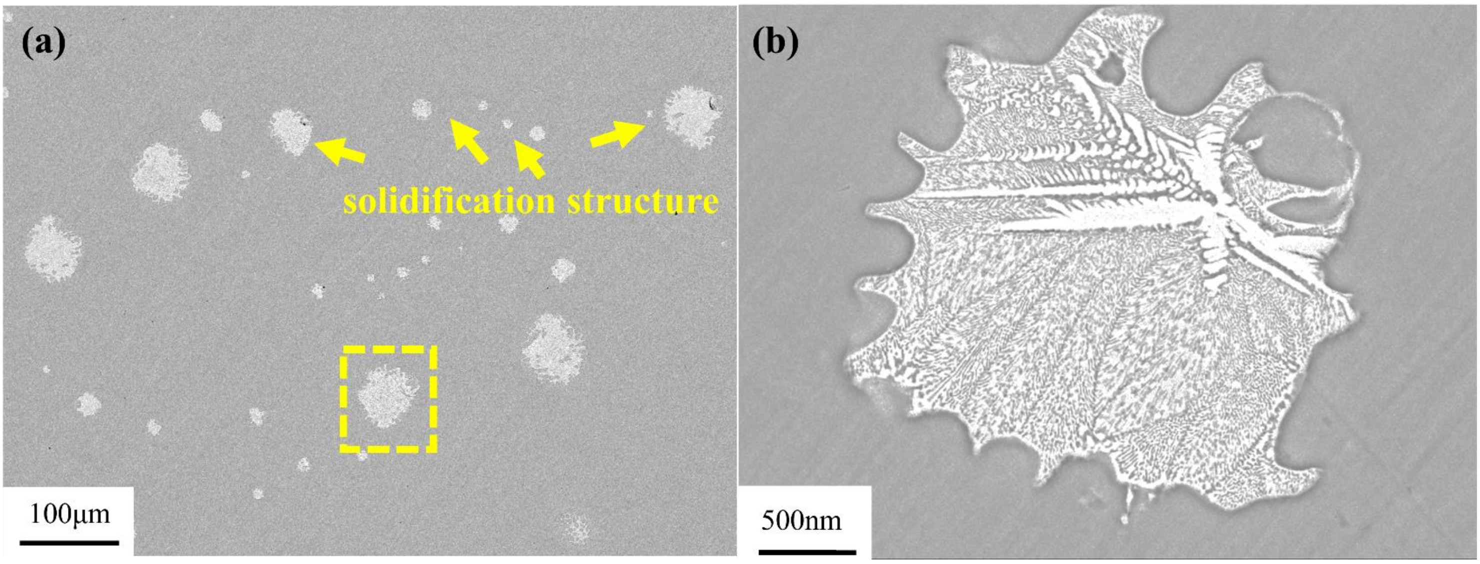

Figure 4-7 Solidification structures after 1200^{o}C /72h homogenization.

doi:10.6342/NTU202302391

4.2.3 Quantitative elements analysis

To find out what is the solute concentration in $(CrCoNi)_{94}Al_3Nb_3$, EPMA analysis was conducted. The following solubility average and standard deviation are calculated by those red dots in Figure 4-8. Figure 4-8a is the result of as-cast $(CrCoNi)_{94}Al_3Nb_3$. The matrix's solubility of Al and Nb is $2.895 \pm 0.052\ at\%$ and $1.195 \pm 0.134\ at\%$ respectively. The niobium becomes Laves phase during the slow cooling process while smelting. As a result, there is not much niobium remaining in the matrix. However, after homogenization at 1100°C for 72 hours followed by water quenching (see Figure 4-8b), the matrix's solubility of Al and Nb is 3.132 ± 0.065 at% and 2.766 ± 0.077 at%. Aluminum and niobium are kept in the FCC matrix as a saturated solid solution. By the EPMA result, the alloy design of $(CrCoNi)_{94}Al_3Nb_3$ successfully predict the saturated solubility of niobium which is closed to 3 at%. Besides, the aluminum saturated solubility is below 3 at%.

Figure 4-9 illustrates the uneven concentration distribution of $(CrCoNi)_{94}Al_3Nb_3$ after homogenization at 1100°C for 72 hours. Figure 4-9a represents the less segregation area. Less Nb-rich Laves phase can be observed. The matrix's solubility of Al and Nb is $3.082 \pm 0.021\ at\%$ and $2.313 \pm 0.101\ at\%$ respectively. On the other hand, Figure 4-9b represents the frequent segregation area. The matrix's solubility of Al and Nb is $3.132 \pm 0.065\ at\%$ and $2.766 \pm 0.077\ at\%$ respectively. There is

doi:10.6342/NTU202302391

approximately 0.4 at% difference of niobium in the same material after the same homogenization treatment. As a result, the element distribution may contribute to microstructure variations after aging.

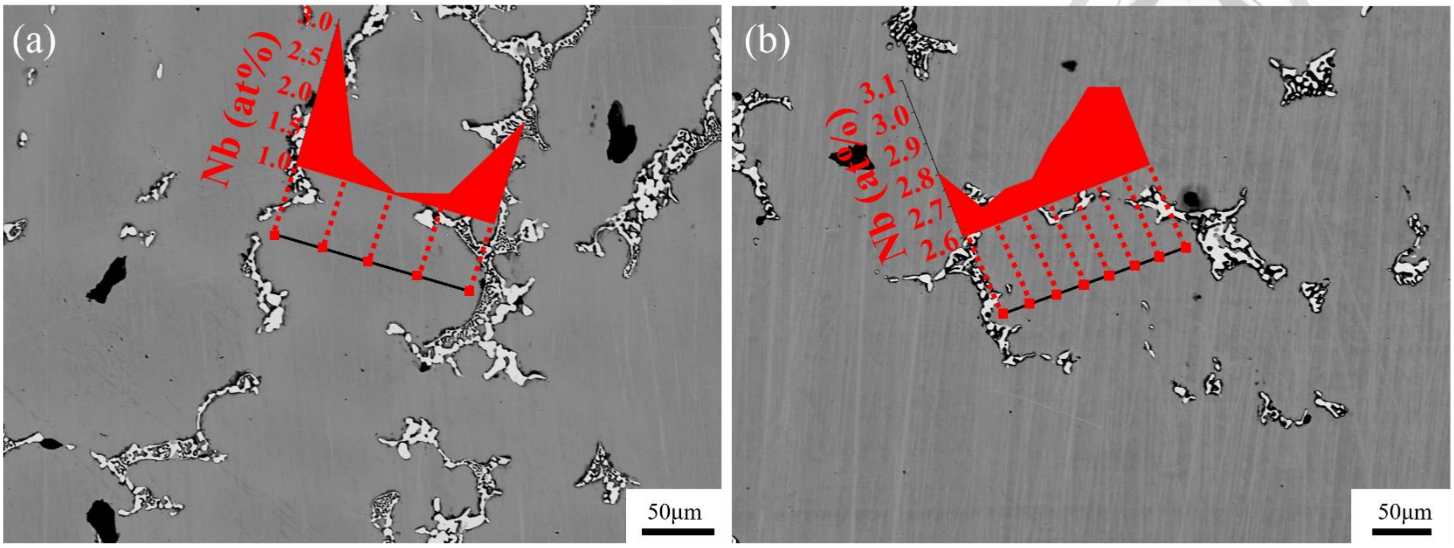

Al solubility = 2.895 ± 0.052 at%

Nb solubility = **1.195 ± 0.134 at%**

Al solubility = 3.132 ± 0.065 at%

Nb solubility = **2.766 ± 0.077 at%**

Figure 4-8 EPMA element concentration quantitively analysis (a) as-cast (b) homogenization at 1100°C for 72 hours.

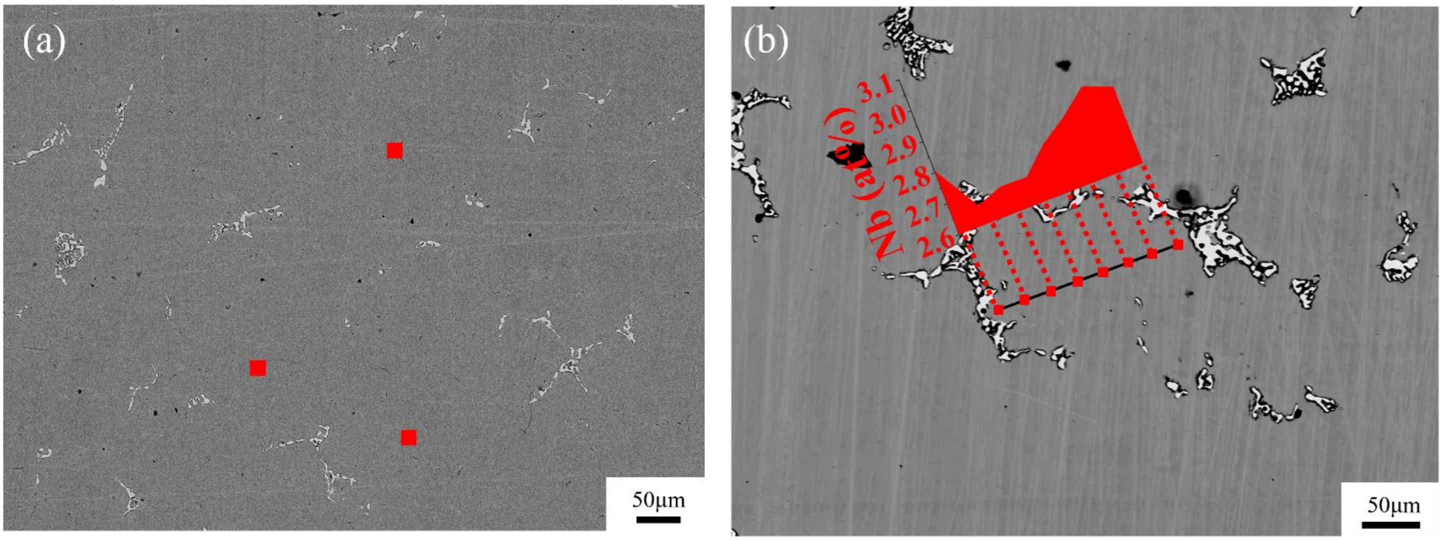

average Al solubility = 3.082 ± 0.021 at%

average Nb solubility = **2.313 ± 0.101 at%**

Al solubility = 3.132 ± 0.065 at%

Nb solubility = **2.766 ± 0.077 at%**

Figure 4-9 EPMA element concentration quantitively analysis (a) homogenization at 1100°C for 72 hours taken at less segregation region (b) homogenization at 1100°C for 72 hours taken at segregation region.

4.2.4 Optimal recrystallization processes

To have a fully recrystallization structure before aging treatment, a post annealing process is necessary after hot rolling because there might have been some portions that are not fully recrystallization. Therefore, finding an optimal recrystallization process is crucial. For example, brittle TCP phases need to be avoided. Grain size should be well-controlled as fine-grain. Otherwise, the hot rolling process would be useless.

Hardness is a good identification of finding an optimal recrystallization process. Some data needs to be clarified. The as-receive, homogenization and hot rolled hardness results shown as Table 4-1. The hardness of as-receive, homogenized and hot-rolled samples are $337.9 \pm 69.2\,\mathrm{Hv}$, $194.3 \pm 9.3\,\mathrm{HV}$, and $319.3 \pm 11.9\,\mathrm{Hv}$ respectively.

Figure 4-10 demonstrates the hardness of hot-rolled sample after 900^{o}C post annealing. The hardness soon drops to around 260Hv to 280Hv. Although annealing at 900^{o}C for 15 minutes seems to successfully recrystallized, the standard deviation is still higher than 900^{o}C for 1 hour. As a result, the standard deviation may represent that there are non-recrystallized grains in it. Therefore, selecting post annealing at 900^{o}C for 1 hour is a more suitable way.

Figure 4-12 is the EBSD results of post annealing at 900^{o}C for 1 hour. From Figure 4-12b, the image quality map, the grains are already fully recrystallized. Also,

doi:10.6342/NTU202302391

from

Figure 4-12e is the grain size distribution, and the average grain size is $13.39 \pm 6.02\mu m$. The average grain size could definitely be called as “fine-grain” after hot rolling processes. Overall, post annealing at 900°C for 1 hour can achieve a fully recrystallized structure.

As for the longer recrystallization treatment at 900°C, unfavorable TCP phases would show up. Besides, it would make the grains become larger which is not favorable while achieving high yield strength. To elaborate, recrystallization at 1000°C is facing the same problems mentioned above (see Figure 4-11). To be more specific, recrystallization at 1000°C has higher standard deviation in hardness. It represents that the larger grains become coarser, and the TCP phases are showing up to increase the hardness in certain regions.

Table 4-1 Vickers hardness of as-receive, homogenization and hot rolled $(CrCoNi)_{94}Al_3Nb_3$.

	As-receive	Homogenization (1100°C / 72h)	Hot-rolled
Hardness (Hv)	337.9 ± 69.2 Hv	194.3 ± 9.3 HV	319.3 ± 11.9 Hv

doi:10.6342/NTU202302391

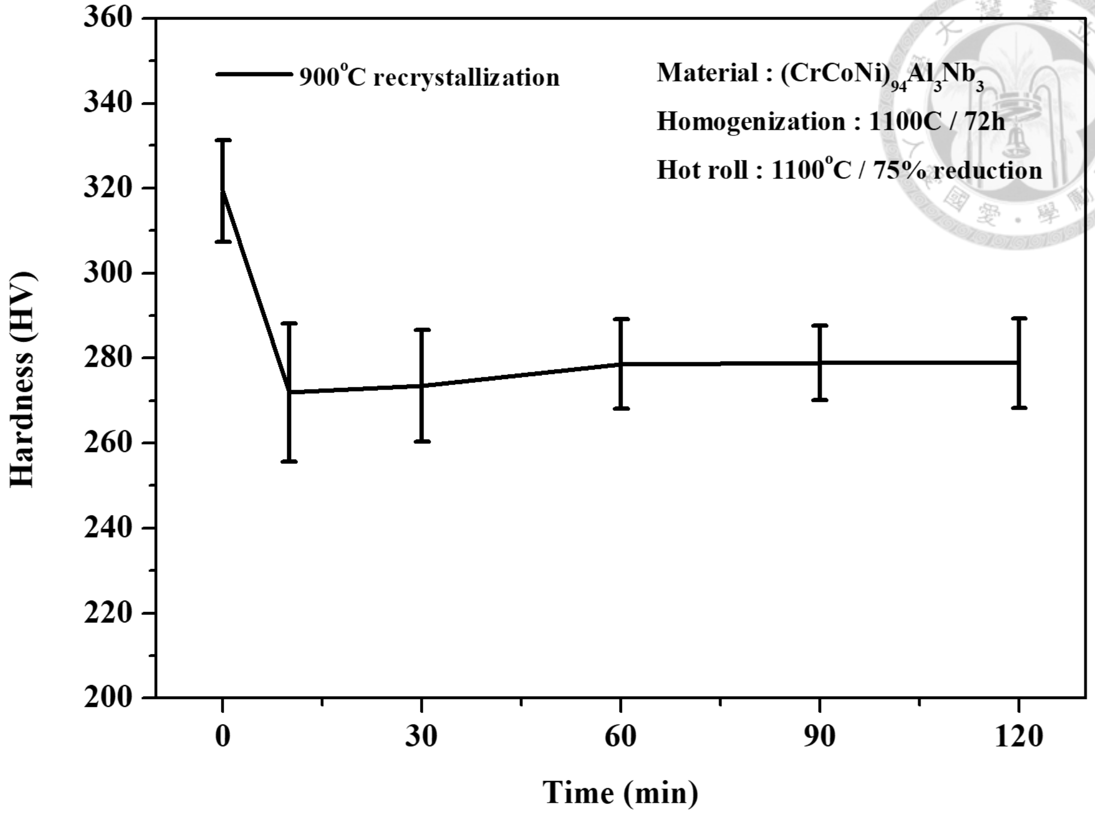

Figure 4-10 Hardness of $(CrCoNi)_{94}Al_3Nb_3$ after 900°C recrystallization treatments.

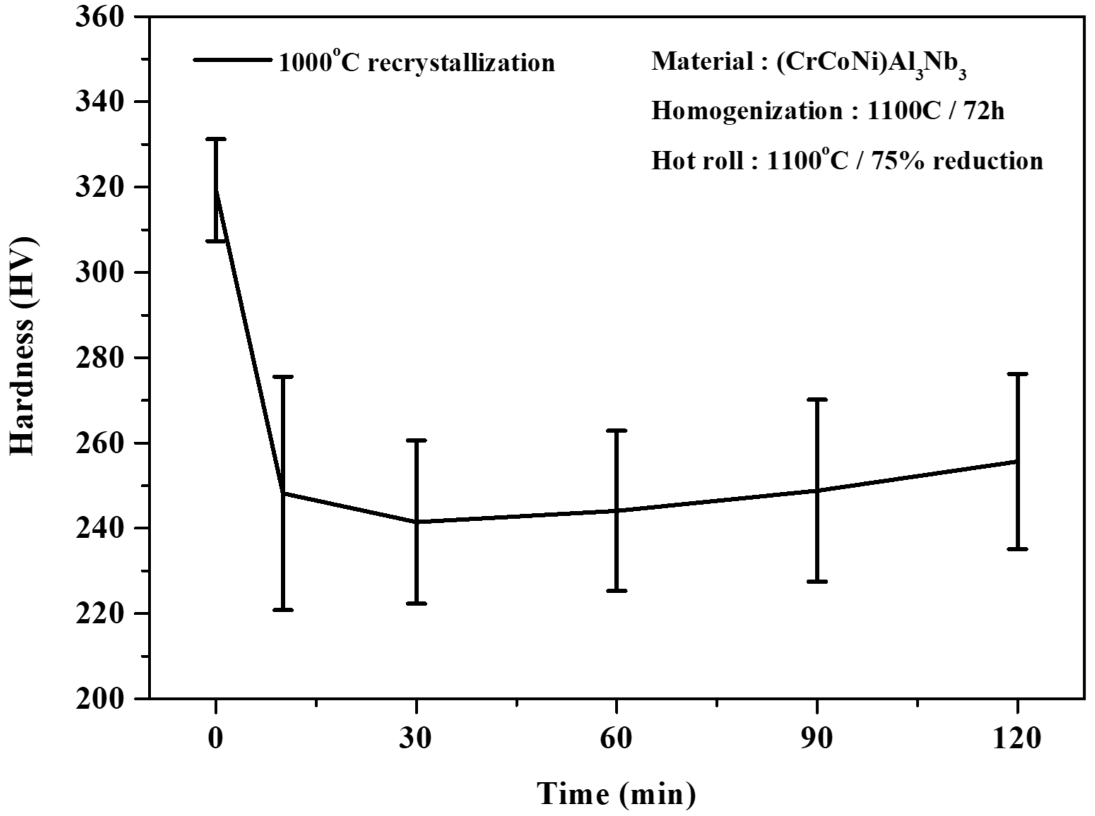

Figure 4-11 Hardness of $(CrCoNi)_{94}Al_3Nb_3$ after 1000°C recrystallization treatments.

doi:10.6342/NTU202302391

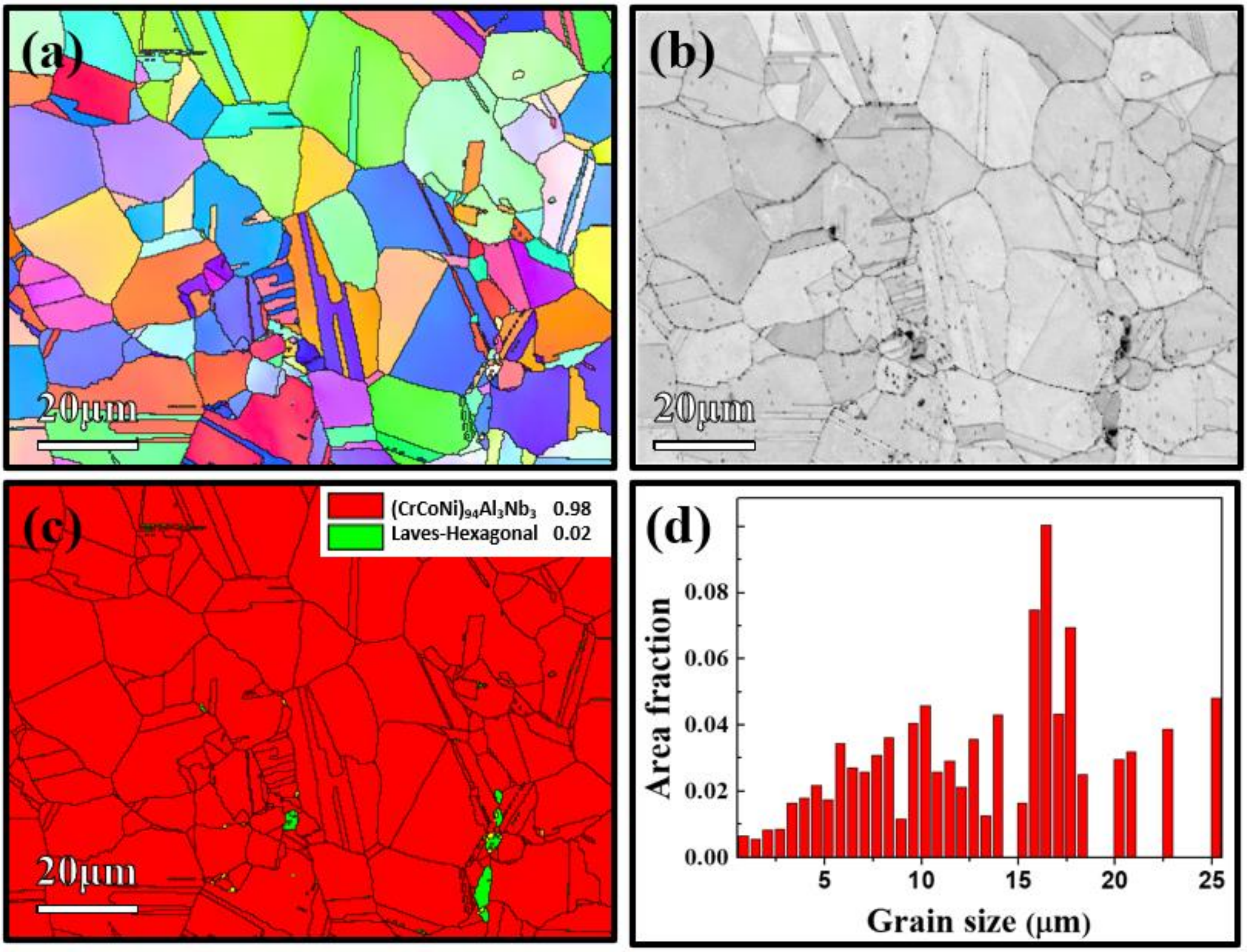

Figure 4-12 EBSD analysis of $(CrCoNi)_{94}Al_3Nb_3$ recrystallization at 900^{o}C for 1 hour (a) inverse pole figure (b) image quality (c) phase map (d)kernel average map (e) grain size distribution.

4.3 Aging and phase identification

4.3.1 Peak aging identification

To distribute fine and uniform coherent $L1_2$ particles, peak aging condition needs to be identified first. In this experiment, aging temperatures were set at 700ºC and 800ºC. Figure 4-13 and Figure 4-14 are the aging hardness results of 700ºC and 800ºC. In Figure 4-13, the peak aging condition at 700ºC is 16 hours, and the peak aging hardness is $469.37 \pm 21.48Hv$. As for the peak aging condition at 700ºC is 8 hours, and the peak aging hardness is $433.87 \pm 15.26Hv$.

Hardness of samples without aging is $278.62 \pm 10.53Hv$. After aging at 700ºC, the hardness increases nearly 70% of its original hardness to $469.37 \pm 21.48Hv$. The result shows that precipitate hardening poses significant effects in this material. In next section, the morphology and the size of precipitates would be discussed.

doi:10.6342/NTU202302391

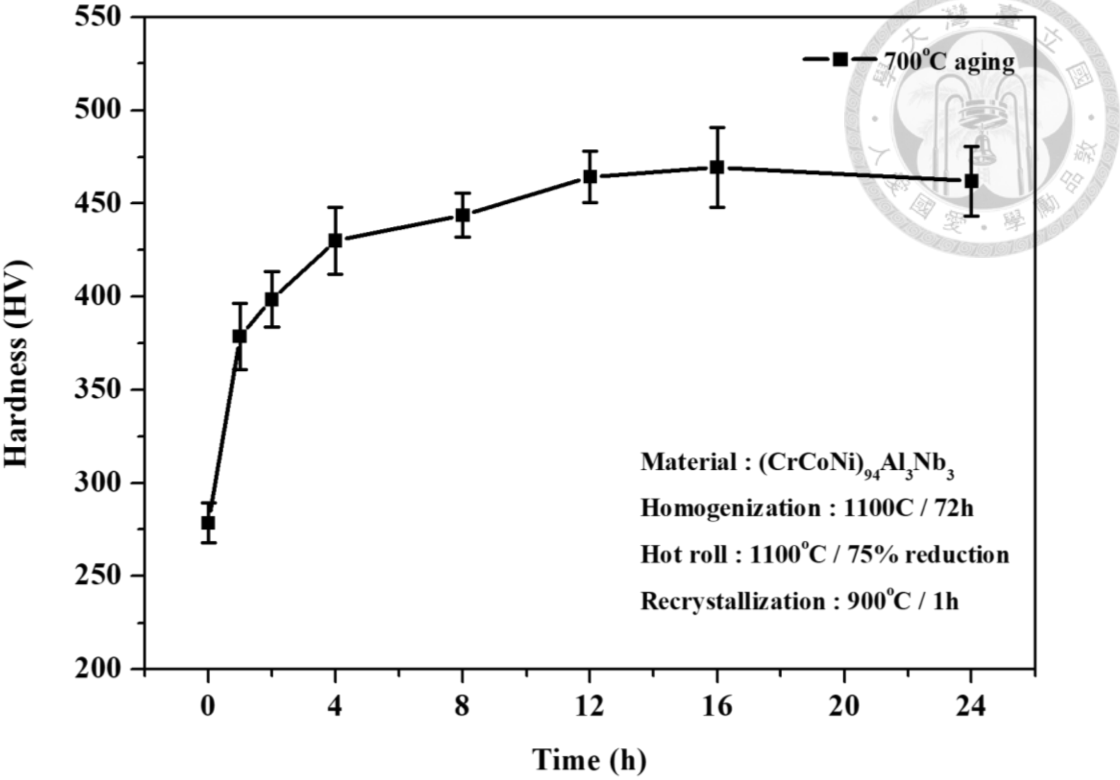

Figure 4-13 Hardness of 700°C aging.

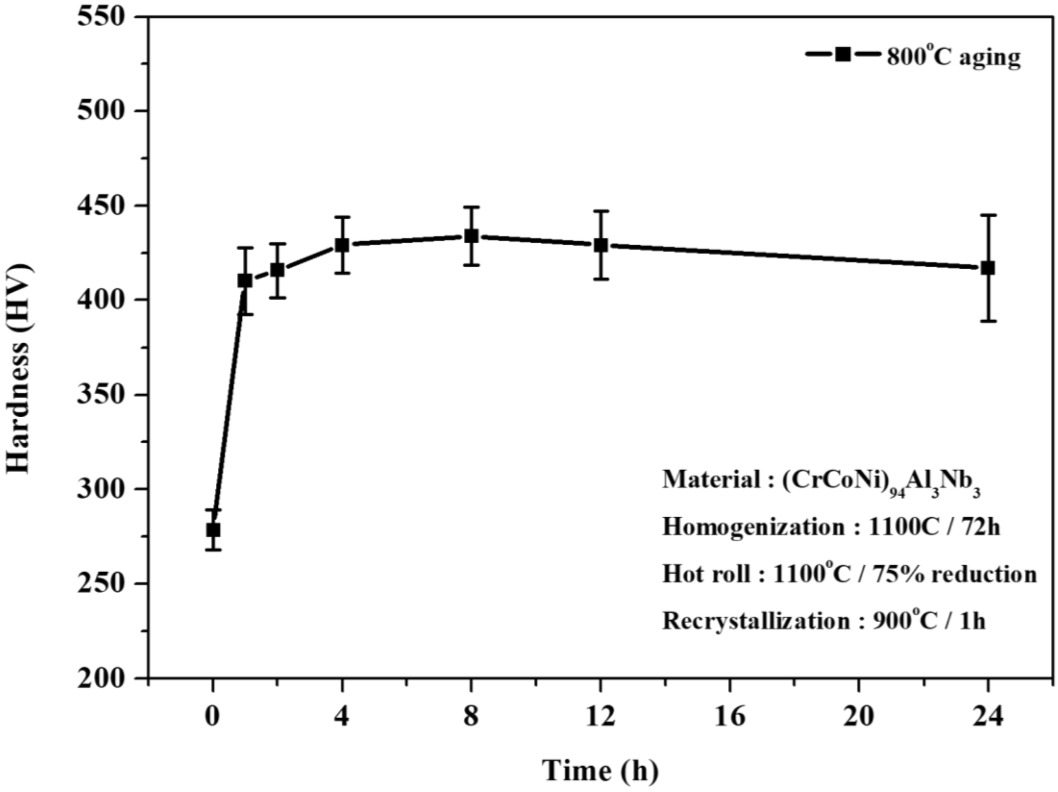

Figure 4-14 Hardness of 800°C aging.

doi:10.6342/NTU202302391

4.3.2 Coherent precipitate analysis

Figure 4-15 is the HADDF image of $(CrCoNi)_{94}Al_3Nb_3$ aging at 700°C for 16 hours. A lot of fine particles uniformly distribute in the FCC matrix. The size of the particles is around 5-10 nm. Compared to the optimal size of $(FeCrCoNi)_{94}Al_4Ti_2$ (20-25nm) [9], the fine particles in $(CrCoNi)_{94}Al_3Nb_3$ is much more smaller.

Figure 4-16 is the EDS mapping of Figure 4-15. By the EDS mapping results, the particles are rich in Ni, Al, and Nb. These are the favor elements of $L1_2$ particles, which is coherent to the FCC matrix. The matrix is rich in Cr and Co because they would not become parts of $L1_2$. As a result, after aging, the matrix is rich in Cr and Co, and the particles are rich in Ni, Al, and Nb. Figure 4-17a is the stacked EDS mapping of Ni, Al, and Nb. Figure 4-17b is the stacked EDS mapping of Cr and Co. Figure 4-17 demonstrates clearer images of element distribution.

doi:10.6342/NTU202302391

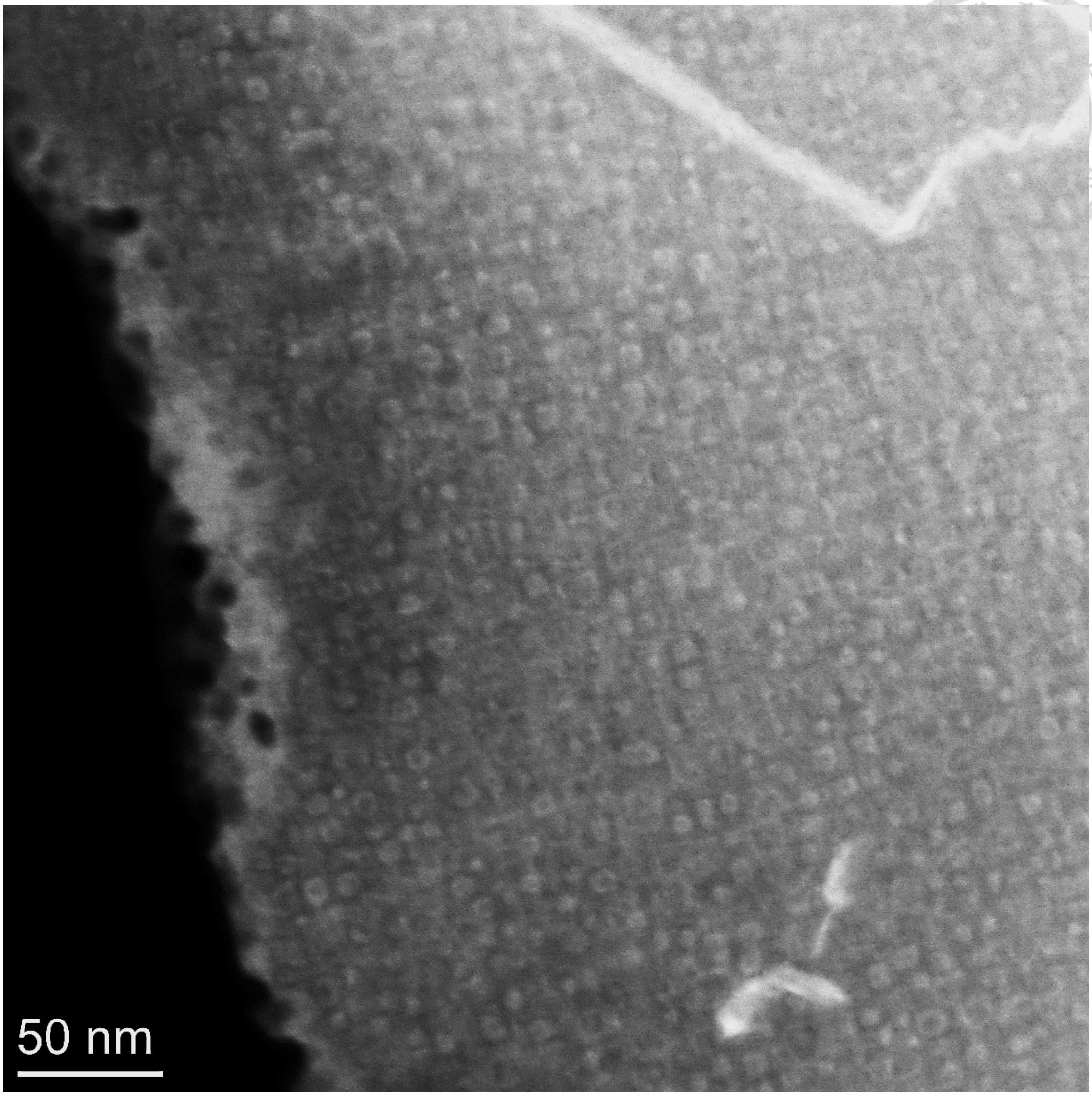

Figure 4-15 HAADF image of $(CrCoNi)_{94}Al_3Nb_3$ aging at 700°C for 16 hours.

doi:10.6342/NTU202302391

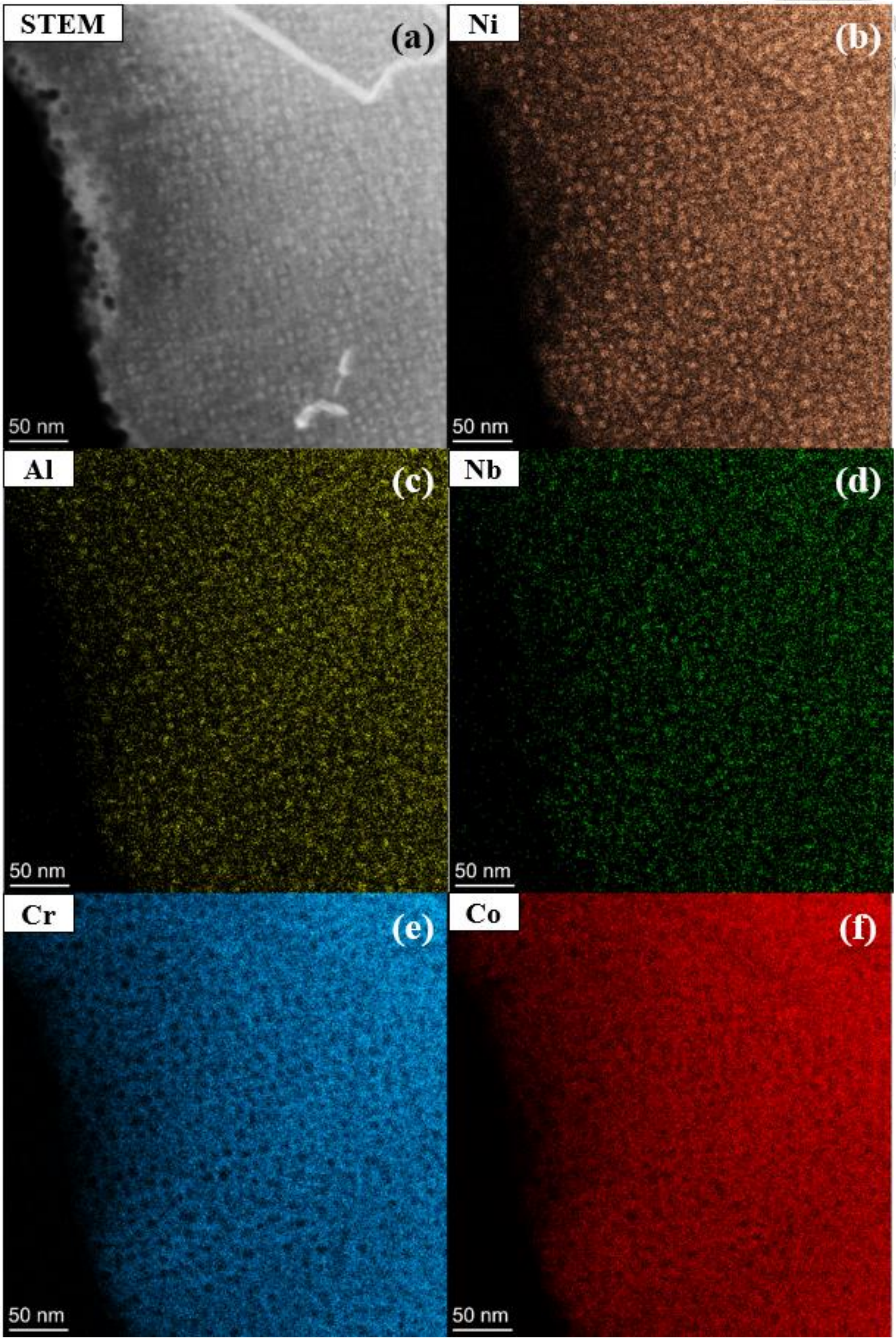

Figure 4-16 HAADF image and EDS mapping of $(CrCoNi)_{94}Al_3Nb_3$ aging at 700°C for 16 hours (a) STEM image (b) Ni (c) Al (d) Nb (e) Cr (f) Co.

doi:10.6342/NTU202302391

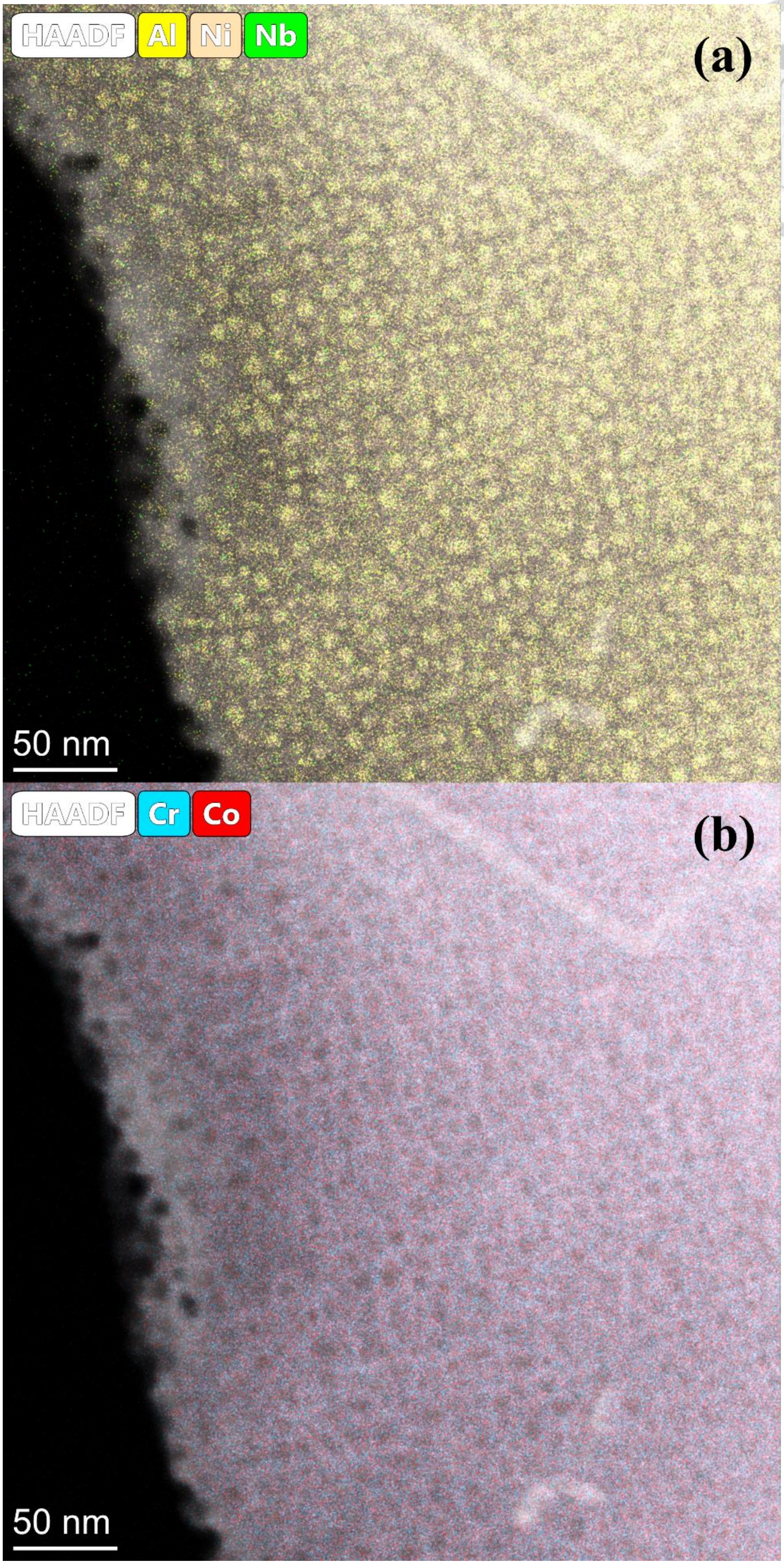

Figure 4-17 HADDF image and EDS mapping stacked diagram of $(CrCoNi)_{94}Al_3Nb_3$ aging at 700^{o}C for 16 hours (a) Ni, Al, and Nb (b) Cr and Co.

doi:10.6342/NTU202302391

Figure 4-18 and Figure 4-19 are the bright field and dark field images of $(CrCoNi)_{94}Al_3Nb_3$ aging at 700°C for 16 hours. These pictures were taken along [100] zone axis. In Figure 4-18, a cubic-on-cubic orientation relationship, $[100]_\gamma//[100]_{\mathrm{L12}}$ and $(100)_\gamma//(100)_{\mathrm{L12}}$ can be observed. The forbidden diffraction spots like 001 in disorder FCC shows up in Figure 4-18 because $L1_2$ precipitates are ordered FCC-based structure. Therefore, $L1_2$ precipitates contribute those forbidden spots like 001, 010, and 011.

In Figure 4-18, a lot of small black points uniformly distribute in the matrix. Based on the diffraction pattern, those black points are identified as $L1_2$ precipitates. In the dark field image (see Figure 4-19), $L1_2$ precipitates can be seen more easily. The dark field image was performed by objective aperture selecting 001 spot. Countless 5-10nm $L1_2$ precipitate distribute in the matrix. Furthermore, even near the grain boundary, the precipitates still keep the shape of globules rather than the abnormal growth in $(FeCrCoNi)_{94}Al_4Ti_2$ (see Figure 1-1) [9]. Figure 4-20 demonstrates the high-resolution TEM image under [100] zone axis. The yellow circles indicate the lattice fringes of $L1_2$ precipitates.

doi:10.6342/NTU202302391

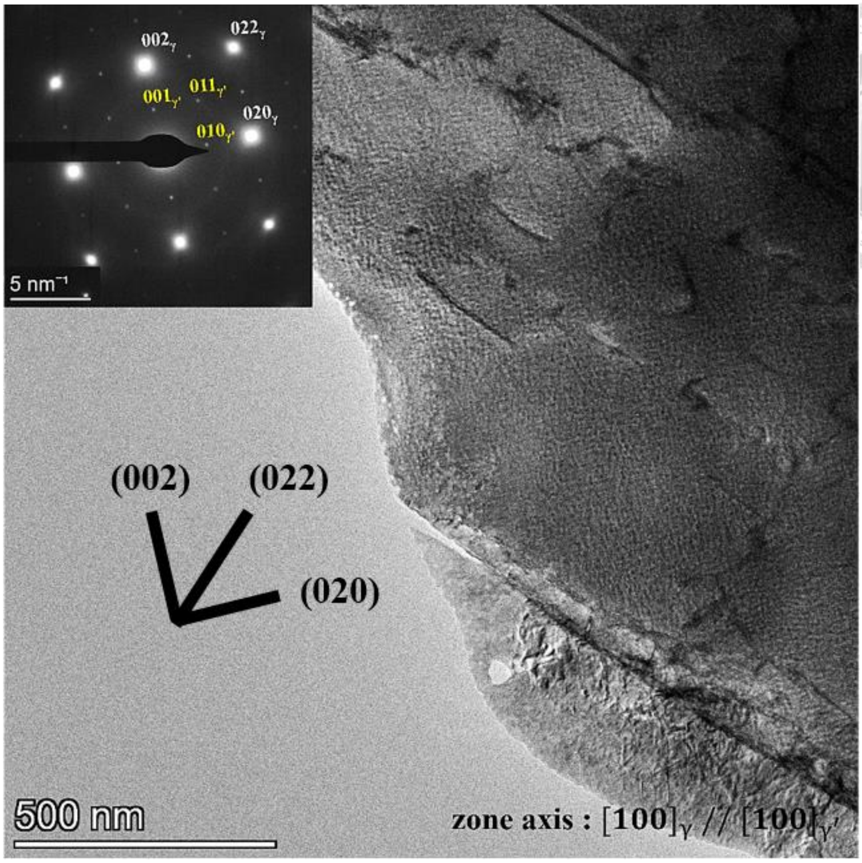

Figure 4-18 Bright field image of $(CrCoNi)_{94}Al_3Nb_3$ aging at 700ºC for 16 hours.

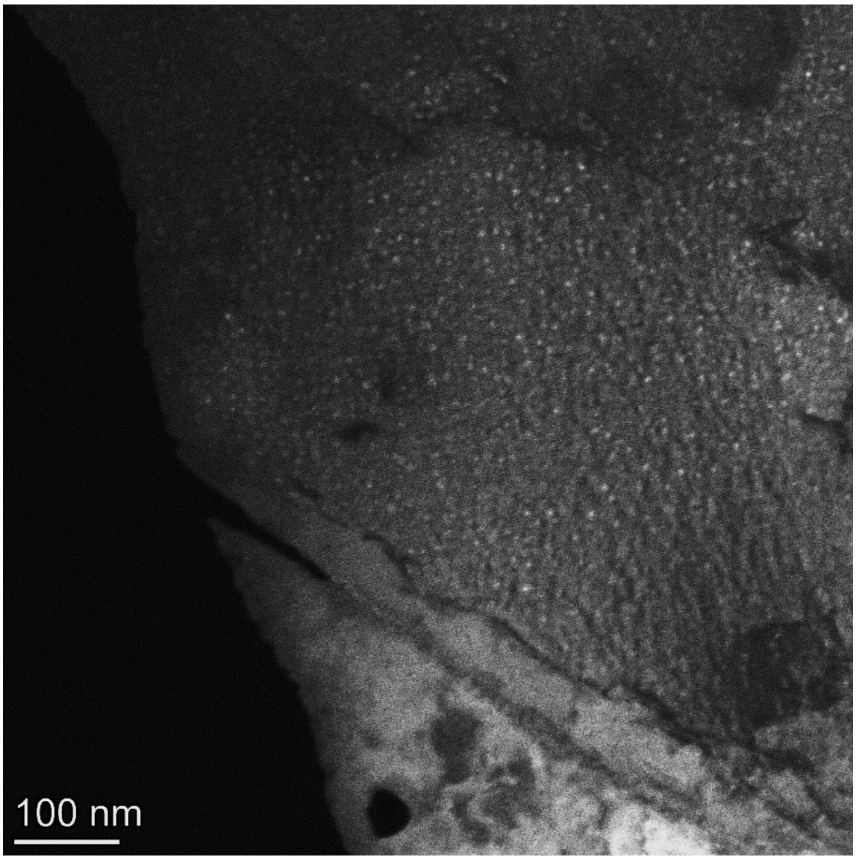

Figure 4-19 Dark field image of $(CrCoNi)_{94}Al_3Nb_3$ aging at 700ºC for 16 hours.

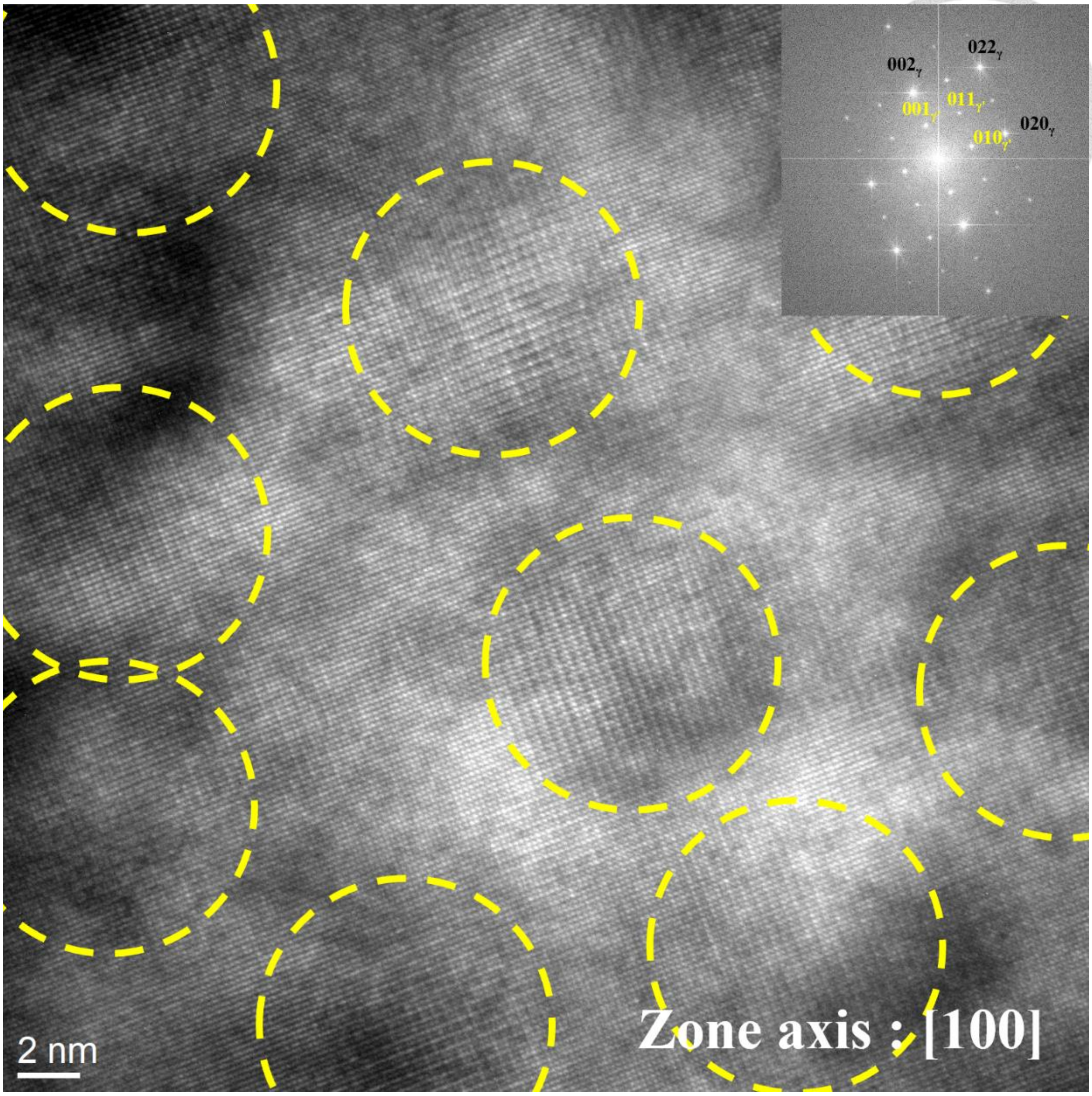

Figure 4-20 HRTEM image of $(CrCoNi)_{94}Al_3Nb_3$ aging at 700°C for 16 hours.

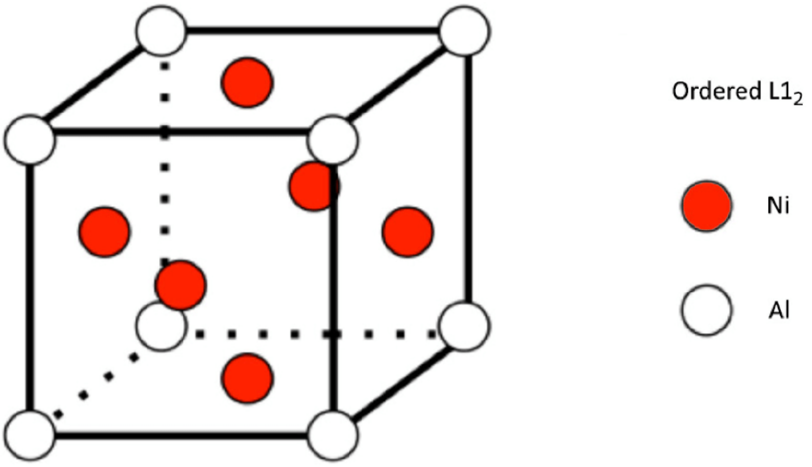

Figure 4-21 Crystal structure of $L1_2$ phase.

doi:10.6342/NTU202302391

Figure 4-22 demonstrates the representative morphology of $(CrCoNi)_{94}Al_3Nb_3$ aging at 800°C for 8 hours. Large cuboid $L1_2$ precipitates are around 50nm, and the globules $L1_2$ precipitates are around 20nm. The mixed morphology can be explained by precipitate growth mechanism, surface energy controlled and stain energy controlled. At the initial stage of precipitate nucleation, the surface energy between different atoms dominates the nucleation. Afterward, when the precipitates become larger, the lattice strain energy dominates the growth. That is to say, the lattice does not favor a large precipitate to distort the stable lattice. Therefore, the precipitates would keep at certain size because of lattice strain energy.

Figure 4-23 and Figure 4-24 are the high-resolution TEM image of $(CrCoNi)_{94}Al_3Nb_3$ aging at 800°C for 8 hours. Under [100] zone axis, clear boundaries of FCC matrix and $L1_2$ precipitates can easily be observed, and the $L1_2$ precipitate is around 20nm.

Figure 4-25 is the HADDF image and EDS mapping of $(CrCoNi)_{94}Al_3Nb_3$ aging at 800°C for 8 hours. It illustrates the same result as the case in 700°C. $L1_2$ particles are rich in Ni, Al, and Nb elements. On the other hand, the matrix is rich in Cr and Co element.

doi:10.6342/NTU202302391

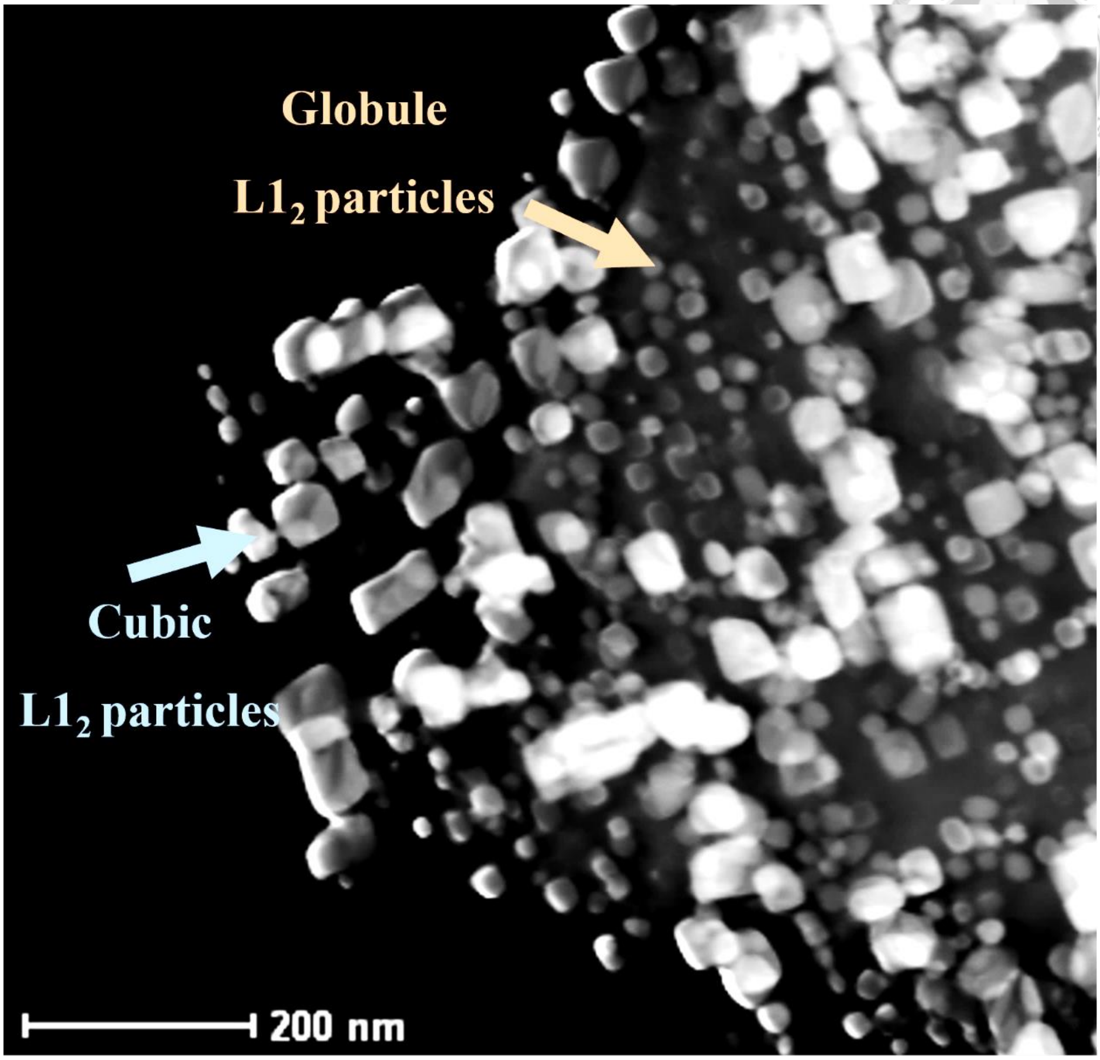

Figure 4-22 HADDF image of $(CrCoNi)_{94}Al_3Nb_3$ aging at 800°C for 8 hours.

doi:10.6342/NTU202302391

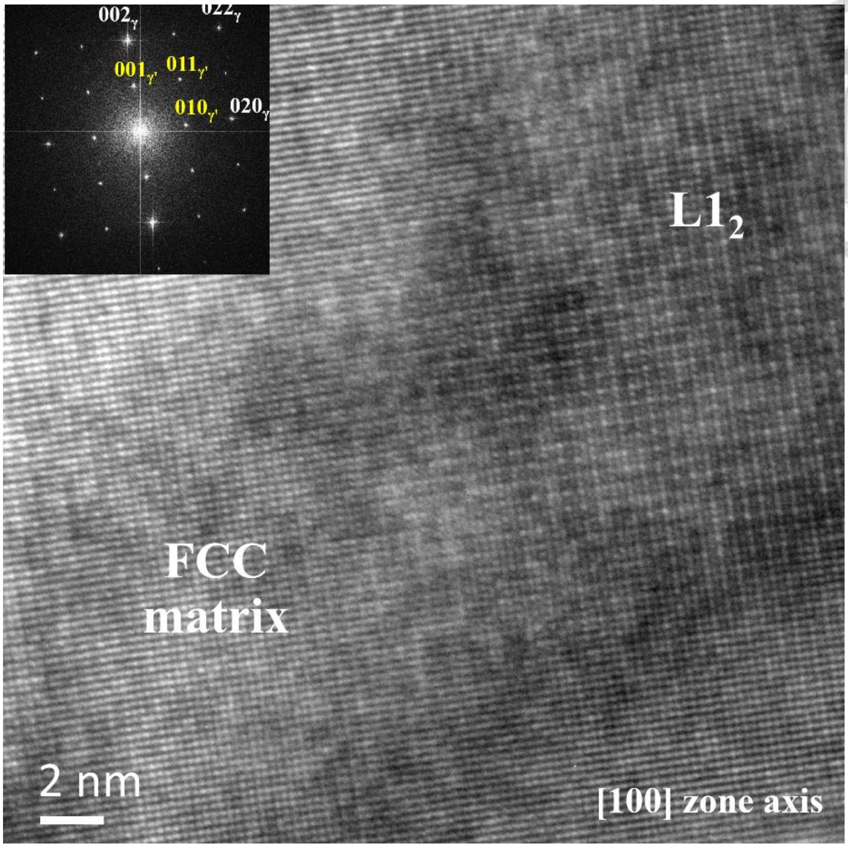

Figure 4-23 HRTEM image of $(CrCoNi)_{94}Al_3Nb_3$ aging at 800°C for 8 hours.

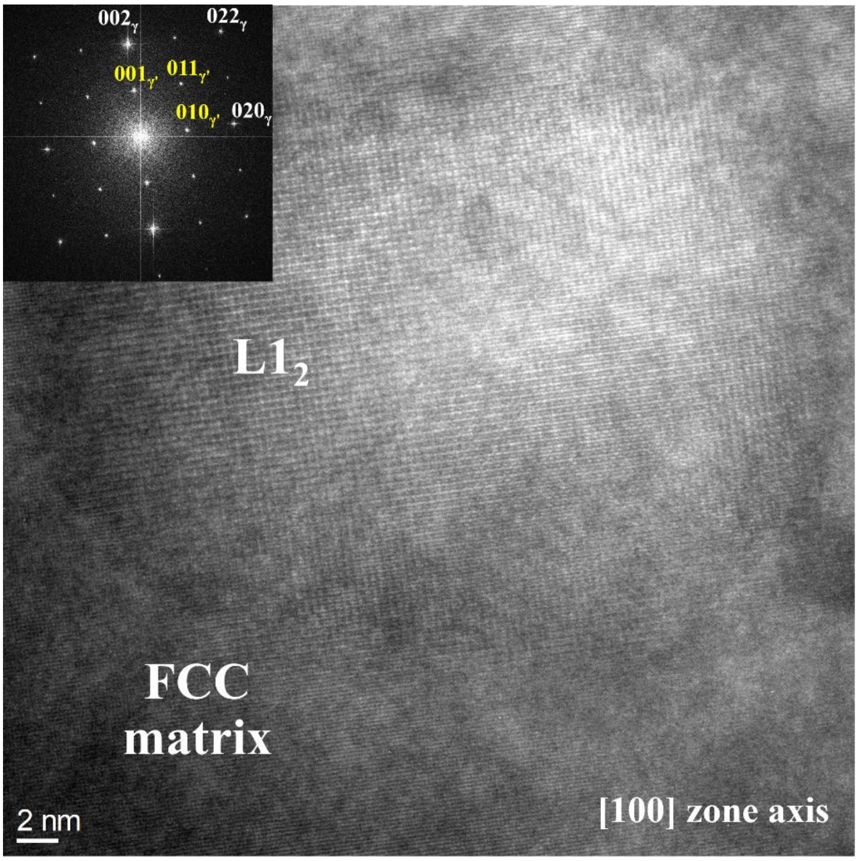

Figure 4-24 HRTEM image of $(CrCoNi)_{94}Al_3Nb_3$ aging at 800°C for 8 hours.

doi:10.6342/NTU202302391

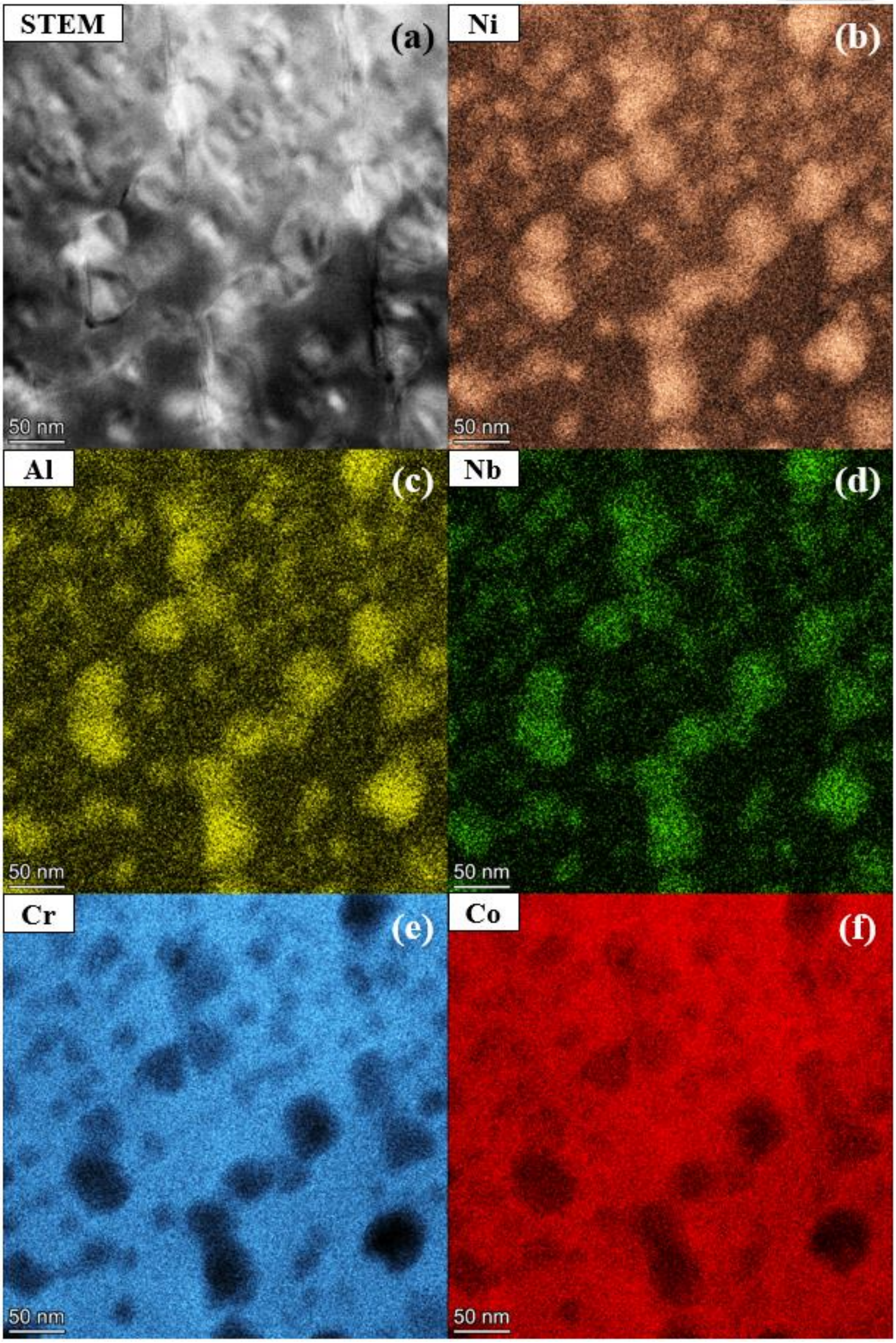

Figure 4-25 HADDF image and EDS mapping of $(CrCoNi)_{94}Al_3Nb_3$ aging at 800°C for 8 hours (a) STEM image (b) Ni (c) Al (d) Nb (e) Cr (f) Co.

doi:10.6342/NTU202302391

4.3.3 Incoherent precipitates analysis

There are two types of incoherent precipitates in $(CrCoNi)_{94}Al_3Nb_3$ during the heat treatment processes, σ phase and δ phase.

1. σ phase

Figure 4-26 is the bright field image of σ phase. σ phase has tetragonal crystal structure (see Supplementary Figure 2 and Supplementary Table 1). Therefore, the diffraction pattern along [011] zone axis could successfully identify σ phase. Besides, the stable state σ phase is rich in Cr and Co. By EDS point analysis, the σ phase has 56 at% Cr and 32% Co. The result is corresponded to the general concept of σ phase.

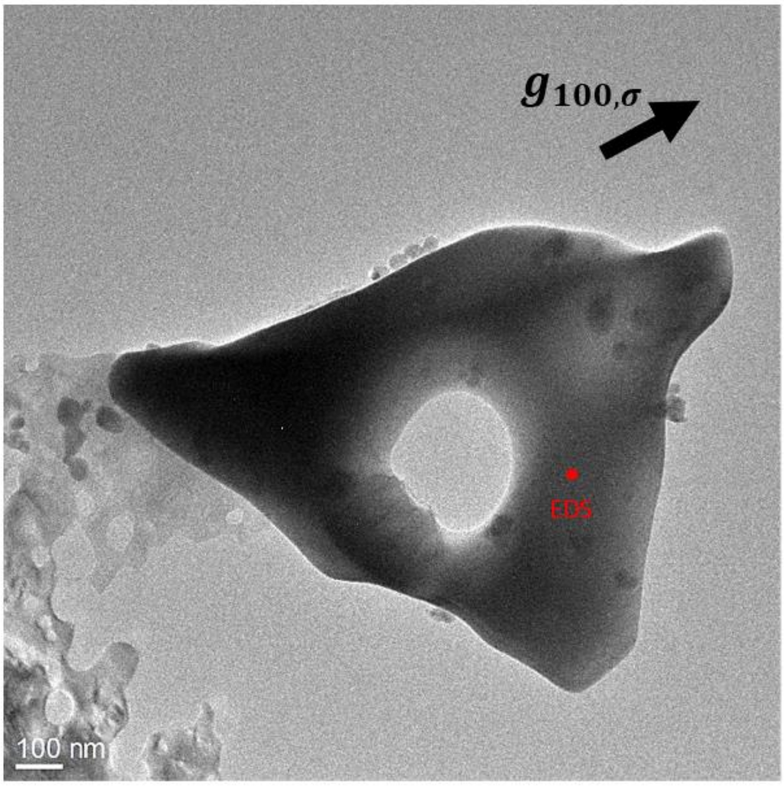

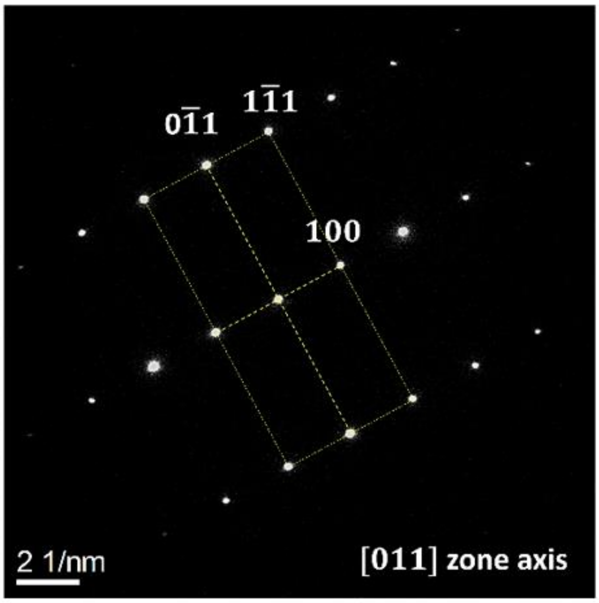

element	Al	Cr	Co	Ni	Nb
at%	0.46	55.77	31.88	10.37	1.53

Figure 4-26 σ phase in $(CrCoNi)_{94}Al_3Nb_3$ aging at 800°C for 8 hours.

doi:10.6342/NTU202302391

2. δ phase

δ phase is very common in Nb-contained superalloys like Inconel 718. Its stoichiometric chemical formula is Ni_3Nb. Supplementary Table 2 is the details of crystal structure of δ phase. δ phase has needle-like morphology, and it has $[011]_\gamma//[100]_\delta$ and $(111)_\gamma//(010)_\delta$ orientation relationship with FCC matrix (see Figure 4-27).

Figure 4-32 is the HADDF image and EDS mapping result at grain boundaries. δ phase is favorable of forming at grain boundaries. Besides, while Ni and Nb elements are drained by δ phase. The Cr and Co elements would tend to become rich in certain areas. Therefore, σ phase tends to form in those Cr-rich and Co-rich areas.

When defects were induced into the material by hot rolling, those nanotwins can be preserved during post annealing because δ phase would come out during recrystallization at twin boundaries (see Figure 4-28, Figure 4-29, and Figure 4-30). Note that these figures are taken without tensile tests. Figure 4-28 is the edge-on condition of δ phase thickness. The thickness approximately 2nm is too small to observe. Thus, none-edge-on condition can provide clear images to identify δ phase. Figure 4-29 suggests that δ phase would not only form at coherent twin boundaries but also incoherent twin boundaries.

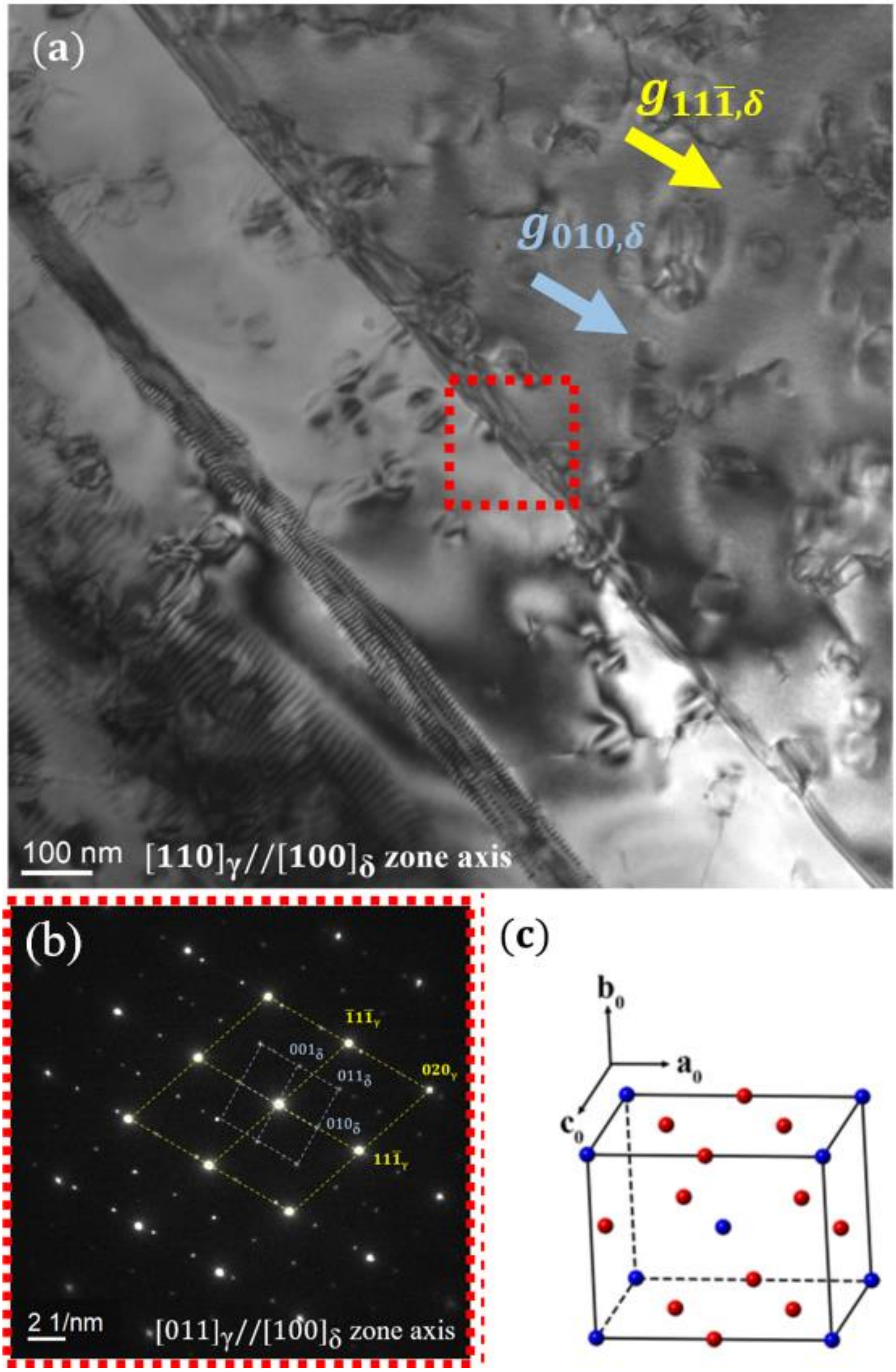

Figure 4-27 δ phase in $(CrCoNi)_{94}Al_3Nb_3$ aging at 800°C for 240 hours (a) TEM bright-field image (b) diffraction pattern (c) delta crystal structure.

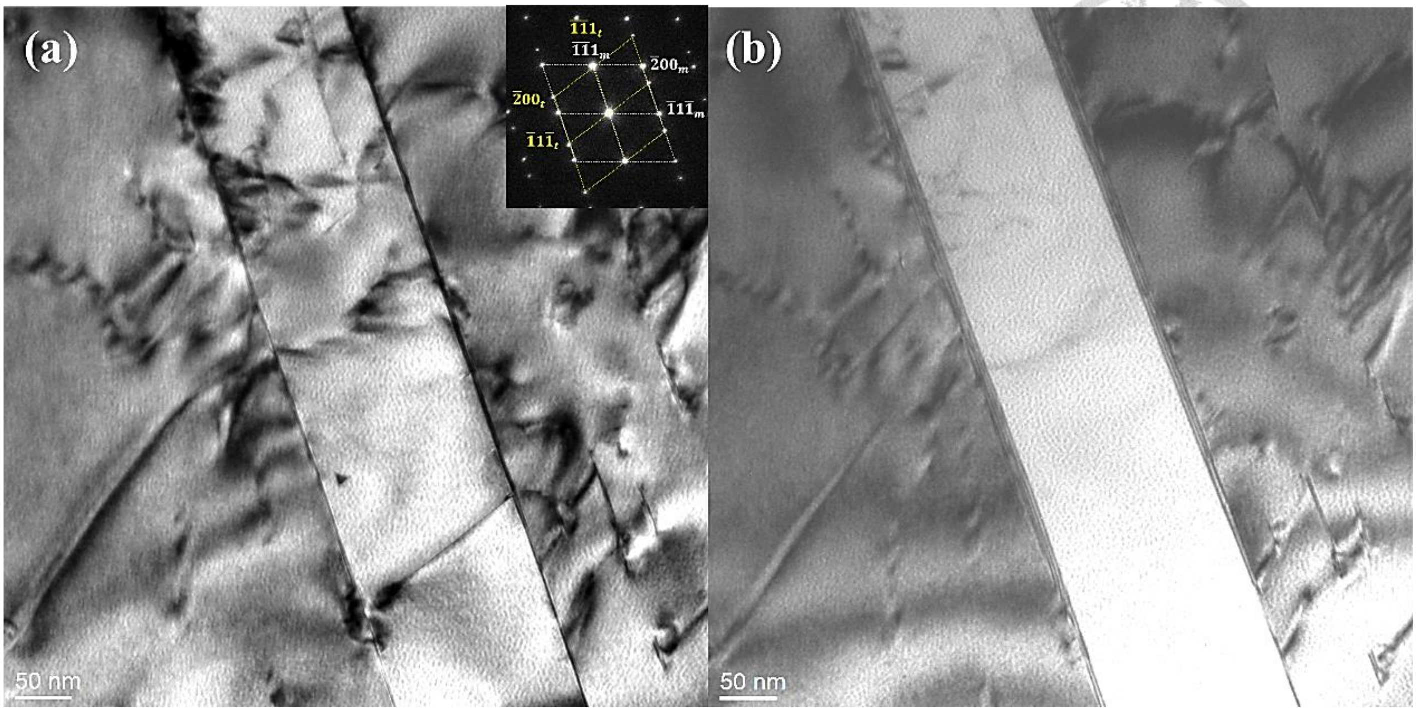

Figure 4-28 TEM image of $(CrCoNi)_{94}Al_3Nb_3$ recrystallization at 900°C for 1 hour (a) [011] edge-on condition (b) none edge-on condition.

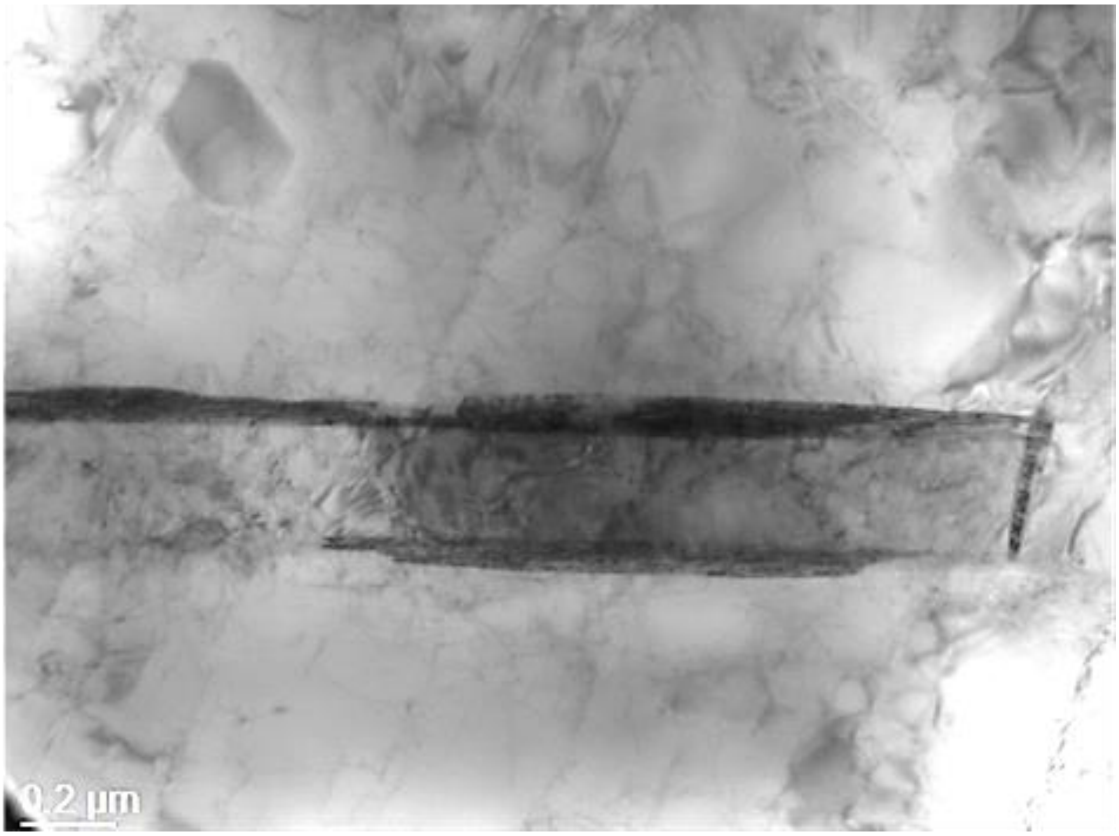

Figure 4-29 TEM image of $(CrCoNi)_{94}Al_3Nb_3$ recrystallization at 900°C for 1 hour with δ in coherent twin boundaries and incoherent twin boundaries.

Figure 4-30 TEM image of $(CrCoNi)_{94}Al_3Nb_3$ recrystallization at 900°C for 1 hour before δ connecting to each other.

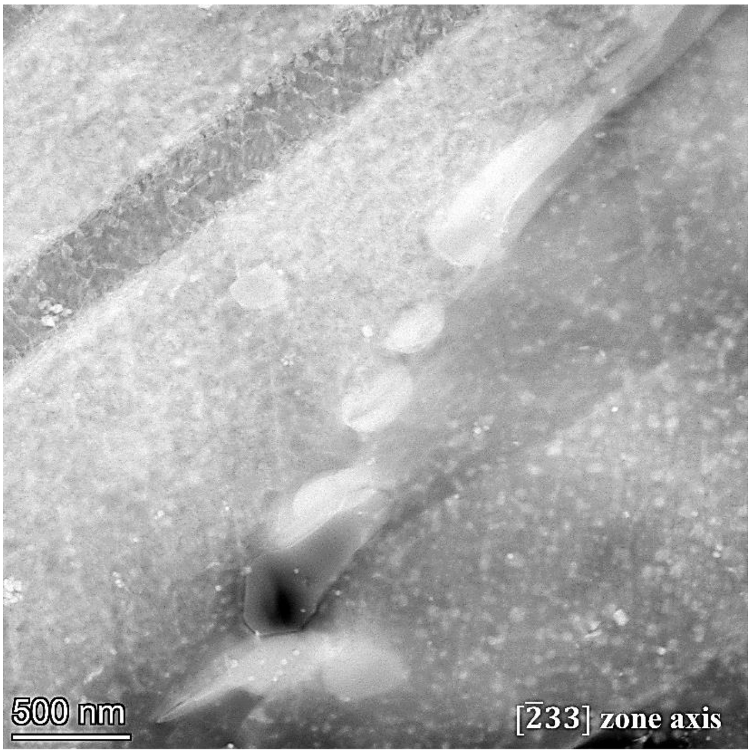

Figure 4-31 δ phase and σ phase in $(CrCoNi)_{94}Al_3Nb_3$ aging at 800°C for 8 hours.

doi:10.6342/NTU202302391

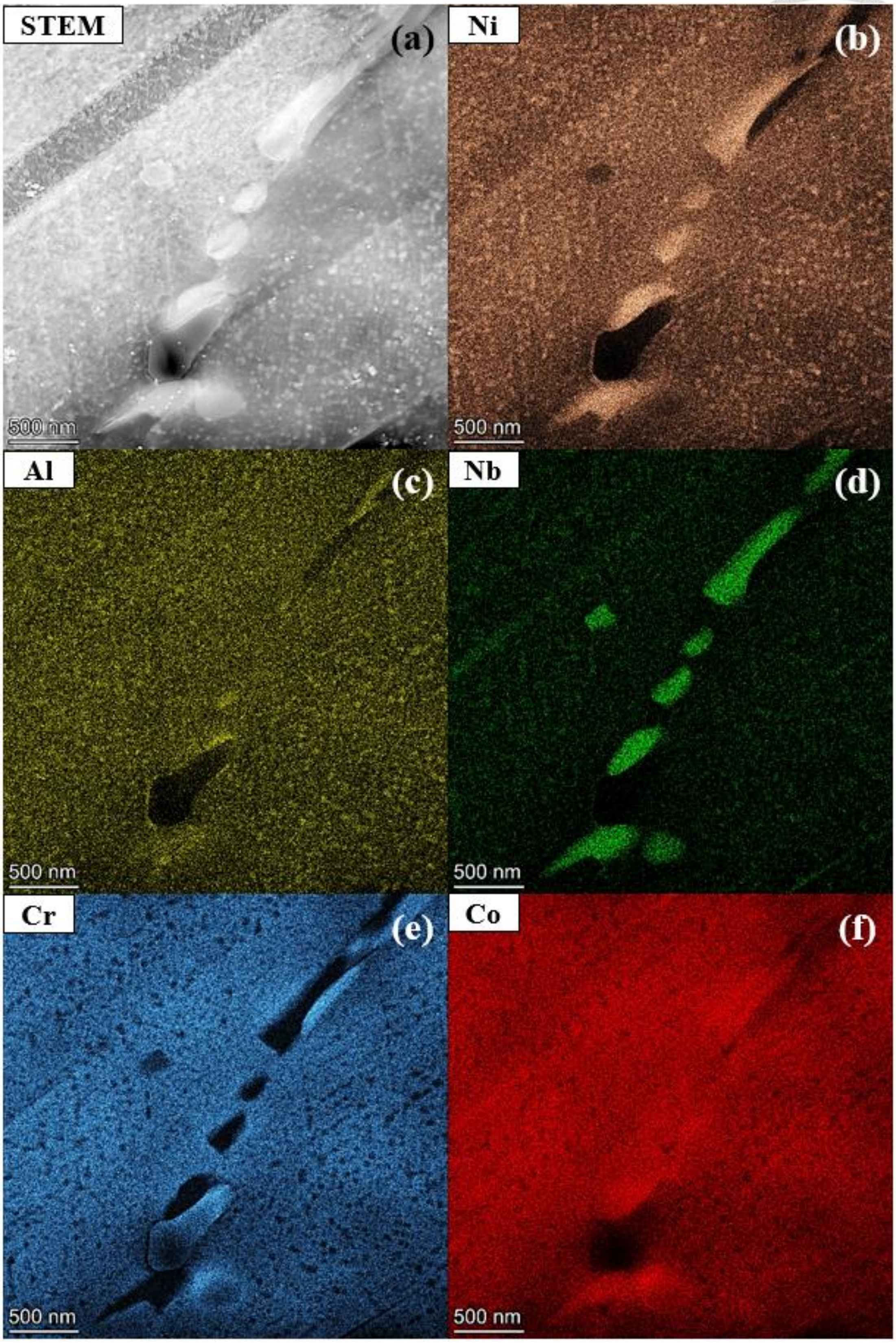

Figure 4-32 HADDF image and EDS mapping of δ phase and σ phase in $(CrCoNi)_{94}Al_3Nb_3$ aging at 800°C for 8 hours (a) STEM image (b) Ni (c) Al (d) Nb (e) Cr (f) Co.

doi:10.6342/NTU202302391

4.3.4 Thermo-calc simulation

This experiment performed Thermo-calc simulation with single point equilibrium and single axis equilibrium. Figure 4-33 is the amount of phase in different temperature. Take some temperatures that were used in this experiment to examine the results of Thermo-calc.

For example, the material is homogenized at 1100°C for 72 hours. The treatment can be recognized as steady-state because the treatment time is so long, and Thermo-calc only simulate the steady-state situation. The simulation described that there are approximately 5% Laves phase in 1100°C, and the rest of 95% is FCC matrix. This result is corresponded to the EBSD phase map (Figure 4-12). Take 700°C as another example, Thermo-calc indicates that $L1_2$, δ and σ would generate under 700°C. Based on TEM analysis of aging at 700°C for 16 hours, the amount of $L1_2$ phase is much more than δ and σ. To elaborate, δ and σ can hardly be found in TEM because aging for 16 hours is still too short to eliminate the influence of kinetics. Once the aging period extend for thousands of hours, the exact number of phases could finally be referred in Figure 4-33. Besides, Figure 4-34 and Figure 4-35 describe the aluminum and niobium contents in specific phases respectively.

doi:10.6342/NTU202302391

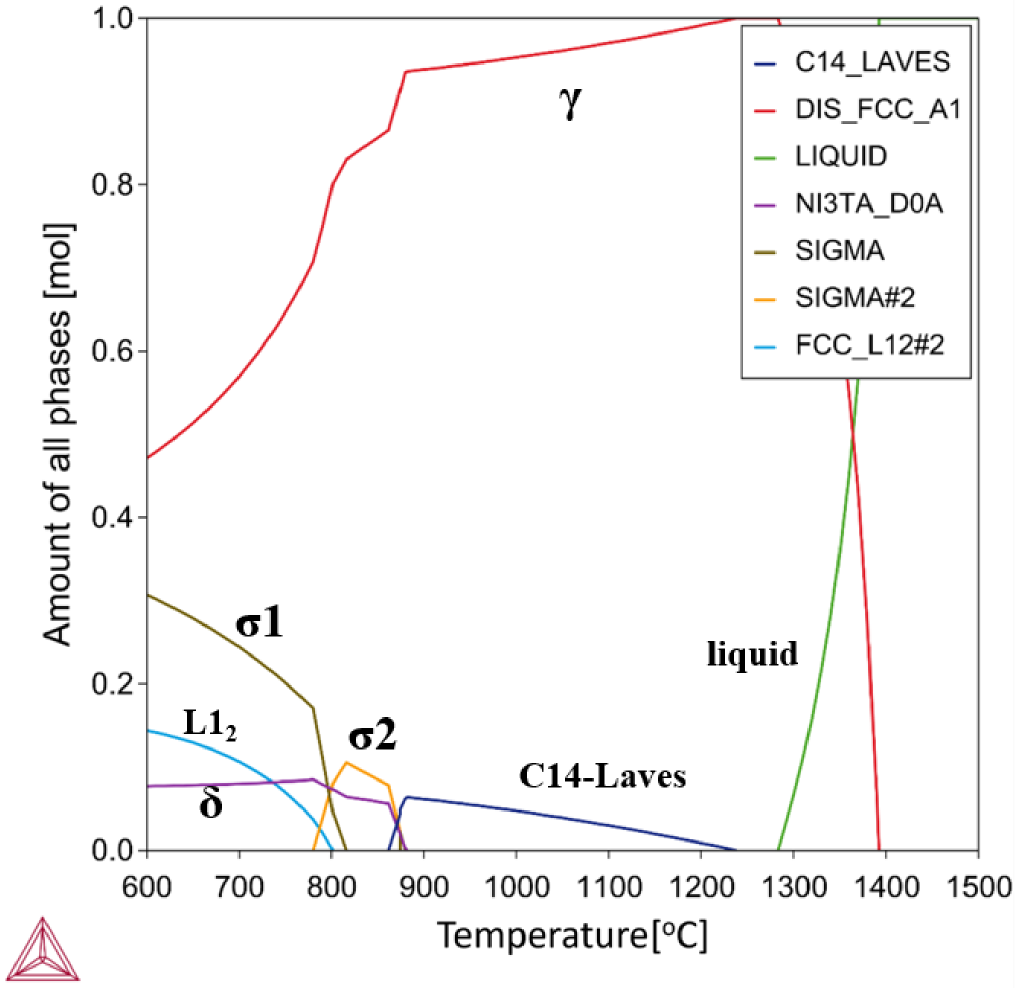

Figure 4-33 Thermo-calc single axis equilibrium simulation.

doi:10.6342/NTU202302391

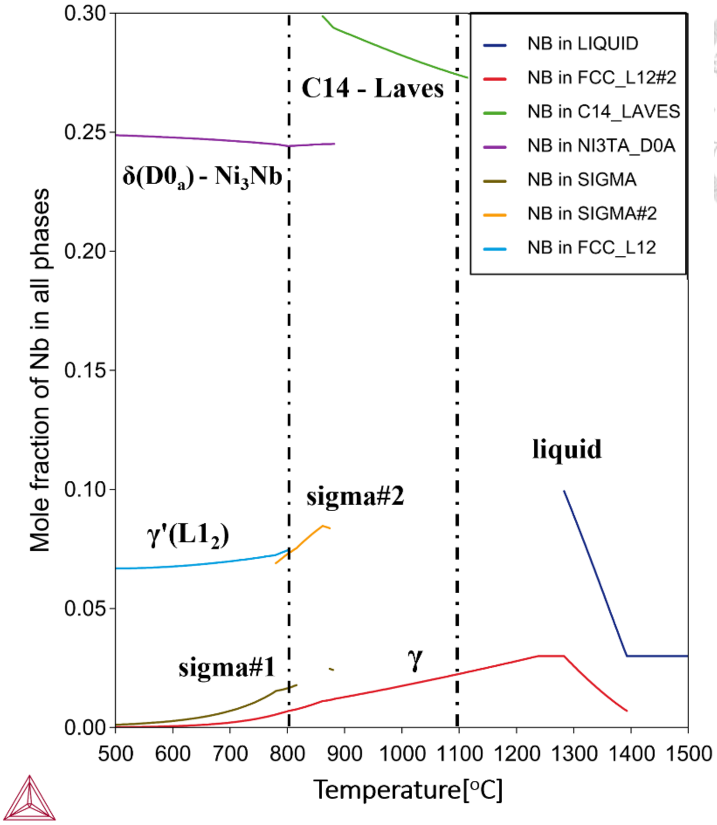

Figure 4-34 Thermo-calc single point equilibrium simulation for niobium.

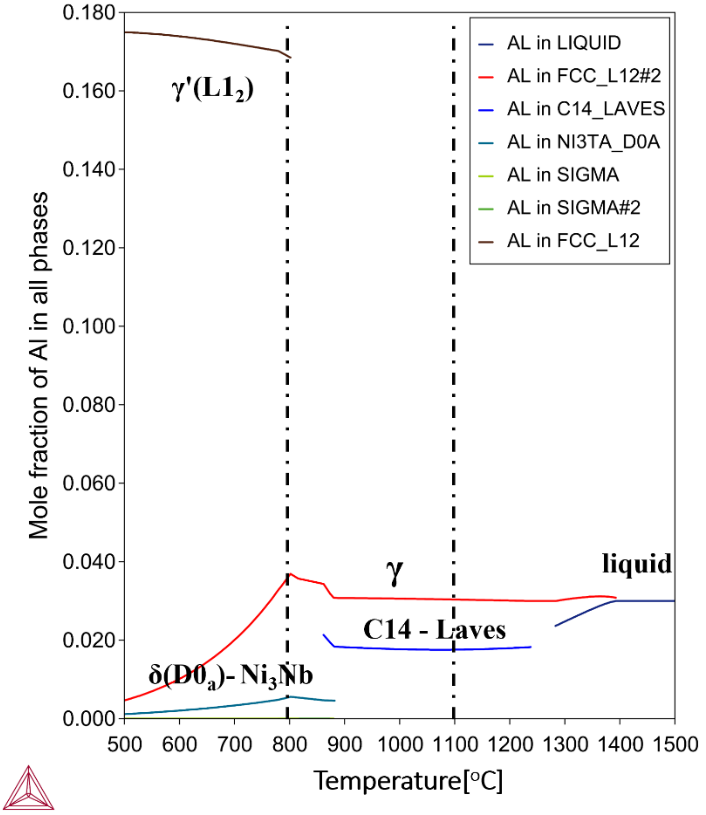

Figure 4-35 Thermo-calc single point equilibrium simulation for aluminum.

4.3.5 Delta phase transformation

Figure 4-36 is the schematic diagram of δ phase and microstructure evolution at different heat treatment stages. In the beginning, Figure 4-36a demonstrates the homogenization microstructure of $(CrCoNi)_{94}Al_3Nb_3$ There was no dislocation or stacking-fault in grains, and a little Laves phase was observed in grain boundaries. After hot-rolling at 1100^oC with 70% thickness reduction, grain refinement was performed shown as Figure 4-36b. Defects were induced into the material through the forms of dislocations and stacking-faults. In Figure 4-36c, defects were eliminated through recrystallization at 900^oC for 1 hour. In addition, δ phase preferential precipitated at twin boundaries. Figure 4-36d showed that the nano scale $L1_2$ precipitates uniformly distribute in grains in the early-stage of aging. At peak aging, Figure 4-36e, new δ phase started to nucleate at the edges of $L1_2$ precipitates with a $[\bar{2}33]_\gamma//[111]_{L12}$ orientation relationship. Figure 4-37 is the STEM and diffraction pattern taken from the sample aging at 800^oC for 8 hours (peak aging condition at 800^oC). There is a clear $[\bar{2}33]_\gamma//[111]_{L12}$, $(01\bar{1})_\gamma//(01\bar{1})_{L12}$ orientation relationship in the diffraction pattern. Figure 4-36f demonstrates the overaging microstructure of $(CrCoNi)_{94}Al_3Nb_3$. $L1_2$ particles would grow bigger to a cubic morphology under [100] zone axis. Furthermore, the δ phase nucleated at the edges of $L1_2$ particles would grow longer through the diagonals of cubic $L1_2$ particles under [100] zone axis. Figure 4-38 and

Figure 4-39 are the STEM images taken under [100] zone axis since there is a cubic-on-cubic orientation relationship between the matrix and $L1_2$ particles. There are a lot of δ phase grow along the diagonal of cubic $L1_2$ particles. In the end, Figure 4-36g is the microstructure of severe over-aging. δ phase completed the growth, and $L1_2$ particles also completed coarsening to cubic morphology. Figure 4-27 is the TEM image taken in the sample aging at 800°C for 240 hours. The matrix and δ phase have the $[011]_\gamma//[100]_\delta$ orientation relationship. The δ phase has almost 20-30nm in width under [011] zone axis observation.

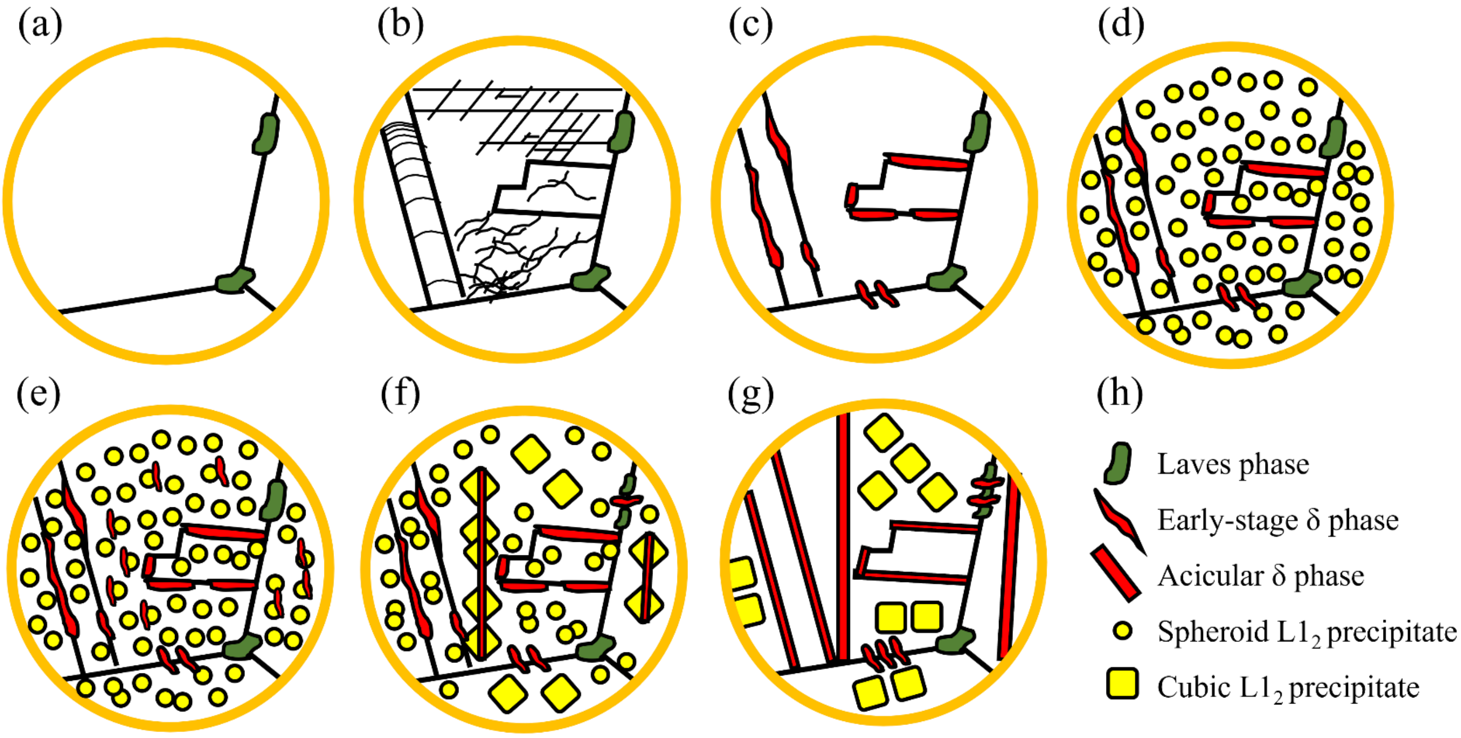

Figure 4-36 Schematic diagram of δ phase and microstructure evolution in $(CrCoNi)_{94}Al_3Nb_3$ at different heat treatment stages (a) homogenization at 1100°C for 72 hours (b) hot-rolling at 1100°C with 70% thickness reduction (c) recrystallization at 900°C for 1 hour (d) aging before peak aging (e) aging at peak aging (f) overaging (g) overaging much longer than peak aging (h) symbol descriptions.

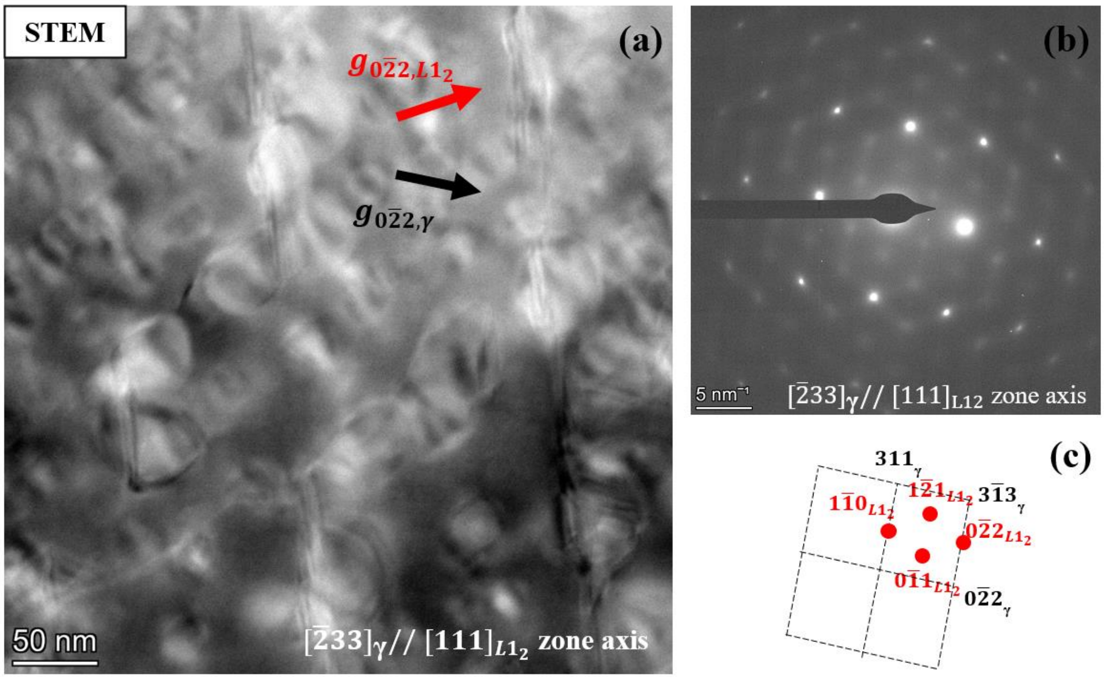

Figure 4-37 HADDF image and diffraction pattern of $(CrCoNi)_{94}Al_3Nb_3$ aging at 800°C for 8 hours (a) STEM image.

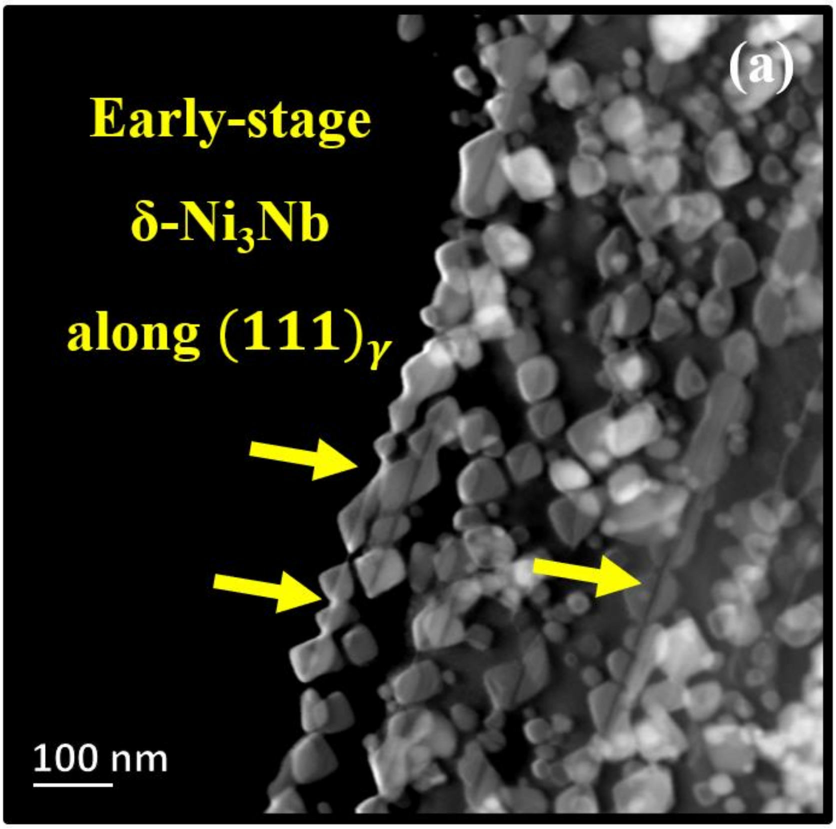

Figure 4-38 HADDF image of $(CrCoNi)_{94}Al_3Nb_3$ aging at 800°C for 8 hours along [110] direction.

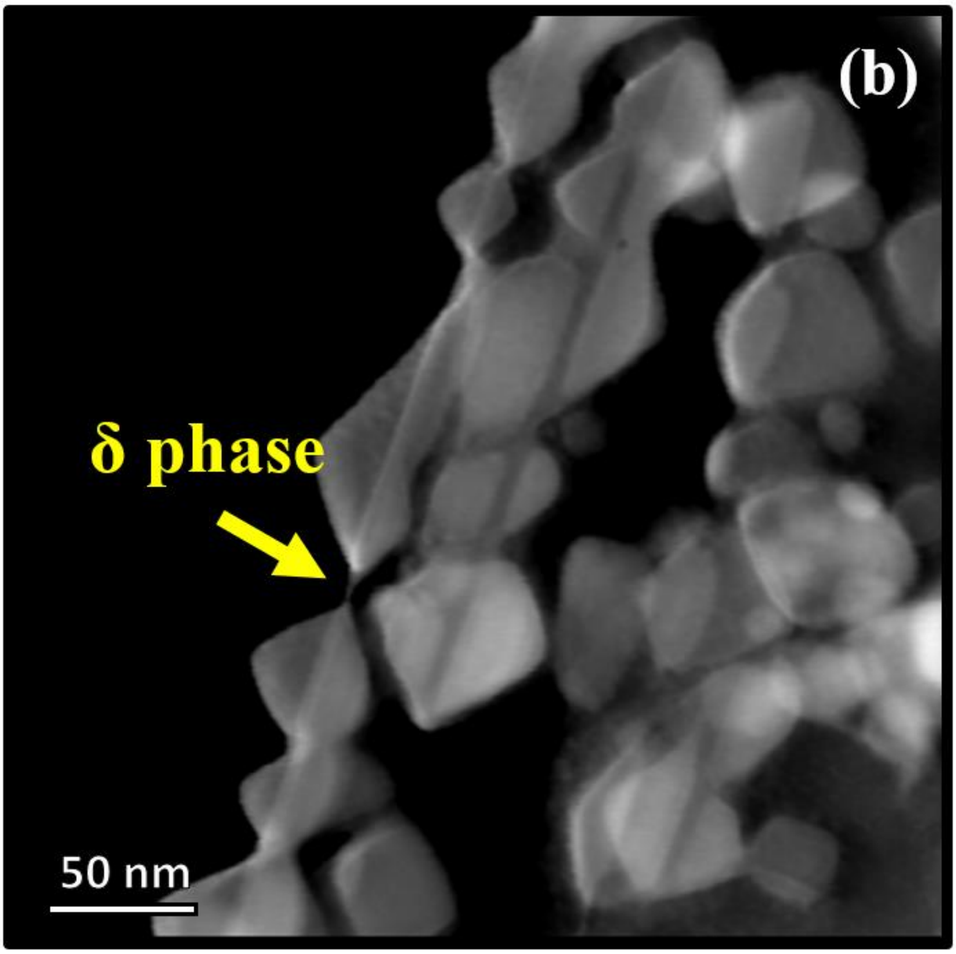

Figure 4-39 HADDF image of $(CrCoNi)_{94}Al_3Nb_3$ aging at 800ºC for 8 hours along [110] direction.

doi:10.6342/NTU202302391

4.4 Mechanical properties

4.4.1 Tensile test

Figure 4-40 is the results of tensile tests under $0.001s^{-1}$ strain rate. The yield strength and ultimate tensile strength of none-aged sample (recrystallization, 900ºC / 1 h) are 1127 ± 20 MPa and 1333 ± 17 MPa respectively. As for the aging sample (aging, 700ºC / 16h), The yield strength and ultimate tensile strength of none-aged sample (recrystallization, 900ºC / 1 h) are 1412 ± 22 MPa and 1553 ± 45 MPa respectively. The yield strength and ultimate tensile strength increase approximately 300MPa and 200MPa. The results demonstrate that aging treatment plays an important role in enhancing strength. The elongation of none-aged sample and aging sample are 12.4 ± 0.25 and 7.8 ± 0.94 respectively. Laves and sigma phases cause the material to become brittle. Dislocations would aggregate at the boundaries and bring about stress concentration. Finally, cracks start to initiate from the boundaries. However, the yield strength and ultimate tensile strength are outstanding. The elongation performances are acceptable with such high-strength performances.

Figure 4-41 is the true stress-strain curves and work-hardening rate of $(CrCoNi)_{94}Al_3Nb_3$. The work-hardening rate can be classified as three segments. Work-hardening rate prior to 0.03 strain can be called as the elastic region. The second region

doi:10.6342/NTU202302391

is located at 0.03 to 0.10 strain. The work-hardening rates do not decrease rapidly in the region. The results suggest that twinning and stacking-faults might have become the deformed mechanism in the material. As for the last part, after 0.10 strain, this part is called as necking region. Materials start to necking and would not become work-hardening anymore.

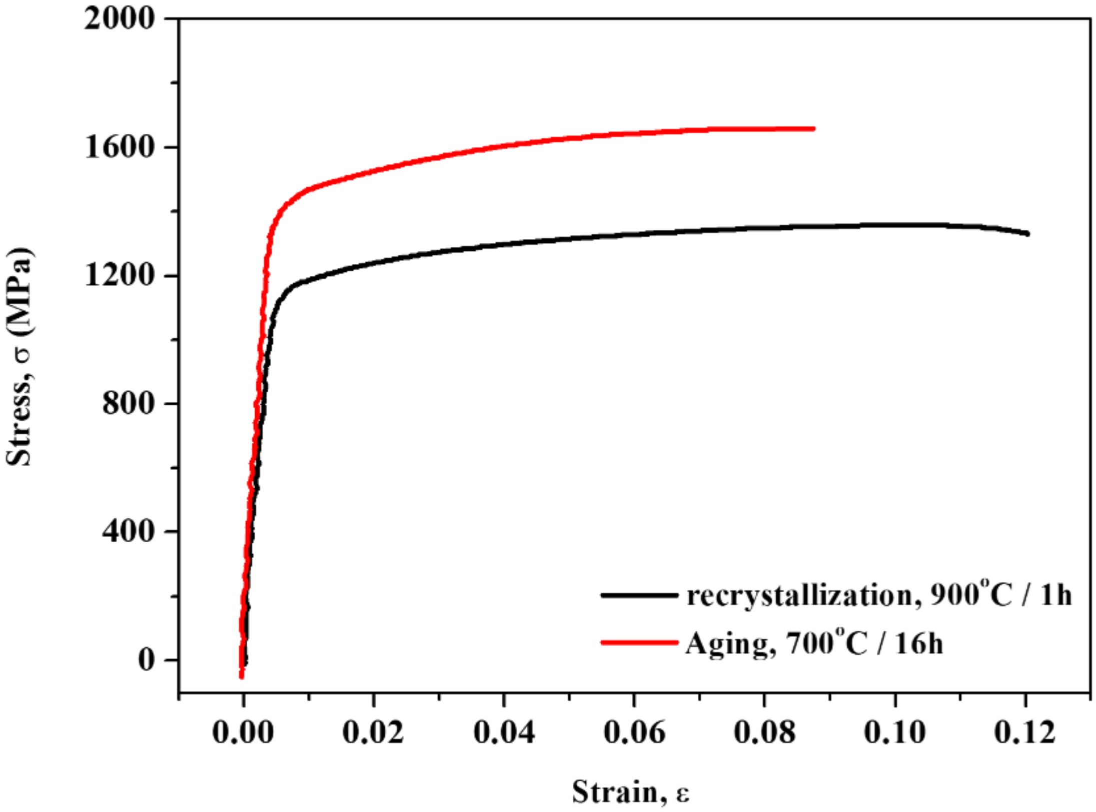

Figure 4-40 Engineering stress-strain curves of $(CrCoNi)_{94}Al_3Nb_3$ tensile tests.

doi:10.6342/NTU202302391

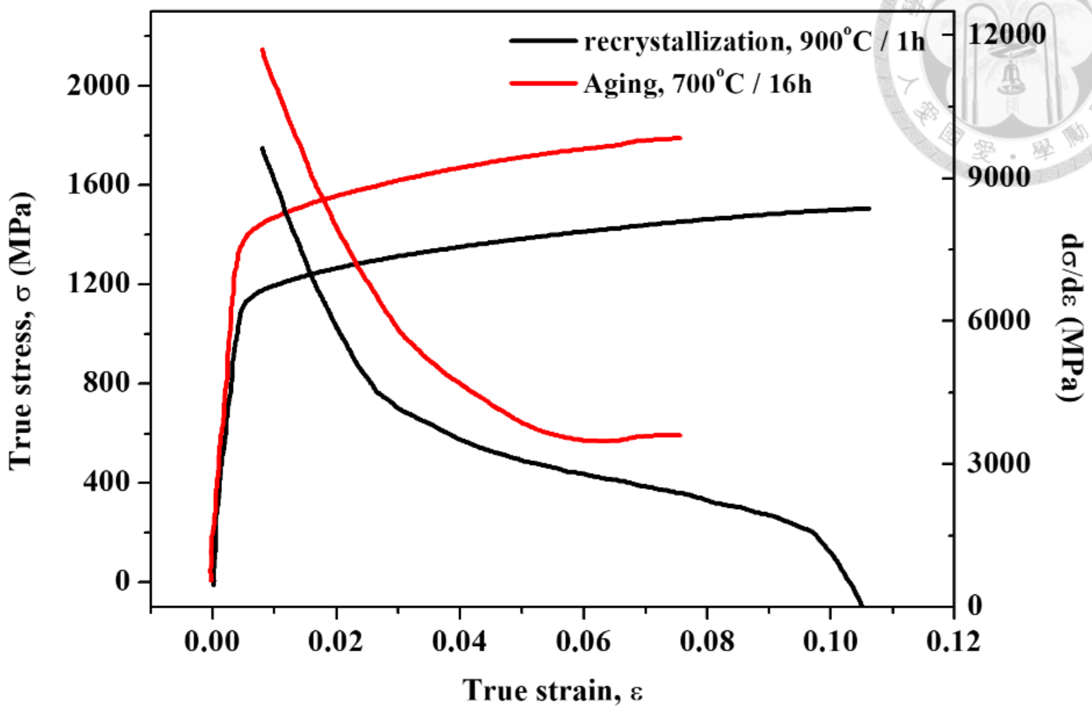

Figure 4-41 True stress-strain curves and work-hardening of $(CrCoNi)_{94}Al_3Nb_3$ tensile tests.

Table 4-2 mechanical properties comparison of $(CrCoNi)_{94}Al_3Nb_3$, $CrCoNiSi_{0.3}$, $(CrCoNi)_{94}Al_4Ti_2$, and Inconel 718.

	Recrystallization 900°C / 1h	**Aging 700°C / 16h**	**$CrCoNiSi_{0.3}$ Cold-rolled 50% 900°C / 1h**	**$(FeCrCoNi)_{94}Al_4Ti_2$ Cold-rolled 70% 650°C / 4 h** [9]
Yield strength(MPa)	**1127 ± 20**	**1412 ±22**	**650**	**1005**
Ultimate tensile strength(MPa)	**1333 ± 17**	**1553 ±45**	**1013**	**1273**
Elongation(%)	**12.4 ±0.25**	**7.8 ± 0. 94**	**17%**	**17**

4.4.2 Tensile test microstructure characterization

Figure 4-42 presents the deformed microstructure of samples aging at 700°C for 16 h subjected to 8% strain. Figure 4-42a and b correspond to deformed regions with relatively mild and severe deformation, respectively. In Figure 4-42a, only the FCC matrix and $L1_2$-$Ni_3(Al,Nb)$ precipitates are observed. During the deformation, the defects are hindered by the presence of $L1_2$ precipitates, providing exceptional strength to this MEA. The MEA possesses a lower stacking-fault energy and exhibits a higher yield strength. As a result, at the onset of deformation, the yield strength already exceeds the critical twinning stress. Consequently, the primary defects are deformation twins and stacking-faults, rather than dislocation motion. Therefore, in Figure 4-42a, a mixed microstructure of deformation twins and stacking-faults can be observed. Within the same 8% strain deformation, Figure 4-42b reveals deformation twins and stacking-faults involving two variants rather than one variant in Figure 4-42a. Under [011] zone axis observation, the two variants are separated by an angle of 70.52° because the slip planes are $\{111\}$. The stacking-faults will undergo $\frac{1}{6} < 11\bar{2} >$ displacements on $\{111\}$. In this region, the FCC matrix and $L1_2$ precipitates are segmented into multiple blocks, and these blocks would further be segmented into finer sub-blocks while experiencing severe deformations.

Both Figure 4-42a and b experience the same 8% strain. However, the microstructural observation indicates that Figure 4-42b undergoes more severe deformation. The result is attributed to the presence of δ-Ni_3Nb precipitates at the nano-annealing twin boundaries, hindering the development of defects. Though δ-Ni_3Nb effectively enhances the strength of the MEA, it also leads to a loss of ductility.

Figure 4-42c to f illustrate the interaction between $L1_2$ precipitates and defects, as well as the deformation microstructure of the surrounding matrix, observed along the [011] zone axis. In Figure 4-42c, clear evidence of shear deformation in $L1_2$ particles can be observed. $L1_2$ particles possess an ordered structure, and the presence of stacking faults within the $L1_2$ phase would lead to antiphase boundaries. Therefore, stacking-faults are not commonly observed in $L1_2$ phase because of the instability. However, numerous stacking faults and deformation twins are observed in the FCC matrix. Figure 4-42d and e present magnified views of the green dashed square and blue dashed square in Figure 4-42c, respectively. Multiple stacking faults and deformation twins are found that do not align along the same (111) plane. In Figure 4-42e, complex interactions between stacking-faults and deformation twins are found at the neighboring (111) planes. Typically, stacking faults or deformation twins would be confined within the same (111) while suffering from shear deformation. As a result, the presence of structures that do not align along the same (111) plane indicates that $L1_2$ particles effectively hinder the development of defects, resulting in a more complex microstructure in the FCC matrix. However, when deformation becomes more severe and $L1_2$ particles can no longer impede defect development, Figure 4-42f demonstrates the $L1_2$ particle that have undergone shear deformation twice.

$$\sigma_{0.2} = \sigma_A + \Delta\sigma_S + \Delta\sigma_G + \Delta\sigma_D + \Delta\sigma_P \qquad \text{Eq. 4-1}$$

In comparison to $(FeCrCoNi)_{94}Al_4Ti_2$ [9], the yield strength of $(CrCoNi)_{94}Al_3Nb_3$ is approximately 400 MPa higher than the yield strength of $(FeCrCoNi)_{94}Al_4Ti_2$. Therefore, the following discussion will focus on the factors contributing to the yield strength. The evaluation of yield strength can be referenced from section 2.5.4 (see Eq. 4-1). The yield strength can be decomposed into several contributing factors, including lattice friction (P-N stress), solid solution strengthening, grain boundary strengthening, dislocation density, and precipitates hardening.

Lattice friction is an intrinsic material property and does not play a critical role in enhancing yield strength unless there is a significant change in the composition. For instance, replacing the FCC base of medium-entropy alloy with a BCC base would not have a significant impact on the yield strength. In the case of $(FeCrCoNi)_{94}Al_4Ti_2$ [9], solid solution strengthening only contributes a few tens of MPa. It is difficult to achieve the required 400 MPa increase solely through solid solution strengthening. Although larger atoms like Nb can contribute slightly to the yield strength through solid solution strengthening, they may not be the main reason for the increase of about 400 MPa. For

doi:10.6342/NTU202302391

dislocation strengthening, although the study did not directly measure dislocation density, the samples were annealed at 900°C for one hour before precipitation hardening to eliminate residual defects and ensured complete recrystallization through EBSD analysis, thereby ruling out the contribution of dislocation strengthening.

Ultimately, in this work, the most effective factors in enhancing the yield strength are believed to be precipitation hardening and grain refinement. Observed through TEM and STEM images, a significant volume fraction of nanoscale $L1_2$-Ni_3(Al,Nb) within the FCC matrix was achieved. The [100] zone axis HRTEM observation indicates that the distance between precipitates is less than 5 nm in 2D-observation, demonstrating a uniform nucleation within the FCC matrix. However, further evaluation is required to fully quantify the precise contribution of these precipitates to the yield strength. Additionally, Figure 4-42b shows that δ phase is generated around twin boundaries, effectively preserving nanoscale annealed twins. Unfortunately, due to limitations in the EBSD grain size assessment (step size restriction), these annealed twins, which are tens of nanometers in size, cannot be identified. As a result, their actual sizes may be much smaller than what EBSD assesses, potentially making it challenging to apply the Hall-Patch equation for discussion. Moreover, there is currently no comprehensive study on how the abundance of annealed twins affects mechanical properties, and at best, it only suggests a trend of stronger materials with more annealed twins. In

doi:10.6342/NTU202302391

conclusion, through TEM image analysis, this work attributes the high yield strength to the presence of uniform and small nanoscale $L1_2$-$Ni_3(Al,Nb)$ precipitates and a large quantity of nanoscale annealed twins.

doi:10.6342/NTU202302391

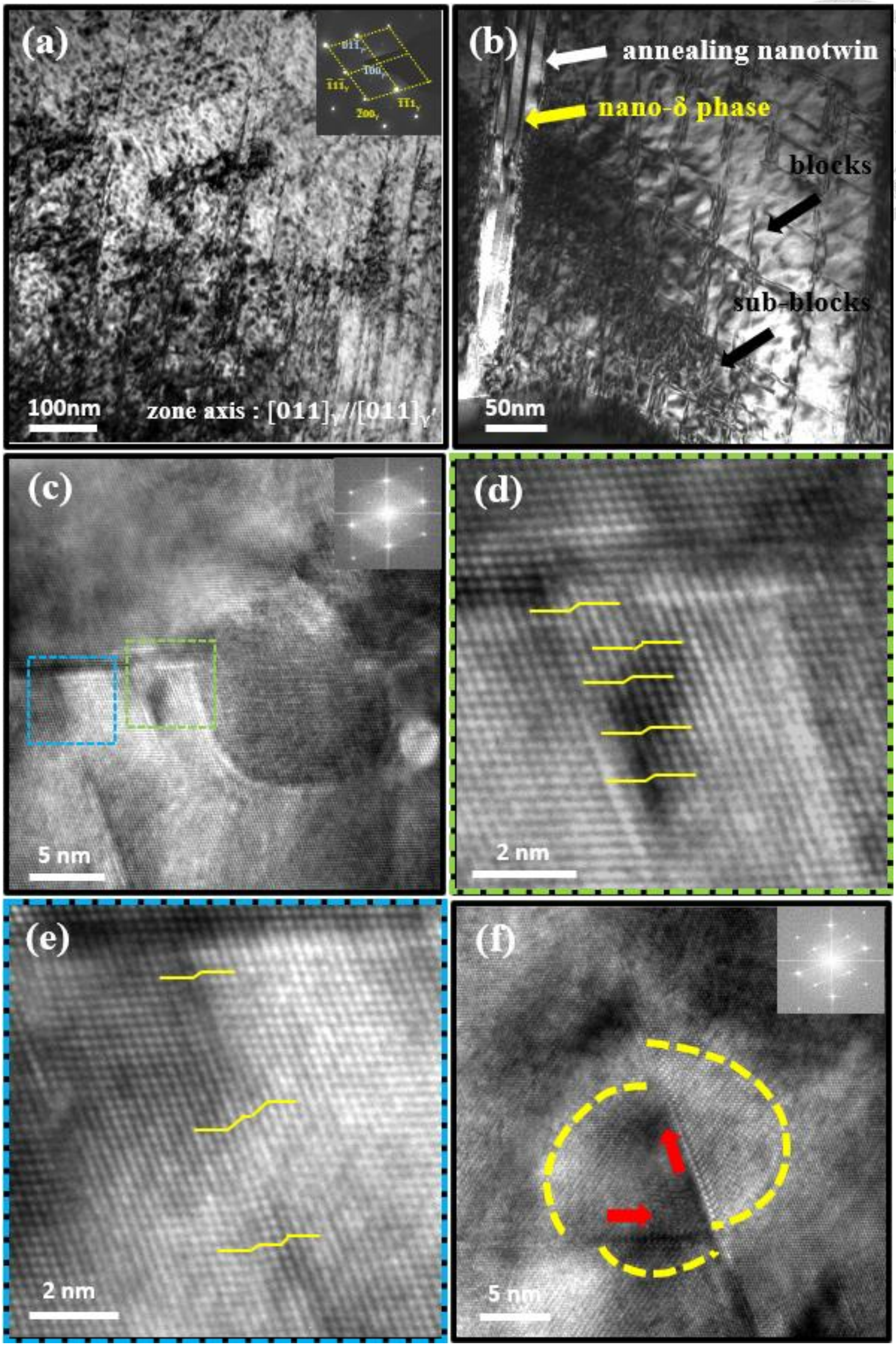

Figure 4-42 TEM analysis of $(CrCoNi)_{94}Al_3Nb_3$ deformed microstructure with 8% strain along [011] zone axis (a) less deformed area with single variant stacking-fault (b) severe deformed area with two variant stacking-fault (c) HRTEM image of sheared $L1_2$ particle (d) an enlarged micrograph of c, stacking-faults not located on the same plane. (e) an enlarged micrograph of c, nanotwins and stacking-faults coexist (f) $L1_2$ particles sheared by two variant stacking-faults.

doi:10.6342/NTU202302391

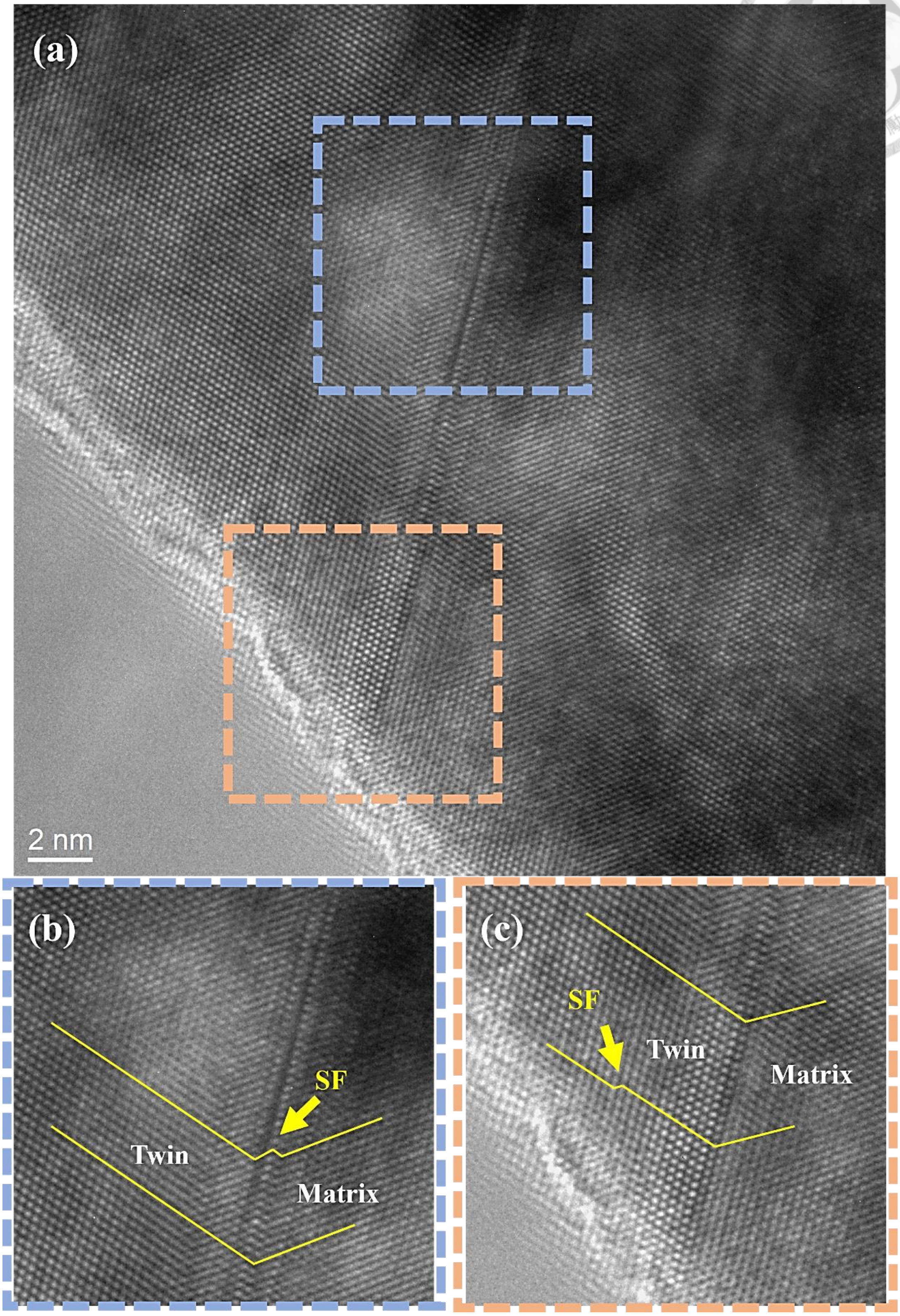

Figure 4-43 tensile test HRTEM image under [011] zone axis at fracture point in $(CrCoNi)_{94}Al_3Nb_3$ aging at 700^{o}C for 16 hours (a) small-scale HRTEM image (b) HRTEM image of blue square in a (c) HRTEM image of blue square in b.

doi:10.6342/NTU202302391

4.4.3 Hopkinson bar compression test

Figure 4-44 is the true stress-strain curve of Hopkinson compression test with $(CrCoNi)_{94}Al_3Nb_3$. Compared none-aged sample and peak-aged sample under the same strain rate ($\dot{\varepsilon}{\sim}5000$), the yield strength and ultimate tensile strength of none-aged sample are 629.3MPa and 1720MPa respectively. The yield strength and ultimate tensile strength of the samples aging at 700°C for 16 hours are 1018.6MPa and 2562.4MPa respectively. This result demonstrates that nano-$L1_2$ precipitates contribute around 400MPa in yield strength and 850Mpa in ultimate tensile strength. Compared peak-aged samples under different strain rate ($\dot{\varepsilon}{\sim}2500$ and $\dot{\varepsilon}{\sim}5000$), the yield strength and ultimate tensile strength under $\dot{\varepsilon}{\sim}2500$ are 817.4MPa and 2287.6MPa respectively. The yield strength and ultimate tensile strength of the peak-aged samples are 1018.6MPa and 2562.4MPa respectively. By increasing the strain rate, the yield strength and ultimate tensile strength increase around 200MPa and 300MPa respectively. Therefore, to achieve high strength in Hopkinson bar compression tests, nano-$L1_2$ precipitate and high strain rate play important roles in the compression tests.

Figure 4-45 is the work hardening rate of $(CrCoNi)_{94}Al_3Nb_3$ Hopkinson bar compression test. By comparing the results, the aging samples have better work hardening rate under the same strain rate. Furthermore, the higher strain rate demonstrates the higher work hardening rate.

doi:10.6342/NTU202302391

Figure 4-46 is the Hopkinson bar result of FeCrCoNi. Take the strength at 20% true strain in FeCrCoNi compared with the strength at 20% true strain in $(CrCoNi)_{94}Al_3Nb_3$, FeCrCoNi demonstrates around 1300MPa at 20% true strain under $\dot{\varepsilon}\sim 7000$, and $(CrCoNi)_{94}Al_3Nb_3$ shows around 2500MPa at 20% true strain under $\dot{\varepsilon}\sim 5000$. The strength increases almost two times for 1300MPa to 2500MPa. The results indicate that the nano-$L1_2$ precipitates did increase the strength a lot.

doi:10.6342/NTU202302391

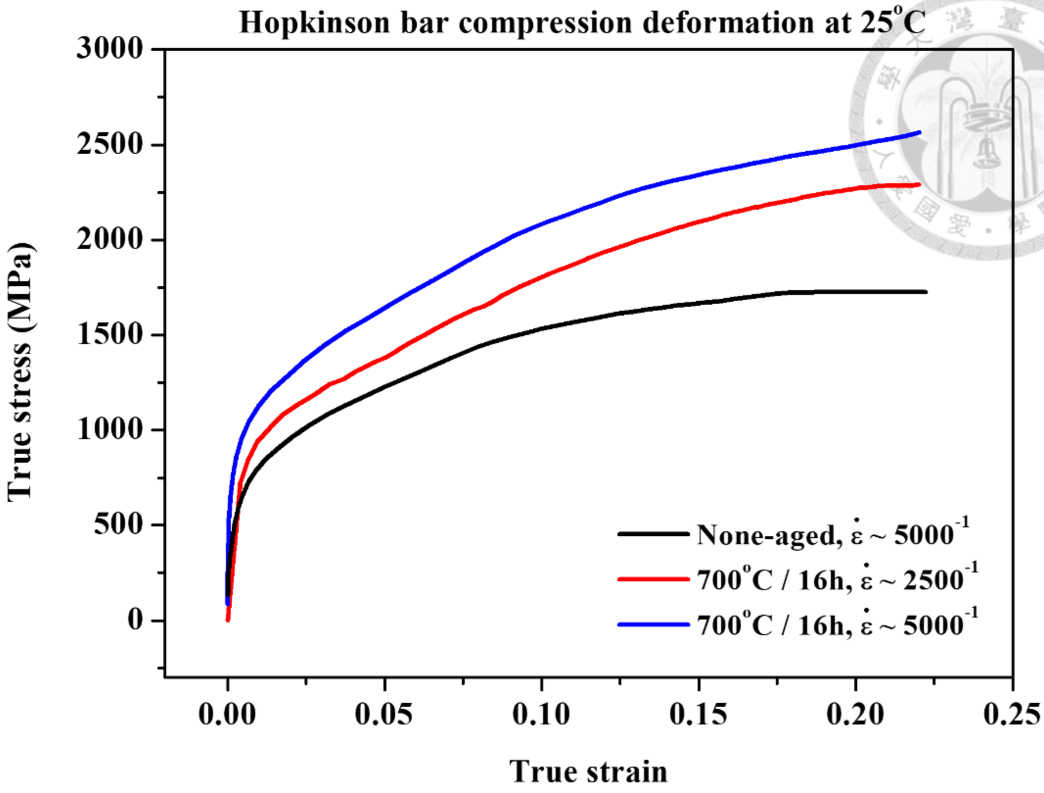

Figure 4-44 Hopkinson bar compression test true stress-strain curves.

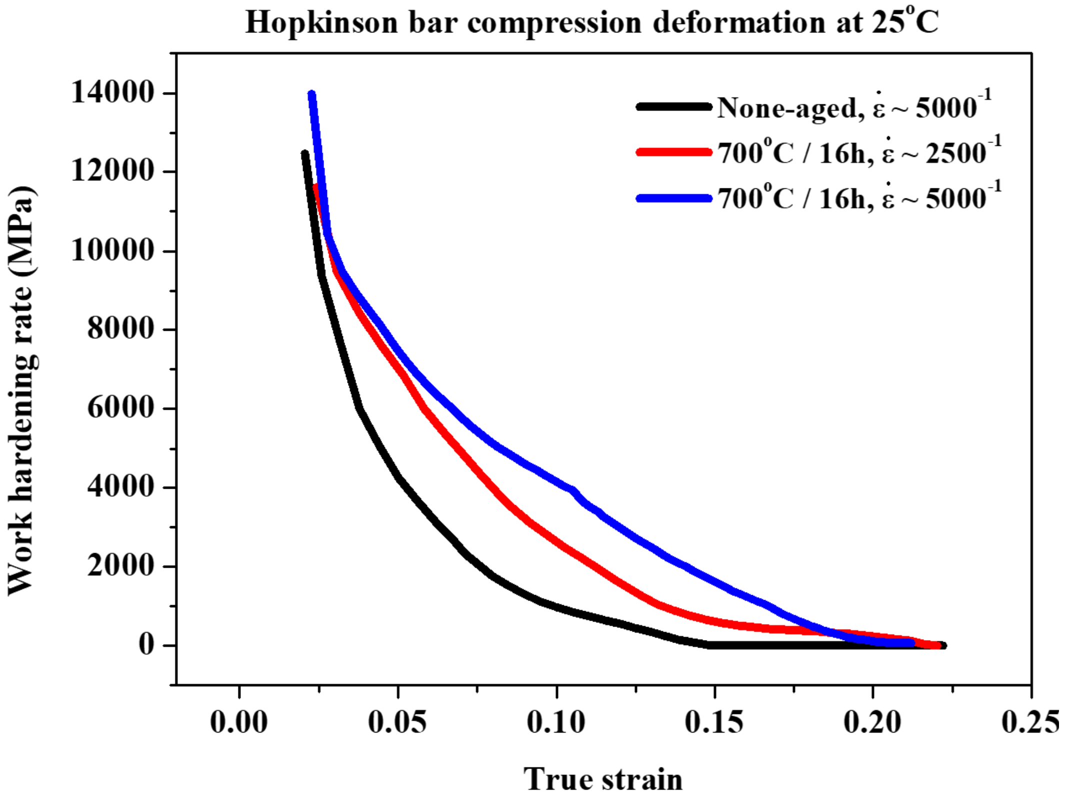

Figure 4-45 Hopkinson bar compression test work hardening rate.

doi:10.6342/NTU202302391

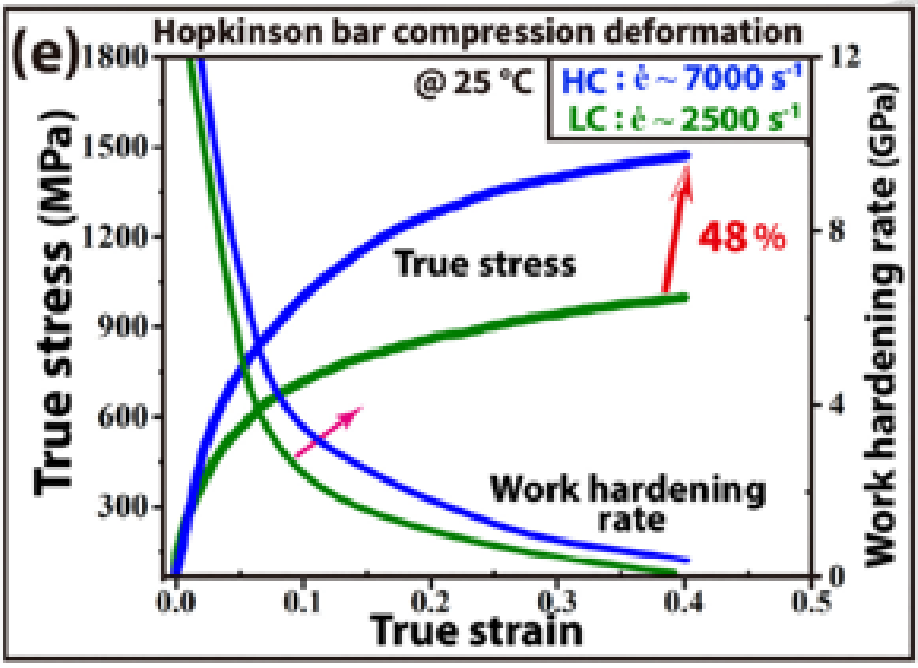

Figure 4-46 FeCrCoNi Hopkinson bar compression test true stress-strain curves and work hardening rate [111].

4.4.4 Hopkinson bar compression test microstructure characterization

Figure 4-47 is the deformation map depending on Zener-Holloman parameter (see Eq. 4-2). Zener-Holloman parameter considers strain rate and temperature as two major factors in affecting the deformed mechanism. Based on Figure 4-47, high strain rate and low temperature can induce twinning-based deformation. Therefore, Hopkinson bar compression test performs high strain rate deformation to distribute nano-twins in the materials.

$$Z = \dot{\varepsilon} \exp\left(\frac{Q}{RT}\right) \qquad \text{Eq. 4-2}$$

Figure 4-48 is the TEM image of $(CrCoNi)_{94}Al_3Nb_3$ after Hopkinson bar compression test with $\dot{\varepsilon}{\sim}5000$. In the right side, a lot of nanoscales stacking-faults can be observed. In the left side, there is a 70° between two variant stacking-faults representing two {110} glide planes under [110] zone axis inspection. The diffraction is taken by SAD selecting the middle of the left part and the right part. The twinning relationship can be analyzed under [011] zone axis.

To discuss the stacking-faults and nano-HCP in this material, HRTEM images were taken under [011] zone axis (see Figure 4-49). Deformation twins can be identified by specific atomic arrangement, ABCABACBA, a symmetric arrangement. There are deformation twins and nano-HCP with only 1nm and 2nm. The results indicate that the TWIP and TRIP effects play important roles in $(CrCoNi)_{94}Al_3Nb_3$. Finally, the matrix and the nano-HCP have a $[011]_{FCC}$ // $[2\bar{1}\bar{1}0]_{HCP}$ and $(111)_{FCC}$ // $(0001)_{HCP}$ orientation relationship.

The interaction of deformation twins and stacking faults to $L1_2$ precipitates is presented in Figure 4-50. The $L1_2$ precipitate has different lattice fringes to the matrix. A stacking-fault locates at the boundary of matrix and the $L1_2$ precipitate. Besides, a nanotwin takes the place of the right boundary of matrix and the $L1_2$ precipitate. However, none of the nanotwins and stacking-faults can be found in the precipitate. The results indicate that the precipitate can act as obstacles while deforming. Figure 4-51 demonstrates curvature boundaries after Hopkinson bar compression. A series of complex boundary aggregate together. This phenomenon also originated from the contribution of $L1_2$ precipitates acting like obstacles.

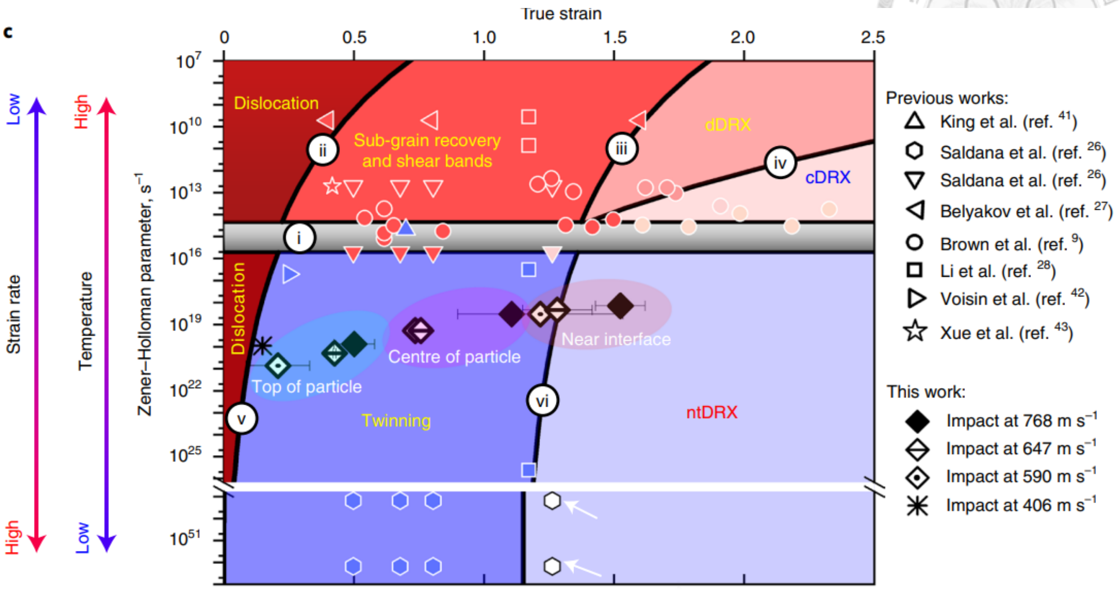

Figure 4-47 Deformation map depends on Zener-Holloman parameter [112].

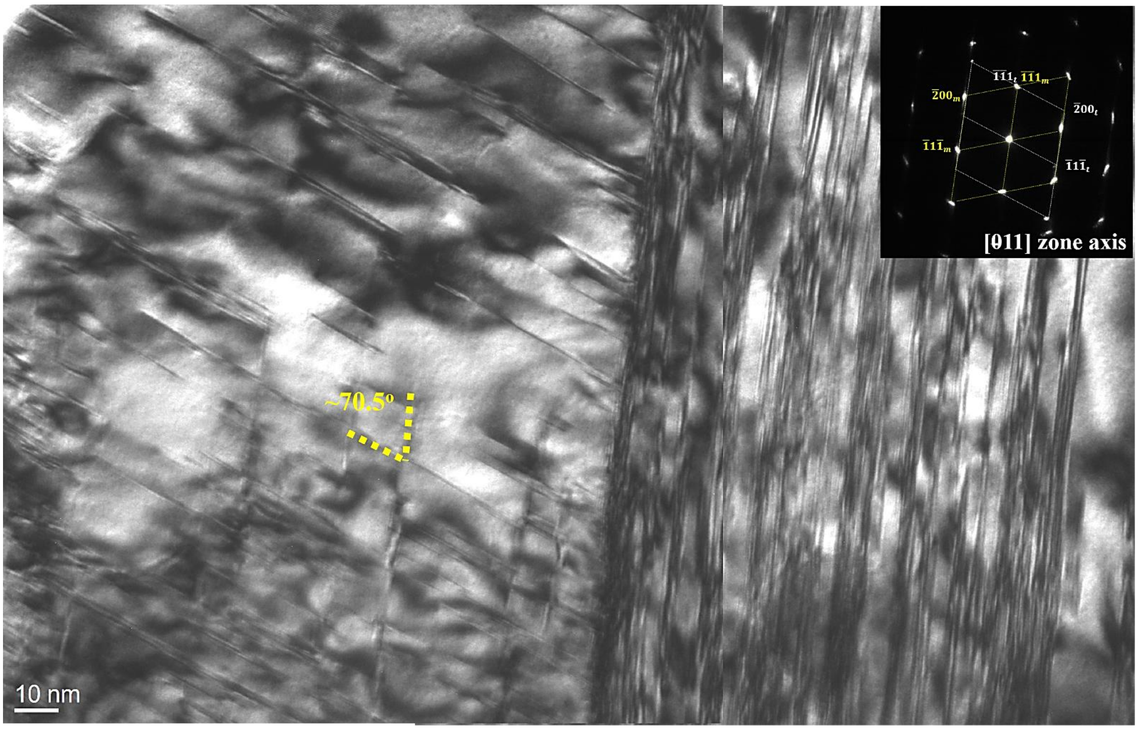

Figure 4-48 TEM image of $(CrCoNi)_{94}Al_3Nb_3$ after Hopkinson bar compression test with $\dot{\varepsilon}$~5000.

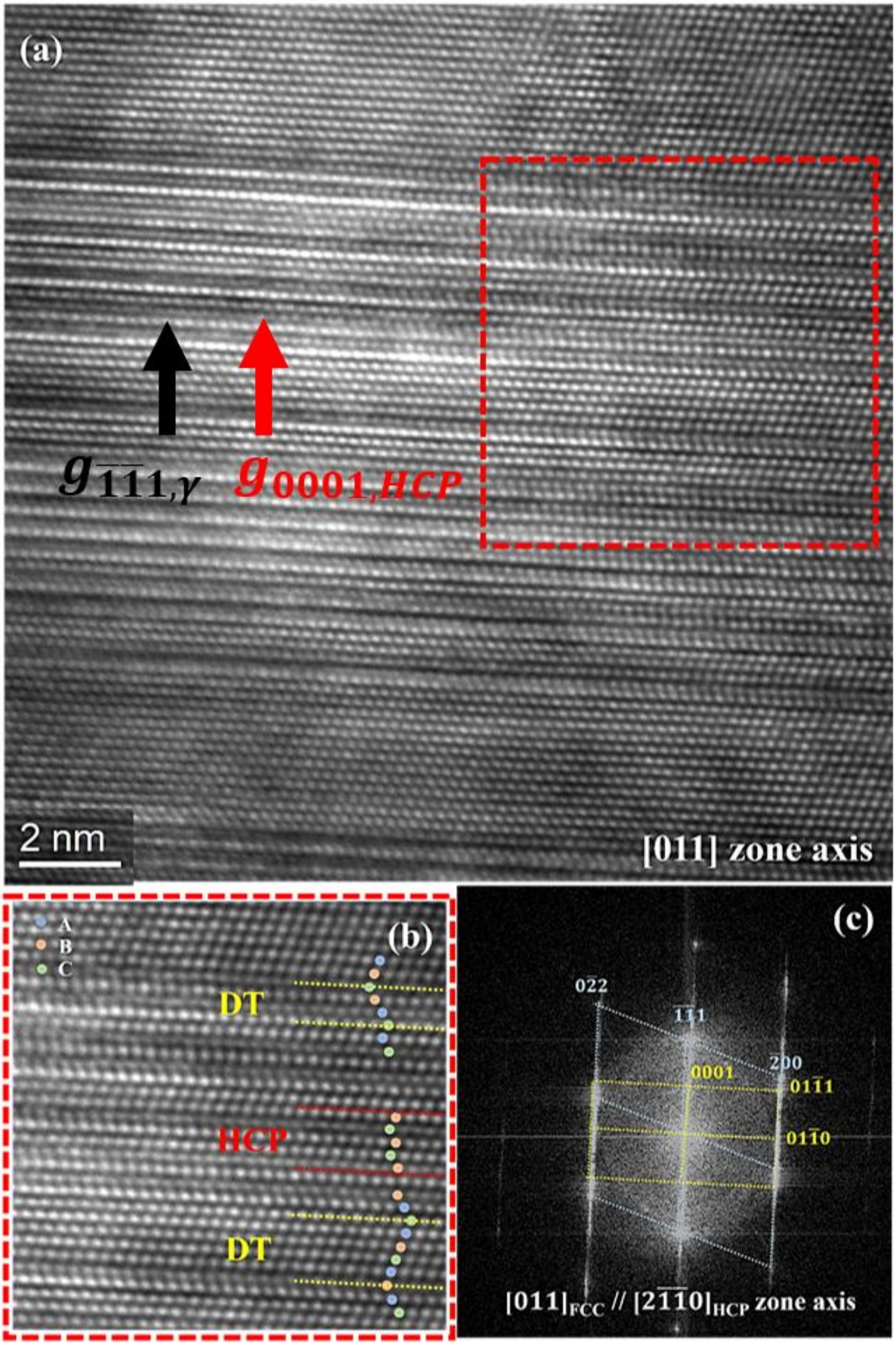

Figure 4-49 HRTEM image of $(CrCoNi)_{94}Al_3Nb_3$ after Hopkinson bar compression test with $\dot{\varepsilon}\sim5000$ (a) HRTEM image (b) deformation twin and HCP characterization (c) FFT of HRTEM in a.

doi:10.6342/NTU202302391

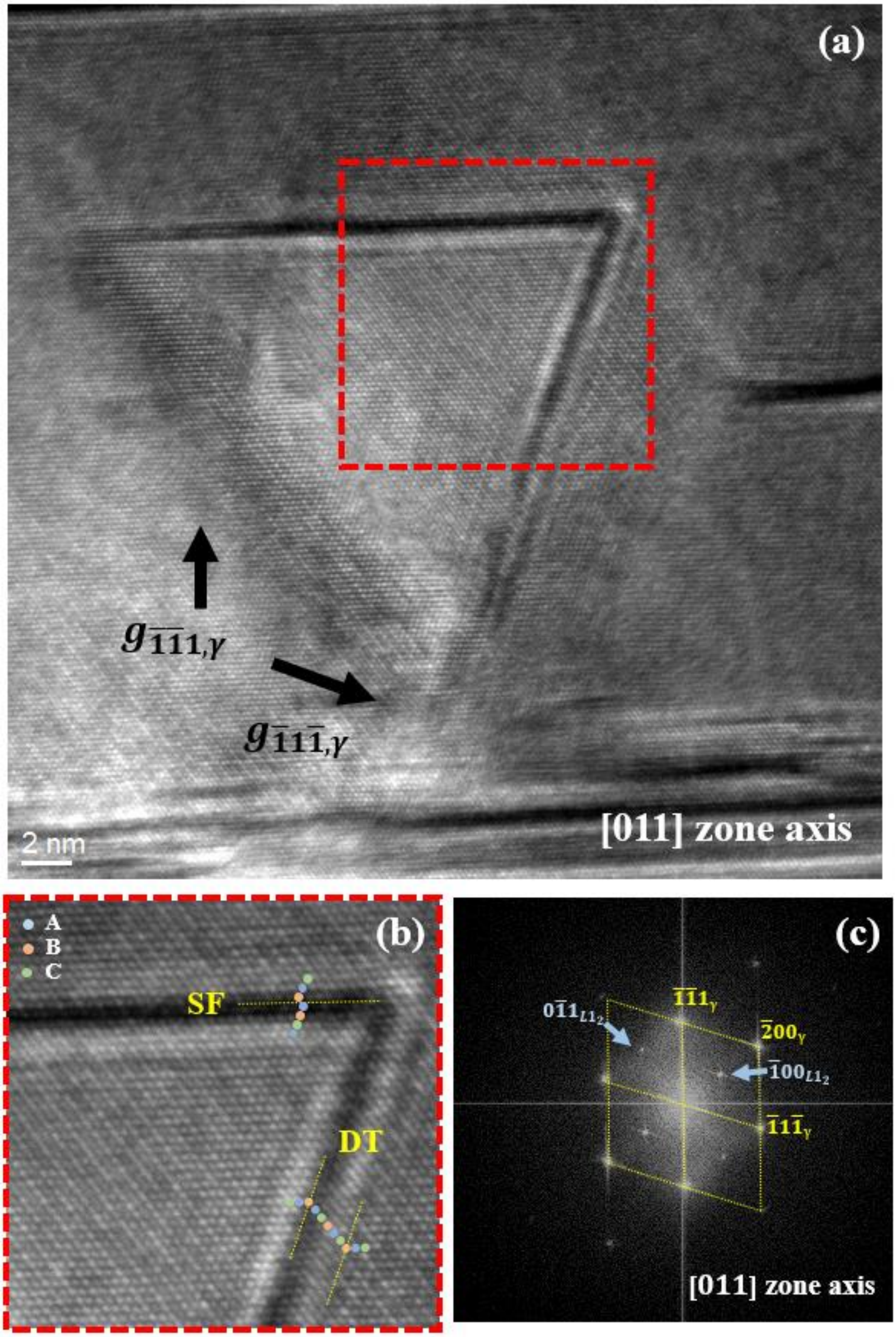

Figure 4-50 HRTEM images of L1$_2$ precipitate in (CrCoNi)$_{94}$Al$_3$Nb$_3$ after Hopkinson bar compression test with $\dot{\varepsilon}\sim5000$ (a) HRTEM image (b) deformation twin and stacking-fault characterization (c) FFT of HRTEM in a.

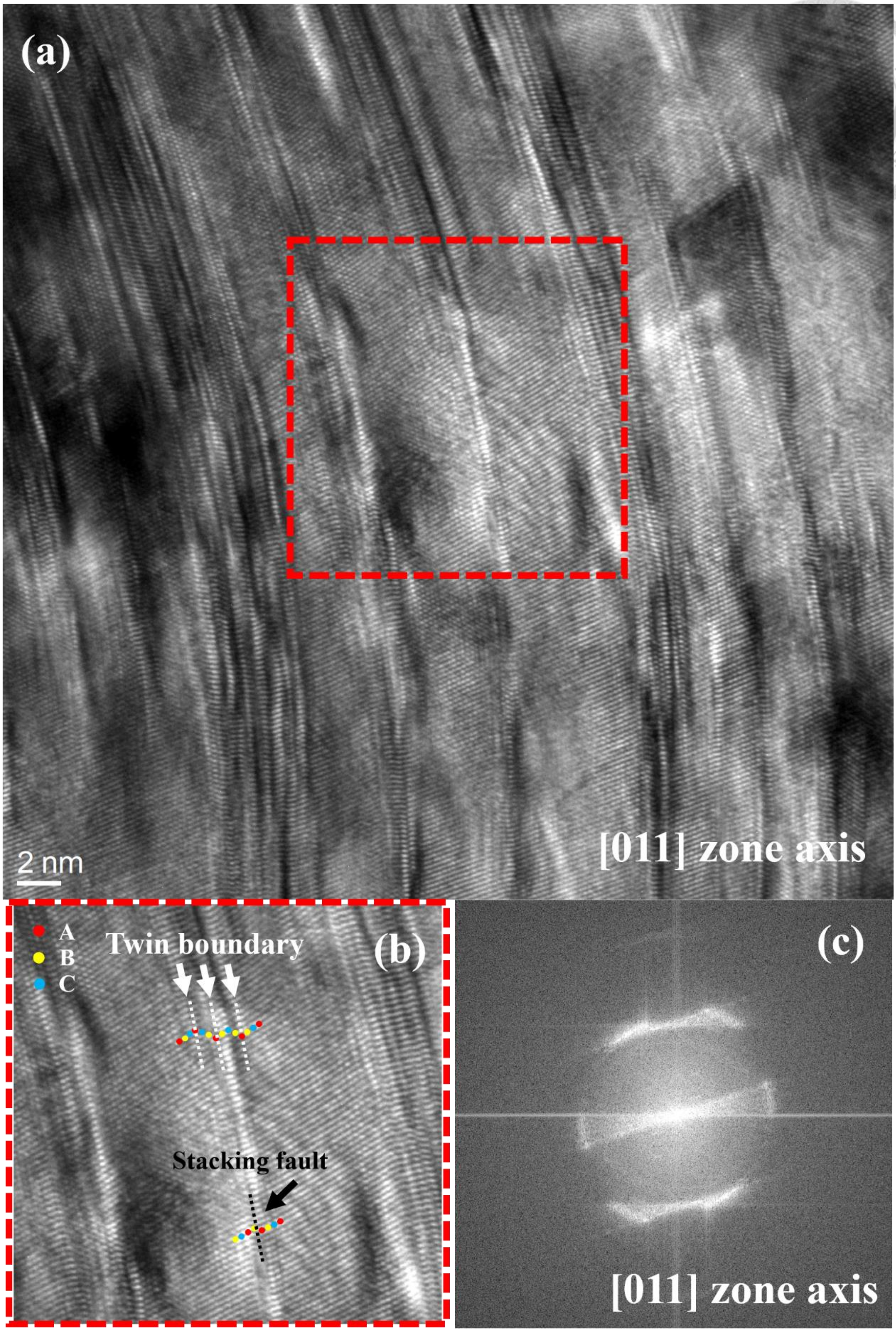

Figure 4-51 HRTEM image of complex twin boundary in (CrCoNi)$_{94}$Al$_3$Nb$_3$ after Hopkinson bar compression test with $\dot{\varepsilon}\sim5000$ (a) HRTEM image (b) deformation twin and HCP characterization (c) FFT of HRTEM in a.

4.5 Conclusion

In conclusion, this work investigates the design and characterization of a L1$_2$-precipitate hardening MEA, $(CrCoNi)_{94}Al_3Nb_3$. The study aims to improve the strength of FCC-based MEAs by introducing uniformly-distributed L1$_2$-Ni_3(Al,Nb) nano-precipitates in the FCC matrix. The experimental results and discussions provide valuable insights into the microstructure, mechanical properties, and deformation behavior of the alloy.

1. The pre-aging microstructure analysis reveals a recrystallized FCC matrix with annealing twins and the segregation of Nb-rich Laves phase. The presence of early-stage δ-Ni_3Nb at annealing twin boundaries is also observed. The addition of Nb effectively inhibits grain growth through pinning and drag effects, leading to a fine-grained microstructure.
2. The aging hardness measurements demonstrate a significant increase in hardness after peak aging treatments at 700°C and 800°C. The microstructure characterization reveals uniform and dense distributions of L1$_2$-Ni_3(Al,Nb) precipitates within the FCC matrix. The chemical composition analysis confirms the presence of L1$_2$-rich and L1$_2$-depleted regions. The interaction between L12 precipitates and defects during deformation is observed, indicating the hindrance

of defect development by $L1_2$ particles.

3. Tensile tests demonstrate remarkable mechanical properties of the $(CrCoNi)_{94}Al_3Nb_3$ alloy, including an exceptional yield strength (1412 ± 22 MPa) and a superior ultimate tensile strength (1553 ± 45 MPa) with an acceptable elongation (7.8 ± 0.94 %). The microstructure analysis of deformed samples shows the formation of deformation twins and stacking-faults, as well as the influence of δ-Ni_3Nb on the deformation behavior. The alloy exhibits high strength with limited ductility due to the segregation of Laves and δ phases.
4. Furthermore, the study provides early-stage evidence of δ-Ni3Nb transformation from $L1_2$ and the formation of disordered and ordered HCP phases in the FCC matrix. The disordered HCP phase is believed to originate from transformation-induced plasticity during the hot rolling process. The formation of ordered HCP precipitates is observed within the HCP matrix.

Overall, this research contributes to the understanding of $L1_2$-precipitate hardening in FCC-based MEAs and sheds light on the microstructural evolution, mechanical properties, and deformation mechanisms of the $(CrCoNi)_{94}Al_3Nb_3$ alloy. The findings suggest the potential for further optimization and development of high-performance MEAs with improved strength and ductility for various applications.

Chapter Five Future Works

In this work, uniform and fine nanoscale $L1_2$ precipitates were successfully formed in the FCC matrix, effectively increasing the yield strength of the FCC-type MEA, $(CrCoNi)_{94}Al_3Nb_3$ to approximately 1400 MPa. However, there are still areas for improvement.

1. In the tensile tests, the MEA exhibited limited ductility, with only about 8% strain to failure. Based on the previous TEM microstructure analysis, the embrittlement of the MEA is attributed to the segregation of Nb-rich phases at grain boundaries. In this study, two Nb-rich phases, Laves phase and δ phase, were identified. Firstly, excessive Nb addition beyond the MEA's supersaturated solubility leads to Laves phase segregation. Thus, reducing the Nb content from 3 at% to 1.5 at% below the supersaturated solubility is recommended to prevent Laves phase precipitation. Secondly, δ phase forms during annealing at temperatures between 750°C to 1050°C. To avoid δ phase formation, annealing at 900°C for one hour should be changed to 1100°C to achieve complete recrystallization and effectively suppress δ phase, especially at twin boundaries. In conclusion, reducing Nb content to 1.5 at% and changing the annealing temperature to 1100°C are expected to mitigate the segregation of Nb-rich phases in the MEA.

doi:10.6342/NTU202302391

2. Both the tensile and Hopkinson bar compressive tests in this study were conducted at 25°C. However, FCC-type MEAs can exhibit lower stacking fault energy and are more likely to develop deformation twins and stacking faults at lower temperatures, potentially leading to improved mechanical properties. Hence, it is recommended to conduct the tensile and Hopkinson bar impact tests at lower temperatures. Additionally, during the Hopkinson bar impact tests, the MEA exhibits significant energy absorption capacity. Attempts to increase the strain rate to explore its behavior at higher strain rates resulted in damage to the strain gauge on the Hopkinson bar, which cannot withstand the impact-induced shock waves, leading to repeated signal failures. Therefore, it is suggested to use strain gauges that can withstand intense shock waves and conduct Hopkinson bar impact tests at higher strain rates.
3. This work suggests that early-stage δ phase appears to evolve from $L1_2$ precipitates, supported by diffraction patterns obtained from TEM analysis, which shows an approximate 10^o rotation between $L1_2$ precipitates and the FCC matrix. However, further atomic EDS analysis is needed to confirm the elemental segregation in δ phase. For another phase identification, the study identified the formation of HCP phase precipitates in the HCP matrix. To definitively identify the HCP phase, observation from three different zone axes is necessary, as a single zone

doi:10.6342/NTU202302391

observation may not be sufficient. Therefore, it is recommended to examine the HCP microstructure from different orientations.

4. The FCC matrix contains numerous nanoscale $L1_2$ precipitates. However, in this study, the precise evaluation of precipitate size and volume fraction's impact on material mechanical properties was not performed. It is suggested to use EELS to measure the material thickness and assess precipitate density through appropriate zone-axis analysis. Furthermore, evaluating the effects of precipitate size and volume fraction on material properties would be beneficial.

doi:10.6342/NTU202302391

Supplementary Materials Crystal Structures of Phases in (CrCoNi)$_{94}$Al$_3$Nb$_3$

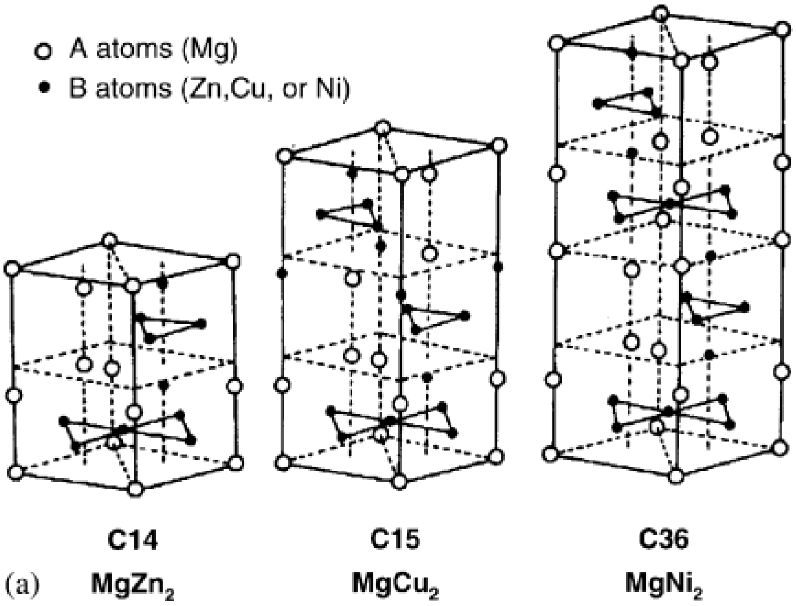

Supplementary Figure 1 Crystal structures of Laves phases [113].

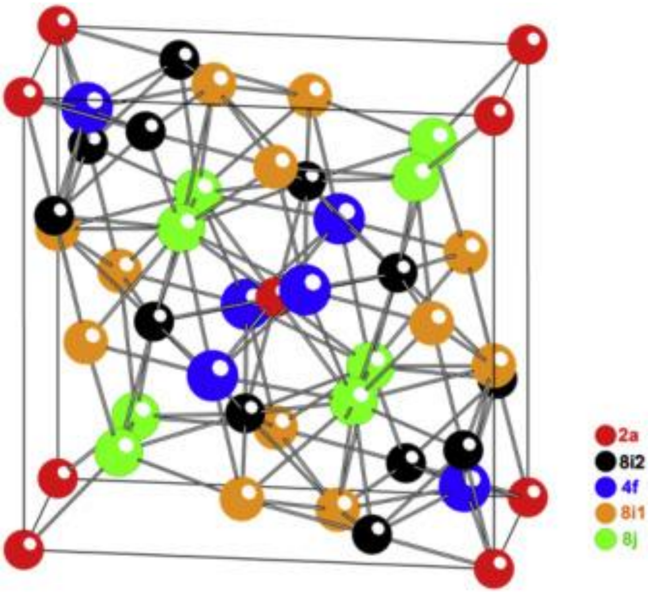

Supplementary Figure 2 Crystal structure of σ phase.

Supplementary Table 1 Crystal structural data of σ phase

Unit Cell Parameters					
a (Å)	b (Å)	c (Å)	α (degrees)	β (degrees)	γ (degrees)
8.80	8.80	4.45	90.0	90.0	90.0

Atomic Position				
Wyckoff	Element	x	y	z
2a	A	0	0.68	0
4f	B	0.40	x	0
8i	C	0.46	0.13	0
8i’	D	0.74	0.07	0
8j	E	0.18	x	0.25

Supplementary Table 2 Crystal structural data of δ phase

Unit Cell Parameters					
a (Å)	b (Å)	c (Å)	α (degrees)	β (degrees)	γ (degrees)
4.22	4.53	5.08	90.0	90.0	90.0

Atomic Position				
Wyckoff	Element	x	y	z
2a	Ni	0	0.68	0
2b	Nb	0	0.65	1/2
4e	Ni	1/2	0.84	0.25

doi:10.6342/NTU202302391

Reference

1. Yeh, J.W., et al., *Nanostructured high-entropy alloys with multiple principal elements: novel alloy design concepts and outcomes.* Advanced engineering materials, 2004. **6**(5): p. 299-303.
2. Cantor, B., et al., *Microstructural development in equiatomic multicomponent alloys.* Materials Science and Engineering: A, 2004. **375**: p. 213-218.
3. Tsai, M.-H. and J.-W. Yeh, *High-Entropy Alloys: A Critical Review.* Materials Research Letters, 2014. **2**(3): p. 107-123.
4. Youssef, K.M., et al., *A novel low-density, high-hardness, high-entropy alloy with close-packed single-phase nanocrystalline structures.* Materials Research Letters, 2015. **3**(2): p. 95-99.
5. Senkov, O.N., et al., *Mechanical properties of Nb25Mo25Ta25W25 and V20Nb20Mo20Ta20W20 refractory high entropy alloys.* Intermetallics, 2011. **19**(5): p. 698-706.
6. Schuh, B., et al., *Mechanical properties, microstructure and thermal stability of a nanocrystalline CoCrFeMnNi high-entropy alloy after severe plastic deformation.* Acta Materialia, 2015. **96**: p. 258-268.
7. Slone, C., et al., *Achieving ultra-high strength and ductility in equiatomic CrCoNi with partially recrystallized microstructures.* Acta Materialia, 2019. **165**: p. 496-507.
8. Hsieh, K.-C., et al., *The microstructure and phase equilibrium of new high performance high-entropy alloys.* Journal of Alloys and Compounds, 2009. **483**(1-2): p. 209-212.
9. He, J., et al., *A precipitation-hardened high-entropy alloy with outstanding tensile properties.* Acta Materialia, 2016. **102**: p. 187-196.
10. Gludovatz, B., et al., *Exceptional damage-tolerance of a medium-entropy alloy CrCoNi at cryogenic temperatures.* Nature communications, 2016. **7**(1): p. 10602.
11. Gan, B., et al., *Superb cryogenic strength of equiatomic CrCoNi derived from gradient hierarchical microstructure.* Journal of Materials Science & Technology, 2019. **35**(6): p. 957-961.
12. Zou, Y., et al., *Size-dependent plasticity in an Nb25Mo25Ta25W25 refractory high-entropy alloy.* Acta Materialia, 2014. **65**: p. 85-97.
13. Senkov, O., et al., *Refractory high-entropy alloys.* Intermetallics, 2010. **18**(9): p. 1758-1765.

14. Nene, S., et al., *Corrosion-resistant high entropy alloy with high strength and ductility.* Scripta Materialia, 2019. **166**: p. 168-172.
15. Qiu, X.-W., et al., *Microstructure and corrosion resistance of AlCrFeCuCo high entropy alloy.* Journal of alloys and compounds, 2013. **549**: p. 195-199.
16. Shi, Y., B. Yang, and P.K. Liaw, *Corrosion-resistant high-entropy alloys: A review.* Metals, 2017. **7**(2): p. 43.
17. Youssef, K., et al., *Effect of stacking fault energy on mechanical behavior of bulk nanocrystalline Cu and Cu alloys.* Acta Materialia, 2011. **59**(14): p. 5758-5764.
18. Kubilay, R.E. and W. Curtin, *Theory of twin strengthening in fcc high entropy alloys.* Acta Materialia, 2021. **216**: p. 117119.
19. Mahajan, S. and G. Chin, *Formation of deformation twins in fcc crystals.* Acta metallurgica, 1973. **21**(10): p. 1353-1363.
20. Su, J., D. Raabe, and Z. Li, *Hierarchical microstructure design to tune the mechanical behavior of an interstitial TRIP-TWIP high-entropy alloy.* Acta Materialia, 2019. **163**: p. 40-54.
21. Okamoto, N.L., et al., *Size effect, critical resolved shear stress, stacking fault energy, and solid solution strengthening in the CrMnFeCoNi high-entropy alloy.* Scientific reports, 2016. **6**(1): p. 35863.
22. Laplanche, G., et al., *Reasons for the superior mechanical properties of medium-entropy CrCoNi compared to high-entropy CrMnFeCoNi.* Acta Materialia, 2017. **128**: p. 292-303.
23. Liu, S., et al., *Stacking fault energy of face-centered-cubic high entropy alloys.* Intermetallics, 2018. **93**: p. 269-273.
24. Otto, F., et al., *The influences of temperature and microstructure on the tensile properties of a CoCrFeMnNi high-entropy alloy.* Acta Materialia, 2013. **61**(15): p. 5743-5755.
25. Liu, D., et al., *Exceptional fracture toughness of CrCoNi-based medium-and high-entropy alloys at 20 kelvin.* Science, 2022. **378**(6623): p. 978-983.
26. Zhang, R., et al., *Short-range order and its impact on the CrCoNi medium-entropy alloy.* Nature, 2020. **581**(7808): p. 283-287.
27. Schneider, M., et al., *Analysis of strengthening due to grain boundaries and annealing twin boundaries in the CrCoNi medium-entropy alloy.* International Journal of Plasticity, 2020. **124**: p. 155-169.
28. Shankar, V., K.B.S. Rao, and S. Mannan, *Microstructure and mechanical properties of Inconel 625 superalloy.* Journal of nuclear materials, 2001. **288**(2-3): p. 222-232.
29. Zhao, S., et al., *Microstructural stability and mechanical properties of a new nickel-based superalloy.* Materials Science and Engineering: A, 2003. **355**(1-2):

p. 96-105.

30. Pollock, T.M. and S. Tin, *Nickel-based superalloys for advanced turbine engines: chemistry, microstructure and properties.* Journal of propulsion and power, 2006. **22**(2): p. 361-374.

31. Wu, Q., et al., *Microstructure of long-term aged IN617 Ni-base superalloy.* Metallurgical and materials transactions A, 2008. **39**(11): p. 2569-2585.

32. Akca, E. and A. Gürsel, *A review on superalloys and IN718 nickel-based INCONEL superalloy.* Periodicals of engineering and natural sciences, 2015. **3**(1).

33. Zhao, Y.L., et al., *Heterogeneous precipitation behavior and stacking-fault-mediated deformation in a CoCrNi-based medium-entropy alloy.* Acta Materialia, 2017. **138**: p. 72-82.

34. Shun, T.-T., et al., *Age heat treatment of the CoCrFeNiTi0. 3 high-entropy alloy.* Materials transactions, 2018. **59**(5): p. 730-733.

35. Tong, Y., et al., *Outstanding tensile properties of a precipitation-strengthened FeCoNiCrTi0. 2 high-entropy alloy at room and cryogenic temperatures.* Acta Materialia, 2019. **165**: p. 228-240.

36. Zhou, J., et al., *Excellent strength-ductility in Ti-alloyed Fe35Ni35Cr20Mn10 high-entropy alloy.* Intermetallics, 2022. **148**: p. 107637.

37. Hung, W.-J., T.-T. Shun, and C.-J. Chiang, *Effects of reducing Co content on microstructure and mechanical properties of CoxCrFeNiTi0. 3 high-entropy alloys.* Materials Chemistry and Physics, 2018. **210**: p. 170-175.

38. Clementi, E. and D.-L. Raimondi, *Atomic screening constants from SCF functions.* The Journal of Chemical Physics, 1963. **38**(11): p. 2686-2689.

39. Zhao, Y., et al., *Heterogeneous precipitation behavior and stacking-fault-mediated deformation in a CoCrNi-based medium-entropy alloy.* Acta Materialia, 2017. **138**: p. 72-82.

40. Chen, D., et al., *Synergistic effect of Ti and Al on L12-phase design in CoCrFeNi-based high entropy alloys.* Intermetallics, 2019. **110**: p. 106476.

41. Wang, Z., et al., *Effect of coherent L12 nanoprecipitates on the tensile behavior of a fcc-based high-entropy alloy.* Materials Science and Engineering: A, 2017. **696**: p. 503-510.

42. Yang, T., et al., *L12-strengthened high-entropy alloys for advanced structural applications.* Journal of Materials Research, 2018. **33**(19): p. 2983-2997.

43. Slone, C., et al., *Deactivating deformation twinning in medium-entropy CrCoNi with small additions of aluminum and titanium.* Scripta Materialia, 2020. **178**: p. 295-300.

44. Hsu, C.-y., et al., *Wear resistance and high-temperature compression strength*

of Fcc CuCoNiCrAl0. 5Fe alloy with boron addition. Metallurgical and Materials Transactions A, 2004. **35**(5): p. 1465-1469.

45. Tsai, K.-Y., M.-H. Tsai, and J.-W. Yeh, *Sluggish diffusion in co–cr–fe–mn–ni high-entropy alloys.* Acta Materialia, 2013. **61**(13): p. 4887-4897.
46. Tong, C.-J., et al., *Microstructure characterization of Al x CoCrCuFeNi high-entropy alloy system with multiprincipal elements.* Metallurgical and Materials Transactions A, 2005. **36**(4): p. 881-893.
47. Tong, C.-J., et al., *Mechanical performance of the Al x CoCrCuFeNi high-entropy alloy system with multiprincipal elements.* Metallurgical and Materials Transactions A, 2005. **36**(5): p. 1263-1271.
48. Zhang, Y., et al., *Solid-solution phase formation rules for multi-component alloys.* Advanced engineering materials, 2008. **10**(6): p. 534-538.
49. Sheng, G. and C.T. Liu, *Phase stability in high entropy alloys: Formation of solid-solution phase or amorphous phase.* Progress in Natural Science: Materials International, 2011. **21**(6): p. 433-446.
50. J.-W. Yeh, S.-K.C., S.-J. Lin,J.-Y. Gan,T.-S. Chin,T.-T. Shun,C.-H. Tsau,S.-Y. Chang, *Nanostructured High-Entropy Alloys with Multiple Principal Elements: Novel Alloy Design Concepts and Outcomes.* Advanced Engineering Materials, 2004.
51. CHUNG-JIN TONG, Y.-L.C., SWE-KAI CHEN, JIEN-WEI YEH, and C.-H.T. TAO-TSUNG SHUN, SU-JIEN LIN and SHOU-YI CHANG, *Microstructure Characterization of AlxCoCrCuFeNi High-Entropy Alloy System with Multiprincipal Elements.* METALLURGICAL AND MATERIALS TRANSACTIONS A, 2005. **36A**.
52. Zhang, Y., S.G. Ma, and J.W. Qiao, *Morphology Transition from Dendrites to Equiaxed Grains for AlCoCrFeNi High-Entropy Alloys by Copper Mold Casting and Bridgman Solidification.* Metallurgical and Materials Transactions A, 2012. **43**(8): p. 2625-2630.
53. Laplanche, G., et al., *Microstructure evolution and critical stress for twinning in the CrMnFeCoNi high-entropy alloy.* Acta Materialia, 2016. **118**: p. 152-163.
54. Laplanche, G., et al., *Reasons for the superior mechanical properties of medium-entropy CrCoNi compared to high-entropy CrMnFeCoNi.* Acta Materialia, 2017. **128**: p. 292-303.
55. Chang, H., et al., *Novel Si-added CrCoNi medium entropy alloys achieving the breakthrough of strength-ductility trade-off.* Materials & Design, 2021. **197**: p. 109202.
56. Miao, J., et al., *Ordering effects on deformation substructures and strain hardening behavior of a CrCoNi based medium entropy alloy.* Acta Materialia, 2021. **210**.

doi:10.6342/NTU202302391

57. Locq, D. and P. Caron, *On some advanced nickel-based superalloys for disk applications.* Aerospace Lab, 2011(3): p. p. 1-9.
58. Ding, Q., et al., *Re segregation at interfacial dislocation network in a nickel-based superalloy.* Acta Materialia, 2018. **154**: p. 137-146.
59. Sims, C. and N. Stoloff, *WC Hagel in Superalloys II*. 1986, Wiley, New York.
60. Sims, C.T., N.S. Stoloff, and W.C. Hagel, *superalloys II*. Vol. 8. 1987: Wiley New York.
61. Durand-Charre, M., *The Microstructure of Superalloys, Gordon and Breach*. 1997, Amsterdam.
62. Biermann, H., M. Strehler, and H. Mughrabi, *High-temperature X-ray measurements of the lattice mismatch of creep-deformed monocrystals of the nickel-base superalloy SRR99.* Scripta metallurgica et materialia, 1995. **32**(9): p. 1405-1410.
63. Biermann, H., M. Strehler, and H. Mughrabi, *High-temperature measurements of lattice parameters and internal stresses of a creep-deformed monocrystalline nickel-base superalloy.* Metallurgical and Materials Transactions A, 1996. **27**(4): p. 1003-1014.
64. Volek, A., et al., *Partitioning of Re between γ and γ´ phase in nickel-base superalloys.* Scripta Materialia, 2005. **52**(2): p. 141-145.
65. Van Sluytman, J. and T. Pollock, *Optimal precipitate shapes in nickel-base γ－γ´ alloys.* Acta Materialia, 2012. **60**(4): p. 1771-1783.
66. Ru, Y., et al., *Interdendritic Mo homogenization and sub-solidus melting during solution treatment in the Mo-strengthening single crystal superalloys.* Journal of Alloys and Compounds, 2016. **662**: p. 431-435.
67. Cheng, K., et al., *Precipitation behavior of μ phase and creep rupture in single crystal superalloy CMSX-4.* Journal of Alloys and Compounds, 2011. **509**(25): p. 7078-7086.
68. Lv, X., J. Zhang, and Q. Feng, *The promotion of Ru on topologically close-packed phase precipitation in the high Cr-containing (～9wt.%) nickel-base single crystal superalloy.* Journal of Alloys and Compounds, 2015. **648**: p. 853-857.
69. Long, H., et al., *Minimum interface misfit criterion for the precipitation morphologies of TCP phases in a Ni-based single crystal superalloy.* Intermetallics, 2018. **94**: p. 55-64.
70. Gwalani, B., et al., *Optimizing the coupled effects of Hall-Petch and precipitation strengthening in a Al0. 3CoCrFeNi high entropy alloy.* Materials & Design, 2017. **121**: p. 254-260.
71. Gwalani, B., et al., *Cu assisted stabilization and nucleation of L12 precipitates in Al0. 3CuFeCrNi2 fcc-based high entropy alloy.* Acta Materialia, 2017. **129**: p.

170-182.

72. Borkar, T., et al., *A combinatorial assessment of AlxCrCuFeNi2 (0< x< 1.5) complex concentrated alloys: Microstructure, microhardness, and magnetic properties.* Acta Materialia, 2016. **116**: p. 63-76.
73. Antonov, S., M. Detrois, and S. Tin, *Design of novel precipitate-strengthened Al-Co-Cr-Fe-Nb-Ni high-entropy superalloys.* Metallurgical and Materials Transactions A, 2018. **49**(1): p. 305-320.
74. Ma, S. and Y. Zhang, *Effect of Nb addition on the microstructure and properties of AlCoCrFeNi high-entropy alloy.* Materials Science and Engineering: A, 2012. **532**: p. 480-486.
75. Tsao, T.-K., A.-C. Yeh, and H. Murakami, *The Microstructure Stability of Precipitation Strengthened Medium to High Entropy Superalloys.* Metallurgical and Materials Transactions A, 2017. **48**(5): p. 2435-2442.
76. Takeuchi, A. and A. Inoue, *Classification of bulk metallic glasses by atomic size difference, heat of mixing and period of constituent elements and its application to characterization of the main alloying element.* Materials transactions, 2005. **46**(12): p. 2817-2829.
77. Karunaratne, M., C. Rae, and R. Reed, *On the microstructural instability of an experimental nickel-based single-crystal superalloy.* Metallurgical and Materials transactions A, 2001. **32**(10): p. 2409-2421.
78. Ritzert, F., D. Keller, and V. Vasudevan, *Investigation of the Formation of Topologically Close Packed Phase Instabilities in Nickel-Based Superalloy Rene N6*. 1999.
79. Zhao, J.-C., M. Larsen, and V. Ravikumar, *Phase precipitation and time–temperature-transformation diagram of Hastelloy X.* Materials Science and Engineering: A, 2000. **293**(1-2): p. 112-119.
80. Yeh, A., et al., *Developing an advanced Si-bearing DS Ni-base superalloy.* Journal of alloys and compounds, 2014. **585**: p. 614-621.
81. Otto, F., et al., *Relative effects of enthalpy and entropy on the phase stability of equiatomic high-entropy alloys.* Acta Materialia, 2013. **61**(7): p. 2628-2638.
82. Troparevsky, M.C., et al., *Criteria for Predicting the Formation of Single-Phase High-Entropy Alloys.* Physical Review X, 2015. **5**(1).
83. Zhao, Y., et al., *Thermal stability and coarsening of coherent particles in a precipitation-hardened (NiCoFeCr) 94Ti2Al4 high-entropy alloy.* Acta Materialia, 2018. **147**: p. 184-194.
84. Fu, B., et al., *Deformation mechanisms in a Co-rich nickel based superalloy with different size of γ′ precipitates.* Materials Letters, 2015. **152**: p. 272-275.
85. Chaturvedi, M., D. Lloyd, and D. Chung, *Yielding behaviour of γ´-*

precipitation-strengthened Co − Ni − Cr superalloys. Metal Science, 1976. **10**(11): p. 373-378.

86. Reppich, B., P. Schepp, and G. Wehner, *Some new aspects concerning particle hardening mechanisms in γ'precipitating nickel-base alloys—II. Experiments.* Acta Metallurgica, 1982. **30**(1): p. 95-104.

87. Miao, J., T.M. Pollock, and J.W. Jones, *Microstructural extremes and the transition from fatigue crack initiation to small crack growth in a polycrystalline nickel-base superalloy.* Acta Materialia, 2012. **60**(6-7): p. 2840-2854.

88. Hansen, N. and D. Kuhlmann-Wilsdorf, *Low energy dislocation structures due to unidirectional deformation at low temperatures.* Materials Science and Engineering, 1986. **81**: p. 141-161.

89. Chen, H.S., J.J. Gilman, and A. Head, *Dislocation Multipoles and Their Role in Strain-Hardening.* Journal of Applied Physics, 1964. **35**(8): p. 2502-2514.

90. Miao, J., et al., *The evolution of the deformation substructure in a Ni-Co-Cr equiatomic solid solution alloy.* Acta Materialia, 2017. **132**: p. 35-48.

91. Byun, T., *On the stress dependence of partial dislocation separation and deformation microstructure in austenitic stainless steels.* Acta Materialia, 2003. **51**(11): p. 3063-3071.

92. Gerold, V. and H. Karnthaler, *On the origin of planar slip in fcc alloys.* Acta Metallurgica, 1989. **37**(8): p. 2177-2183.

93. Idrissi, H., et al., *On the mechanism of twin formation in Fe–Mn–C TWIP steels.* Acta Materialia, 2010. **58**(7): p. 2464-2476.

94. Kamikawa, N., et al., *Stress–strain behavior of ferrite and bainite with nano-precipitation in low carbon steels.* Acta Materialia, 2015. **83**: p. 383-396.

95. Fleischer, R.L., *Substitutional solution hardening.* Acta metallurgica, 1963. **11**(3): p. 203-209.

96. Courtney, T.H., *Mechanical behavior of materials*. 2005: Waveland Press.

97. Toda-Caraballo, I. and P.E. Rivera-Díaz-del-Castillo, *Modelling solid solution hardening in high entropy alloys.* Acta Materialia, 2015. **85**: p. 14-23.

98. Schuh, C., T. Nieh, and H. Iwasaki, *The effect of solid solution W additions on the mechanical properties of nanocrystalline Ni.* Acta Materialia, 2003. **51**(2): p. 431-443.

99. Hall, E., *The deformation and ageing of mild steel: III discussion of results.* Proceedings of the Physical Society. Section B, 1951. **64**(9): p. 747.

100. Williamson, G. and W. Hall, *X-ray line broadening from filed aluminium and wolfram.* Acta metallurgica, 1953. **1**(1): p. 22-31.

101. Williamson, G. and R. Smallman, *III. Dislocation densities in some annealed and*

cold-worked metals from measurements on the X-ray debye-scherrer spectrum. Philosophical magazine, 1956. **1**(1): p. 34-46.

102. Karolus, M. and E. Łągiewka, *Crystallite size and lattice strain in nanocrystalline Ni–Mo alloys studied by Rietveld refinement.* Journal of Alloys and Compounds, 2004. **367**(1-2): p. 235-238.
103. Kumari, S., D.K. Singh, and P. Giri, *Strain anisotropy in freestanding germanium nanoparticles synthesized by ball milling.* Journal of Nanoscience and Nanotechnology, 2009. **9**(9): p. 5231-5236.
104. Zhao, Y., et al., *Microstructures and mechanical properties of ultrafine grained 7075 Al alloy processed by ECAP and their evolutions during annealing.* Acta Materialia, 2004. **52**(15): p. 4589-4599.
105. Wen, H., et al., *Strengthening mechanisms in a high-strength bulk nanostructured Cu–Zn–Al alloy processed via cryomilling and spark plasma sintering.* Acta Materialia, 2013. **61**(8): p. 2769-2782.
106. Ma, K., et al., *Mechanical behavior and strengthening mechanisms in ultrafine grain precipitation-strengthened aluminum alloy.* Acta Materialia, 2014. **62**: p. 141-155.
107. Seidman, D.N., E.A. Marquis, and D.C. Dunand, *Precipitation strengthening at ambient and elevated temperatures of heat-treatable Al (Sc) alloys.* Acta Materialia, 2002. **50**(16): p. 4021-4035.
108. Booth-Morrison, C., D.C. Dunand, and D.N. Seidman, *Coarsening resistance at 400 C of precipitation-strengthened Al–Zr–Sc–Er alloys.* Acta Materialia, 2011. **59**(18): p. 7029-7042.
109. Pollock, T. and A. Argon, *Creep resistance of CMSX-3 nickel base superalloy single crystals.* Acta Metallurgica et Materialia, 1992. **40**(1): p. 1-30.
110. Knorovsky, G., et al., *Inconel 718: a solidification diagram.* Metallurgical transactions A, 1989. **20**(10): p. 2149-2158.
111. Chung, T.-F., et al., *Hierarchical nanotwins in Fe27Co24Ni23Cr26 high-entropy alloy subjected to high strain-rate Hopkinson bar deformation.* Materials Characterization, 2022. **185**: p. 111737.
112. Tiamiyu, A.A., et al., *Nanotwinning-assisted dynamic recrystallization at high strains and strain rates.* Nature Materials, 2022. **21**(7): p. 786-794.
113. Stein, F., M. Palm, and G. Sauthoff, *Structure and stability of Laves phases. Part I. Critical assessment of factors controlling Laves phase stability.* Intermetallics, 2004. **12**(7-9): p. 713-720.